Improving earthquake forecast models for PSHA with geodetic data, applied on Ecuador

Judith Mariniere

▶ To cite this version:

Judith Mariniere. Improving earthquake forecast models for PSHA with geodetic data, applied on Ecuador. Earth Sciences. Université Grenoble Alpes [2020-..], 2020. English. NNT : 2020GRALU019 . tel-03276307

HAL Id: tel-03276307
https://theses.hal.science/tel-03276307

Submitted on 2 Jul 2021

HAL is a multi-disciplinary open access archive for the deposit and dissemination of scientific research documents, whether they are published or not. The documents may come from teaching and research institutions in France or abroad, or from public or private research centers.

L'archive ouverte pluridisciplinaire **HAL**, est destinée au dépôt et à la diffusion de documents scientifiques de niveau recherche, publiés ou non, émanant des établissements d'enseignement et de recherche français ou étrangers, des laboratoires publics ou privés.

THÈSE

Pour obtenir le grade de

DOCTEUR DE L’UNIVERSITÉ GRENOBLE ALPES

Spécialité : Terre Solide (CETSOL)

Arrêté ministériel : 25 mai 2016

Présentée par

Judith MARINIERE

Thèse dirigée par **Céline BEAUVAL**, chercheur
et codirigée par **Jean-Mathieu NOCQUET**, Directeur, Université Côte d'Azur

préparée au sein du **Laboratoire Institut des Sciences de la Terre**
dans **l'École Doctorale Terre, Univers, Environnement**

Amélioration des modèles prédictifs de séismes pour le PSHA grâce aux données géodésiques : application en Equateur

Improving earthquake forecast models for PSHA with geodetic data, applied on Ecuador

Thèse soutenue publiquement le **8 octobre 2020**,
devant le jury composé de :

Madame CELINE BEAUVAL
CHARGE DE RECHERCHE, IRD DELEGATION ALPES, Directrice de thèse
Monsieur JEAN-MATHIEU NOCQUET
DIRECTEUR DE RECHERCHE, IRD, Co-directeur de thèse
Monsieur NICOLA D'AGOSTINO
DOCTEUR EN SCIENCES, INST. NAL GEOPHY. & VULCANOLOGIE - ROME, Rapporteur
Monsieur MARCO PAGANI
DOCTEUR EN SCIENCES, FONDATION GEM - PAVIE - ITALIE, Rapporteur
Madame ANDREA WALPERSDORF
DIRECTRICE DE RECHERCHE, CNRS DELEGATION ALPES, Présidente
Monsieur KRIS VANNESTE
DOCTEUR EN SCIENCES, OBSERVATOIRE ROYAL DE BELGIQUE, Examinateur
Monsieur STEPHANE MAZZOTTI
PROFESSEUR DES UNIVERSITES, UNIVERSITE DE MONTPELLIER, Examinateur
Monsieur PHILIPPE CHARVIS
DIRECTEUR DE RECHERCHE, IRD DELEGATION COTE D'AZUR, Examinateur

Acknowledgements

I would like to thank all the people who contributed, closely or indirectly, to the development of this thesis.

First, I would like to thank my PhD advisor, Céline Beauval who gave me the opportunity to work on this exciting project, helping me through the course of my PhD to make all of this possible. I am very grateful for her support, enthusiasm and the confidence she puts in me since my very first internship. I would also like to thank my co-PhD advisor, Jean-Mathieu Nocquet for his patience, his positivity and for being such a great teacher in geodesy. I enjoyed working with him both in Quito and in Paris.

I would also like to thank the members of my jury. A special mention to my rapporteurs, Marco Pagani and Nicola D'Agostino for agreeing to read and to correct my manuscript during the summer vacation. Their comments and feedback were very valuable and helpful to this manuscript. I would also like to thank my reviewers, Philippe Charvis, Stéphane Mazzotti, Kris Vanneste and Andrea Walpersdorf who took the time to read my thesis in this period of health crisis and provide good comments and insights on my work.

A special thanks to the Instituto Geofisico team in Quito, with a particular mention to Hugo Yepes, who co-supervised this thesis, Alexandra Alvarado and all the other researchers in Quito. This thesis would not have been possible without the strong support of the Instituto of Geofisico. Many thanks also to Aurore who guided me during my stay in Quito and with whom I had a very good time discovering the Ecuadorian culture.

But above all, I could not have performed this PhD without the constant support of a lot of people in ISTerre! A first big thanks to Jeremie and Johann, with whom I have shared so much, I am greatly thankful for your patience, kindness and support in all the aspect of the thesis and in life! Thanks to you I learned coding, but also how to drain a car! I would also like to thank the first generation of PhD students and interns, such as Olivier, Simon, Emma, Caroline, Capucine, Chloe, Philippe, Camille, Claudia, Laura, Jorge, Yacine, Maureen, Cyril, Jean, Francois, Anne and Lauren, who made my arrival at the lab so easy. I had such great time with all of you, in and out of the lab, at the Familys, at Kfee des jeux or during the numerous hikes around Grenoble. Many thanks to all the second generation of PhD students, who supported me at the end of my thesis! Margot, Estelle, Antoine, Sylvain, Dorian, Andy, Renaldo, Axel, Paul, Hugo, Kavé, Noélie, Cyrielle, Gaelle, Louise, Sylvie and Sandrine in Chambéry! I enjoyed the morning breaks (and the lunch breaks… and afternoon breaks..!), playing music with you, compete on the best cake, the bbq evenings, climbing, hiking, skiing and kayaking!

A huge thanks as well to the not-so-much-PhD anymore, my two mentors, Mikael for always believing in me since my very first beginning from Grenoble, Paris, Strasbourg and Canada! And Laurent for all the great moments and for our intensive training in skating!

I would not end this thank-you list without a word on my family: thanks to my parents for everything you did to help me get there, my brother Paul and my niece and nephew, Mathilde and Charles and also my family-in-law! And a last huge final thanks to my US ex-husband Romain, but still French partner, to be my example of a great researcher and who ended up knowing my subject more than myself.

Abstract

Probabilistic Seismic Hazard Assessment (PSHA) relies on long-term earthquake forecasts, and ground-motion models. Up to now, geodetic data has been rather underused in PSHA, although it provides unique and unprecedented information on the deformation rates of tectonic structures from local to regional scales. The aim of this thesis is to improve earthquake recurrence models by quantitatively including the information derived from geodetic measurements, with an application to Ecuador, a country exposed both to shallow crustal earthquakes and megathrust subduction events. After a first chapter of introduction, the second chapter presents a collective effort of building a probabilistic seismic hazard model for Ecuador, using historical and contemporary seismicity, recent knowledge about active tectonics, geodynamics, and geodesy. I contributed in two ways: 1) the building of earthquake catalogs from global seismic datasets; 2) the establishment of average slip rates on a set of simplified crustal faults, from GPS velocities. The hazard calculations led at the country scale indicate that uncertainties are largest for sites on the northern coast and along the faults in the Cordillera. The third chapter of this thesis focuses on the determination of the seismic potential of the Quito fault system. Quito lies on the hanging wall of a ∼60-km-long reverse active fault, posing significant risks due to the high population density. I constrain the present-day strain accumulation associated with the fault system with GPS data and Persistent Scatterer Interferometric Synthetic Aperture Radar (PS-InSAR) analysis. 3-D spatially variable locking models show that a large part of the fault is presently experiencing shallow creep, hence reducing the energy available for future earthquakes, which has a significant impact for hazard analysis. In the last chapter of this thesis, I evaluate the ability of geodetic data to constrain earthquake recurrence models for the subduction zone in northern Ecuador. I quantify the annual rate of moment deficit accumulation at the interface using interseismic coupling models, and identify the uncertainties related to the conversion in terms of total seismic moment release. Based on a newly developed earthquake catalog, I propose recurrence models that match both the catalog-based seismicity rates and the geodetic moment budget. I set up a logic tree for exploring the uncertainties on the seismic rates and on the geodetic moment budget to be released in earthquakes. The exploration of the logic tree leads to a distribution of possible maximal magnitudes M_{max} bounding the earthquake recurrence model; I extract only those models that lead to M_{max} values compatible with the extent of the interface segment according to earthquakes scaling laws. This new method allows 1) to identify which magnitude-frequency form is best adapted for the Ecuadorian subduction; 2) to generate a distribution of moment-balanced recurrence models representative of uncertainties and propagate this uncertainty up to the uniform hazard spectra; and 3) to evaluate a range for the aseismic component of the slip on the interface. Considering the recent availability of massive quantity of geodetic data, this new approach could be used in other regions of the world to develop recurrence models consistent both with past seismicity and measured tectonic deformations.

Résumé

L'évaluation probabiliste de l'aléa sismique (PSHA) s'appuie sur des modèles de prédictions sismiques long terme et des modèles de mouvements du sol. Jusqu'à présent, les données géodésiques sont restées sous-utilisées dans le cadre du PSHA, bien qu'elles fournissent des informations uniques et sans précédent sur les taux de déformation des structures tectoniques, de l'échelle locale à l'échelle régionale. L'objectif de cette thèse est d'améliorer les modèles de récurrence des séismes en incluant quantitativement les informations dérivées des mesures géodésiques, avec une application à l'Équateur, un pays exposé à la fois aux séismes de faible profondeur de la croûte terrestre et aux mégathrusts de la zone de subduction. Après un premier chapitre d'introduction, le deuxième chapitre présente un effort collectif de construction d'un modèle probabiliste d'aléa sismique pour l'Équateur, en utilisant la sismicité historique et récente, les connaissances actuelles sur la tectonique active, la géodynamique et la géodésie. J'ai contribué de deux manières : 1) la création de catalogues sismiques à partir d'ensembles de données sismiques mondiales ; 2) l'établissement de taux de glissement moyens sur un ensemble de failles crustales simplifiées, à partir des vitesses GPS. Les calculs d'aléas effectués à l'échelle du pays indiquent que les incertitudes sont plus grandes pour les sites de la côte nord et le long des failles de la Cordillère. Le troisième chapitre de cette thèse se concentre sur la détermination du potentiel sismique du système de failles de Quito. La ville de Quito est traversée par une faille inverse de ∼60 km de long, représentant un risque important en raison de la forte densité de population. Nous contraignons l'accumulation actuelle des contraintes associées au système de failles avec les données GPS et l'analyse du radar à ouverture synthétique (PS-InSAR). Les modèles de blocage variables dans l'espace en 3D montrent qu'une grande partie de la faille subit actuellement un glissement à faible profondeur, réduisant ainsi l'énergie disponible pour les futurs séismes, ce qui a un impact significatif sur les calculs d'aléa. Dans le dernier chapitre de cette thèse, nous évaluons la capacité des données géodésiques à contraindre les modèles de récurrence des séismes pour la zone de subduction dans le nord de l'Équateur. À l'aide de modèles de couplage intersismique, nous mesurons le taux annuel d'accumulation du déficit de moment sur l'interface et identifions les incertitudes liées à la conversion en termes de relâchement du moment sismique total. Sur la base d'un catalogue de séismes nouvellement développé, nous proposons d'établir des modèles de récurrence qui correspondent à la fois aux taux de sismicité basés sur le catalogue et au budget du moment géodésique. Nous établissons un arbre logique pour explorer les incertitudes sur les taux de sismicité et sur le budget du moment géodésique à libérer lors des séismes. L'exploration de l'arbre logique conduit à une distribution des magnitudes maximales M_{max} possibles délimitant le modèle de récurrence des séismes ; nous n'extrayons que les modèles qui fournissent des M_{max} compatibles avec la longueur du segment interface. Cette nouvelle méthode permet 1) d'identifier quelle forme de modèle de récurrence est la mieux adaptée à la subduction équatorienne ; 2) de générer une distribution de modèles de récurrence équilibrés en termes de moments représentatifs des incertitudes et de propager cette incertitude jusqu'aux spectres à risque uniforme (UHS) ; et 3) d'évaluer une gamme de valeurs pour la composante sismique du glissement sur l'interface. Compte tenu de la disponibilité récente d'une quantité massive de données géodésiques, cette nouvelle approche pourrait être utilisée dans d'autres régions du monde pour développer des modèles de récurrence cohérents à la fois avec la sismicité passée et la déformation tectonique mesurée.

Resumen

La Evaluación Probabilística de la Amenaza Sísmica (PSHA) se basa en la predicción de terremotos a largo plazo y en modelos de movimiento del suelo. Hasta ahora, la información geodésica ha sido subutilizados en el PSHA, a pesar de que estos proporcionan información única y sin precedentes sobre las tasas de deformación de las estructuras tectónicas a escalas locales y regionales. El objetivo de esta tesis es mejorar los modelos de recurrencia sísmica incluyendo cuantitativamente información derivada de observaciones geodésicas, con una aplicación en Ecuador, país expuesto tanto a terremotos corticales en superficie como a eventos de la interface de subducción. Después de un primer capítulo introductorio, el segundo capítulo presenta un esfuerzo colectivo para construir un modelo probabilístico de amenaza sísmica para Ecuador, considerando sismicidad histórica y contemporánea, así como avances recientes en el estado del arte de la tectónica activa, la geodinámica y la geodesia. He contribuido de dos maneras: 1) la generación de catálogos de terremotos a partir de set de datos sísmicos globales; 2) la estimación de tasas de deslizamiento promedio en un conjunto simplificado de fallas corticales, a partir de las velocidades de GPS. Los cálculos de amenaza realizados a escala nacional muestran mayor incertidumbre en los sitios de la costa norte y a lo largo de las fallas de la Cordillera. El tercero capítulo de esta tesis se centra en la determinación del potencial sísmico del sistema de fallas de Quito. La ciudad de Quito se encuentra en el hanging wall de este sistema activo de falla inversa de ∼60-km de largo, lo que representa un riesgo significativo debido a su alta densidad de población. Se estimó la acumulación de deformación actual asociada al sistema de fallas usando datos de GPS y análisis de Dispersión Persistente de Interferometría Radar de Apertura Sintética (PS-InSAR). Los modelos de acoplamiento sísmico espacialmente variables en 3D muestran que una gran parte de la falla experimenta actualmente creep superficial, limitando la energía disponible en futuros terremotos, lo que tiene un impacto significativo en el cálculo de amenaza. En la ultima parte de esta tesis, se evalúa la capacidad de los datos geodésicos para limitar los modelos de recurrencia de sísmica de la zona de subducción del norte de Ecuador. Utilizando mapas de acoplamiento inter-sísmico, se estimó la tasa anual de acumulación de déficit de momento sísmico de la interface de subducción, y se identificó la incertidumbre asociada a la conversión en términos de liberación total de momento sísmico. Basándose en un catálogo de terremotos recientemente desarrollado, se propone el establecimiento de modelos de recurrencia sísmica que coincidan tanto con las tasas de sismicidad basadas en el catálogo como con la tasa de liberación de momento geodésico. Se creó un árbol lógico para explorar las incertidumbres en las tasas de sismicidad y en las tasas de liberación de momento geodésico de terremotos. La exploración del árbol lógico conduce a una distribución de magnitudes máximas posibles que delimitan el modelo de recurrencia de terremotos; se extrajo sólo aquellos modelos que entregan M_{max} compatible con la extensión del segmento de interface de subducción. Este nuevo método permite: 1) identificar qué relación de magnitud-frecuencia se adapta a la subducción ecuatoriana; 2) generar una distribución de modelos de recurrencia de momento-balanceado representativo de la incertidumbre y propagar esta incertidumbre a los espectros de peligro uniformados (Uniform Hazard Espectra); y 3) evaluar un rango para la componente asísmica del deslizamiento en la interface de subducción. Considerando la reciente disponibilidad de una enorme cantidad de datos geodésicos, este nuevo enfoque podría ser utilizado en otras regiones del mundo para el desarrollo de modelos de recurrencia coherentes tanto con la sismicidad pasada como con la deformación tectónica observada.

Contents

List of Figures

List of Tables

CHAPTER 1

General introduction

Contents

This chapter is a general introduction on the context and the objectives of the thesis. A part of this chapter is dedicated to explain the concepts that will be used throughout the manuscript. We present the different steps required to assess the probabilistic seismic hazard and introduce the notion of geodetic moment, how it is calculated and used in recurrence models. Finally, we present the geodynamic context of Ecuador, which is the study region that was chosen for this thesis.

1.1 Context of the thesis

This thesis is part of the ANR REMAKE project, Seismic **R**isk in **E**cuador: **M**itigation, **A**nticipation and **K**nowledge of **E**arthquakes funded from 2016 to 2020, which is part of the SVAN (**S**éismes et **V**olcans dans les **A**ndes du **N**ord - *Earthquakes and Volcanoes in the Northern Andes*) International Joint Laboratory (LMI) created in 2012 and renewed in 2017. This LMI, which aims to better understand the processes that control seismic and volcanic activity, gathers the Geophysical Institute of the National Polytechnic School (IG-EPN) in Quito, Ecuador and in France, Geoazur, in Nice, ISTerre in Grenoble and LMV in Clermont-Ferrand. A 10-year collaboration between the IG-EPN, ISTerre and Geoazur laboratories has led to the creation of a best-estimate model of PSHA for the LMI (Beauval et al. (2014); Yepes et al. (2016)), an access to seismological data (Mothes et al. (2013, 2018); Alvarado et al. (2018)), development of geodetic network (Nocquet et al. (2014); Chlieh et al. (2014)), database on active fault systems (Baize et al. (2013); Alvarado et al. (2014, 2016), and a solid scientific environment within the SVAN International Joint Laboratory.

The ANR REMAKE aims to develop a new earthquake prediction model for the Ecuador-Peru zone by integrating the complete knowledge on faults, including their seismic potential evaluated from geodetic, seismological and geological approaches. Several aspects are developed in this ANR in order to assess the capacity to produce large earthquakes in the subduction zone: the construction of an active database on crustal faults, seismic hazard models (for the whole of Ecuador and specifically in Quito), the rapid determination of earthquake source parameters and the institutionalization of scientific knowledge on seismic risk.

This IRD-funded thesis is part of Work Package WP3, entitled Building Seismic Hazard Models. The objective of this WP3 is to update the PSHA by integrating the latest data and methods from geodesy, seismology and tectonics in order to identify and reduce the highest sources of uncertainties that will ultimately impact hazard calculations. As a consequence, this thesis aims at connecting specialists in seismology and in geodesy in order to build a new seismic prediction model that accounts for all available geophysical and geological constraints.

1.2 What is PSHA?

The objective of Probabilistic Seismic Hazard Assessment (PSHA) is to deliver reference ground motions to structural engineers, in order to build earthquake-resistant infrastructure. It is a fundamental input also for insurers, governments and industry as it will have a direct impact on the human and economic losses.

Currently two main approaches for assessing seismic hazard are being used: the deterministic type approach (DSHA) and the probabilistic type approach (PSHA). The objective of the DSHA approach (McCalpin (2009)) is to identify a single scenario that induces the largest ground motion. The scenario is based on the study of earthquakes that have already occurred and have been recorded in the region of interest. On the other hand, the objective of probabilistic approaches is to identify all seismic scenarios that can contribute to the hazard estimate and to measure their respective contributions. It considers uncertainties related to the earthquake location (spatial uncertainties), magnitude (recurrence laws), the ground motion models and the temporal uncertainties.

In the seismic hazard community, the PSHA approach is the most frequently used (Cornell (1968); Reiter (1990); Kramer (1996); Field et al. (2014); Beauval et al. (2020)) even if the DSHA approach (Scotti et al. (2014)) is still performed by the French or Japanese nuclear safety authority to define its rule for nuclear installations

The implementation of the PSHA approach requires the development of four steps which are: (1) the definition of source zones corresponding to areas that have the potential to generate earthquakes; (2) the modelling of earthquake recurrence rates as a function of their magnitude for each defined source zones; (3) the ground motion estimation and (4) the determination of ground motion exceedance rates (Figure 1.1).

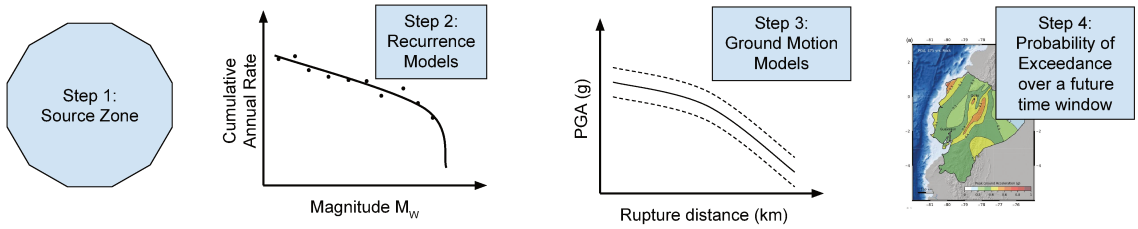

Figure 1.1: Illustration of the four steps used in the definition of the PSHA approach.

In the following parts I will describe into more details these four steps leading to the estimation of PSHA.

1.2.1 Source model definition

Seismotectonic zoning is the first step in the assessment of probabilistic seismic hazard. The aim of this part is to define earthquake sources that are capable of producing ground motions. Depending on the current seismotectonic understanding of the zone, the earthquake source geometry can be a point, a fault or an entire area. For a point source, earthquakes only occur at a single point. On the other hand, a fault source encompasses an active fault where earthquakes can only occur at the surface of the fault. When the fault system is unknown, it is common to define an area source, where earthquakes can occur anywhere within this volume. These sources are defined to be homogeneous in terms of seismicity, tectonics, etc. in order to characterize the magnitude-frequency distribution within the zone. Earthquakes are usually homogeneously distributed inside the zone. Source-to-site distances (the closest distance to the finite rupture) are estimated for all ruptures.

1.2.2 Recurrence models

Statistical analysis of Californian seismicity has enabled Gutenberg and Richter (1944) to observe an exponential decrease in earthquake frequencies as a function of their magnitude. The authors determined a law (eq. 1.1), called Gutenberg-Richter's law (GR) describing this distribution:

$$\log_{10}(N(M \geq m) = a - bm \tag{1.1}$$

where $N(M \geq m)$ is the total number of earthquakes with magnitudes equal to and above magnitude m and is determined from the parameter a (y-axis intercept and can be thought of as the productivity) and b (slope of the rate of earthquakes with respect to m). This law (Figure 1.2) describes the behaviour of the seismicity distributed in a source zone and model how often an earthquake greater than a specific magnitude happens.

While the number of small earthquakes is usually high for a specific source, there is a lack of observation for higher magnitudes. If the rates for low-to-moderate magnitudes follow a straight line in semilog scales, they are multiple options to extrapolate the recurrence models to higher magnitudes. For example, one can modify the GR law to add a maximum magnitude bound (Youngs and Coppersmith (1985), Anderson and Luco (1983), Molnar (1979)). The maximum bound (M_{max}) is calculated through the historical seismicity or scaling laws of the zone. The GR model is therefore truncated at this bound (Figure 1.2, dashed line). Another alternative is the characteristic earthquake model (Schwartz and Coppersmith (1984), suggesting that faults have repeated occurrences of characteristic earthquakes at a higher rate than the GR model. The rate of characteristic earthquake is often defined from geological studies (trenches, etc.). For example, Youngs and Coppersmith (1985) proposes a recurrence model based on the characteristic earthquake for the M_{max}

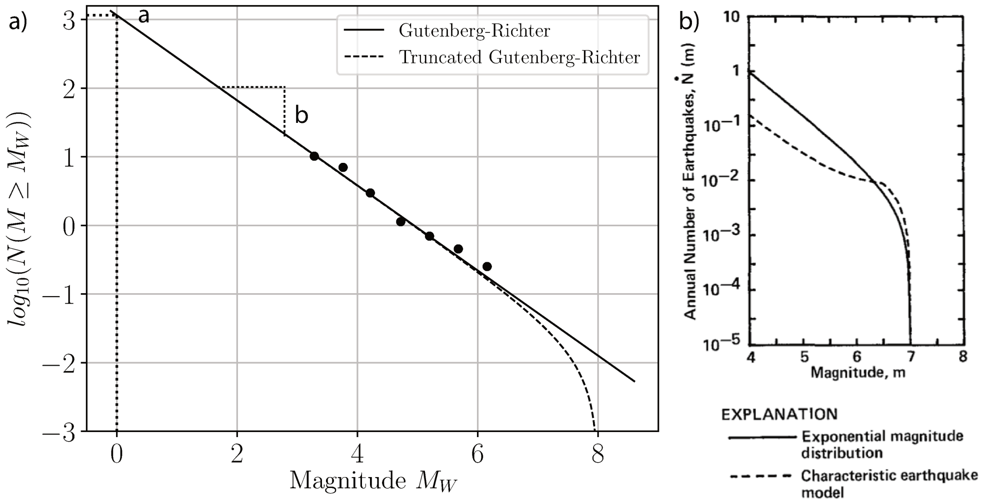

Figure 1.2: Example of recurrence models, a) Gutenberg-Richter model (solid line) and truncated Gutenberg-Richter model (dashed line) fitting the observed magnitude rates (black circles); parameters a and b describing this law. b) Comparison of truncated and characteristic GR recurrence models in their cumulative form (from Youngs and Coppersmith (1985)).

and for lower magnitudes, this recurrence model follows an exponential distribution (Figure 1.2).

1.2.3 Ground Motion Models

The next step is to establish ground motion models. These models predict the probability density function of ground motions, as a function of magnitude and distance $f(M, R)$, as well as the properties of the earthquake source such as the faulting mechanism and site conditions (V_{S30}). They are developed using statistical regression on strong motion databases from different tectonic regions.

Four classes of tectonic regimes are used for ground motion models used in seismic hazard assessments: active crustal region (ACR), stable continental region (SCR), volcanic and subduction. The subduction can be divided into two subtypes: interface and intraslab. In the case of ACR, the latest ground motion models have been developed in 2014 using ground motions recording from the western USA in the frame of the NGA West project (Next Generation Attenuation for the western United States). We can also note Akkar and Bommer (2010), which use Europe and Middle East ground motions recording to develop ground-motion models and Zhao (2006), based on Japanese data. For subduction sources, the major models are from Abrahamson et al. (2016) using a global dataset and Zhao (2006) using a Japanese dataset. Each model developed different ground motion equations for subduction interface and intraslab. For SCR, Atkinson and Boore (2006) developed a model for Eastern North America.

In other regions where no ground motion models exist, it is common to use ground motion models developed for similar tectonic regions.

1.2.4 Probability of exceedance of an acceleration level over a given time window

In this last part, we combine all information from earthquake recurrence models and ground motion models. We integrate the knowledge on the recurrence models, the magnitudes and distances of earthquakes, and the distribution of ground motions to result in a hazard curve (Figure 1.3). The hazard curve is the annual rates of exceedance of a series of target accelerations at a site.

The most frequently used probabilistic model for calculating the probability of occurrence in time of an earthquake and an acceleration is the Poissonian model. It is based on the fact that earthquakes occur independently and randomly in time and space. It doesn't have the memory of time, size and location of past events. Therefore, for these time-independent models, it does not consider the physics of the seismic cycle, which states that the probability of occurrence of a major earthquake on a fault that has already produced a major earthquake is very low as long as the elapsed time has not made it possible to re-accumulate stresses on the fault.

For a poissonian phenomenon occurring at an average annual rate of occurrence λ, the probability P that the phenomenon occurs at least once over the time period t is (Ang and Tang (1975)):

$$P = 1 - e^{-\lambda t} \tag{1.2}$$

In PSHA computation, we will calculate the probability that a target acceleration is exceeded over the future time window t. For example, the mean poissonian rate λ corresponding to a probability P of 10% over t=50 years is 0.0021 per year and correspond on average to 1 occurrence every 475 years (return period). We can retrieve the target acceleration at this return period of 475 years from the hazard curve by interpolation (Figure 1.3).

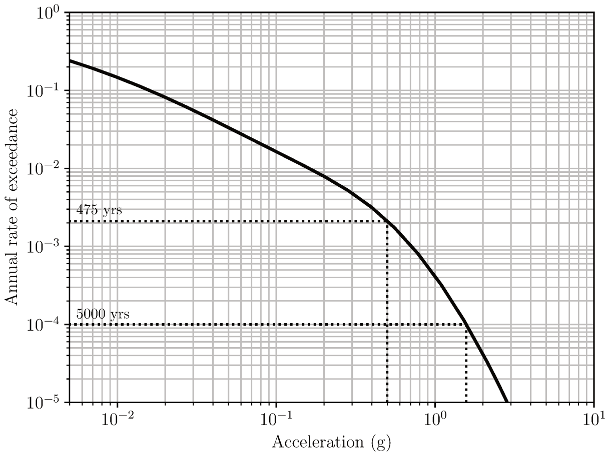

Figure 1.3: Example of an hazard curve for a single site. Combining all information from earthquake recurrence models and ground motion models to compute the annual rate of exceeding a given acceleration (year^{-1}).

1.3 Geodesy

In this section, we first describe the geodetic techniques, and how they can be used to monitor surface displacement due to earthquake deformation and derive interseismic coupling models. Finally, we introduce how we calculate geodetic-based models using Interseismic Coupling (ISC) maps that are integrated inside PSHA.

1.3.1 Measurements of surface displacements

Since the beginning of the satellite era, the study of earth sciences has completely changed. Specifically, the development of methods based on Global Position System (GPS) or satellite radar interferometry has revolutionized the monitoring of earthquake deformation to an unprecedented level of precision.

The Global Positioning System (GPS) is a powerful tool that has first been developed in the 1970s by the military, in order to precisely determine their location around the world. The system consists of 1) 24 satellites, orbiting 20,000 km above the Earth in 12-hour circular orbits, 2) GPS ground station and 3) a data center. The satellites send radio signals to the earth surface that contain information about their position. These signals are detected by GPS ground-based stations, which are composed of a receiver and an antenna. At each station, the signal is picked up by the antenna and transmitted to the receiver. The receiver records pseudo-distance measurements (i.e. distance but with a clock error) and measurements of the phase of the electromagnetic wave. These measurements are then used to calculate millimeter positions. During an earthquake, the GPS data provides the total amount that a station has been displaced. This technology has completely changed the way to study earthquakes, by allowing scientists to infer slip rates at the order of a millimeter, which could not be detected in the past. One of the drawbacks of GPS measurements is the spatial coverage, with point measurements at each GPS station that needs to be installed and maintained regularly on the field.

The principle of **Synthetic Aperture Radar interferometry (InSAR)** is based on the phase difference of two satellite radar images of the same zone acquired from the almost same orbits. This difference is a precise measurement of the change in length between the ground and the satellite, hence can be used to monitor the displacement at the earth surface, caused for example by an earthquake, a volcano or glacier flow. One of the most notorious applications of this technique was performed in 1992, to measure the seismic deformation caused by the Landers Earthquakes in California (M_W 7.3), at precision better than 3 cm. Using a single pair of ESA's ERS-1 satellite, the authors provided for the first time in history, the image of the static displacement induced by an earthquake.

1.3.2 From surface displacements to ISC models

We want to quantify the rate of slip deficit accumulated along a fault. To do so, we assume that the observed surface displacement can be explained by a set of dislocations at depth in a homogeneous elastic half-space. A common approach is to consider the back-slip model (Savage (1983), McCaffrey (2005), Figure 1.4), where the surface deformation is the sum of the long-term deformation (steady state in Figure 1.4) modelled by rigid block motion and a virtual back-slip component that counterbalances the long-term motion on the locked portion of the fault. The steady-state term is equivalent to stable sliding along the whole thrust fault from the surface to its down-dip extension. This back-slip assumption is summarized in Figure 1.4 and has been frequently used for elastic kinematic models.

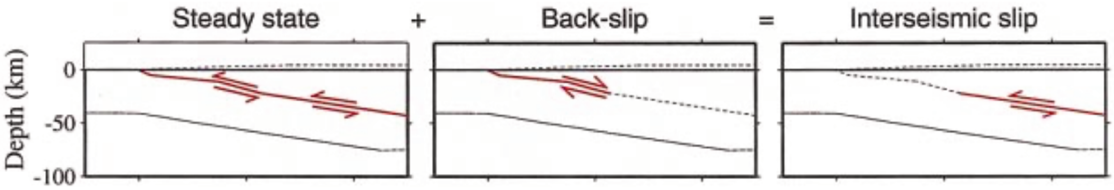

Figure 1.4: Back-slip model theory proposed by Savage (1983) to model interseismic deformation (from Vergne et al. (2001)).

Following this approach, we can invert the model parameters using the geodetic observations and we obtain a spatially variable slip 3-D interseismic model.

The interseismic coupling can be calculated as the ratio between the deficit of slip and the long-term slip of the fault.

$$\chi = 1 - \frac{s}{v_{plate}} \tag{1.3}$$

where s is the creep rate seen during the interseismic period. χ is 0 for a fault patch creeping at the long-term slip rate and 1 for a fully locked patch. An example of an interseismic coupling map on the subduction zone in Ecuador and Peru from Nocquet et al. (2014) is illustrated on the Figure 1.5.

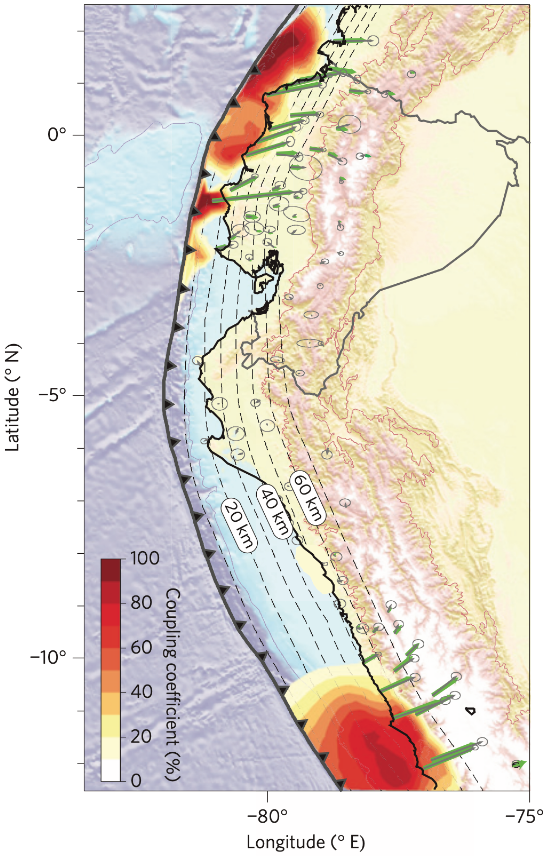

Figure 1.5: Spatial distribution of interseismic coupling along the subduction plate interface (from Nocquet et al. (2014)). Model showing no interseismic coupling between 10°S and 3°S. Dashed lines are depth contours of the subduction interface every 10 km. Coupling level is indicated by the colour scale. Green arrows are the model predicted velocities. The misfit (wrms, weighted root mean square) to the observed velocities (grey arrows) for this model is 0.9 mm/yr.

1.3.3 Geodetic-based earthquake recurrence models

Using the values of slip rates deficit along a fault or in interseismic coupling models, we can calculate the geodetic moment rate, which can be used inside recurrence models, hence in the seismic hazard assessment.

Indeed, using only long-term earthquake forecast models, usually derived from earthquake catalogs, can have several drawbacks. First, earthquake catalogs including all known events in a given region usually show strong discrepancy in quality and completeness between historical and instrumental periods. Second, the model usually mostly relies on the rates low-to-moderate magnitudes during the instrumental period which is extrapolated up to a maximum magnitude. Including geodetic data could help constrain those recurrence models.

Therefore, we estimate the geodetic moment deficit buildup rate $\dot{M}_0$ from the slip rate $\dot{S}$ using the formula from Brune (1968):

$$\dot{M}_0 = \mu \dot{S} L W \tag{1.4}$$

where μ is the shear modulus, $\dot{S}$ is the slip rate deficit on the fault, L and W length and width of the fault.

During interseismic period, assuming there is aseismic creep occurring, the width of the fault that is coupled represents only a fraction of the actual width. Therefore, from interseismic models, we can re-calculate the geodetic moment deficit buildup rate $\dot{M}_0$ through the following relation:

$$\dot{M}_0 = \int_{rupture} \mu \dot{V} \chi_i \mathrm{d}s \tag{1.5}$$

where $\dot{V}$ is the long-term slip rate deficit and χ_i the interseismic coupling integrated over the rupture ds.

The advantage of using an interseismic coupling model is that we take into account the space variability of slip deficit and therefore of the moment. On the contrary, the moment derived from equation 1.4 is based on a single slip rate value for the entire rupture and doesn't take into account the creeping patches.

We integrate the number n and magnitude m of earthquakes, assuming a GR law $n(m)$, and the relation between the moment M_0 and magnitude m, $M_0(m) = 10^{cm+d}$ (from Hanks and Kanamori (1979), where c=1.5 and d=9.1 for M_0 in units of N.m), to obtain the total moment release $\dot{M}_0^T(m)$:

$$\dot{M}_0^T(m) = \int_{-\infty}^{M_{max}} M_0(m) n(m) \mathrm{d}m \tag{1.6}$$

The result of the equation 1.6 can be converted into moment-based recurrence models such as equation 1.7, for a recurrence model of a form $N(m) = 10^{a-bm}$:

$$N(m) = \dot{M}_0^T \frac{(c-b)}{c} 10^{(b-c)M_{max}-bm-d} \tag{1.7}$$

1.4 Geodynamics context in Ecuador

Ecuador is located south of Colombia and north of Peru (see Figure 1.6). The country lies on the subduction zone where the Nazca oceanic plate slides under the South American continental plate (SOAM). The subduction zone extends along 8000 km from Colombia to Chile. This subduction zone is the source of numerous earthquakes, many of which that happened in Ecuador are among the largest ever recorded, such as the Esmeraldas earthquake in 1906 (M_W 8.6).

The shape of this margin is complex, shaped by numerous changes in the direction of the trench along the subduction, especially in its northern part where its direction evolves successively (from north to south) from N40° to the Colombian Andes, N10° to the Ecuadorian Andes, and finally N115° close to the Peruvian Andes. Using geodetic data, Kendrick et al. (2003) and Nocquet et al. (2014) have shown that the current convergence of the Nazca plate is oblique to the direction of the Ecuadorian trench (direction N83°E with a velocity of 56 mm/yr) inducing in part, an EW shortening of the continental plate and the escape of the North Andean Sliver (NAS) towards the NE (Trenkamp et al. (2002); White et al. (2003)) along the crustal faults.

The structure of the Ecuadorian margin has been progressively shaped by continuous subduction since 25 Ma (Stauder (1975); Hey (1977)). During the last 5 Ma, part of the Ecuadorian margin (between 0.5°N and 2°S) has been under the influence of the subduction from the Carnegie Ridge (Gutscher et al. (1999); Collot et al. (2009)), an oceanic shelf about 2 km shallower and thicker than the rest of the Nazca oceanic plate (Graindorge (2004); Sallares and Charvis (2003)).

Currently more than 50 % of Ecuadorians live on the coast, close to the subduction zone, and ∼2 million lives on the capital of Quito, which is located on an active reverse fault. As a consequence, the country is prone to important seismic risk, with the majority of the population living in insecure housing directly on the most exposed regions.

1.5 Content of the thesis

The central axis of this thesis aims at reducing the uncertainties in seismic hazard assessment by integrating the information provided by new geodetic data. To achieve this objective, this thesis is subdivided into four parts:

- In the beginning of my PhD, I contributed to the development of a new seismic hazard model for Ecuador. This study is the result of a ten-year collaboration between France and Ecuador on active tectonics, geodesy, seismology and seismic hazard assessment. My main contribution focuses on the construction of

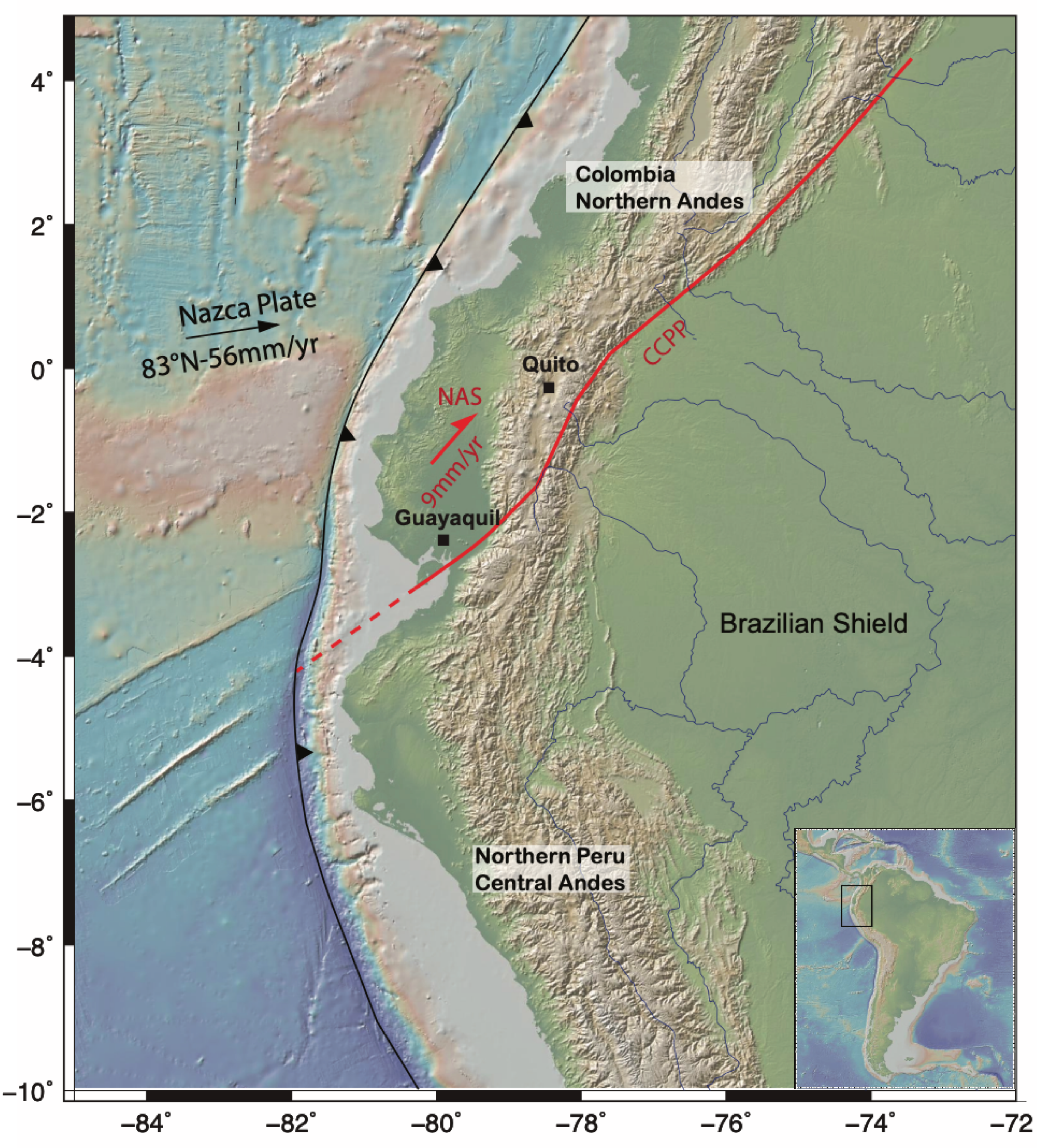

Figure 1.6: Geodynamics framework of Ecuador and neighboring countries (modified from Yepes et al. (2016)). The Nazca plate is converging at equatorial latitudes relatively to the Brazilian shield at 56 mm/yr (Trenkamp et al. (2002)). Due to the acute convexity of the margin (trench is the thick black line with indents), oblique convergence is driving two different continental slivers away from each other. The North Andean Block (NAB) is moving toward the NNE at 9 mm/yr along localized right-lateral strike-slip or reverse faults - CCPP fault system.

homogeneous earthquake catalogs and the estimation of slip rates. The hazard results of this new model were the starting point of my PhD work. This paper has been published in 2018 in the *Bulletin of the Seismological Society of America* as:

C. Beauval, J. Marinière, H. Yepes, L. Audin, J.-M. Nocquet, A. Alvarado, S. Baize, J. Aguilar, J.-C. Singaucho, H. Jomard; A New Seismic Hazard Model for Ecuador. *Bulletin of the Seismological Society of America* ; 108 (3A): 1443–1464.

I also specifically examined the declustering methods used in the final step of the building of the seismic catalog. Since probabilistic models suppose that earthquakes occur independently in time, it is crucial to remove foreshocks and aftershocks from earthquake catalogs. While the role of these declustering methods are fundamental, they are not extensively described and are often used as black-box algorithm. As a consequence, I compare and analyze two declustering methods and assess the related uncertainties in the specific case of the Ecuadorian seismic catalog. These points are described in detail in section 2.2.

- The second part focuses on improving our current understanding of the geodynamic processes in the Quito fault system. In this section, we worked on the inversion of GPS and InSAR data in order to establish the first interseismic coupling map of the Quito fault system. The results are used to interpret the creep processes involved and establish first geodetic-based recurrence models for Quito. This section was published in 2020 in *Geophysical Journal International* as:

  J. Mariniere, J.-M. Nocquet, C. Beauval, J. Champenois, L. Audin, A. Alvarado, S. Baize, A. Socquet, Geodetic evidence for shallow creep along the Quito fault, Ecuador, *Geophysical Journal International*, Volume 220, Issue 3, March 2020, Pages 2039–2055.

- Finally, the third part focuses on the integration of the geodetic data into the recurrence models. We propose a methodology for generating a series of moment-balanced Gutenberg-Richter recurrence models, that matches the past seismicity rates and that is consistent with the moment rates inferred from geodetic measurements. We quantify the uncertainties associated with the Gutenberg-Richter a and b parameters, as well as on the slip budget available for earthquakes as inferred from interseismic coupling models in order to better constrain seismic hazard assessment in the subduction zone of Ecuador. This work is submitted in *Bulletin of the Seismological Society of America.*

CHAPTER 2

A New Seismic Hazard Model for Ecuador

Contents

A new seismic hazard for Ecuador from Beauval C., Mariniere J. et al. published in 2018 in *Bulletin of the Seismological Society of America* was the second paper that I co-authored. This work was the result of a 10 years collective effort between French and Ecuadorian laboratories, involving a multidisciplinary expertise gathering seismologists, geodesists and geologists. I integrated the project in April 2016. I was hired at ISTerre on an engineer position to provide technical support. In January 2017 I finally started a PhD and benefitted in spring of a 2-month IRD "Mission Longue Durée" (*Long Duration Mission*) to go to the IG-EPN lab (Geophysical Institute of the National Polytechnic School) in Quito, Ecuador. It gave me the opportunity to interact with both geodesists and geologists, hence work in synergy with a full team of experts. Thus, I was part of the discussion and decision-making process for each crucial step of the paper.

Within this project, I was in charge of: 1) the creation of homogeneous seismic catalogs for Ecuador and bordering regions and 2) the calculation of slip rates on crustal faults. I also contributed as technical support to other aspects (automatization of files and procedures, production of maps).

First, in order to assess the uncertainties related to the catalogs and to provide alternative recurrence models, I was in charge of building two homogeneous catalogs using only global datasets on the whole country. The first one combined the ISC-GEM, ISC event and GCMT catalogs, whereas the second one was based on the NEIC catalog. I developed an automatic processing chain to integrate the most up-to-date global catalogs and establish a priority scheme to select events. Magnitude conversion and declustering process were also performed in order to obtain homogeneous catalogs. This work is described in the section *Earthquake Catalogs* of the paper, on Table 1, Table 2, Figure 3 and the declustering will be detailed on the section 2.2 of this manuscript.

Second, I was in charge of the determination of active crustal faults slip rates based on GPS measurements. For this part, I used the GPS horizontal velocity field of 53 sites and the module pyacs developed by J.-M. Nocquet. I tested two different methods, such as using faults as block limits or calculating the relative horizontal velocity between pairs of GPS located on either side of the fault. The method is detailed in section *Geodetic Slip Rates* of the paper and the results are represented in Table 6 and Figure 9.

These hazard results were the starting point of my PhD work. I worked on improving the estimation of the seismic potential of the Quito Fault, located underneath Quito city, with the generation of an Interseismic Coupling (ISC) map. Secondly, I studied the integration of interseismic coupling estimates into recurrence models, to improve probabilistic seismic hazard assessment for sites located on the Ecuadorian coast.

2.1 Beauval C., Mariniere J. et al. *BSSA 2018*

Bulletin of the Seismological Society of America, Vol. 108, No. 3A, pp. 1443–1464, June 2018, doi: 10.1785/0120170259

A New Seismic Hazard Model for Ecuador

by C. Beauval, J. Marinière, H. Yepes, L. Audin, J.-M. Nocquet,* A. Alvarado,
S. Baize, J. Aguilar, J.-C. Singaucho, and H. Jomard

Abstract We present a comprehensive probabilistic seismic hazard study for Ecuador, a country exposed to a high seismic hazard from megathrust subduction earthquakes and moderate-to-large shallow crustal earthquakes. Building on knowledge gained during the last decade about historical and contemporary seismicity, active tectonics, geodynamics, and geodesy, several alternative earthquake recurrence models have been developed. We propose an areal seismic zonation for the seismogenic crustal, inslab, and interface sources, modified from Yepes *et al.* (2016), to account for the information gained after the 2016 M_w 7.8 Pedernales megathrust earthquake. Three different earthquake catalogs are used to account for uncertainties in magnitude–frequency distribution modeling. This first approach results in low hazard estimates for some areas near active crustal fault systems with low instrumental seismicity, but where geology and/or geodesy document rapid slip rates and high seismic potential. Consequently, we develop an alternative fault and background model that includes faults with earthquake recurrence models inferred from geologic and/or geodetic slip-rate estimates. The geodetic slip rates for a set of simplified faults are estimated from a Global Positioning System (GPS) horizontal velocity field from Nocquet *et al.* (2014). Various scenarios are derived by varying the percentage of motion that takes place aseismically. Combining these alternative earthquake recurrence models in a logic tree, and using a set of selected ground-motion models adapted to Ecuador's different tectonic settings, mean hazard maps are obtained with their associated uncertainties. At the sites where uncertainties on hazard estimates are highest (difference between 84th and 16th percentiles > 0.4g), the overall uncertainty is controlled by the epistemic uncertainty on the source model.

Introduction

During the last decade, the French–Ecuadorian scientific collaboration has produced new results in most of the fields required for a probabilistic seismic hazard assessment (PSHA). Historical earthquakes were studied, providing new locations and magnitudes (Beauval *et al.*, 2010). A homogeneous earthquake catalog was compiled using historical and instrumental earthquake catalogs (Beauval *et al.*, 2013). New insights into active tectonics significantly improved the understanding of the active fault systems in the country (Alvarado *et al.*, 2014, 2016; Baize *et al.*, 2015). A new view of Ecuador's complex geodynamics has been developed, and new seismic source zones for PSHA have been defined (Yepes *et al.*, 2016). Deformation observed through geodetic and seismological measurements led to the development of better detailed plate tectonic models for the region and a better understanding of the Ecuadorian subduction interface's ability to produce large earthquakes (Chlieh *et al.*, 2014; Nocquet *et al.*, 2014, 2016). The 2016 M_w 7.8 Pedernales earthquake, responsible for more than 650 casualties and considerable destruction, was a terrible reminder that most of Ecuador faces a high seismic risk. Aside from subduction zone earthquakes, several strong earthquakes have occurred along the fault system bordering the Interandean Valley during the last 500 years (e.g., 1868 M_w 7.1–7.7 Ibarra earthquake; 1797 M_w 7.5–7.9 Riobamba earthquake; Beauval *et al.*, 2010). Events that occur along shallow crustal faults have the potential to be much more destructive than megathrust events. To limit the number of casualties, buildings should be built or reinforced to resist strong ground motions. The goal of PSHA is to provide authorities with a basis and reference from which ground motions should be considered for earthquake resistant design (earthquake building code for design or retrofit).

PSHA methods were introduced in the late 1960s (Cornell, 1968; Esteva, 1968) and are now considered state-of-the-art methods to estimate seismic hazard in most regional, national, and international seismic regulations (e.g.,

---

*Also at Institut de Physique du Globe de Paris, Sorbonne Paris Cité, Université Paris Diderot, UMR 7154 CNRS, Paris, France.

Eurocode 8, 2004; U.S. National Seismic Hazard Maps, Petersen *et al.*, 2014). PSHA aims to interpret knowledge about the sources and the magnitudes that may occur in terms of rates of occurrence (source model). Thanks to empirical models, the ground motions produced by these future events can be estimated (ground-motion model [GMM]). The source model and the GMM are then combined to determine the exceedance probabilities of ground-motion levels at sites of interest over future windows of time.

The first Ecuadorian Building Code (EBC) was launched in 1951 after the 1949 M_w 6.4 central Ecuador crustal earthquake (~6000 casualties). Although no seismic hazard calculation was made, earthquake-resistant measures were suggested for retrofitting damaged structures. Important amendments based on the California Uniform Building Code were made in 1976 after the small M_w 6.6 Esmeraldas City interface earthquake, and a single seismic zone was adopted for the country. Several PSHA academic studies were performed in the 1990s (e.g., Bonilla *et al.*, 1992) but the results were not used for establishing zoning. In 2001, the EBC was updated (Código Ecuatoriano de la Construcción [CEC], 2001), as a response to the 1998 M_w 7.1 Bahía de Caráquez interface earthquake. EBC relied on probabilistic seismic hazard calculations (53 areal source zones and two GMMs, one for subduction interface and one for crustal earthquakes), and subdivided the country into four seismic zones. The EBC was updated again in 2015 (Norma Ecuatoriana de la Construcción [NEC], 2015), based on a seismic zoning map outlined from an earlier version of our seismic hazard model, calculated with a trial version of the OpenQuake PSHA software. A new version is expected in light of recommendations still to be drawn from the weak performance of structures during the 2016 M_w 7.8 interface earthquake. The new seismic hazard model presented here will be used to redefine the national seismic zoning map and provide peak ground acceleration (PGA) and associated uncertainty values for design response spectra.

In this study, we describe a comprehensive PSHA calculation for Ecuador, relying on the most up-to-date information available. This article is organized as follows. First, the so-called area model is described, in which we introduce the seismogenic sources, earthquake catalogs, and magnitude–frequency distributions derived for all crustal, interface, and intraslab sources. An alternative fault model is developed, including the crustal faults for which relevant data have been collected. Earthquake recurrence on these fault sources is inferred from geodetic and/or geologic slip rates. GMMs are selected from recently published models. A logic tree is built exploring the uncertainty on the source model and on the prediction of ground motions. Probabilistic seismic hazard is calculated over a grid of rock sites (V_{S30} 760 m/s) that cover the entire country to produce mean probabilistic hazard maps and 16th and 84th percentile hazard maps. Finally, a specific study is led in the cities of Quito, Guayaquil, and Esmeraldas, in order to compare the contributions of source model uncertainty and GMM uncertainty to overall uncertainty.

Area Model

Seismogenic Sources

Yepes *et al.* (2016) proposed a set of seismogenic sources to model earthquake occurrences along crustal shallow faults, at the subduction interface, and inside the slab at depth (Figs. 1 and 2). The crustal area source model encloses the main fault system that delineates the southern border of the North Andean Sliver (NAS; Nocquet *et al.*, 2014; Alvarado *et al.*, 2016). This fault system includes four groups of transpressive structures (namely the Puna, Pallatanga, Cosanga, and Chingual fault systems, Fig. 1). In addition, the Quito-Latacunga thrust fault system is enclosed in a source zone connected in the north to the El Angel strike-slip fault system; whereas the eastern sub-Andean thrust-and-fold belt is split into the wide Cutucu source zone to the south and the Napo source zone to the north (Fig. 1). In addition to the Yepes *et al.* (2016) shallow crustal source zones, two background sources are added to account for the diffuse seismicity off the main fault systems (north and to south of the Puna source, Fig. 1). The intraslab events are grouped into volumes defined at increasing depths to model the dipping slab (Fig. 2). The Grijalva rifted margin separates two different subducting slabs with many more events in the southern part (Farallon slab). The Farallon slab is modeled by four dipping volumes; the Morona zone at 100–130 km depth is the most seismically active. A precise description of the crustal and intraslab sources can be found in Yepes *et al.* (2016).

The subduction interface segmentation has been revised with respect to the one described in the Yepes *et al.* (2016) model after new interpretations emerged following the 16 April 2016 M_w 7.8 Pedernales megathrust earthquake. The strongly coupled Esmeraldas segment, which hosted the 1906 M_w 8.4–8.8 earthquake (Kanamori and McNally, 1982; Di Giacomo *et al.*, 2015; Ye *et al.*, 2016), is now extended 50 km farther to the south (Fig. 1) with respect to the model from Yepes *et al.* (2016). The 2016 M_w 7.8 Pedernales earthquake rupture stopped slightly south of the Esmeraldas source zone southern boundary proposed in Yepes *et al.* (2016) and Nocquet *et al.* (2016). The new Esmeraldas zone includes the entire seismically highly coupled area modeled by Chlieh *et al.* (2014) and Nocquet *et al.* (2016). The Bahia source zone in Yepes *et al.* (2016), south of the Esmeraldas source segment, is thus reduced with respect to the 2016 model and is now called La Plata. It includes a weakly locked corridor as well as a highly locked shallow patch around La Plata island imaged from Global Positioning System (GPS) interseismic velocities (latitude −1.3°; Vallée *et al.*, 2013; Chlieh *et al.*, 2014; Collot *et al.*, 2017). This area appears to release a significant fraction of strain by frequent slow-slip events, possibly precluding the occurrence of large

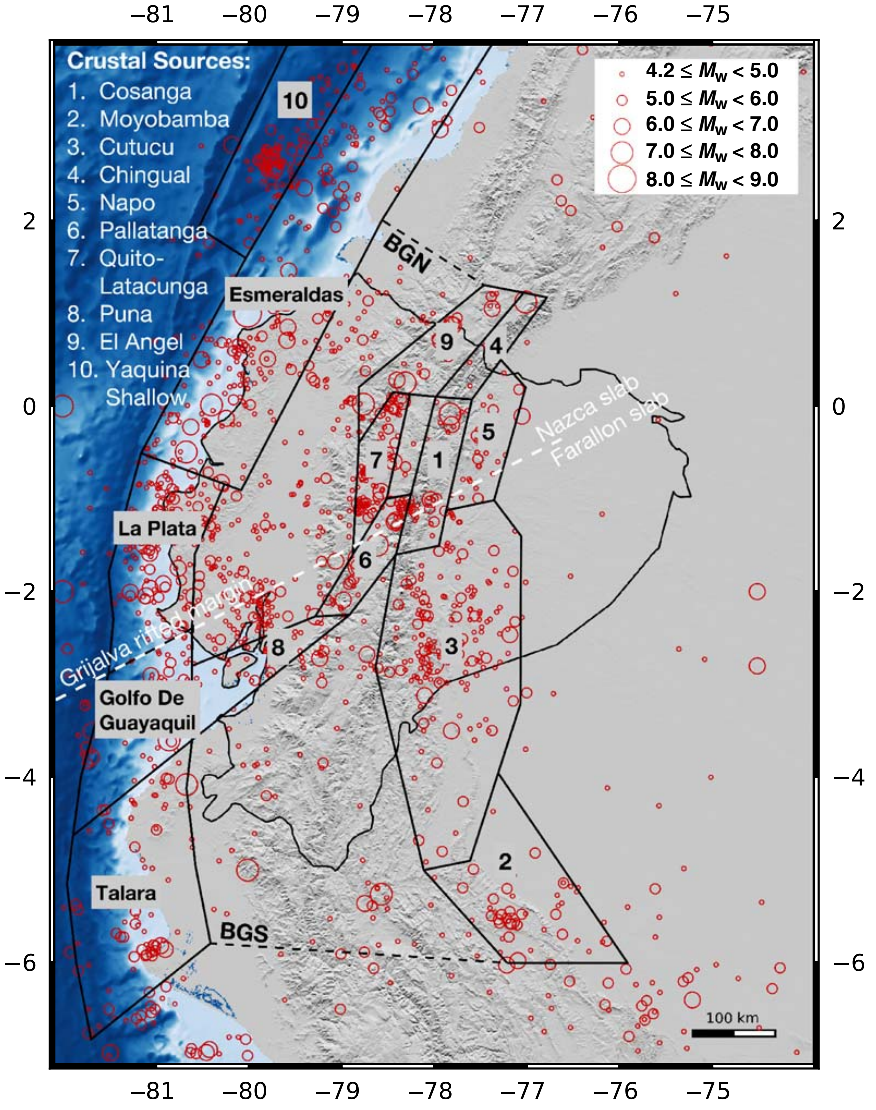

Figure 1. Seismogenic sources: interface-dipping planes and crustal area sources, earthquakes with depth ≤ 35 km (Beauval *et al.*, 2013; BSSA2013 catalog, see the Earthquake Catalogs section). The color version of this figure is available only in the electronic edition.

earthquakes (Collot *et al.*, 2017). South of the Guayaquil Gulf, the previous Talara source zone showing weak to negligible interplate locking (Nocquet *et al.*, 2014; Villegas-Lanza *et al.*, 2016) is now split into two smaller zones, Golfo de Guayaquil (a transition zone) and Talara. Its southern limit corresponds to the southwestern continuation of the Tumbes-Zorritos detachment system and the Banco Peru fault (Witt *et al.*, 2006) as the possible southern boundary of the NAS in the Gulf of Guayaquil area. Overall, the proposed changes with respect to Yepes *et al.* (2016) result in a zonation consistent with the interseismic coupling information derived from GPS data and the history of large subduction earthquakes.

Earthquake Catalogs

Three Alternative Earthquake Catalogs. An earthquake catalog is required to model magnitude–frequency distributions within each source zone. Building a unified and homogeneous earthquake catalog for seismic hazard assessment is a difficult task that requires meticulous work. The resulting catalog inevitably suffers from significant uncertainties because

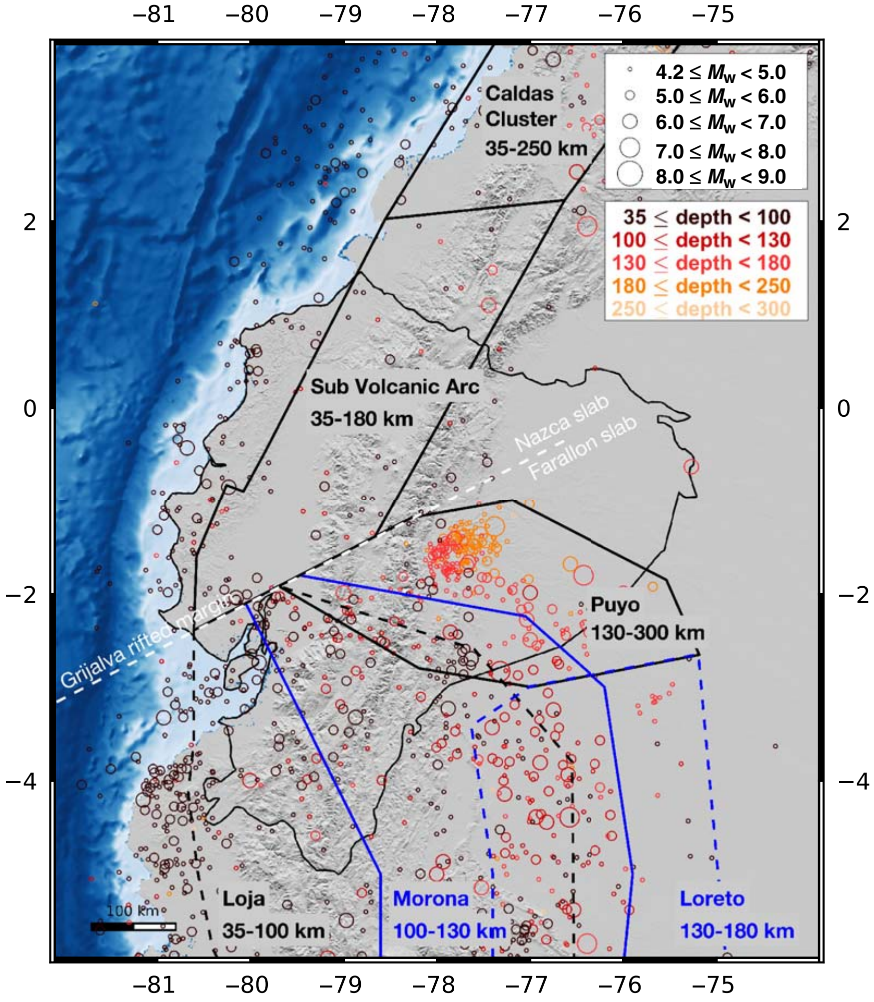

Figure 2. Seismogenic sources: intraslab sources (volumes), earthquakes deeper than 35 km (BSSA2013 catalog, see the Earthquake Catalogs section). The color version of this figure is available only in the electronic edition.

data that encompass different time periods, from historical and early instrumental earthquakes to events recorded by advanced instrumental networks, are gathered. Alternative reliable catalogs provide alternative recurrence models and a means to quantify the uncertainty on the recurrence. To explore uncertainty in the earthquake catalog, three alternative earthquake catalogs are developed for the spatial window −7° to +4° in latitude, and −82° to −74° in longitude.

- The Beauval *et al.* (2013; hereafter, BSSA2013) homogeneous and unified earthquake catalog, covering the time window 1541–2009, was used in the PSHA for Quito (Beauval *et al.*, 2014). It includes historical and instrumental data from local and global earthquake catalogs. As described in detail in Beauval *et al.* (2013), work has been performed to merge the different reliable catalogs available at the time, to identify the best solutions in magnitude and location, and to homogenize earthquake magnitudes.
- The International Seismological Centre (ISC)-based earthquake catalog, covering the time window 1901–2014 (Table 1), is built from three global instrumental catalogs: the new global ISC-Global Earthquake Model (GEM) catalog (Storchak *et al.*, 2015), the ISC event catalog, and the Global Centroid Moment Tensor (CMT) catalog. This catalog is more homogeneous in terms of magnitude than the BSSA2013 catalog. It is possible to ignore historical earthquakes because recurrence models rely mostly on the

Table 1

International Seismological Centre (ISC)-Based Earthquake Catalog, All Events with Proxy $M_w \geq 4.2$

Catalog	Author	Type Magnitude	Minimum Magnitude	Maximum Magnitude	Minimum Year	Maximum Year	Total Number of Events
GEM	Various	M_w	5.1	7.8	1920	2000	106
GEM	Global CMT	M_w	5.56	8.09	1965	2013	101
GEM supp	Various	Proxy M_w	6.12	8.35	1906	1928	5
Global CMT	Global CMT	M_w	4.8	5.8	1977	2013	169
ISC	Global CMT	M_w	4.9	6.3	2007	2014	7
ISC	ISC	Proxy M_w from MS	6.4	6.5	1952	1953	2
ISC	ISC	Proxy M_w from m_b*	4.28	6.16	1964	2014	2022*
ISC	NEIC	Proxy M_w from M_s	4.2	4.2	1990	1990	1
ISC	NEIC	Proxy M_w from m_b*	4.28	5.6	1985	2014	25*
ISC	NEIS	Proxy M_w from m_b*	4.28	5.21	1971	1978	44*
ISC	USCGS	Proxy M_w from m_b*	4.28	6.02	1965	1965	18*
ISC	ABE1	m_b surrogate for M_w	7.1	7.2	1917	1937	2
ISC	AN2	M_s surrogate for M_w	7	7	1907	1912	2
ISC	P&S	M_w	7.2	7.2	1901	1901	1
ISC	PAS	M_s surrogate for M_w	6.5	6.8	1954	1958	4
ISC	PAS	M_s surrogate for M_w	5.5	6.8	1930	1950	21

GEM, Global Earthquake Model; CMT, Centroid Moment Tensor; NEIC/NEIS, National Earthquake Information Center; USCGS, United States Coast and Geodetic Survey; ABE1, Abe (1981); AN2, Abe and Noguchi (1983); P&S, Pacheco and Sykes (1992); PAS, Gutenberg and Richter (1965).

*Magnitude m_b converted in M_w applying $M_w = \exp(0.741 + 0.210 m_b) - 0.785$ (Lolli *et al.*, 2014, global equation).

most populated magnitude bins based on the instrumental part of the catalog (however, historical earthquakes are considered when proposing maximum magnitudes). For earthquakes with m_b and M_s teleseismic magnitudes, M_w proxies are estimated by applying Lolli *et al.* (2014) global conversion equations. Catalog details are provided in the second part of this section.

- The National Earthquake Information Center (NEIC)-based catalog is provided by the NEIC of the U.S. Geological Survey (see Data and Resources). It includes the NEIC solutions, as well as solutions from other global and local catalogs. Since the 1970s, the NEIC delivers solutions earlier and uses fewer stations than the ISC. Although it is not as complete as the ISC Bulletin, it advantageously covers the time window 1900–2017, including the 2016 megathrust event. For earthquakes with m_b and M_s teleseismic magnitudes, M_w proxies are estimated applying Lolli *et al.* (2014) conversion equations.

In the final logic tree, a weight of 0.5 is attributed to the BSSA2013 catalog branch because this catalog is considered the most complete in terms of both instrumental and historical earthquakes. A weight of 0.4 is attributed to the ISC-based catalog branch, as it contains improved locations and magnitudes for instrumental events with $M_w \geq 5.5$. Lastly, a weight of 0.1 is attributed to the NEIC-based catalog branch. When modeling earthquake recurrence in the source zones, the NEIC-based catalog appeared to be the least complete. The ISC-based catalog and the NEIC-based catalog are declustered and completeness time periods are identified using the same procedures as for the BSSA2013 catalog (see details in Beauval *et al.* 2013). Around 20% of clustered events are discarded from the ISC-based and NEIC-based catalogs. Table 2 summarizes the time period of completeness obtained from graphics that represent the cumulative number of events versus time.

Building the ISC-Based Catalog. The final homogenized ISC-based catalog is displayed in Figure 3 (magnitudes of events vs. time) and summarized in Table 1. It is built from the ISC-GEM, ISC, and Global CMT catalogs. The ISC-GEM instrumental catalog is updated regularly (1900–2013, Storchak *et al.*, 2015; v. 4.0 released in January 2017). This catalog results from an extensive effort to collect and digitize a new parametric earthquake bulletin. Hypocenters have been computed from the original arrival-time data using the same technique and velocity model (Di Giacomo *et al.*, 2015). Uniform procedures have been applied to determine magnitude throughout the entire catalog; surface wave M_s and short-period body wave m_b were recomputed; M_w magnitudes are derived either from the Global CMT project (Dziewonski *et al.*, 1981; Ekström *et al.*, 2012), or computed from published estimates of seismic moment or from proxy values obtained by converting the M_s and m_b magnitudes. Overall, 212 earthquakes (M_w 5.1–8.4) fall in our spatial window of interest, including five events that belong to the ISC-GEM supplement catalog (see Storchak *et al.*, 2015).

Solutions for earthquakes with lower magnitudes or earthquakes in the early instrumental period that were not included in the ISC-GEM project are retrieved from the ISC event catalog. The ISC Bulletin is the most complete source of earthquake solutions on a global scale. It reports both revised and preliminary locations using a merged data-set of arrival times provided by global, regional, and local

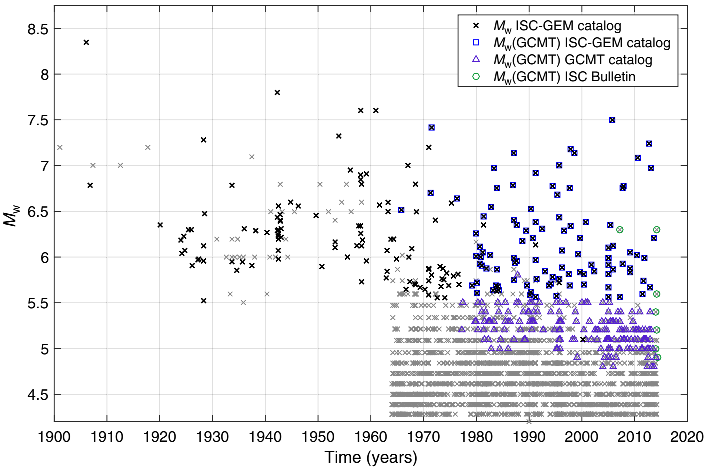

Figure 3. Final International Seismological Centre (ISC)-based earthquake catalog, built from the ISC-Global Earthquake Model (GEM), ISC, and Global Centroid Moment Tensor (GCMT) catalogs, homogenized in magnitude M_w. The color version of this figure is available only in the electronic edition.

contributing institutions. Here, we use the ISC event catalog, which provides a preferred (prime) location and the list of all magnitudes available for an event. The reviewed period extends to 2014. When available, the location calculated by the ISC is always selected as prime location. In the early instrumental period (1900–1963), there were 32 events in the ISC catalog that were not included in the ISC-GEM catalog (Fig. 3). Solutions for these events are more uncertain than ISC-GEM solutions; nonetheless they are taken into account. Of these events, 27 have a magnitude estimated by Pasadena (PAS) (Gutenberg and Richter, 1965), 1 by P&S (Pacheco and Sykes, 1992), 2 by AN2 (Abe and Noguchi, 1983), and 2 by ISC. Magnitudes in the early instrumental period are considered surrogates to the moment magnitude. From 1964 on, the list of magnitudes available can be long and a priority scheme is required. For each event, the preferred magnitude is selected from the following magnitude authors list, applying a ranking for authors and magnitude type: M_w Global CMT/HRV > M_w NEIC > m_b ISC > m_b NEIC or NEIS or United States Coast and Geodetic Survey (decreasing order of priority). Because many Global CMT M_w magnitudes are lacking in the ISC event catalog, we extracted them directly from the original Global CMT catalog (see Data and Resources). Body-wave magnitudes m_b and surface-wave magnitudes M_s are converted into M_w by applying Lolli *et al.* (2014) global equations (Fig. 4).

The 2319 earthquakes from the ISC event catalog (M_w proxy ≥ 4.2) are appended to the 212 events from the ISC-GEM catalog ($M_w \geq 5.5$, one exception with M_w 5.1, Table 1). The final ISC-based catalog contains 2531 events with $M_w \geq 4.2$ (Fig. 3). For the first half of the century (1900–1963), only magnitudes down to M_w 5.5 are reported in the catalog. Original magnitude types and authors are summarized in Table 1, showing that around 88% of all events in the final catalog are described by a magnitude m_b converted into M_w with the Lolli *et al.* (2014) equation.

Table 2

Completeness Periods per Magnitude Interval for the Three Homogenized and Declustered Earthquake Catalogs

Magnitude of Completeness	ISC-Based Catalog	NEIC-Based Catalog	BSSA2013 Catalog
4.2	1969	1973	1995
4.5	1964	1973	1963
4.8	1964	1973	1963
5.1	1964	1973	1963
5.4	1964	1971	1963
5.7	1957	1965	1963
6.0	1925	1930	1900
6.3	1925	1920	1900
6.6	1925	1920	1900
6.9	1900	1900	1900
7.2	1900	1900	1800
≥ 7.5	1900	1900	1750

BSSA2013, Beauval *et al.* (2013).

Magnitude–Frequency Distributions

The most widely used model to estimate frequencies of earthquakes in seismogenic sources is the Gutenberg–Richter model (Gutenberg and Richter, 1944). The logarithm of the number of earthquakes decreases linearly with magnitude in most source zones in Ecuador. However, depending on the available data, the Gutenberg–Richter parameters are sometimes poorly constrained and the uncertainty on the recurrence model needs to be taken into account. Even in sources with many events, the modeling of the recurrence bears significant uncertainties: uncertainties on earthquake hypocentral locations and magnitudes, the scheme established to select the best solutions, the choice of magnitude conversion equations, the identification of clustered events, the determination of completeness periods, the magnitude range and magnitude bin width used to model the recurrence, and the method selected to estimate recurrence parameters. Therefore, we decided to use three alternative earthquake catalogs, each with their own advantages and disadvantages, as a way to estimate the uncertainty on the recurrence model within the source zones. The three alternative recurrence models are included in the logic tree.

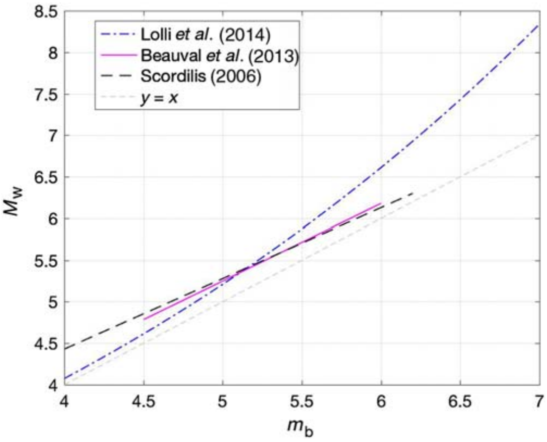

Figure 4. Magnitude conversion equations, m_b into M_w. Lolli *et al.* (2014) is used for the ISC-based and National Earthquake Information Center (NEIC)-based catalogs (see the Earthquake Catalogs section). Beauval *et al.* (2013) is used in the BSSA2013 catalog. The color version of this figure is available only in the electronic edition.

In the Fault and Background Model section, we present a set of the best-characterized crustal fault sources. For each crustal source zone that encloses a fault, maximum magnitude bounding the recurrence model is inferred from the area of the fault by applying the Leonard (2010) scaling relationship (see Tables 5 and 6, and the Fault and background Model section). In two sources, Pallatanga and El Angel, the magnitude of the largest historical event estimated from intensities (67th percentile, Beauval *et al.*, 2010) is larger than the magnitude obtained from the scaling relationship; therefore, the maximum observed magnitude is used instead. For intraslab sources, an arbitrary 0.5 degree is added to the maximum observed magnitude. The interface source zones are modeled as dipping planes. The maximum magnitudes for the segments of the interface source zones are obtained from the Strasser *et al.* (2010) scaling relationship for interface events ($M_w = a + b \log_{10}(L)$, in which $a = 4.868$ and $b = 1.392$), considering the maximum length of the segment at 50 km depth for Esmeraldas (627 km) and at 40 km depth for La Plata (181 km), Golfo de Guayaquil (134 km), and Talara (246 km). Maximum magnitudes for all sources are given in Table 3.

Table 3

Area Model, Parameters of Magnitude–Frequency Distributions, and Supplementary Information for Each Source Zone (relying on the BSSA2013 catalog)

Zone	a	b	$\lambda_{M_w \geq 4.5}$	M_0 for GR	Number of Events $\geq M_0$	M_{maxobs}	M_{max}	Depth Range
Cosanga	2.7701	0.71	0.3866	4.8	13	7.1	7.8	0–35*
Moyobamba	4.4484	0.98	1.082	4.8	28	6.9	7.7	0–35*
Cutucu	5.4443	1.17	1.436	4.5	69	7.0	7.8	0–35*
Chingual	3.0831	0.98†	0.046	4.2	3	7.4	7.6	0–35*
Napo	3.4369	0.98†	0.106	4.5	5	5.6	7.8	0–35*
Pallatanga	2.8012	0.73	0.341	4.5	18	7.6	7.9	0–35*
Quito Latacunga	2.6797	0.70	0.336	4.5	17	6.4	7.3	0–35*
Puna	3.5830	0.98†	0.149	4.5	7	5.2	7.5	0–35*
El Angel	3.4503	0.98†	0.127	4.5	9	7.2	7.7	0–35*
Yaquina Shallow	6.7516	1.39	3.012	4.8	55	6.1	6.6	0–50*
Esmeraldas	4.0002	0.81	2.341	4.8	74	8.8(8.4‡)	8.8	3–50§
La Plata	3.5598	0.80	0.915	4.5	46	6.7	8.0	3–40§
Golfo de Guaya	3.4765	0.84	0.492	4.5	25	7.5	7.8	3–40§
Talara	4.3639	0.91	1.916	4.8	53	7.1	8.2	3–40§
Loja	6.8273	1.33	6.718	4.8	130	7.2	7.7	35–100*
Morona	4.4742	0.89	2.958	4.8	84	7.3	7.8	100–130*
Puyo	5.3015	1.05	3.6	4.8	88	7.5	8.0	130–300*
Subvolcanic arc	5.0710	1.11	1.141	4.5	55	6.7	7.2	35–180*
Caldas cluster	4.7058	1.05	0.987	4.8	24	6.7	7.2	35–250*
Loreto	7.3757	1.62	1.279	4.8	20	7.5	8.0	130–180*
BGN$^{\|}$	4.5245	1.09	0.428	4.8	10	6.4	7.0	0–35*
BGS$^{\|}$	4.5428	1.04	0.697	4.5	36	7.2	7.5	0–35*

a- and *b*-values of the Gutenberg–Richter (GR) model using the BSSA2013 catalog, annual exceedance rate of M_w 4.5, minimum magnitude used in the recurrence modeling, number of events to derive the model (inside periods of completeness), maximum observed magnitude, and maximum magnitude bounding the recurrence model.

*A probability density function for the depth is built from the depths of earthquakes belonging to each source, distributing earthquakes between the minimum and maximum depths.

†*b*-value estimated over the whole Cordillera and coastal plain.

‡Magnitude M_w of the 1906 event estimated 8.4 in the ISC-GEM catalog (Di Giacomo *et al.*, 2015).

§The recurrence model is built from earthquakes falling inside the volume, then distributed over a dipping fault plane extending from the minimum to the maximum depth.

$^{\|}$Two background sources added with respect to Yepes *et al.* (2016) crustal model.

Table 4
Parameters Used in the Probabilistic Seismic Hazard Assessment (PSHA) Calculation

Parameter	Value Used
M_{min}	M_{w} 5.0
Maximum distance	250 km
Truncation of σ	+4
V_{S30}	760 m/s

Minimum magnitude used for integrating the magnitude–frequency distributions, maximum source–site distance taken into account, truncation level of the Gaussian predicted by the GMM, and V_{S30} of the generic sites.

A set of recurrence parameters (*a*- and *b*-values) is obtained from each earthquake catalog, yielding three alternative areal source models. Recurrence parameters are estimated using the maximum-likelihood method of Weichert (1980), with a 0.3 magnitude interval and a minimum magnitude varying from M_{w} 4.2 to 4.8, depending on the source. Table 3 summarizes the values obtained from the BSSA2013 catalog. Figure 5 displays the recurrence curves modeled from the three alternative earthquake catalogs for eight example sources that contributed significantly to the hazard. For intraslab sources, all magnitude–frequency distributions except one (Loreto) are well constrained and rely on many events (55–130 events inside periods of completeness), and the three earthquake catalogs provide close recurrence curves. Recurrences obtained for Loja (35–100 km depth), Morona (100–130 km), and subvolcanic arc (35–180 km) are displayed in Figure 5. The thickness of the Morona source is only 30 km; this source presents the highest earthquake density among intraslab sources.

Magnitude–frequency distributions are rather well constrained in only five out of nine crustal sources (Cutucu, Moyobamba, Pallatanga, Cosanga, and Quito-Latacunga).

Table 5
Fault Parameters—Geologic Model

Fault	Mechanism	L (km)*	Slip Rate (mm/yr)	Maximum Depth	Dip (°)	Width	Alpha (10^{-4})†	M_{max} from A‡	M_{max} Final	b-Value§	a-Value Calculated
Chingual	SS	136	9.8	18	90	18	0.2012	7.4	7.6	0.98	4.65
Cosanga	R	189	9.0	25	40	36	0.2088	7.8	7.8	0.71	3.0
Quito	R	80	1.0	25	55	28	0.2411	7.3	7.3	0.70	1.93
Latacunga	R	48	2.1	25	45	32	0.2626	7.2	7.2	0.70	2.27
Pallatanga	SS	180	3.1	18	75	19	0.1920	7.5	7.9	0.73	2.53
Puna	SS	172	6.0	18	90	18	0.1935	7.5	7.5	0.98	4.42

SS, strike slip; R, reverse.

*Length of the fault estimated from the trace.

†Ratio of the average displacement (Dav) in the largest earthquake rupturing the fault to the fault length. Dav estimated from length L, applying Leonard (2010) scaling relationship: Dav $= 10^{0.833\times\log_{10}(L)-1.34}$ for strike-slip events, and Dav $= 10^{0.833\times\log_{10}(L)-1.30}$ for reverse events.

‡Maximum magnitude estimated from the area $A = LW$, applying Leonard (2010) scaling relationship: $M_{\mathrm{w}} = \log_{10}(A) + 3.99$ for strike-slip events, and $M_{\mathrm{w}} = \log_{10}(A) + 4.00$ for reverse events.

§b-values of area source zones enclosing the fault systems (in this case, based on the BSSA2013 catalog).

Table 6
Fault Parameters—Geodetic Model (No Aseismic Component)

Fault	Mechanism	L (km)*	Slip Rate (mm/yr)	Maximum Depth	Dip (°)	Width	Alpha (10^{-4})†	M_{max} from A‡	M_{max} Final	b-Value§	a-Value Calculated
Chingual	SS	136	8.1	18	90	18	0.2012	7.4	7.6	0.98	4.57
Cosanga	R	189	9.5	25	40	36	0.2088	7.8	7.8	0.71	3.02
El Angel	SS	118	2.0	18	90	18	0.2061	7.3	7.7	0.98	3.98
Quito	R	80	4.5	25	55	28	0.2411	7.3	7.3	0.70	2.59
Latacunga	R	48	1.0	25	45	32	0.2626	7.2	7.2	0.70	1.95
Pallatanga	SS	180	7.4	18	75	19	0.1920	7.5	7.9	0.73	2.91
Puna	SS	172	7.1	18	90	18	0.1935	7.5	7.5	0.98	4.50
Napo	R	151	2.5	25	30	46	0.2168	7.8	7.8	0.98	4.29

*Length of the fault estimated from the trace.

†Ratio of the average displacement (Dav) in the largest earthquake rupturing the fault to the fault length. Dav estimated from length L, applying Leonard (2010) scaling relationship: Dav $= 10^{0.833\times\log_{10}(L)-1.34}$ for strike-slip events, and Dav $= 10^{0.833\times\log_{10}(L)-1.30}$ for reverse events.

‡Maximum magnitude estimated from the area $A = LW$, applying Leonard (2010) scaling relationship: $M_{\mathrm{w}} = \log_{10}(A) + 3.99$ for strike-slip events, and $M_{\mathrm{w}} = \log_{10}(A) + 4.00$ for reverse events.

§b-values of area source zones enclosing the fault systems (in this case, based on the BSSA2013 catalog).

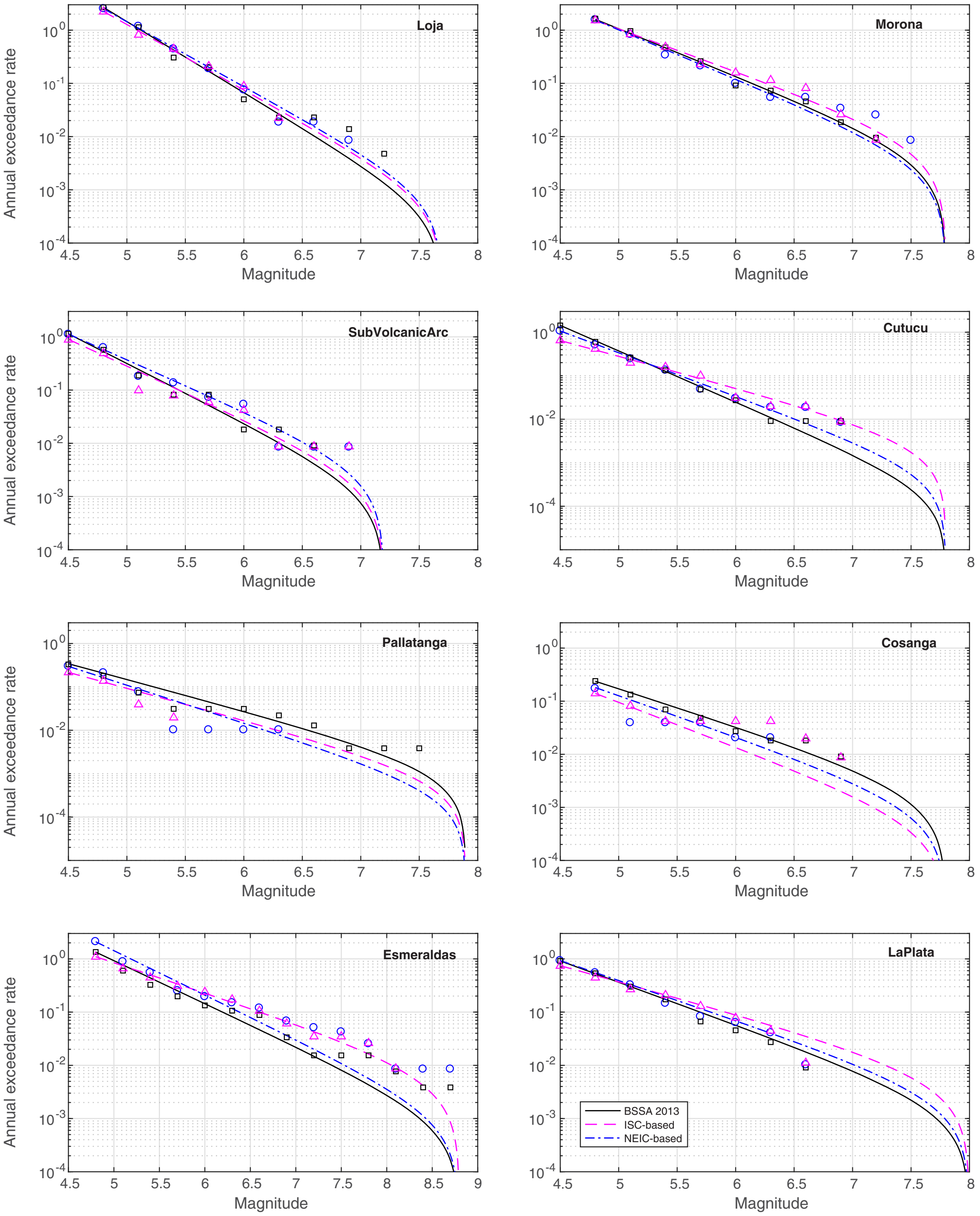

Figure 5. Truncated exponential magnitude–frequency distributions for example source zones significantly contributing to the hazard in Ecuador. Symbols: observed magnitude rates. Three alternative catalogs are used: BSSA2013 catalog (1541–2009, squares), ISC-based catalog (1900–2014, triangles), and NEIC-based catalog (1900–2017, circles). See the Earthquake Catalogs and Magnitude-Frequency Distributions sections. The color version of this figure is available only in the electronic edition.

Crustal earthquakes were extracted from the earthquake catalog using a cutoff value of 35 km (Yepes *et al.*, 2016). The models for the Cutucu (Fig. 5) and Moyobamba sources are derived from 69 ($M_w \geq 4.5$) and 28 ($M_w \geq 4.8$) events, respectively, inside completeness time periods (numbers given for the BSSA2013 catalog). The Cutucu zone is expected to significantly influence the hazard for sites in Ecuador. The influence of Moyobamba will be smaller because it is located in Peru at distances greater than 60 km from Ecuador's southeastern border. There are fewer events inside the Pallatanga, Cosanga, and Quito-Latacunga source zones, but there are still enough to derive a recurrence model (Table 3 and Fig. 5). In the four remaining source zones (Chingual, El Angel, Napo, and Puna), there are too few events to derive reliable recurrence parameters, and the model is built from the observed cumulated annual rate at the minimum magnitude considered associated with a regional b-value (calculated over the whole Cordillera and coastal plain area).

Magnitude–frequency distributions are rather well constrained for interface sources. In the Esmeraldas zone, the model is built from 74 events with magnitude higher or equal to M_w 4.8 inside the completeness periods (down to 50 km depth). The recurrence models inferred from the BSSA2013 and NEIC-based catalogs are similar for magnitudes larger than M_w 6.0, but the recurrence model inferred from the ISC-based catalog predicts much higher rates (Fig. 5). Recurrence parameters for La Plata are rather well constrained, estimated from magnitudes M_w 4.5 to 6.7 (maximum observed magnitude in the BSSA2013 catalog). The recurrence model is then extrapolated up to the maximum magnitude M_w 8.0 (Fig. 5). The Golfo de Guayaquil source is the less active of the interface sources with a recurrence curve established from 25 events with $M_w \geq 4.5$ (Table 3). North of −2.5° latitude, sites on the Ecuadorian coast located over the interface rupture plane are thus at short distances from the rupture plane (shortest distances 20–30 km for the coastal region between Pedernales and Esmeraldas, Fig. 1). South of −2.5° latitude, sites in Ecuador are at greater distances from the interface rupture plane.

We notice that for the crustal source Cutucu and the interface source Esmeraldas, the rates based on the ISC-based catalog are significantly larger than the rates determined from the BSSA2013 catalog for magnitudes larger than $M_w \sim 5.5$ (the opposite occurs for magnitudes lower than $M_w \sim 5.5$). One explanation might be the use of the Lolli *et al.* (2014) equation to convert m_b magnitudes into M_w in the ISC-based catalog, whereas an equation developed from data in and around Ecuador, very similar to the global Scordilis (2006) equation, was used in BSSA2013. Figure 4 displays these conversion equations. The Lolli *et al.* (2014) equation has been carefully developed on a much larger global dataset than previous equations, applying a chi-square general orthogonal regression method that accounts for measurement errors. Considering Lolli *et al.* (2014) the most reliable conversion equation, the BSSA2013 equation might overestimate M_w for magnitudes lower than $m_b \sim 5.2$ and underestimate M_w for larger m_b. As observed in these two sources, the decisions taken to homogenize an earthquake catalog can strongly impact the Gutenberg–Richter curve modeling. However, this discrepancy is only observed in some sources, thus the choice of the conversion equation might not be an unique explanation.

For each source, the three earthquake catalogs yield three recurrence models, which are considered representative of the uncertainty on the recurrence modeling. These alternative models are included in the logic tree.

Selection of Ground-Motion Models

Several GMMs must be selected from published robust models to represent the epistemic uncertainty in ground-motion prediction (Stewart *et al.*, 2015). Although the models developed for crustal events are numerous, there are fewer models predicting ground motions for subduction interface and intraslab events (Douglas and Edwards, 2016). When strong-motion recordings are available, the models that best fit the data should be selected. However, for the selection to be reliable, the accelerometric data must be well distributed over a large magnitude range (from moderate magnitudes to magnitudes close to the maximum magnitude) and a large distance range (including short distances that control the hazard). Except for earthquakes at the Esmeraldas interface, such a dataset does not yet exist for Ecuador. The strong-motion network started in 2009 with nine stations installed in the framework of the French–Ecuadorian research project Andes du Nord (ADN). At present, the national strong-motion network (Red Nacional de Acelerógrafos [RENAC]) includes more than 80 stations, progressively installed since 2011. The network is still in development, with ~30% of the stations telemetered and the characterization of the sites undergoing.

Three robust GMMs are considered for subduction earthquakes: the global model Abrahamson *et al.* (2016; hereafter, Aetal2016), the Chilean model Montalva *et al.* (2017; hereafter, Metal2017), and the Japanese model Zhao *et al.* (2006; hereafter, Zetal2006). The Aetal2016 model is intended to replace older global GMMs. The Metal2017 median model is based on Chilean data, using the same functional form as the Aetal2016 model. The Aetal2016 and Zetal2006 models were ranked among the best-fitting models in several studies comparing predictions with recordings from South America (e.g., Arango *et al.*, 2012; Beauval, Cotton, *et al.*, 2012). Beauval *et al.* (2017) compared the ground motions from the 2016 M_w 7.8 Pedernales megathrust earthquake and its two largest aftershocks (M_w 6.7 and 6.9) to the predictions of these three GMMs. The comparison between observed and predicted ground motions showed that the three models properly predict the amplitudes attenuation in the fore-arc domain. The analysis also demonstrated that the high-frequency attenu-

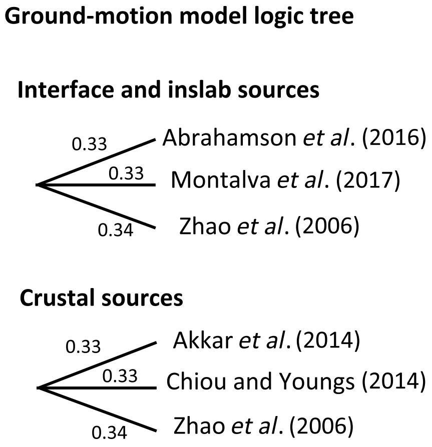

Figure 6. Ground-motion logic tree.

ation is stronger for sites located in the back-arc region with respect to sites located in the fore-arc region, an effect that only the Aetal2016 model takes into account. However, the contribution of interface subduction sources is negligible for rock sites in the arc and back-arc region in Ecuador (for the PGA and return periods ≥ 475 yrs, as will be shown in the Hazard Estimates for Area Source Models section), so the three models are included in the ground-motion logic tree (Fig. 6). The Pedernales earthquake produced a large sequence of aftershocks, with eight events having magnitude equal to or higher than M_w 6.0. Candidate GMMs should be tested against this dataset by applying quantitative methods to potentially refine the selection (e.g., Scherbaum *et al.*, 2009; Beauval, Tasan, *et al.*, 2012). Zhao *et al.* (2016) published an update of the 2006 interface model (as well as crustal and inslab models), but we need to test it against observations before using it.

For intraslab sources, the same three models are selected. Intraslab volumes are defined down to 300 km depth (Table 3). Aetal2016 recommend a depth limit of 120 km for intraslab events when applying the model. The Zetal2006 and Metal2017 databases include intraslab events with focal depths shallower than 125 and 180 km, respectively. Aetal2016 and Zetal2006 must be extrapolated at depths larger than 120–130 km—four sources include such large depths, including the very active Puyo source (130–300 km, Yepes *et al.*, 2016). We calculated the hazard with and without these sources, and we observed that their contribution is not significant. Historical intraslab earthquakes in Ecuador have shown that intensities up to VI–VII are observed at the coast for large deep intraslab earthquakes (e.g., 1971 M_w 7.4, 120 km depth, located in the Morona source), whereas much lower intensities are observed for sites above the hypocenter. This effect, related to the lower attenuation of waves inside the slab (high-Q zone, Fukushima, 1997), is not accounted for in current GMMs.

Because the RENAC database does not include enough crustal events of significant magnitude to perform a meaningful test against GMM candidates, the selection of active crustal GMMs take inspiration from the outputs of the South America Risk Assessment (SARA) GMM working group (Drouet *et al.*, 2017). GMMs were tested against a homogeneous strong-motion database gathering data from Colombia, Chile, Ecuador, and Venezuela. The dataset from Ecuador includes only small events with magnitudes between M_w 4.0 and 5.0. The log-likelihood method was applied to rank the models according to their fit to the data (Scherbaum *et al.*, 2009). Obtained log-likelihood values (see Scherbaum *et al.*, 2009) are quite high for all models (2.8–3.7 for the PGA and 0.2 s, table 2 in Drouet *et al.*, 2017), indicating that none of the models are able to satisfactorily predict the South American dataset. Drouet *et al.* (2017) note that the observed variability is greater than the GMMs prediction, suggesting that more efforts are needed to improve the database, particularly the estimation of V_{S30} values. According to Garcia *et al.* (2017), the three models finally selected for SARA hazard calculations are Akkar *et al.* (2014), Bindi *et al.* (2014), and Boore *et al.* (2014). For hazard calculations in Ecuador, we decided to select Akkar *et al.* (2014), which was established from Mediterranean and Middle East strong motions (Reference Database for Seismic Ground-Motion in Europe [RESORCE] data bank). From the Next Generation Attenuation-West2 models, developed from western United States and international data, the Chiou and Youngs (2014) model is preferred over the Boore *et al.* (2014) model because it accounts for some factors that affect earthquake ground motions (e.g., hanging wall and rupture directivity). Lastly, rather than selecting a second model based on the RESORCE data bank (Bindi *et al.*, 2014), the Zhao *et al.* (2006) Japanese model is selected. The equation is based on data recorded in a tectonic environment close to the Ecuadorian Cordillera hosting many volcanoes. Tested against diverse strong-motion datasets, this equation proved to be robust and stable over the full frequency range (e.g., Beauval, Tasan, *et al.*, 2012; Delavaud *et al.*, 2012). The V_{S30} values must be mapped to site classes following table 2 in Zhao *et al.* (2006). The final GMM logic tree is described in Figure 6.

In this study, probabilistic seismic hazard calculations are performed with the OpenQuake engine (Pagani, Monelli, Weartherhill, Danciu, *et al.*, 2014; GEM, 2017). OpenQuake represents the seismogenic source as a finite rupture. For an area source, a mesh is created over the area and virtual ruptures are generated at each node. The scaling of the rupture depends on the scaling relation selected and the orientation on a set of parameters (nodal plane distribution, hypocentral depth distribution, and upper and lower seismogenic depths; see Monelli *et al.*, 2014). As for fault sources, using the simple fault typology (here for crustal faults) or the complex fault typology (for interface segments), the ruptures are distributed along the fault surface. A mesh is created across the

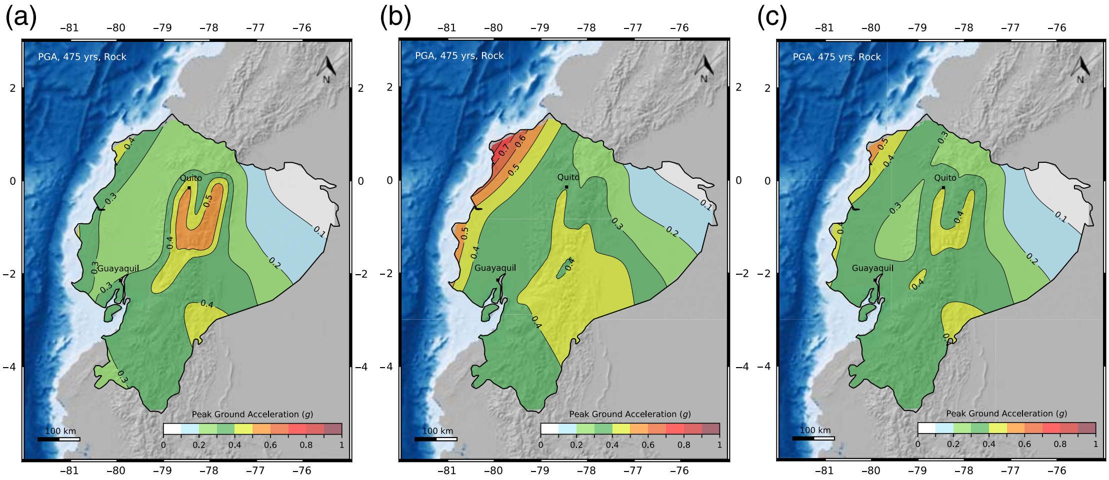

Figure 7. Mean hazard map at 475-yr return period, for peak ground acceleration (PGA) (V_{S30} 760 m/s), using one area source model and the full ground-motion model (GMM) logic tree. Area model based on (a) the BSSA2013 earthquake catalog (50% weight in the final logic tree); (b) the ISC-based earthquake catalog (40% weight); and (c) the NEIC-based earthquake catalog (10% weight). The color version of this figure is available only in the electronic edition.

fault surface and individual ruptures are represented by a subset of nodes within that mesh. Rupture distance is determined from the shortest distance between the target site and the individual rupture. Joyner and Boore distance is determined from the shortest distance between the target site and the surface projection of the fault. More details can be found in the OpenQuake-engine Hazard Book (Pagani, Monelli, Weatherill, and Garcia, 2014).

Hazard Estimates for Area Source Models

Three hazard maps corresponding to the three alternative area source models are calculated for the PGA and for the return period 475 yrs. Results based on recurrence parameters obtained from the BSSA2013, ISC-based, and NEIC-based catalogs are displayed respectively in Figure 7a–c. Parameters used to perform PSHA calculations throughout the article are indicated in Table 4. These maps are mean hazard maps, because the full ground-motion prediction logic tree is considered. South of latitude −2°, acceleration values vary in a 0.1*g* interval from one model to the other, with the highest hazard value 0.4–0.5*g* from the ISC-based model (highest recurrence rates for the Cutucu source zone). Inside the Quito source zone accelerations also differ within a 0.1*g* interval, with the highest accelerations (0.5–0.6*g*) obtained using the BSSA2013 model. The difference in acceleration is larger for sites located inside the Cosanga source zone; the highest accelerations are obtained using the BSSA2013 model, in agreement with the recurrence models obtained in this source zone (Fig. 5). The most striking difference is obtained for sites at the coast north of latitude −1°, located above the Esmeraldas source rupture plane. The recurrence model determined from the ISC-based catalog leads to much higher PGA values (0.5–1.0*g*) than the model that relies on the BSSA2013 catalog (0.3–0.5*g*) or on the NEIC-based catalog (0.3–0.6*g*).

The mean hazard map that relies on the three alternative area models with associated weights, combined with the full GMM logic tree, is displayed in Figure 8a. At 475 yrs, and PGA, accelerations are higher than 0.4*g* at sites on the coast, with maximum values around 0.6–0.7*g* at latitudes around +0.7°. In the Cordillera, values vary between 0.2*g* and 0.5*g*, with the highest hazard for sites inside the Quito-Latacunga, Cosanga, Pallatanga, and Cutucu source zones (see Fig. 1 for names of source zones). In addition, to identify which sources control the hazard, accelerations at 475-yr return period resulting from interface sources only, crustal sources only, and intraslab sources only are determined (Fig. 8b,d). Each mean hazard map is based on the three alternative source models (with associated weights) and the full GMM logic tree. For sites located on the coast, the interface-dipping planes fully control the hazard. For sites located inside the Cordillera, located north of −2°, contributions come mainly from shallow crustal sources, whereas for sites located south of −2°, contributions come both from intraslab and crustal sources.

The area model exhibits low hazard levels in three crustal sources in which late Holocene active faulting has been evidenced (sources El Angel, Chingual, and Puna). The El Angel source is characterized by low seismicity levels in the instrumental period, although a destructive earthquake occurred in 1868 with a magnitude M_w 7.2 estimated from intensity observations (7.1–7.7 within 67% confidence inter-

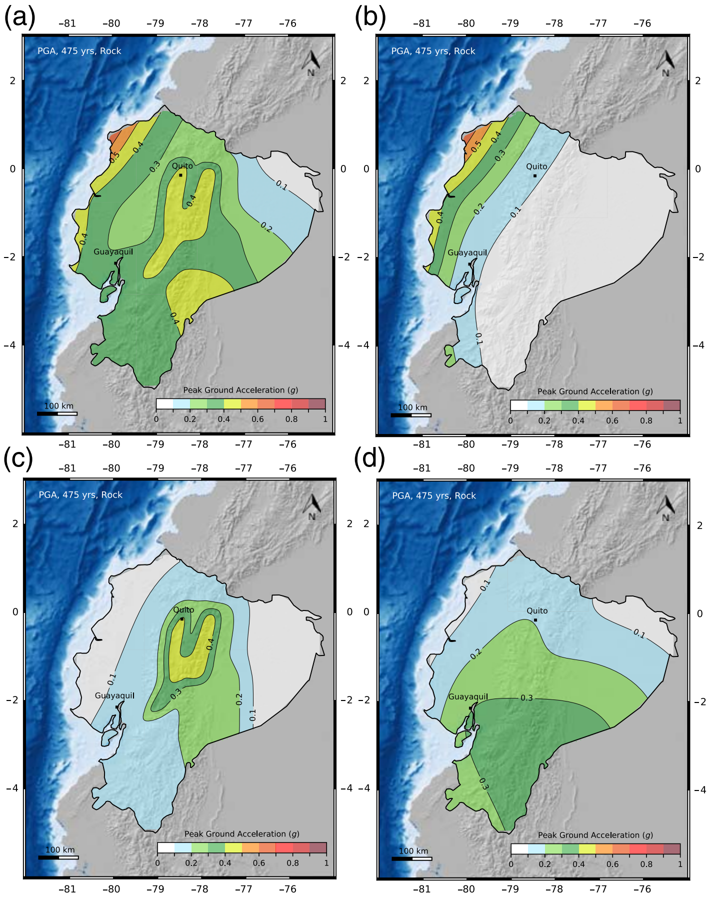

Figure 8. Hazard maps at 475-yr return period for PGA (V_{S30} 760 m/s). (a) Mean obtained from the three alternative area source models (and associated weights) and the full GMM logic tree; (b) same calculation considering only interface source zones; (c) considering only crustal sources; and (d) considering only intraslab sources. The color version of this figure is available only in the electronic edition.

val, Beauval *et al.*, 2010). The seismicity level is also low in the Chingual source zone, although in 1834 a strong earthquake destroyed Sibundoy in the northern edge of the zone (M_w 7.2–7.6, Beauval *et al.*, 2013). Various tectonic and geodetic studies have demonstrated the activity of the El Angel and Chingual fault systems (see Yepes *et al.*, 2016). Because these faults represent a significant threat to the dense population living in the Andean Cordillera, they must be accounted for in the seismic hazard assessment. In the Puna source zone, there is no known historical earthquake, but the activity of the Puna fault system has been demonstrated, with geologic slip rates up to 5.5–6.6 mm/yr (Dumont *et al.*, 2005). A slightly higher value of 7 mm/yr was found by deriving the relative motion between the North Andean and Inca slivers (Nocquet *et al.*, 2014). A fault model is therefore developed to integrate the recent geodetic and active tectonics results.

Fault and Background Model

Here, we describe how we developed a fault model with earthquake recurrences inferred from geologic and/or geodetic slip rates. Because knowledge about these crustal faults is still incomplete, strong hypotheses are necessary to propose fault-plane geometries and evaluate the fault capacity to produce earthquakes. However, the fault-source model offers the advantage of including existing information about active faults, which is not integrated in the area source model. Interface and in-slab sources remain unchanged.

Defining the Set of Active Faults

Along the Ecuadorian margin, oblique subduction induces lithospheric deformation of the overriding continental plate. Active continental deformation is presently localized along a major fault system, connecting several fault segments from the Gulf of Guayaquil to the eastern Andean Cordillera. The crustal deformation is concentrated along the Chingual-Cosanga-Pallatanga-Puna (CCPP) fault system, the Quito-Latacunga fault system, the Eastern Subandean belt, and the El Angel fault system (figs. 1 and 7 in Yepes *et al.*, 2016; Alvarado *et al.*, 2014, 2016; Baize *et al.*, 2015). The CCPP can be considered a continental microplate boundary because it accommodates around 8–10 mm/yr of relative motion between the NAS (Fig. 9) and South American plate (SOAM; Nocquet *et al.*, 2014). Its segmentation comprises northeast-striking right-lateral transpressional faults from the Gulf of Guayaquil into the Andean Cordillera (Puna and Pallatanga), with continuation along the north–south-striking transpressive faults in the eastern Andes (Cosanga) and pure strike-slip right-lateral faults further north (Chingual). In northern Ecuador, west of the CCPP boundary, the north-northeast–south-southwest fault system of El Angel comprises a series of right-lateral strike-slip faults and probably represents the southern prolongation of the major Romeral-Cauca-Patia fault system described in Colombia (Ego *et al.*, 1996; Taboada *et al.*, 2000; Yepes *et al.*, 2016). Furthermore, east of the NAS, shortening across the active Andean back-arc takes place along the eastern sub-Andean thrust-and-fold belts (Ego *et al.*, 1995; Bès de Berc *et al.*, 2005; Alvarado *et al.*, 2016).

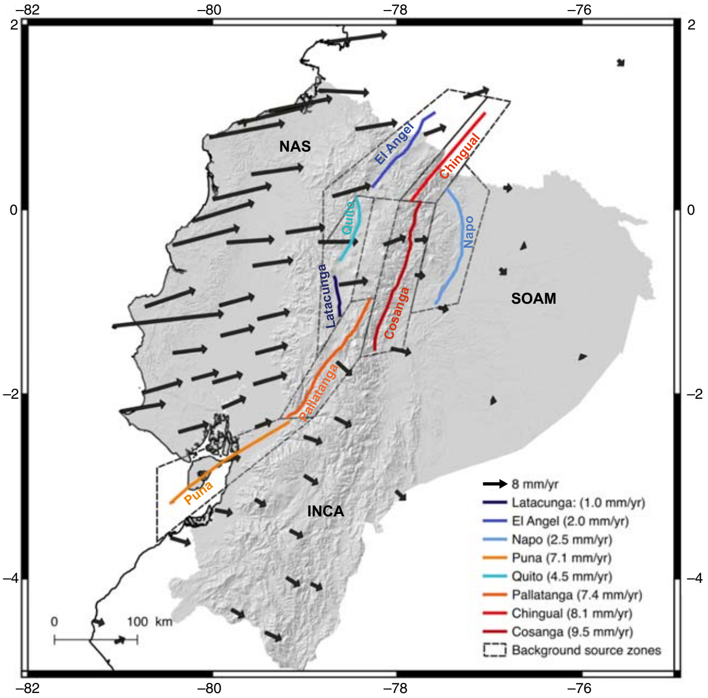

Figure 9. Global Positioning System velocity field and main faults accounted for in the probabilistic seismic hazard calculations. The slip rates estimated for each fault are indicated. Area sources enclosing faults are used as background sources (off-fault seismicity). NAS, North Andean Sliver; SOAM, South American plate; INCA, Inca sliver. The color version of this figure is available only in the electronic edition.

A set of eight crustal fault sources is defined (Fig. 9, Tables 5 and 6). Many fault segments are left aside, with respect to the active fault map (Neotec database, see Data and Resources; Audin *et al.*, 2014), because only the best-characterized segments can be included in the model. The eight fault sources have been defined by analyzing geologic data, earthquake epicenters, focal mechanisms, and GPS results. Geologic slip rates are available for six out of the eight fault sources. For the Chingual fault, Tibaldi *et al.* (2007) estimated slip rates from 7.7 to 11.9 mm/yr based on several late Pleistocene deposits displaced by various branches of the fault. They also estimated Holocene slip rates of 4.3 ± 2.2 mm/yr for the north–south reverse faults south of Chingual fault, which we considered to be part of the Cosanga transpressive fault system (northern section, Yepes *et al.*, 2016). At the southern end of the Cosanga system, Bès de Berc *et al.* (2005) report uplifting velocities of up to 9–10 mm/yr during the Holocene in the upper Pastaza valley by comparing the river incision rates with the fold-and-thrust fault uplift rates located further east. The Quito and Latacunga segments accommodate crustal east–west shortening at rates ranging from 1 to 2.1 mm/yr, respectively (Lavenu *et al.*, 1995; Ego and Sebrier, 1996).

Based on paleoseismological trenching along the southern section of the Pallatanga fault, Baize *et al.* (2015) estimated an average slip rate of ~2.5 mm/yr during the Holocene. Winter *et al.* (1993), from detailed topographic leveling, showed that moraine displacements yield a mean Holocene slip rate of 2.9–4.6 mm/yr in this area. For the Puna segment, Dumont *et al.* (2005) calculated a minimum mean slip rate of 5–7 mm/yr from one particular location on the Puna island during late Pleistocene. Average values of the above-mentioned studies are used in the hazard calculations (Table 5).

In regard to the faults dip, Tibaldi *et al.* (2007) extensively verified in the field the vertical nature of the northeast–southwest right-lateral strike-slip Chingual fault system. The northern section of the Cosanga fault system shows reverse faults dipping ~70° to the east (Tibaldi *et al.*, 2007), consistent with the nodal planes derived from the 1987 M_{w} 6.4 (73°) and 7.1 (64°) earthquakes focal mechanisms (Global CMT catalog). At the southern end of the Cosanga system, Bès de Berc *et al.* (2005) report that the sub-Andean uplift is likely related to the presence of a regional scale low-angle westerly dipping thrust ramp underlying the sub-Andean folds belt. Three focal mechanisms in 1987 associated with the Cosanga faults show nodal plane dips around 40° to the west (Global CMT catalog). It is conceivable that this transpressive section of the microblock boundary evolves from almost vertical at the transition from the transcurrent Chingual system to the north to more gently dipping as the fault strike becomes more orthogonal to the regional compressive stresses to the south.

For the reverse Quito fault, microseismicity reveals a 55° dipping plane to the west (Alvarado *et al.*, 2014), which is corroborated by nodal planes derived from the 1990 M_{w} 5.3 (55°) and 2014 M_{w} 5.1 focal mechanisms (44°, Global CMT catalog). The Latacunga system shows divergently dipping faults dipping 70°–80° to the west along the western side of the Interandean Valley and to the east along the eastern side (Fiorini and Tibaldi, 2012). Representative focal mechanisms for these faults are 1976 M_{w} 5.7 (71°, Ego *et al.*, 1996) and 1996 M_{w} 5.9 (69°, Global CMT catalog). Using the 1996 NEIC focal mechanism solution to constrain the initial parameters, Fiorini and Tibaldi (2012) modeled the fold that results from this blind thrust. The preferred result showed a gently dipping fault plane (28°) to the west. Blind thrusts tend to align vertically as they get closer to the surface because of development of folds or secondary shallower faults. The right-lateral strike-slip Pallatanga faults strike

N30°E and dip ~75° to the west, as Winter *et al.* (1993) found by modeling the fault trace intersection with the topography. The Puna segment also shows a right-lateral strike-slip movement with a positive flower structure identified by Dumont *et al.* (2005) at the Puna and Santa Clara islands. This suggests a near-vertical structure at depth. The average dip values attributed to the set of simplified faults are reported in Tables 5 and 6.

For the hazard calculations, we assume that an earthquake can break over the entire area of the fault. Lengths are defined from the segmentation based on the surface fault trace and we use a maximum depth of 18 km for strike-slip faults and 25 km for thrusts. These depths are based on the analysis of the hypocentral depth distribution of earthquakes in Ecuador (Yepes *et al.*, 2016), estimates of fault widths in existing global databases (e.g., Leonard, 2010), and estimates of locking depths from geodesy and seismology along well-known faults (e.g., Smith-Konter *et al.*, 2011). Fault widths are inferred from the maximum depth and dip values associated with each fault (Tables 5 and 6). Maximum magnitudes are then determined from the resulting area, applying the Leonard (2010) scaling relationship. The depth and width assumption has a major impact on the calculated hazard, because in addition to the length, the width also contributes to define the rupture area and hence the annual seismic moment rate to be released at the fault.

Geodetic Slip Rates

The GPS horizontal velocity field of 53 sites presented in Nocquet *et al.* (2014) is used to determine the slip rate along the eight simplified faults. In a first approach, the Euler poles for the NAS and Inca Sliver (Nocquet *et al.*, 2014) are used to calculate the relative velocity along the fault delimiting their boundaries. In this case, the fault portion is assumed to accommodate all the relative motion between the two adjacent blocks. Slip rates for the Puna and Pallatanga (Inca sliver/NAS boundary) and Cosanga and Chingual segments (NAS/SOAM boundary) are determined using this approach. As an alternative method, we also use the relative horizontal velocities between pairs of GPS located on either side of the fault, far enough (~30 km) from the fault trace so that the elastic contribution from the locked portion of the faults remains small. Slip rates can thus be estimated for inter-Andean and sub-Andean faults for which no block model has been proposed yet. We also carefully checked our selection of GPS stations so that the effects of neighboring crustal faults and of subduction interface are negligible. These slip rates potentially account for internal deformation within the North Andean and Inca blocks. For the faults forming the CCPP corridor, a weighted mean value from slip rates obtained using both approaches has been used for the subsequent fault model.

Only the best-characterized fault sources are considered; thus all motion is assumed to take place along these faults. This is a strong assumption, because the deformation might be distributed over a broader area and secondary faults (e.g., Aktug *et al.*, 2009). A second issue is that, given the density of available GPS sites for continental deformation monitoring, no locking depth or coupling coefficient is available for crustal faults in Ecuador, except for Quito (Alvarado *et al.*, 2014). To account for this lack of information in our PSHA calculation, we considered two alternative cases: one calculation is made assuming faults locked over the entire seismogenic thickness and another is made with an aseismic deformation component arbitrarily fixed to 50% of the total slip rate.

Obtained geodetic slip rates are close to geologically determined slip rates for some faults (Chingual, Latacunga, Puna, and Cosanga), while they significantly disagree at some others (Pallatanga and Quito). Similar discrepancies have been found worldwide (e.g., Polonia *et al.*, 2004) and are most likely due to local variations of coupling during the earthquake cycles (e.g., Chuang and Johnson, 2011). Another simple explanation relies on the fact that geodetic models assume all relative motion to be accommodated by a single idealized fault. We also recognize that our knowledge of active faults in some areas is incomplete. Figuring out which value is most relevant for PSHA is uncertain. Next, we show some sensitivity results using different slip-rate estimates.

Hazard Estimates Based on the Fault and Background Source Model

Assuming deformation remains steady in time, the earthquake recurrence model for a fault is inferred from the average slip rate following the same methodology as Woessner *et al.* (2015; European fault model) and Beauval *et al.* (2014; Quito fault). Ignoring aseismic creep, the annual total seismic moment rate on the fault is estimated as $\dot{M}_0 = \mu S A$, in which S is the slip rate per year, μ is the shear modulus (taken as 3×10^{11} dyn/cm^2), and A is the rupture area. Assuming 50% of creep, only half of $\dot{M}_0$ is then available to generate earthquakes. A recurrence model is required to distribute the seismic moment rate that will be released on the fault through earthquakes of various magnitudes. The Anderson and Luco (1983) exponential function is selected, constrained by the slip rate, a b-value, and the maximum magnitude on the fault (for more details, see Beauval *et al.*, 2014). For each fault segment, the b-value has been estimated from the earthquake catalog in the source zone enclosing the fault. The a-values estimated for each fault are reported in Tables 5 and 6. For each fault, a magnitude–frequency distribution is established. Magnitudes larger than or equal to M_w 6.0 are distributed on the fault, whereas magnitudes lower than M_w 6.0 are distributed inside the source zone enclosing the fault as background seismicity. The fault is assumed to be the only structure in the area able to host large magnitudes. To complete the model, areas without faults remain unchanged with respect to the area model, as well as interface and inslab sources.

The probabilistic seismic hazard calculation is performed with the full ground-motion prediction logic tree.

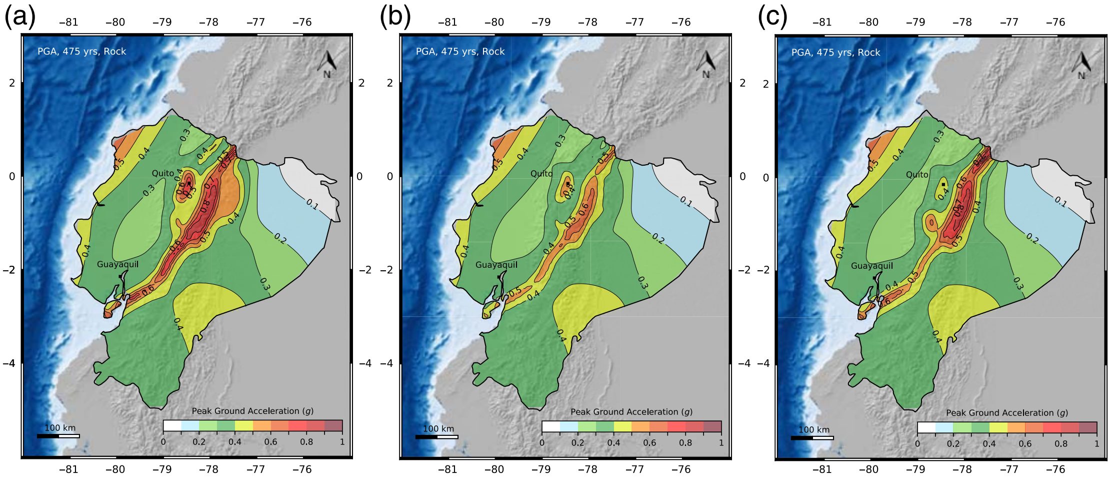

Figure 10. Mean hazard maps based on the fault and background source models, at the PGA, 475-yr return period (V_{S30} 760 m/s). Earthquake recurrence source model relying on (a) the geodetic slip rates without creep; (b) the geodetic slip rate with 50% creep; and (c) the geologic slip rate. Parameters of faults are reported in Tables 5 and 6. Exploration of the three branches corresponding to three alternative earthquake catalogs (b-values of the fault model; areas without faults), and full GMM logic tree (Fig. 6). The color version of this figure is available only in the electronic edition.

At 475-yr return period and for PGA, the source model based on geodetic slip rates (no aseismic component) yield accelerations higher than or equal to $0.6g$ for sites located along the CCPP fault sources (slip rates from 7.1 to 9.5 mm/yr, Table 6), as well as along the Quito fault source (4.5 mm/yr). The largest hazard values ($\geq 0.8g$) are obtained for sites right above the Cosanga thrust fault plane, as well as for those close to the Chingual strike-slip fault source (Fig. 10a). Lower values (0.4–$0.6g$) are obtained for sites above the Napo (2.5 mm/yr) and Latacunga (1.0 mm/yr) fault planes and along the El Angel strike-slip fault source (2.0 mm/yr). Arbitrarily considering 50% of aseismic deformation, the hazard obtained is much lower (Fig. 10b). For sites along the CCPP fault sources, and along the Quito fault source, accelerations are between $0.5g$ and $0.6g$; whereas for sites along the El Angel, Latacunga, and Napo fault sources, accelerations are between $0.3g$ and $0.4g$. Moreover, hazard maps are calculated considering geologic slip rates on the six faults where they are available (Table 5 and Fig. 10c). For sites along fault sources where geologic slip rates are close to estimated geodetic slip rates, obtained hazard values are comparable: Chingual, Cosanga, Puna (PGA $> 0.6g$). For the Quito fault source, the geologic slip rate (1 mm/yr) is much lower than the geodetic slip rate (4.5 mm/yr) and lower values are obtained ($0.4g$–$0.5g$). The opposite is observed for sites along the Latacunga fault source with values between $0.4g$ and $0.6g$ based on the geologic slip rate (2.1 mm/yr).

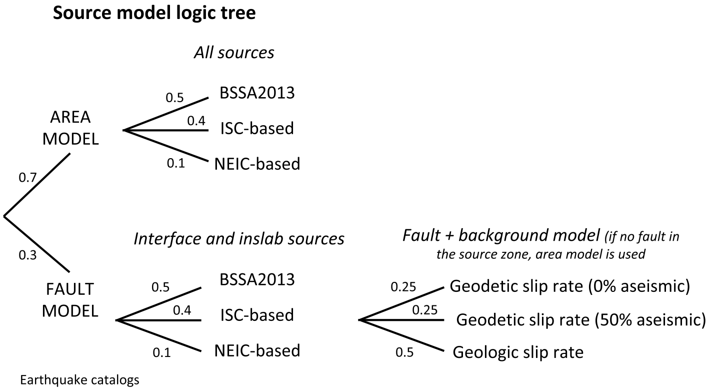

Figure 11. Source model logic tree; the combination of the branches leads to 12 alternative source models.

Complete Logic Tree

An area source model was developed in which magnitude–frequency distributions are based on three different earthquake catalogs. This area model is rather well constrained in most sources, except in four out of nine crustal sources in which regional b-values must be applied. A fault model is developed to take advantage of available geologic and geodetic slip rates estimated for the main crustal faults.

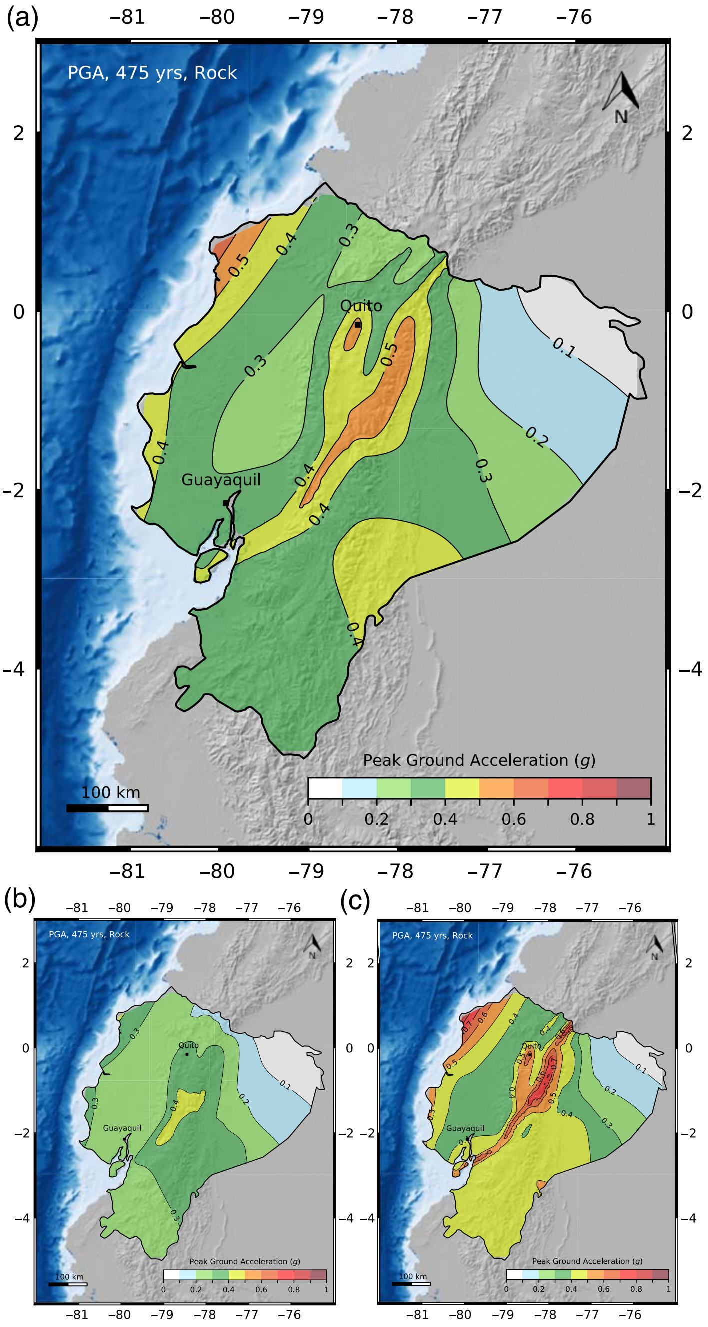

Figure 12. (a) Mean hazard map at the PGA, 475-yr return period (V_{S30} 760 m/s), from the complete logic tree, combining the source model logic tree (Fig. 11) and the ground-motion prediction logic tree (Fig. 6), as well as hazard maps corresponding to (b) the 16th and (c) 84th percentiles. The color version of this figure is available only in the electronic edition.

The area and fault models constitute two alternative source models to populate the logic tree. The fault model relies on several strong hypotheses, such as the assumption that the main structures accommodate all the measured or modeled deformation, or assumptions about the percentage of aseismic slip. Therefore, in the final logic tree more weight is given on the area model (70%) than on the fault model (30%). The scheme detailing the final source logic tree is displayed in Figure 11. Combining the source model (12 alternative models) and the GMM (3 alternative models per source type), the final logic tree is made of 324 different combinations (12 × 3 × 3 × 3).

For simplicity and to limit the number of figures, results are shown for PGA and for the return period 475 yrs, considering a generic site with V_{S30} 760 m/s. The final mean hazard map is displayed in Figure 12, together with the maps corresponding to the 16th and 84th percentiles. Comparing the final mean values with the mean area model (Fig. 8a), including the crustal fault model in the calculation has consequences for all sites located along the CCPP corridor, as well as for sites above the Quito thrust fault plane (0.1–0.2g increase). The uncertainty on the hazard estimates is significant. Considering the hazard map corresponding to the 16th percentile, most of the country presents PGAs lower than 0.4g. Considering the 84th percentile, all sites on the coast and in the Cordillera present PGAs higher than 0.4g, reaching maximum values around 0.8g on the coast and 0.7g in the Cordillera. The uncertainty obtained is not a surprise, keeping in mind the differences in hazard obtained from different earthquake catalogs (Fig. 7), as well as the differences obtained if choosing a fault model rather than an area model (Fig. 10a–c with respect to Fig. 8a). The difference between the 16th and 84th percentile maps is displayed in Figure 13, showing that uncertainty on hazard estimates is high for sites along the northern coast (above −1°, up to 0.4–0.5g difference), and inside the Puna, Cosanga, and Chingual source zones. The largest uncertainty is found for sites inside the Chingual source zone (0.6g difference at maximum between the 16th and 84th percentiles).

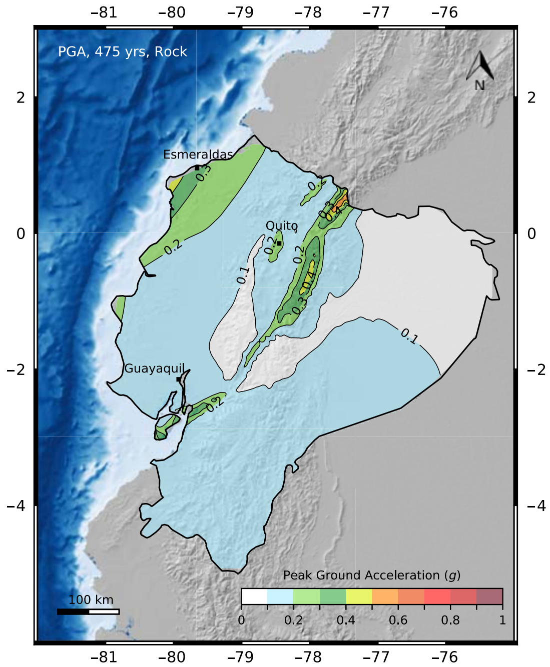

Figure 13. Uncertainty on the PGA at 475-yr return period: difference between accelerations corresponding to 84th and 16th percentiles (Fig. 12b,c). Percentiles are obtained exploring the complete logic tree (source model and ground-motion logic trees). The color version of this figure is available only in the electronic edition.

The uncertainty on the source model is responsible for a large part of the uncertainties on the final hazard estimate. The ground-motion prediction component also carries significant uncertainties. Figure 14 displayed the three hazard maps obtained by exploring the full source logic tree (Fig. 11) but fixing the GMM used for each source type. From one map to another, the models for predicting the ground motions produced by interface events and crustal events are modified. For the PGA at 475-yr return period, the Metal2017 model leads to higher hazard values for the coast than the Aetal2016 and Zetal2006 models (around $0.2g$ difference). Applying the Akkar *et al.* (2014) model rather than the Chiou and Youngs (2014) model leads to increased hazard estimates for sites in the Cordillera (around $+0.1g$).

To assess the respective contribution of the source model uncertainty and GMM uncertainty on the overall uncertainty, the hazard is calculated exploring only the source model logic tree (fixing the GMMs used), then exploring only the ground-motion logic tree (fixing the source model used). Results are displayed for three important cities in Ecuador (Fig. 15): the capital Quito, the largest city in the country Guayaquil, and Esmeraldas city, which plays a key role in the oil business. Results show that the component controlling the overall uncertainty depends on the site: in Quito and Esmeraldas, the uncertainty related to the source model is higher (or much higher) than the uncertainty related to the GMM, whereas in Guayaquil the opposite is observed.

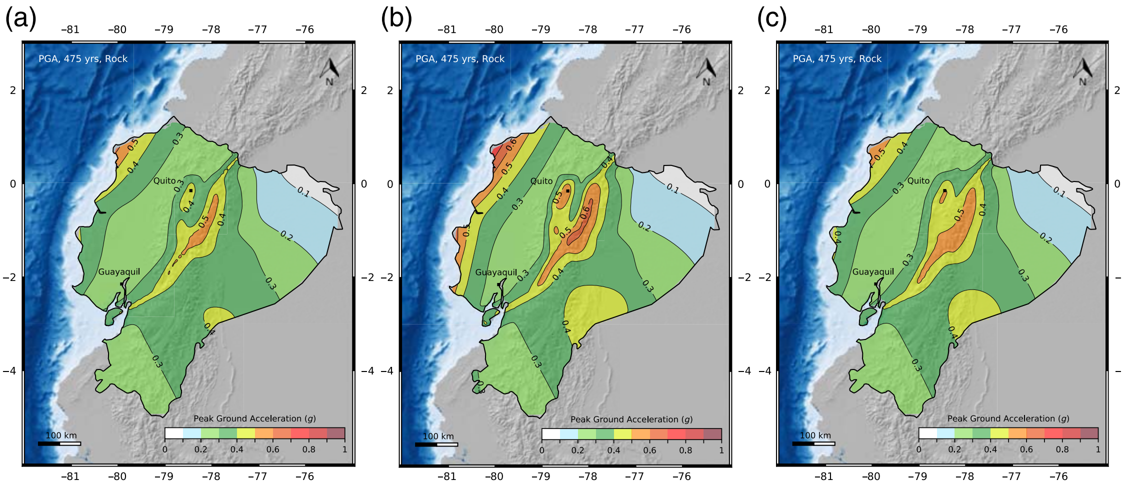

Figure 14. Mean hazard maps, full source logic tree (Fig. 11), only 1 GMM per source type: (a) Abrahamson *et al.* (2016) for interface subduction events, Chiou and Youngs (2014) for crustal events; (b) Montalva *et al.* (2017) for interface events, Akkar *et al.* (2014) for crustal events; and (c) Zhao *et al.* (2006) for interface events and for crustal events. Abrahamson *et al.* (2016) is always used for inslab events. Results for the PGA and for the 475-yr return period are shown. The color version of this figure is available only in the electronic edition.

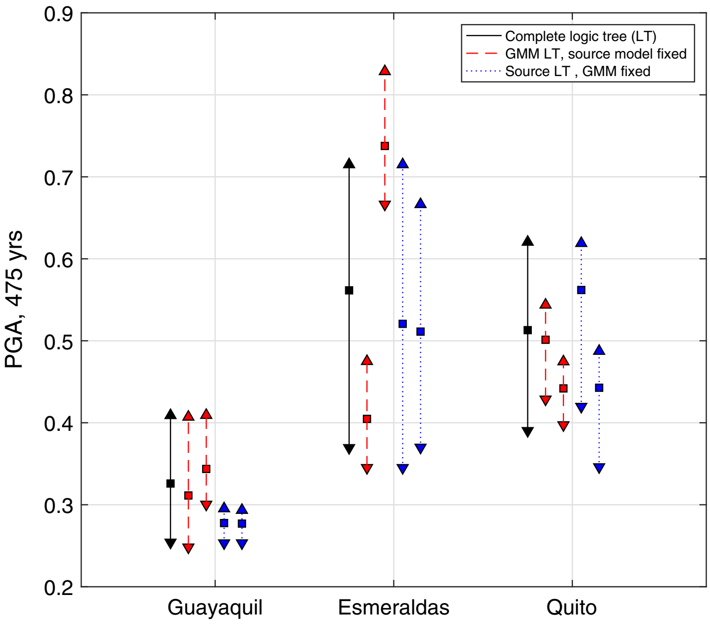

Figure 15. Hazard estimates for the PGA, at 475-yr return period, in three cities: Guayaquil, Esmeraldas, and Quito (see locations in Fig. 13). Three calculations: solid line, exploration of the complete logic tree (source model and GMM logic trees); dashed line, the full GMM logic tree is explored keeping the source model fixed (first calculation with area model based on the BSSA2013 catalog, second calculation with area and crustal faults model based on the ISC-based catalog); dotted line, the full source model logic tree is explored, using a unique selection of GMMs (first calculation with interface Aetal2016, inslab Aetal2016, crustal Akkar *et al.*, 2014; and second calculation with interface Zetal2006, inslab Aetal2016, crustal Chiou and Youngs, 2014). The color version of this figure is available only in the electronic edition.

Conclusions

Based on the work done during the last decade in Ecuador, a source model logic tree is proposed to estimate probabilities of occurrence of subduction and crustal earthquakes that represent a threat to sites in Ecuador. This source model logic tree is made of alternative models: the area model as well as fault and background seismicity models, relying on different types of data and representing, as much as possible, actual knowledge about earthquake occurrences in the country. A set of GMMs is selected to capture the epistemic uncertainty on the prediction of ground motions in Ecuador. Results for different combinations of the logic-tree branches are displayed to understand how the decisions on the source model and the GMM impact the hazard estimates.

Exploring the full logic tree, mean hazard maps show that most of Ecuador is characterized by a high hazard level, with PGA mean values at 475-yr return period higher than $0.3g$ almost everywhere except in some regions of the coastal plain and Amazonia. Regions presenting mean values larger than $0.4g$ are located along the coast and inside the Cordillera. Moreover, the results show that the uncertainty on the hazard estimates depends on the site and can be considerable. The difference between accelerations corresponding to the 16th and 84th percentiles varies from $0g$ to $0.6g$ depending on the location. The uncertainties on the source model and on the GMM both contribute to the overall uncertainty. At the sites where uncertainties on hazard estimates are highest (difference between 84th and 16th percentiles $> 0.4g$), the overall uncertainty is controlled by the epistemic uncertainty on the source model.

Much remains to be done to improve the models and hopefully reduce the uncertainties. The variability of the hazard estimates in the Esmeraldas interface source zone shows that more complex models than the Gutenberg–Richter recurrence model need to be looked for to predict earthquake occurrences in this zone. As for the crustal fault model, it will be possible to define more detailed fault segments only after extensive fieldwork is done to characterize the activity of crustal faults (segmentation, extension in 3D, slip-rate estimates, and past earthquakes). Remoteness and dense jungle coverage of principal segments of many active faults make this task complicated. More data are needed before more realistic time-dependent models can be proposed to predict earthquake occurrence on active faults. The strong-motion dataset is growing and efforts should be put into building a reliable well-organized database, to enable a thorough analysis of the attenuation of ground motions in Ecuador, and comparison tests of recorded ground motions with predictions from published GMMs.

The complete results will be available on the website of the Geophysical Institute in Quito (hazard curves, uniform hazard spectra, and maps for different return periods and different spectral periods).

Data and Resources

The data used in this article are from International Seismological Centre (ISC) online bulletin (http://www.isc.ac.uk/iscbulletin/search/bulletin/, last accessed December 2017); ISC-Global Earthquake Model (GEM) Global Instrumental Earthquake Catalogue v. 4.0 (1900–2013; http://www.isc.ac.uk/iscgem/index.php, last accessed January 2017); National Earthquake Information Center (NEIC) earthquake catalog (https://earthquake.usgs.gov/earthquakes/search/, last accessed June 2017); Global Central Moment Tensor earthquake catalog (http://www.globalcmt.org/CMTsearch.html, all events 1976–2013, catalog available in ASCII “ndk” format, last accessed December 2017); OpenQuake Engine (https://www

.globalquakemodel.org/openquake, last accessed January 2018); and Neotec database (http://neotec-opendata.com/, last accessed December 2017).

Acknowledgments

This work was supported by the Institut de Recherche pour le Développement (IRD), the Geophysical Institute in Quito, part of the Escuela Politecnica Nacional, ISTerre laboratory, and the French National Research Agency through the project REMAKE (2016–2019, Grant Number ANR-15-CE04-004). Instrumentation installed thanks to two projects: SENACYT PIN-08-EPNGEO-00001 (Fortalecimiento del Instituto Geofisico: Ampliacion y Modernizacion del Servicio Nacional de Sismologia Y Vulcanologia) and SENPLADES (Generación de capacidades para la difusión de alertas tempranas y para el desarrollo de instrumentos de decisión ante las amenazas sísmicas y volcánicas dirigidos al Sistema Nacional de Gestión de Riesgos). This work has been carried out in the frame of the Joint International Laboratory "Seismes & Volcans dans les Andes du Nord" (IRD LMI SVAN). The authors are grateful to the Global Earthquake Model Modeling Facility and to the IT ISTerre team for constant support on the OpenQuake software and server. The authors finally thank Associate Editor Mark Stirling, as well as Ivan Wong and an anonymous reviewer, who provided detailed and constructive reviews.

References

Abe, K. (1981). Magnitudes of large shallow earthquakes from 1904 to 1980, *Phys. Earth Planet. In.* **27,** 72–92.

Abe, K., and S. Noguchi (1983). Revision of magnitudes of large shallow earthquakes 1897–1912, *Phys. Earth Planet. In.* **33,** 1–11.

Abrahamson, N., N. Gregor, and K. Addo (2016). BC hydro ground motion prediction equations for subduction earthquakes, *Earthq. Spectra* **32,** no. 1, 23–44.

Akkar, S., M. A. Sandikkaya, and J. J. Bommer (2014). Empirical ground-motion models for point- and extended-source crustal earthquake scenarios in Europe and the Middle East, *Bull. Earthq. Eng.* **12,** no. 1, 359–387.

Aktug, B., J. M. Nocquet, A. Cingöz, B. Parsons, Y. Erkan, P. England, O. Lenk, M. A. Gürdal, A. Kilicoglu, H. Akdeniz, *et al.* (2009). Deformation of western Turkey from a combination of permanent and campaign GPS data: Limits to block-like behavior, *J. Geophys. Res.* **114,** no. B10404, doi: 10.1029/2008JB006000.

Alvarado, A., L. Audin, J. M. Nocquet, E. Jaillard, P. Mothes, P. Jarrín, M. Segovia, F. Rolandone, and D. Cisneros (2016). Partitioning of oblique convergence in the northern Andes subduction zone: Migration history and present-day boundary of the North Andean Sliver in Ecuador, *Tectonics* **35,** doi: 10.1002/2016TC004117.

Alvarado, A., L. Audin, J. M. Nocquet, S. Lagreulet, M. Segovia, Y. Font, G. Lamarque, H. Yepes, P. Mothes, F. Rolandone, *et al.* (2014). Active tectonics in Quito, Ecuador, assessed by geomorphological studies, GPS data, and crustal seismicity, *Tectonics* **33,** no. 2, 67–83, doi: 10.1002/2012TC003224.

Anderson, J. G., and J. E. Luco (1983). Consequences of slip rate constraints on earthquake occurrence relations, *Bull. Seismol. Soc. Am.* **73,** no. 2, 471–496.

Arango, M., F. Strasser, J. Bommer, J. Cepeda, R. Boroschek, D. Hernandez, and H. Tavera (2012). An evaluation of the applicability of current ground-motion models to the south and central American subduction zones, *Bull. Seismol. Soc. Am.* **102,** 143–168.

Audin, L., L. Torlay, H. Castro, J. Aguilar, S. Debard, C. Benavente, and A. Alvarado (2014). Neotec Open-data Base de données "Neotectonica" en open access: Failles Actives en Amérique du Sud, Conférence SAGEO, "Innovations géomatiques pour la gestion des risques naturels et technologiques", http://www.neotec-opendata.com (last accessed March 2018) (in French).

Baize, S., L. Audin, T. Winter, A. Alvarado, L. Pilatasig Moreno, M. Taipe, P. Reyes, P. Kauffman, and H. Yepes (2015). Paleoseismology and tectonic geomorphology of the Pallatanga fault (central Ecuador), a major structure of the South-American crust, *Geomorphology* **237,** 14–28, doi: 10.1016/j.geomorph.2014.02.030.

Beauval, C., F. Cotton, N. Abrahamson, N. Theodulidis, E. Delavaud, L. Rodriguez, F. Scherbaum, and A. Haendel (2012). Regional differences in subduction ground motions, *World Conference on Earthquake Engineering*, Lisbon, Portugal, 24–28 September, 10 pp.

Beauval, C., J. Marinière, A. Laurendeau, J.-C. Singaucho, C. Viracucha, M. Vallée, E. Maufroy, D. Mercerat, H. Yepes, M. Ruiz, *et al.* (2017). Comparison of observed ground-motion attenuation for the 16 April 2016 M_w 7.8 Ecuador megathrust earthquake and its two largest aftershocks with existing ground-motion prediction equations, *Seismol. Res. Lett.* **88,** no. 2A, 287–299.

Beauval, C., H. Tasan, A. Laurendeau, E. Delavaud, F. Cotton, P. Guéguen, and N. Kuehn (2012). On the testing of ground-motion prediction equations against small magnitude data, *Bull. Seismol. Soc. Am.* **102,** no. 5, 1994–2007.

Beauval, C., H. Yepes, L. Audin, A. Alvarado, J.-M. Nocquet, D. Monelli, and L. Danciu (2014). Probabilistic seismic hazard assessment in Quito, estimates and uncertainties, *Seismol. Res. Lett.* **85,** no. 6, doi: 10.1785/0220140036.

Beauval, C., H. Yepes, W. Bakun, J. Egred, A. Alvarado, and J.-C. Singaucho (2010). Locations and magnitudes of historical earthquakes in the Sierra of Ecuador (1587-1996), *Geophys. J. Int.* **181,** no. 3, 1613–1633, doi: 10.1111/j.1365-246X.2010.04569.x.

Beauval, C., H. Yepes, P. Palacios, M. Segovia, A. Alvarado, Y. Font, J. Aguilar, L. Troncoso, and S. Vaca (2013). An earthquake catalog for seismic hazard assessment in Ecuador, *Bull. Seismol. Soc. Am.* **103,** 773–786, doi: 10.1785/0120120270.

Bès de Berc, S., J. C. Soula, P. Baby, M. Souris, F. Christophoul, and J. Rosero (2005). Geomorphic evidence of active deformation and uplift in a modern continental wedge-top–foredeep transition: Example of the eastern Ecuadorian Andes, *Tectonophysics* **399,** 351–380, doi: 10.1016/j.tecto.2004.12.030.

Bindi, D., M. Massa, L. Luzi, G. Ameri, F. Pacor, R. Puglia, and P. Augliera (2014). Pan-European ground motion prediction equations for the average horizontal component of PGA, PGV and 5%-damped PSA at spectral periods of up to 3.0 s using the RESORCE dataset, *Bull. Earthq. Eng.* **12,** no. 1, 391–430.

Bonilla, L. F., M. C. Ruiz, and H. Yepes (1992). Evaluation of seismic hazard in Ecuador, *Simposio Internacional sobre Prevención de Desastres Sísmicos, Mem.*, UNAM, Mexico, 118–125.

Boore, D. M., J. P. Stewart, E. Seyhan, and G. Atkinson (2014). NGA-West2 equations for predicting PGA, PGV, and 5% damped PGA for shallow crustal earthquakes, *Earthq. Spectra* **30,** no. 3, 1057–1085.

Código Ecuatoriano de la Construcción (CEC) (2001). *Requisitos generales de diseño: Peligro sísmico, espectros de diseño y requisitos mínimos de cálculo para diseño sismo-resistente*, Instituto Ecuatoriano de Normalización (INEN), Quito, Ecuador, 1–32 (in Spanish).

Chiou, B. S.-J, and R. Youngs (2014). Updated of the Chiou and Youngs NGA model for the average horizontal component of peak ground motion and response spectra, *Earthq. Spectra* **30,** no. 3, 1117–1153.

Chlieh, M., P. A. Mothes, J.-M. Nocquet, P. Jarrin, P. Charvis, D. Cisneros, Y. Font, J.-Y. Collot, J.-C. Villegas-Lanza, F. Rolandone, *et al.* (2014). Distribution of discrete seismic asperities and aseismic slip along the Ecuadorian megathrust, *Earth Planet. Sci. Lett.* **400,** 292–301, doi: 10.1016/j.epsl.2014.05.027.

Chuang, Y., and K. M. Johnson (2011). Reconciling geologic and geodetic model fault slip-rate discrepancies in southern California: Consideration of nonsteady mantle flow and lower crustal fault creep, *Geology* **39,** 627–630, doi: 10.1130/G32120.1.

Collot, J.-Y., E. Sanclemente, J.-M. Nocquet, A. Leprêtre, A. Ribodetti, P. Jarrin, M. Chlieh, D. Graindorge, and P. Charvis (2017). Subducted oceanic relief locks the shallow megathrust in central Ecuador, *J. Geophys. Res.* doi: 10.1002/2016JB013849.

Cornell, C. A. (1968). Engineering seismic risk analysis, *Bull. Seismol. Soc. Am.* **58,** no. 1, 1583–1606.

Delavaud, E., F. Cotton, S. Akkar, F. Scherbaum, L. Danciu, C. Beauval, S. Drouet, J. Douglas, R. Basili, M. A. Sandikkaya, *et al.* (2012). Toward a ground-motion logic tree for probabilistic seismic hazard assessment in Europe, *J. Seismol.* doi: 10.1007/s10950-012-9281-z.

Di Giacomo, D., I. Bondár, D. A. Storchak, E. R. Engdahl, P. Bormann, and J. Harris (2015). ISC-GEM: Global instrumental earthquake catalog (1900–2009): III. Re-computed M_s and m_b, proxy M_w, final magnitude composition and completeness assessment, *Phys. Earth Planet. In.* **239,** 33–47, doi: 10.1016/j.pepi.2014.06.005.

Douglas, J., and B. Edwards (2016). Recent and future developments in earthquake ground motion estimation, *Earth Sci. Rev.* **160,** 203–219.

Drouet, S., G. Montalva, M. C. Dimaté, L. F. Castillo, G. A. Fernandez, C. Morales, N. Bastias, M. Pirchiner, J. C. Singaucho, and G. Weatherhill (2017). Building a ground-motion logic tree for South America within the GEM-SARA project framework, *16th World Conference on Earthquake Engineering*, Santiago, Chile, 9–13 January, Paper Number 2759, 12 pp.

Dumont, J. F., E. Santana, W. Vilema, K. Pedoja, M. Ordóñez, M. Cruz, N. Jiménez, and I. Zambrano (2005). Morphological and microtectonic analysis of Quaternary deformation from Puná and Santa Clara Islands, Gulf of Guayaquil, Ecuador (South America), *Tectonophysics* **399,** nos. 1/4, 331–350, doi: 10.1016/j.tecto.2004.12.029.

Dziewonski, A. M., T.-A. Chou, and J. H. Woodhouse (1981). Determination of earthquake source parameters from waveform data for studies of global and regional seismicity, *J. Geophys. Res.* **86,** 2825–2852, doi: 10.1029/JB086iB04p02825.

Ego, F., and M. Sebrier (1996). The Ecuadorian Inter-Andean valley: A major and complex restraining bend and compressive graben since Late Miocene time, *Ann. Tect.* **10,** nos. 1/2, 31–59.

Ego, F., M. Sébrier, A. Lavenu, H. Yepes, and A. Egüez (1996). Quaternary state of stress in the northern Andes and the restraining bend model for the Ecuadorian Andes, *Tectonophysics* **259,** nos. 1/3, 101–116.

Ego, F., M. Sébrier, and H. Yepes (1995). Is the Cauca-Patia and Romeral fault system left or right lateral? *Geophys. Res. Lett.* **22,** 33–36.

Ekström, G., M. Nettles, and A. M. Dziewonski (2012). The Global CMT project 2004–2010: Centroid-moment tensors for 13,017 earthquakes, *Phys. Earth Planet. In.* **200/201,** 1–9.

Esteva, L. (1968). Bases para la formulacion de decisiones de diseño sismico, *Ph.D. Thesis* and *Report 182*, Universidad Autonoma Nacional de Mexico (in Spanish).

Eurocode 8 (2004). Design of structures for earthquake resistance—Part 1: General rules, seismic actions and rules for buildings, EN 1998–1, European Committee for Standardization, Brussels, Belgium.

Fiorini, E., and A. Tibaldi (2012). Quaternary tectonics in the central Interandean Valley, Ecuador: Fault-propagation folds, transfer faults and the Cotopaxi volcano, *Global Planet. Change* **90/91,** 87–103, doi: 10.1016/j.gloplacha.2011.06.002.

Fukushima, Y. (1997). Comment on "Ground Motion Attenuation Relations for Subduction Zones," *Seismol. Res. Lett.* **68,** 947–949.

Garcia, J., G. Weatherhill, M. Pagani, L. Rodriguez, V. Poggi, and the SARA Hazard Working Group (2017). Building an open seismic hazard model for South America: The SARA-PSHA model, *16th World Conference on Earthquake Engineering*, Santiago, Chile, 9–13 January, Paper Number 2145, 13 pp.

Global Earthquake Model (GEM) (2017). The OpenQuake-engine User Manual, *Global Earthquake Model (GEM) Technical Report 201710*, 187 pp.

Gutenberg, B., and F. Richter (1944). Frequency of earthquakes in California, *Bull. Seismol. Soc. Am.* **34,** 185–188.

Gutenberg, B., and C. F. Richter (1965). *Seismicity of the Earth and Associated Phenomena*, Princeton University Press, Princeton, New Jersey, 1954; reprinted, Stechert-Hafner.

Kanamori, H., and K. C. McNally (1982). Variable rupture mode of the subduction zone along the Ecuador-Colombia coast, *Bull. Seismol. Soc. Am.* **72,** no. 4, 1241–1253.

Lavenu, A., T. Winter, and F. Dávila (1995). A Pliocene-Quaternary compressional 899 basin in the Interandean depression, central Ecuador, *Geophys. J. Int.* **121,** 279–300.

Leonard, M. (2010). Earthquake fault scaling: Relating rupture length, width, average displacement, and moment release, *Bull. Seismol. Soc. Am.* **100,** no. 5A, 1971–1988.

Lolli, B., P. Gasperini, and G. Vannucci (2014). Empirical conversion between teleseismic magnitudes (m_b and M_s) and moment magnitude (M_w) at the Global, Euro-Mediterranean and Italian scale, *Geophys. J. Int.* **199,** 805–828.

Monelli, D., M. Pagani, G. Weatherill, L. Danciu, and J. Garcia (2014). Modeling distributed seismicity for probabilistic seismic-hazard analysis: Implementation and insights with the OpenQuake Engine, *Bull. Seismol. Soc. Am.* doi: 10.1785/0120130309.

Montalva, G., N. Bastias, and A. Rodriguez-Marek (2017). Ground-motion prediction equation for the Chilean subduction zone, *Bull. Seismol. Soc. Am.* **107,** no. 2, doi: 10.1785/0120160221.

Nocquet, J.-M., P. Jarrin, M. Vallée, P. A. Mothes, R. Grandin, F. Rolandone, B. Delouis, H. Yepes, Y. Font, D. Fuentes, *et al.* (2016). Supercycle at the Ecuadorian subduction zone revealed after the 2016 Pedernales earthquake, *Nature Geosci.* doi: 10.1038/ngeo2864.

Nocquet, J.-M., J. C. Villegas-Lanza, M. Chlieh, P. A. Mothes, F. Rolandone, P. Jarrin, D. Cisneros, A. Alvarado, L. Audin, F. Bondoux, *et al.* (2014). Continental deformation and creeping subduction in the Northern Andes, *Nature Geosci.* **7,** 287–291.

Norma Ecuatoriana de la Construcción (NEC) (2015). Norma Ecuatoriana de la Construcción, Sub-capítulo 2, *Peligro Sísmico y Requisitos de Diseño Sismo Resistente*, Ministerio de Desarrollo Urbano y Vivienda, Convenio MIDUVI-Cámara de la Construcción de Quito, 1–139 (in Spanish).

Pacheco, J. F., and L. R. Sykes (1992). Seismic moment catalog of large shallow earthquakes, 1900 to 1989, *Bull. Seismol. Soc. Am.* **82,** 1306–1349.

Pagani, M., D. Monelli, G. Weatherill, L. Danciu, H. Crowley, V. Silva, P. Henshaw, L. Butler, M. Nastasi, L. Panzeri, *et al.* (2014). OpenQuake-engine: An open hazard (and risk) software for the global earthquake model, *Seismol. Res. Lett.* **85,** 692–702.

Pagani, M., D. Monelli, G. A. Weatherill, and J. Garcia (2014). The OpenQuake-engine Book: Hazard, *Global Earthquake Model (GEM) Technical Report 2014-08*, 67 pp.

Petersen, M. D., M. P. Moschetti, P. M. Powers, C. S. Mueller, K. M. Haller, A. D. Frankel, Y. Zeng, S. Rezaeian, S. C. Harmsen, O. S. Boyd, *et al.* (2014). Documentation for the 2014 update of the United States national seismic hazard maps, *U.S. Geol. Surv. Open-File Rept. 2014-1091*, 243 pp., doi: 10.3133/ofr20141091.

Polonia, A., L. Gasperini, A. Amorosi, E. Bonatti, G. Bortoluzzi, N. Cagatay, L. Capotondi, M. H. Cormier, N. Gorur, C. McHugh, *et al.* (2004). Holocene slip rate of the North Anatolian fault beneath the Sea of Marmara, *Earth Planet. Sci. Lett.* **227,** 411–426, doi: 10.1016/j.epsl.2004.07.042.

Scherbaum, F., E. Delavaud, and C. Riggelsen (2009). Model selection in seismic hazard analysis: An information-theoretic perspective, *Bull. Seismol. Soc. Am.* **99,** no. 6, 3234–3247.

Scordilis, E. M. (2006). Empirical global relations converting M_s and m_b to moment magnitude, *J. Seismol.* **10,** 225–236.

Smith-Konter, B., D. Sandwell, and P. Shearer (2011). Locking depths estimated from geodesy and seismology along the San Andreas Fault System: Implications for seismic moment release, *J. Geophys. Res.* **116,** no. B06401, doi: 10.1029/2010JB008117.

Stewart, J. P., J. Douglas, M. Javanbarg, N. A. Abrahamson, Y. Bozorgnia, D. M. Boore, K. W. Campbell, E. Delavaud, M. Erdik, and P. J. Stafford (2015). Selection of ground motion prediction equations for the global earthquake model, *Earthq. Spectra* doi: 10.1193/013013EQS017M.

Storchak, D. A., D. Di Giacomo, E. R. Engdahl, J. Harris, I. Bondár, W. H. K. Lee, P. Bormann, and A. Villaseñor (2015). The ISC-GEM Global Instrumental Earthquake Catalog (1900–2009): Introduction, *Phys. Earth Planet. In.* **239,** 48–63, doi: 10.1016/j.pepi.2014.06.009.

Strasser, F. O., M. C. Arango, and J. J. Bommer (2010). Scaling of the source dimensions of interface and intraslab subduction-zone earthquakes with moment magnitude, *Seismol. Res. Lett.* **81,** 941–950.

Taboada, A., L. A. Rivera, A. Fuenzalida, A. Cisternas, H. Philip, H. Bijwaard, J. Olaya, and C. Rivera (2000). Geodynamics of the northern Andes: Subductions and intracontinental deformation (Colombia), *Tectonics* **19,** 787–813.

Tibaldi, A., A. Rovida, and C. Corazzato (2007). Late Quaternary kinematics, slip-rate and segmentation of a major Cordillera-parallel transcurrent fault: The Cayambe-Afiladores-Sibundoy system, NW South America, *J. Struct. Geol.* **29,** no. 4, 664–680, doi: 10.1016/j.jsg.2006.11.008.

Vallée, M., J. M. Nocquet, J. Battaglia, Y. Font, M. Segovia, M. Régnier, P. Mothes, P. Jarrin, D. Cisneros, S. Vaca, *et al.* (2013). Intense interface seismicity triggered by a shallow slow slip event in the central Ecuador subduction zone, *J. Geophys. Res.* **118,** 2965–2981, doi: 10.1002/jgrb.50216.

Villegas-Lanza, J. C., M. Chlieh, O. Cavalie, H. Tavera, P. Baby, J. Chire-Chira, and J. M. Nocquet (2016). Active tectonics of Peru: Heterogeneous interseismic coupling along the Nazca megathrust, rigid motion of the Peruvian Sliver, and Subandean shortening accommodation, *J. Geophys. Res.* **121,** no. 10, 7371–7394, ISSN 2169–9313.

Weichert, D. H. (1980). Estimation of the earthquake recurrence parameters for unequal observation periods for different magnitudes, *Bull. Seismol. Soc. Am.* **70,** no. 4, 1337–1346.

Winter, T., J. P. Avouac, and A. Lavenu (1993). Late Quaternary kinematics of the Pallatanga strike-slip fault (Central Ecuador) from topographic measurements of displaced morphological features, *Geophys. J. Int.* **115,** no. 3, 905–920.

Witt, C., J. Bourgois, F. Michaud, M. Ordonez, N. Jimenez, and M. Sosson (2006). Development of the Gulf of Guayaquil (Ecuador) during the Quaternary as an effect of the North Andean block tectonic escape, *Tectonics* doi: 10.1029/2004TC001723.

Woessner, J., L. Danciu, D. Giardini, H. Crowley, F. Cotton, G Grünthal, G. Valensise, R. Arvidsson, R. Basili, M. B. Demircioglu, *et al.* (2015). The 2013 European seismic hazard model: Key components and results, *Bull. Earthq. Eng.* **13,** no. 12, 3553–3596, doi: 10.1007/s10518-015-9795-1.

Ye, L., H. Kanamori, J.-P. Avouac, L. Li, K.-F. Cheung, and T. Lay (2016). The 16 April 2016, M_w 7.8 (M_s 7.5) Ecuador earthquake: A quasi-repeat of the 1942 M_s 7.5 earthquake and partial re-rupture of the 1906 M_s 8.6 Colombia-Ecuador earthquake, *Earth Planet. Sci. Lett.* doi: 10.1016/j.epsl.2016.09.006.

Yepes, H., L. Audin, A. Alvarado, C. Beauval, J. Aguilar, Y. Font, and F. Cotton (2016). A new view for the geodynamics of Ecuador: Implication in seismogenic source definition and seismic hazard assessment, *Tectonics* **35,** doi: 10.1002/2015TC003941.

Zhao, J. X., X. Liang, F. Jiang, H. Xing, Y. Zhang, C. Zhao, X. Lan, D. A. Rhoades, P. G. Somerville, K. Irikura, *et al.* (2016). Ground-motion prediction equations for subduction interface earthquakes in Japan using site class and simple geometric attenuation functions, *Bull. Seismol. Soc. Am.* **106,** no. 4, doi: 10.1785/0120150034.

Zhao, J. X., J. Zhang, A. Asano, Y. Ohno, T. Oouchi, T. Takahashi, H. Ogawa, K. Irikura, H. K. Thio, P. G. Somerville, *et al.* (2006). Attenuation relations of strong ground motion in Japan using site classification based on predominant period, *Bull. Seismol. Soc. Am.* **96,** no. 3, 898–913.

Université Grenoble Alpes, Université Savoie Mont Blanc, CNRS, IRD, IFSTTAR, ISTerre
38000 Grenoble
France
celine.beauval@univ-grenoble-alpes.fr
(C.B., J.M., L.A.)

Escuela Politécnica Nacional
Instituto Geofísico
Ladrón de Guevara E11-253
Apartado 2759 Quito, Ecuador
(H.Y., A.A., J.A., J.-C.S.)

Geoazur, Université Côte d'Azur, IRD, CNRS, Observatoire de la Côte d'Azur
Campus CNRS Azur, 250 rue A. Einstein
Valbonne, France
(J.-M.N.)

Institut de Radioprotection et Sûreté Nucléaire
BP17, 92262 Fontenay-aux-Roses
France
(S.B., H.J.)

Manuscript received 9 September 2017;
Published Online 3 April 2018

2.2 Declustering

2.2.1 Introduction

The probabilistic method from Cornell-McGuire used in seismic hazard assessment assumes that a subset of independent earthquakes is expected to be homogeneous in time, hence following a stationary Poisson process. In reality, earthquakes are not independent from each other, as we know that a major earthquake is preceded by foreshocks and followed by a sequence of aftershocks. When an earthquake happens, it modifies the surrounding stress field and interfers on the capacity of the faults to produce earthquakes. As Poissonian models do not consider the dependency of earthquakes, it is required to decluster earthquake catalogs. Declustering is defined as the removal of foreshocks and aftershocks related to an event with respect the stationary Poisson process. To determine which event is an aftershock or a foreshock, we focus on spatial and temporal parameters. An event B will be considered the aftershock of an event A if it occurs within a given spatial and time window directly related to the spatial and time window of the event A. The declustering is essential for probabilistic seismic hazard studies, since it will have a direct impact on the recurrence models. For example, non-declustered catalogs will contain a higher proportion of lower magnitude earthquakes. As a consequence, the Gutenberg-Richter recurrence models, built on the lower to moderate magnitude range, may underestimate the rate of larger magnitudes, due to the increase of the slope of the recurrence model.

Different outputs of declustered catalogs can be obtained depending on the method used. Many declustering algorithms are developed (Van Stiphout et al. (2012)). Among them, those developed using window-based methods, such as Gardner and Knopoff (1974), and those using cluster-based methods, such as Reasenberg (1985), are the most common, mainly because of the simplicity of their implementation. As the declustered catalog is an input in source models' construction, the different algorithms should be tested by varying the spatio-temporal parameters.

During this chapter, we will test the two methods of Gardner and Knopoff (1974) and Reasenberg (1985) on the homogeneous global catalog with a completeness magnitude of 4.5 that we developed previously in this chapter 2, section *Earthquake Catalogs*. We should keep in mind that a catalog incomplete or not homogeneous can affect declustering by impacting triggering chains and result by identifying the wrong number of clusters.

2.2.2 Declustering methods

Window-based method

The window-based method is one of the simplest forms of aftershocks identification algorithms. A specified distance interval d, and time interval t are defined for each earthquake of magnitude m. Earthquakes are then identified as aftershocks if they occur within this predefined spatio-temporal window. The mainshock is defined by the earthquake having the largest shock in the sequence, within this given window. This algorithm does not consider foreshocks. If the largest earthquake happens later in the sequence, the foreshock is considered as an aftershock. Hence, the time-space windows are reset according to the magnitude of the largest event in the sequence. An example is illustrated on Figure 2.1, where the mainshock is represented by the red star. The spatial-time window of this mainshock is given by the parameters d and t, respectively in Figure 2.1a and 2.1b. The diagrams show the aftershocks as yellow stars inside the blue circle or rectangle representing the spatial-time window. Earthquakes happening outside the spatial-time window are not considered as aftershocks (green stars on Figure 2.1a and 2.1b).

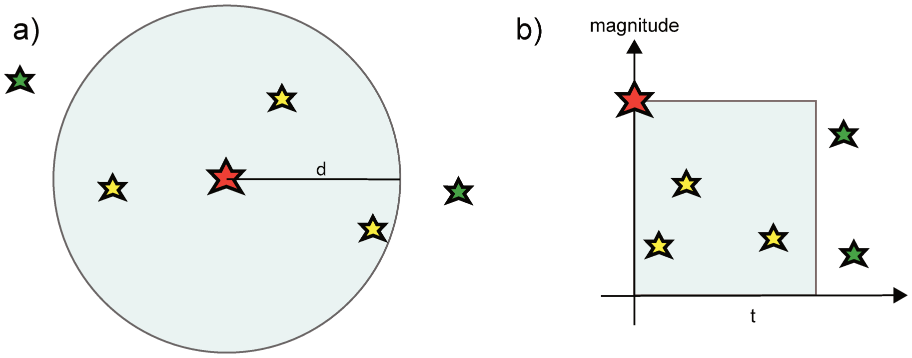

Figure 2.1: Diagrams illustrating the window-based method. The mainshock (red star) triggers aftershocks (yellow stars). a) The blue circle represents the maximal distance d from the mainshock. b) The blue rectangle represents the maximal time t from the mainshock. As they do not belong to the time-space window defined by the mainshock, the green stars are not part of the cluster.

This method was developed in southern California, from the observation of the aftershocks distribution from a series of major events during the period of 1934-1957 of magnitudes $M \geq 3$. The statistical study showed a link between two following events (Knopoff and Gardner (1972)) and from these conclusions Gardner and Knopoff (1974) developed relationships to define the spatial (d in km, eq. 2.1) and temporal (t in days, eq. 2.2) windows from an earthquake of magnitude m (Table 2.1). However, this method does not consider second-degree aftershocks (aftershocks of aftershocks). Also, as the spatial window is represented by a circle centered around the mainshock, they ignore the fault extension for larger events.

We define the space window (in km) from Gardner and Knopoff (1974) as:

$$d = 10^{0.1238m+0.983} \tag{2.1}$$

The time-window (in days) from Gardner and Knopoff (1974) is expressed as:

$$\begin{aligned} t &= 10^{0.032m+2.7389} && \text{for } M \geq 6.5 \\ t &= 10^{0.5409m-0.547} && \text{for } M < 6.5 \end{aligned} \tag{2.2}$$

For example, using Gardner and Knopoff (1974) (eqs. 2.1 and 2.2), for a mainshock of magnitude 7.0, the distance-window gives 70.73 km long and the time-window, 918 days. Those values are rounded in the Table 2.1.

Table 2.1: Aftershock identification windows for $M \geq 4.5$ (Gardner and Knopoff (1974)).

M	L (km)	T (days)
4.5	35	83
5.0	40	155
5.5	47	290
6.0	54	510
6.5	61	790
7.0	70	915
7.5	81	960
8.0	94	985

Cluster-based method

Principle Reasenberg (1985)'s algorithm, unlike Gardner and Knopoff (1974) method, allows to link foreshocks and aftershocks in the same cluster. The research was done in central California between 1969 and 1982 for sequences of aftershocks with magnitudes $M \geq 4.0$. The theory developed is that A can be the mainshock of B, who can be the mainshock of C. In this case, all A, B and C are considered to belong to the same cluster. The largest event is considered to be the mainshock. Reasenberg (1985)'s algorithm also includes Omori's law (1894) for its temporal dependency.

The spatial interaction between events is defined in the Reasenberg (1985)'s public code, CLUSTER2000, available at https://www.usgs.gov/software/cluster2000 by the following relationships:

$$r = r_{fact} \times a(m) \tag{2.3}$$

$$a(m) = 0.011 \times 10^{0.4 \times m} \tag{2.4}$$

where $a(m)$ is the radius of a circular crack (Kanamori and Anderson (1975)) corresponding to an earthquake of magnitude m, assuming a constant stress drop of $d\sigma = 30$ bars (Kanamori and Anderson (1975)). r_{fact} is the amount of crack radii surrounding each earthquake in order to consider its potential association with the cluster's main event.

The time window τ of the Reasenberg (1985) algorithm is defined by the following relationship (eq. 2.5), based on Omori's law (1894) where the number of earthquake decreases by $1/t^{\alpha}$ with $\alpha = 1$ (representative value, Mogi (1962)). We define:

$$\tau = \frac{-\ln(1-p_1)t}{10^{2(\Delta M-1)/3}} \tag{2.5}$$

where τ is the required interval to wait in order to be p_1 confident of observing the next event in the sequence. The parameters τ_{min} and τ_{max} are the lower and upper bound of τ. We express the variable ΔM from equation 2.5 as:

$$\Delta M = M_{mainshock} - x_{meff} \tag{2.6}$$

where x_{meff} is the "effective" lower magnitude cut-off for the earthquake catalog. To take into account uncertainties on the value of x_{meff}, it is raised above its base value by the factor $x_k \times M_{mainshock}$ during clusters, which results in rewriting ΔM as follows:

$$\Delta M = (1-x_k)M_{mainshock} - x_{meff} \tag{2.7}$$

Parametrization Most studies use the standard parameter values (Table 2.2) defined by Reasenberg (1985), however, there are no detailed studies that validate the choice of these variables. To avoid using arbitrary parameters, Schorlemmer and Gerstenberger (2007) created more than 10,000 declustered catalogs by performing a Monte Carlo search over a limited range of parameters to keep a reasonable declustered catalog. The parameters derived from this study are summarized in Table 2.2.

Table 2.2: Tested parameters for the declustering algorithm of Reasenberg (1985). Standard parameters of the declustering algorithm by Reasenberg (1985). Minimal to maximal values from the test center RELM in California (Schorlemmer and Gerstenberger (2007)). Our selection of values adapted to the Ecuadorian catalog.

Parameters	Standard	Min	Max	Our selection
τ_{min} (days)	1	0.5	2.5	10
τ_{max} (days)	10	3	15	30
p_1	0.95	0.9	0.99	0.99
x_k	0.5	0	1	0.2
x_{meff}	1.5	1.6	1.8	4.5
r_{fact}	10	5	20	20

We test this set of parameters in our Ecuadorian catalog and particularly on three large mainshocks, the 1970 M_W 7.2, the 1979 M_W 8.1 and the 2016 M_W 7.8. We calibrate the Reasenberg (1985) algorithm depending on the distribution of the aftershocks from these major earthquakes.

We estimate the cut-off magnitude of our catalog, x_{meff} at 4.5, as our catalog is complete above 4.5. This parameter has a certain influence on the declustering process. Depending on its value, some independent cluster could connect to each other or some major cluster could be separated in different smaller cluster.

x_k is a factor in the ΔM equation 2.7. The aim is to increase the completeness magnitude x_{meff} to take into account its uncertainties in the case of a larger event. To keep ΔM a positive value ($\Delta M = M_{mainshock} - x_{meff}$), the value of x_k has to be small. For example, if a mainshock is 7.8 and $x_k = 0.5$, $\Delta M = (1 - 0.5) \times 7.8 - 4.5 = -0.6$. Therefore, we reduce the factor x_k to 0.2 to have realistic ΔM values at lower mainshocks.

For the parameters τ_{min}, τ_{max}, p_1 and r_{fact}, we successively test the standard, minimum and maximum values, from Table 2.2 and select the results that provide the most realistic declustering. When we decluster our catalog with the standard parameters of Reasenberg (1985), the percentage of aftershocks identified in the Ecuadorian catalog is 16%. We take a closer look on the impact of declustering on large megathrusts earthquakes and we note that the sequence of aftershocks is not complete (Figure 2.2). Using the RELM maximum values (Table 2.2), we increase the number of aftershocks identified in the sequence and remove to 20%, which improve the results by completing the sequence of aftershocks. On the contrary, if we use the RELM minimum values, it decreases the percentage to 12%. Hence, we choose to keep the maximum value of the RELM for the p_1 and r_{fact} parameters, respectively 0.99 and 20, and to increase even more the window size using $\tau_{min} = 10$ and $\tau_{max} = 30$.

In the example of the 2016 M_W 7.8 Pedernales earthquake, τ (calculated with equation 2.5) reaches very fast, in 10 days after the mainshock, the value of τ=15 days (maximal value from the test center RELM, Table 2.2) as seen in Figure 2.3. By increasing τ_{max} to 30 days, we extend the look-ahead time, and we allow τ to take values based on the Omori law for more events. This selection allows to improve the declustering on the catalog (Figure 2.2) and give a final percentage of aftershocks of 23%.

Figure 2.2 illustrates the cumulated number of events inside a frame of ± 1° latitude and longitude centered on the mainshock of the 1970 earthquake M_W 7.2 (green square on Figure 2.2c), located around latitude -4° on the coast, at the border with Peru. We observe a step of cumulated events at the time of the mainshock, in December 1970, visible on the curve before declustering (black curve) and on the curve representing the cluster (blue curve). The difference that we observe between the blue curve and the black curve are other aftershocks within the same frame but not related to this cluster, coming from another sequence of aftershock. For this area and time, this sequence of aftershocks is causing the step in the catalog as the blue

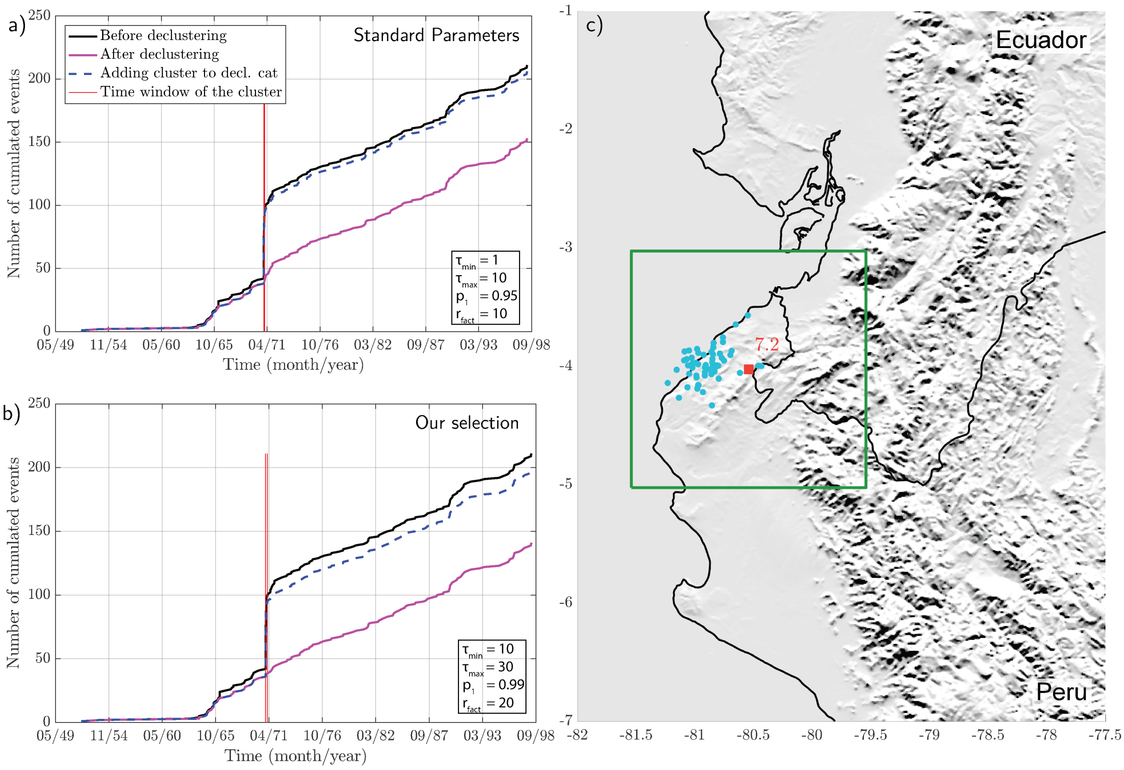

Figure 2.2: Temporal distribution of the cumulated events $M_W \geq 3.6$ for the M_W 7.2 1970 earthquake, comparing the standard parameters with our selection for Reasenberg (1985). Black curve is the original catalog, with the M_W 7.2 1970 earthquake noticeable through the rapid increase in the number of earthquakes due to the presence of aftershocks. Magenta curve represents the distribution after declustering based a) on standard parameters or b) on our own selection of parameters. The red lines are the time window of the cluster. The blue curve is the cluster added to the declustered catalog. c) Location of the M_W 7.2 1970 earthquake. All earthquakes represented from a) and b) are within the green square.

curve is almost reaching the level of the black curve. We compare the standard parameters from Reasenberg (1985) (Figure 2.2a) with our own parameters selection (Figure 2.2b). In Figure 2.2a we still notice a step after the time window in the magenta declustered curve, whereas in Figure 2.2b the slope remains constant, meaning our selection of parameters better removed the sequence of aftershock.

We should keep in mind that Reasenberg (1985) limits the interaction distance to one crustal thickness (if interaction distance $r > 30$ km then $r = 30$ km). We should also note that we adjust for hypocentral errors by reducing the hypocentral distance by the hypocentral uncertainty. If we do not consider the correction for hypocentral errors, the declustering is less efficient. For example, for the 2016 M_W 7.8 Pedernales earthquake, with our selection of parameters we find 122 events in the cluster, whereas if we do not consider the correction for hypocentral errors, we find only 104 events, which is not sufficient to decluster this sequence as it leaves a step of cumulated events at the time of the mainshock.

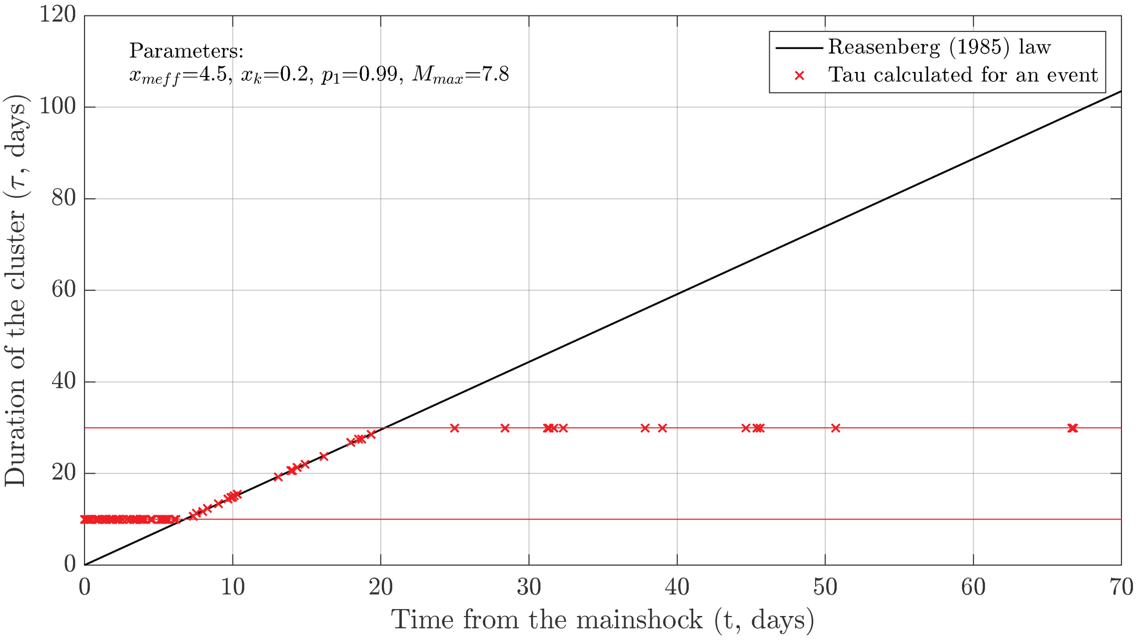

Figure 2.3: Look-ahead time window τ for building clusters for the 2016 7.8 M_W Pedernales earthquake. In black: τ estimated with equation 2.5 of Reasenberg (1985) time-window law; red lines: τ_{min}=10 and τ_{max}=30 used in this run; red crosses: effective τ values in this run for events belonging to the M_W 7.8 2016 cluster.

The Figure 2.3 represents the values of τ calculated for the 2016 M_W 7.8 Pedernales earthquake. In this case, τ is the required interval to wait in order to be 0.99 confident of observing the next event in the sequence. The lower and upper bound of τ are defined such as τ_{min}=10 and τ_{max}=30 (red lines in Figure 2.3). If the values of τ are bounded by τ_{min} and τ_{max}, between those bounds they follow the Reasenberg (1985) time-window law (equation 2.5).

We compare the spatial and temporal windows of Reasenberg (1985) with those of Gardner and Knopoff (1974) for each mainshock of the Ecuadorian catalog (Figure 2.4). The distance-windows, Figure 2.4a, show some similarities between the two algorithms, except for the largest magnitudes, where the maximal distances calculated with the Reasenberg (1985) algorithm (black squares) show larger values. For example, for the M_W 8.1, Gardner and Knopoff (1974) has a maximal window of 96 km, whereas Reasenberg (1985) has 255 km, reaching the length of the fault rupture. Even if Reasenberg (1985) uses a circular crack radius to search for aftershocks, the cluster-based method manages, however, to retrieve the right number of aftershocks along the fault rupture, by linking the sequence of aftershocks along the rupture plane. For the time-windows, the values obtained with Gardner and Knopoff (1974) algorithm (blue crosses) differ strongly from the values calculated with the Reasenberg (1985) algorithm (black squares). Indeed, Reasenberg (1985) algorithm has lower time windows. For example, in the range of magnitudes 5-6, the mean time-window for Gardner and Knopoff (1974) is around 156 ± 127 days whereas it is around 11 ± 17 days for Reasenberg (1985).

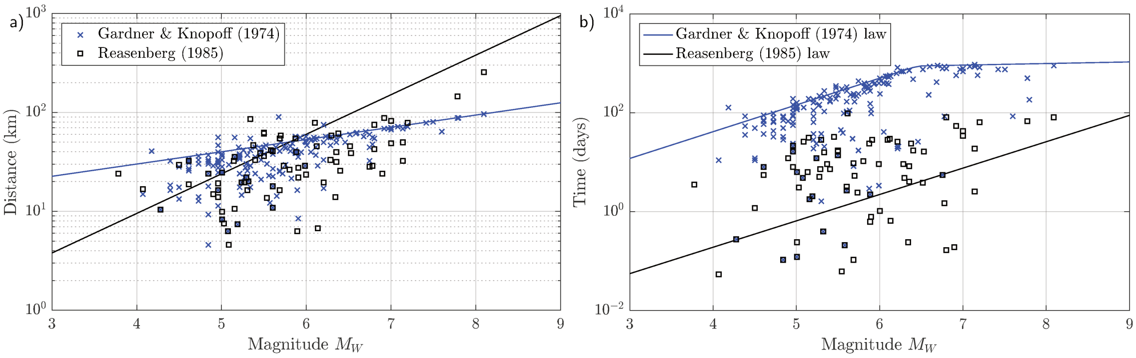

Figure 2.4: Spatial and temporal windowing as a function of magnitude from Gardner and Knopoff (1974) and Reasenberg (1985). From the Ecuadorian catalog, we calculated in a) the maximal distance and in b) the maximal time windows for clusters containing at least 3 earthquakes above M_W 3.6 with the algorithm of Gardner and Knopoff (1974) (blue crosses) and with the algorithm of Reasenberg (1985) (black squares). The blue line is the law from Gardner and Knopoff (1974) and the black line is the law from Reasenberg (1985) for a) distance-windowing and for b) time-windowing.

2.2.3 Methods comparison

We compare the declustering algorithms of Gardner and Knopoff (1974) and Reasenberg (1985) on an Ecuadorian scale to measure the impact on the whole catalog and on specific earthquakes.

Ecuadorian scale

At the scale of Ecuador, Gardner and Knopoff (1974) algorithm declusters the catalog at 40% (Table 2.3 and Figure 2.5) and obtains 398 clusters, whereas Reasenberg (1985) algorithm declusters at 23%, and obtains 191 clusters. Gardner and Knopoff (1974) find more links between two events than Reasenberg (1985). We note on Figure 2.5, that the two declustering algorithms remove proportionally the same number of aftershocks for each magnitude bin, i.e. the trend of removal with magnitude is similar.

Table 2.3: Results of the earthquake catalog declustering in Ecuador ($-7° < \text{lat} < 4°$, $-82° < \text{lon} < -74°$, $1906 - 2017$, $M_W \geq 3.6$) using, for Gardner and Knopoff (1974), ZMAP codes by J. Woessner (Wiemer (2001)) and for Reasenberg (1985), CLUSTER2000 available at https://www.usgs.gov/software/cluster2000.

Methods	Total	Clusters	Mainshocks	Aftershocks
Reasenberg (1985)	3868	191	2978	890
Gardner & Knopoff (1974)		398	2337	1531

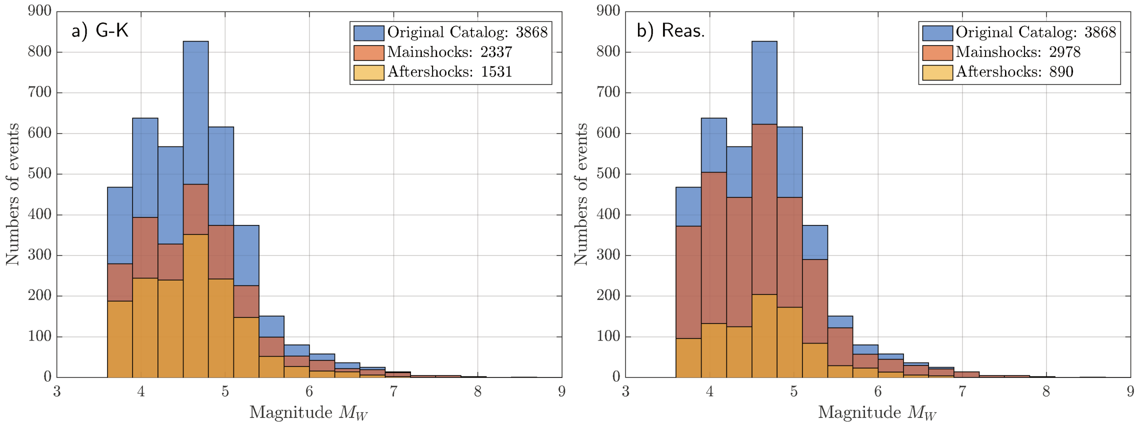

Figure 2.5: Histograms of Ecuadorian earthquake catalog for different declustering algorithms. The number of earthquakes is calculated for each bin of magnitude (0.3), starting at $M_{min} = 3.6$. a) Gardner and Knopoff (1974) algorithm (G-K). b) Reasenberg (1985) algorithm (Reas.). The distribution of the original catalog is in blue, mainshocks in brown and aftershocks in orange.

If Gardner and Knopoff (1974) identify more clusters than Reasenberg (1985) (398 versus 199), for both algorithms, the distribution is dominated by small clusters. This is particularly striking in the Figure 2.6 where we observe a high proportion of small clusters. There are 115 clusters containing only 2 events for Reasenberg (1985) and 224 clusters for Gardner and Knopoff (1974). In proportion Reasenberg (1985) finds that 62% of the total number of clustered events belong to clusters of fewer than 3 events, whereas Gardner and Knopoff (1974) finds 58%. If we look for clusters containing five of fewer events, then Reasenberg (1985) finds 89% whereas Gardner and Knopoff (1974) find 85%.

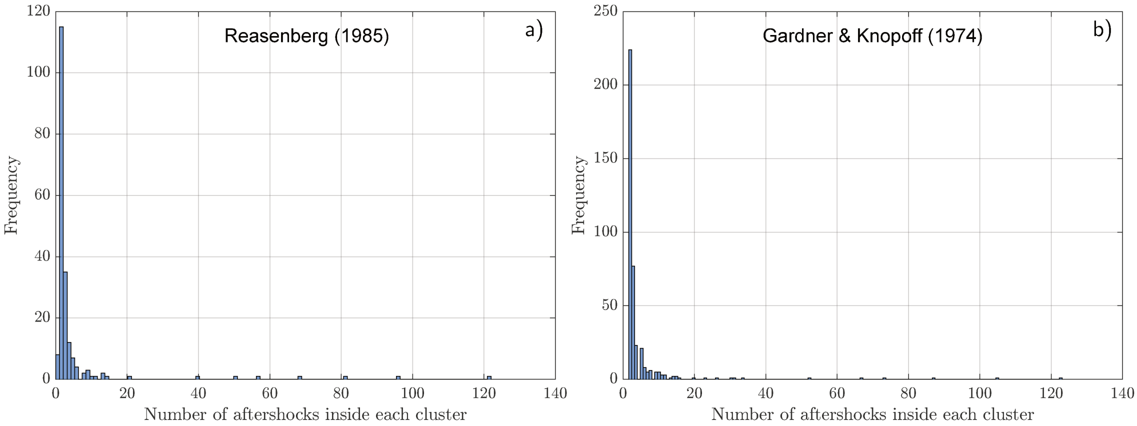

Figure 2.6: Histograms of the number of events in each cluster for a) Reasenberg (1985) and b) Gardner and Knopoff (1974)

The difference in declustering is also visible in Figure 2.8. Either on the whole

Ecuadorian catalog or only in the subduction zone, the catalog is more declustered with the Gardner and Knopoff (1974) algorithm. In the Figure 2.8a, for both algorithms, the clusters of the earthquakes of 1970 M_W 7.2, 1979 M_W 8.1 and 2016 M_W 7.8 are successfully identified, as the slope of the declustered cumulative number of earthquakes remains constant. Since the subduction zone has a north-south orientation, the spatio-temporal distribution of seismicity can be observed along the latitudinal axis. It appears in Figure 2.8c and d, same as for Figure 2.8a that for these two algorithms, clusters are well identified and aftershocks removed.

Earthquakes scale

The analysis of the spatio-temporal distribution of the clusters for three major earthquakes (the 2016 M_W 7.8 Pedernales earthquake, Figure 2.7, the earthquake of December 12, 1979 of $M_W = 8.1$, Figure 2.9 and the earthquake of December 10 1970 of $M_W = 7.2$, Figure 2.10) allows to better quantify the difference in between the algorithms.

The time window for the 2016 M_W 7.8 Pedernales earthquake is represented in Figure 2.7. There is a major difference in the duration of the cluster between the two algorithms. With Reasenberg (1985), the sequence of events lasted two months and a half, whereas with Gardner and Knopoff (1974) it lasted for 9 months.

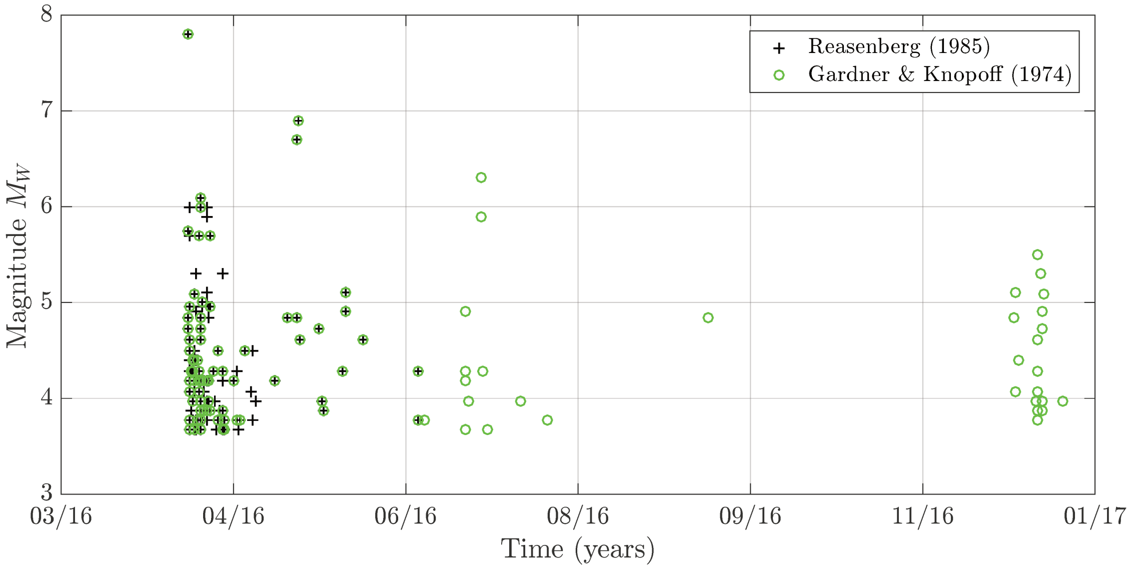

Figure 2.7: Time-window for events associated to the 2016 7.8 M_W Pedernales earthquake. Comparison between Reasenberg (1985) (black crosses) and Gardner and Knopoff (1974) (green circles).

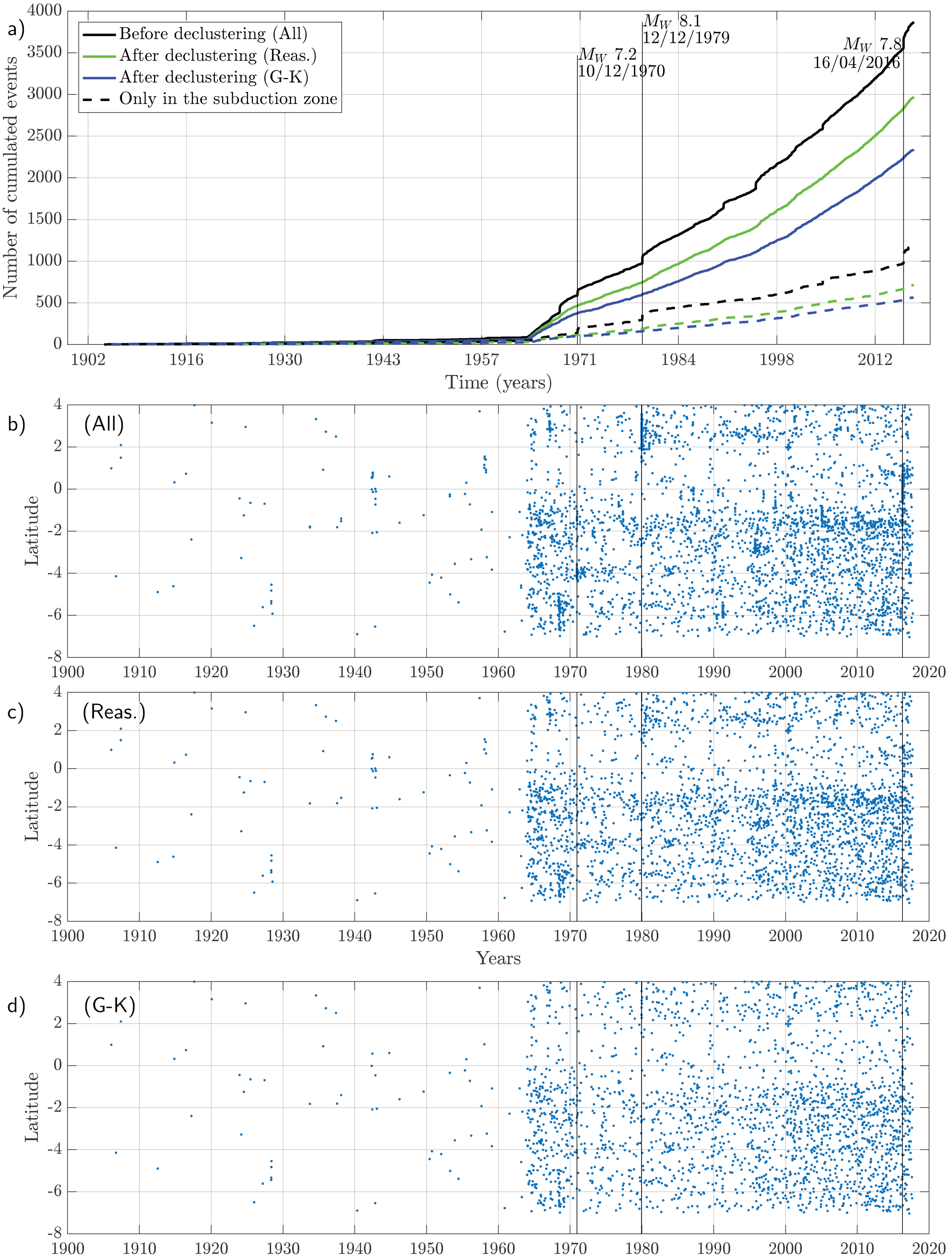

Figure 2.8: Temporal distribution of earthquakes for the original catalog, the declustered catalog with Reasenberg (1985) and the declustered catalog with Gardner and Knopoff (1974) for $M_W \geq 3.6$. a) Cumulative number of events (plain line: the whole catalog, dashed line: specific catalog including only the subduction zone). b) Spatial distribution of the original catalog (All). c) Spatial distribution of the declustered catalog with Reasenberg (1985) (Reas.) d) Spatial distribution of the declustered catalog with Gardner and Knopoff (1974) (G-K). The earthquakes are projected on a north-south axis.

The earthquake of December 12, 1979, $M_W = 8.1$ (Figure 2.9) happened on the southern extent of its rupture plan. The rupture has spread north, but the algorithm of Gardner and Knopoff (1974) cannot identify aftershocks propagating along a rupture plane. On Figure 2.9a, the selection of the aftershocks corresponds spatially to the earthquakes falling into the purple circle, selecting 52 earthquakes, whereas for the Reasenberg (1985) algorithm, the aftershocks location is not limited to a circle but allows aftershocks of aftershocks to happen, expanding the space window to the north of the rupture. Therefore, for large megathrusts earthquake propagating along a plane, the Reasenberg (1985) algorithm is more robust.

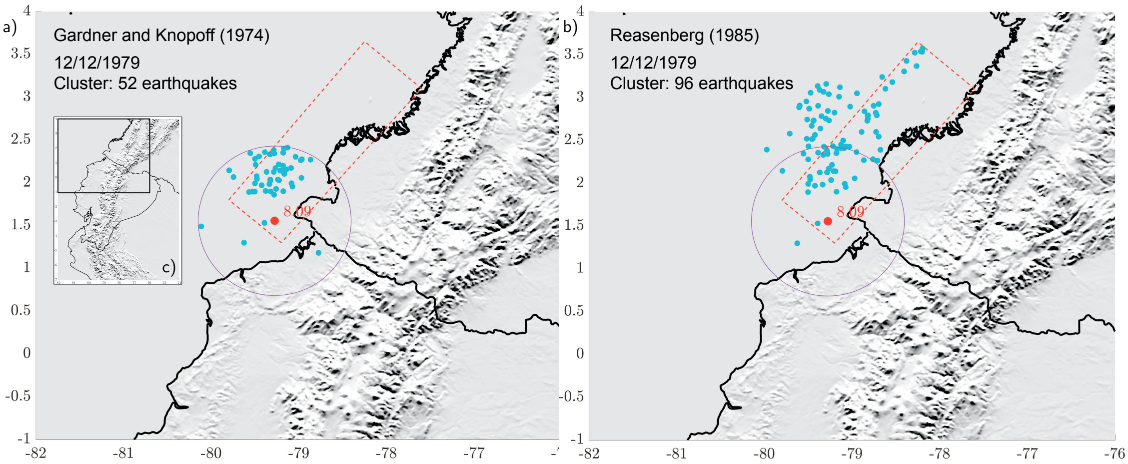

Figure 2.9: Spatial distribution of clusters associated with the earthquake of December 12, 1979 of magnitude $M_W = 8.1$ with a) the cluster defined by the method of Gardner and Knopoff (1974), b) the method of Reasenberg (1985). The blue dots correspond to the aftershocks. The purple circle is the Gardner and Knopoff (1974) spatial window. The dotted red rectangle delimits the earthquake rupture zone.

A second example (Figure 2.10) show the difference in time. The earthquake of December 10 1970, $M_W = 7.2$ happened close to the trench in southern Ecuador. Using Gardner and Knopoff (1974), we use a time-window of 816 days and remove 73 earthquakes. The Figure 2.10a attests of the excess of declustering with the flat magenta curve during the time-window. In comparison, Reasenberg (1985) remove 57 earthquakes in a smaller temporal window of 63 days. The resulting declustering curve (Figure 2.10b) has a constant increase, without any step or flat curve.

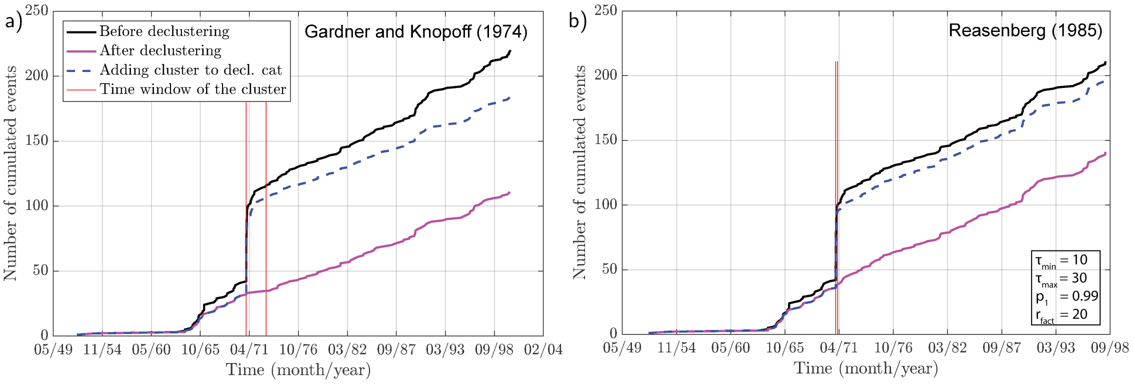

Figure 2.10: Temporal distribution of the cumulated events $M_W \geq 3.6$ for the sequence of aftershocks of the 1970 $M_W = 7.2$ earthquake, comparing Gardner and Knopoff (1974) with our selection for Reasenberg (1985). Black curve is the original catalog, with the 1970 earthquake notable through the rapid increase in the number of earthquakes due to the presence of aftershocks. Magenta curve represents the distribution after declustering based a) on Gardner and Knopoff (1974) declustering algorithm or b) on Reasenberg (1985). The red lines are the time window of the cluster. The blue curve is the cluster added to the declustered catalog.

2.2.4 Conclusion

Due to the uncertainties and unknown nature of earthquake sequences, it is not possible to make an accurate comparison between results of those two declustering methods, but within this study we estimate that Reasenberg (1985) declustered more accordingly to the rupture fault for the sequence of aftershocks in the subduction zone and that Gardner and Knopoff (1974) tend to remove too much aftershocks. In the following part of the thesis, we will consider only the declustering algorithm of Reasenberg (1985).

However, the major flaw in these methods is that they involve constant parameters that are fixed by the user and therefore fixed subjectively. Hence an extensive parameters study is needed in order to select the correct constants for the declustering. Moreover, these techniques propose a binary separation of the events: either the events are aftershocks and are linked to seismic triggering processes, or they are isolated earthquakes. Other methods exist, such as the ETAS (Epidemic Type Aftershock Sequence) model (Van Stiphout et al. (2012)), and propose to avoid this binary separation by calculating the probability of an event to be independent or triggered.

In this thesis, for our Ecuadorian catalog, we don't consider ETAS methods as they do not assure that the mainshock is automatically the strongest event in the sequence and therefore can remove the major events of the catalog.

CHAPTER 3

Geodetic evidence for shallow creep along the Quito fault, Ecuador

Contents

This chapter is the subject of an article co-signed by Judith Marinière, Jean-Mathieu Nocquet, Céline Beauval, Johann Champenois, Laurence Audin, Alexandra Alvarado, Stéphane Baize, and Anne Socquet. It was published in the *Geophysical Journal International* (doi: 10.1093/gji/ggz564) in March 2020. This chapter analyses the GPS data and PS-InSAR around the Quito reverse fault system, the capital of Ecuador. From these data, we derived three-dimensional spatially variable locking models and observe spatially heterogeneous strain accumulation. We observe that if the northern and southern segments of the fault system host larger slip deficit accumulation rates, the center segment of the fault shows aseismic slip at shallow depth.

Summary

Quito, the capital city of Ecuador hosting ~2 million inhabitants, lies on the hanging wall of a ~60 km long reverse fault offsetting the Inter-Andean Valley in the northern Andes. Such an active fault poses a significant risk, enhanced by the high density of population and overall poor building construction quality. Here, we constrain the present-day strain accumulation associated with the Quito fault with new Global Positioning System (GPS) data and Persistent Scatterer Interferometric Synthetic Aperture Radar (PS-InSAR) analysis. Far field GPS data indicate 3 to 5 mm/yr of horizontal shortening accommodated across the fault system. In the central segment of the fault, both GPS and PS-InSAR results highlight a sharp velocity gradient, which attests for creep taking place along the shallowest portion of the fault. Smoother velocity gradients observed along the other segments indicate that the amount of shallow creep decreases north and south of the central segment. Two-dimensional elastic models using GPS horizontal velocity indicate very shallow (<1 km) locking depth for the central segment, increasing to a few km south and north of it. Including InSAR results in the inversion requires locking to vary both along dip and along strike. Three-dimensional spatially variable locking models show that shallow creep occurs along the central 20 km long segment. North and south of the central segment, the interseismic coupling is less resolved, and data still allows significant slip deficit to accumulate. Using the interseismic moment deficit buildup resulting from our inversions and the seismicity rate, we estimate recurrence time for magnitude 6.5+ earthquake to be between 200 and 1200 years. Finally, PS-InSAR time series identify a 2 cm transient deformation that occurred on a secondary thrust, east of the main Quito fault between 1995 and 1997.

3.1 Introduction

Subduction zones not only produce the largest earthquakes on Earth through seismic slip at the megathrust, but also induce long-term strain within the overriding plate, accommodated by earthquakes occurring on crustal faults. Although of lower magnitude than the largest subduction earthquakes, crustal earthquakes rupturing at shallow depths pose a significant hazard often directly threatening highly populated areas.

Along the Nazca/South America subduction zone, the Ecuadorian Andes is among the areas where crustal earthquakes have been particularly damaging. For instance, in 1797, one of the largest crustal earthquakes ever documented in South America (M 7.6-7.9, Beauval et al. (2010)) led to a complete destruction of the city of Riobamba in central Ecuador (Figure 3.1a). In 1949, a M_W 6.8 earthquake occurred in the Inter-Andean Valley near Ambato, generating numerous landslides and killing more than 5000 people (e.g. https://earthquake.usgs.gov/learn/today/index.php?month=8day=5) (Figure 3.1a).

Both the 1797 and 1949 earthquakes occurred along the Chingual - Cosanga - Pallatanga - Puna fault system (hereafter referred to as the CCPP) delimiting the eastern boundary of the North Andean Sliver, a continental domain moving northeastward at 8-10 mm/yr with respect to the stable part of the South America plate (Pennington (1981); Nocquet et al. (2014); Alvarado et al. (2016); Yepes et al. (2016); Mora-Paez et al. (2019)). Although crustal faults bounding the North Andean Sliver show the fastest slip rates in Ecuador (Dumont et al. (2006); Tibaldi et al. (2007); Nocquet et al. (2014); Baize et al. (2015); Alvarado et al. (2016)), large historical earthquakes (Beauval et al. (2010, 2013)), seismologically recorded moderate size earthquakes (Vaca et al. (2019)) and geomorphic markers of neotectonics faulting (Alvarado et al. (2016)) witness active deformation distributed within the North Andean Sliver. In central Ecuador, Alvarado et al. (2016) proposed the existence of an additional Latacunga-Quito block encompassing the Inter-Andean valley and the eastern cordillera from latitude 1.5°S to the strike-slip Guayllabamba fault (lat. 0°), connecting the Quito fault system north of Quito to the CCPP (Figure 3.1a).

Here, we focus on the 60 km long north-south striking Quito fault, that delimits the western boundary of the Latacunga-Quito block, where ∼2 million people are living in the capital city of Ecuador and its surroundings. In that area, the 20 km wide Inter-Andean depression separating the western and eastern Andean cordillera is offset by a series of en echelon thrusts separating the lower Los Chillos Valley from the higher Quito Basin, with an average cumulated uplift of 400 m (Figure 3.1c). Fault related folds in quaternary volcanoclastic deposits, hanging paleo-valleys and records of disrupted drainage patterns confirm the recent activity of the Quito thrust fault (Alvarado et al. (2014)).

Since the development of the Ecuadorian seismic network in the early 90s, 7 earthquakes of magnitude (m_b) above 4.0 have been recorded in the Quito area. Among them, the Pomasqui earthquake (M_W 5.3, August 11, 1990) killed 3 people, damaged about 900 buildings and houses and triggered many landslides along the panamerican road (https://www.igepn.edu.ec/servicios/noticias/466-sismo-de-pomasqu%C3%AD-10-de-agosto-de-1990). More recently, the August 12, 2014 (M_W 5.1) earthquake killed 4 people, and triggered landslides north of Quito. The historical records spanning almost five centuries, show that the city experienced MSK (Medvedev-Sponheuer-Karnik) intensities in the ranges VII to VIII at least five times (Pino and Yepes (1990); Egred (2009)). Using the historical intensity records, Beauval et al. (2010) estimated a 6.3-6.5 magnitude for an event in 1587 at a location near Guayllabamba in the northern part of the Quito fault system (Figure 3.1b). The most damaging earthquake recorded for Quito occurred in 1859 (Intensity VII-VIII), but whether it occurred on a crustal fault remains unclear (Beauval et al. (2010)). Focal mechanisms show predominantly reverse mechanisms (Guillier et al. (2001); Alvarado et al. (2014), Vaca et al. (2019)) in agreement with a dominant east-west shortening across the Quito fault. Secondary thrusts and strike slip faults are documented east of the main fault in the Los Chillos Valley and regularly host small earthquakes (Alvarado et al. (2014)).

Preliminary GPS results along a profile in central Quito showed 4 mm/yr of shortening across the fault. Using simple two-dimensional elastic screw dislocation models, Alvarado et al. (2014) suggest a shallow locking depth of 3 km. In this study, we use an augmented GPS velocity field and spatially dense InSAR data to precisely quantify the kinematics in the Quito area and to evaluate the current rate of slip deficit accumulation along the different segments of the fault. We first derived optimal values for the fault geometry and its slip deficit using a two-dimensional Bayesian inversion. Finally, the results of the two-dimensional modelling are used as input parameters to constrain a spatially variable interseismic coupling model of the fault.

3.2 Dataset

3.2.1 GPS Data

We use a combination of 18 campaign mode GPS sites with 11 continuous GPS in the area of Quito (Figure 3.1b, Table 3.1). Campaign sites have a minimum observation span of 8 years (except LACH, 3.5 years) and of 3.2 years for continuous GPS. All data used in this study were collected before the 2016 M_W 7.8 Pedernales earthquake that induced coseismic offsets of a few centimeters (Nocquet et al. (2016); Mothes et al. (2018)) and centimeters level post-seismic deformation (Rolandone et al. (2018)) in the Quito area. The GPS dataset spatially samples the whole Quito area with a higher density in its central part.

We process the 24-hour-long session data using the GAMIT/GLOBK 10.70 software (Herring et al. (2018)) to obtain daily loosely constrained solutions. We derive the time series by expressing the loosely constrained solutions in the ITRF2014 (Altamimi et al. (2016)) with a 7-parameter transformation using regional IGS sites (http://www.igs.org). For the continuous GPS data, we first evaluate the time

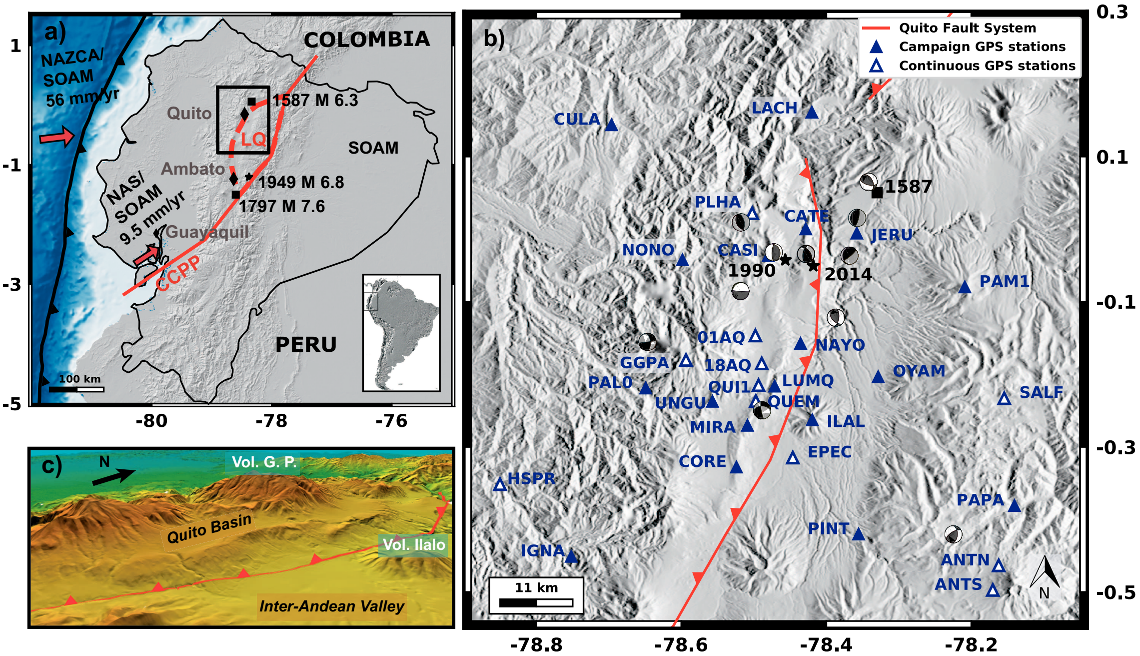

Figure 3.1: Ecuador geodynamic and seismotectonic settings. The continuous red line indicates the CCPP (Chingual-Cosanga-Pallatanga-Puna´) fault system (after Alvarado et al. (2016)), delimiting the eastern boundary of the North Andean Sliver (NAS). LQ is the Latacunga-Quito block proposed in Alvarado et al. (2014) with its western boundary indicated by the dashed red line. Black squares and stars are historical and instrumental earthquakes respectively. The black line with triangles indicates the location of the trench. The black rectangle indicates the area shown in b). b) Seismotectonic map of the Quito region. Blue triangles are campaign GPS stations and white triangles are continuous GPS stations. The simplified surface trace of the Quito reverse Fault System is shown by the barbed red line. Focal mechanism solutions of earthquakes above magnitude 4, during the 1990 – 2011 period, are from Alvarado et al. (2014). GPS PLHA is located on the top of the Pululahua Volcano, GPS GGPA is on top of the Guagua Pichincha and ILAL is on the top of the Ilalo. Square: 1587 M6.3 historical earthquake (location from Beauval et al. (2010)), stars: 1990 M_W equivalent 5.3 Pomasqui and 2014 M_W 5.1 earthquakes. c) 3D view of Quito in the Inter-Andean Depression. Los Chillos Valley is the Inter-Andean Valley represented east of the QFS. In white letters are the volcanoes cited in the text. Vol G. P.: Volcano Guagua Pichincha.

correlated noise for a model including white and flicker noise using the Maximum Likelihood Estimation algorithm embedded in the CATS software (Williams (2005)). We then convert the flicker noise parameters obtained from the CATS analysis to equivalent random noise parameters that can then be used in the GLOBK Kalman filter (Floyd et al. (2010)). For the campaign data, we apply noise parameters corresponding to the median value obtained from the continuous GPS analysis. The final velocity solution is obtained running the GLOBK Kalman filter. Such an approach provides conservative estimates of velocity uncertainties. Campaign mode sites with ∼15 years of measurements and 3 campaign show velocity uncertainties between 0.15 and 0.35 mm/yr at the 1-σ confidence level and continuous GPS sites with 3 to 8 years of data have uncertainties between 0.2 and 0.6 mm/yr depending on the length and noise properties of the time series. For subsequent modelling, we express our velocity field in a reference frame corresponding to the non-deforming part of the fault footwall (Figure 3.4). This is achieved by estimating a rigid body motion using the velocities from a subset of GPS sites (ANTN, ANTS, OYAM, PAM1, PAPA & PINT) showing negligible internal deformation (weighted root-mean-square of 0.26 mm/yr). We also estimated the vertical rates for 3 continuous GPS stations close to the Quito fault: QUEM (2007.9-2016.3), QUI1 (2000.0-2010.3), EPEC (2013.0-2016.3). In the ITRF2014, their vertical velocity estimates are QUEM: -1.4 ± 0.8, QUI1: -0.8 ± 0.8, EPEC: -0.6 ± 1.0, all values in mm/yr and positive upwards with their associated uncertainty provided at the 95% confidence level. These values indicate a relative vertical subsidence of GPS sites located on the hanging wall with respect to the footwall, but uncertainties leave also the possibility of opposite motion. Alternatively, we estimate the relative velocity of QUEM with respect to EPEC using the baseline time series (QUI1 and EPEC do not have a common observation period, see Figure 3.2). We now find an uplift rate of QUEM with respect to EPEC of 0.4 ± 1.0 mm/yr. Because of these contradictory results, we chose not to use the vertical rates in the subsequent modelling.

3.2.2 InSAR data

Additionally, we use InSAR results from 19 European Remote Sensing (ERS) acquisitions collected in descending mode between May 1993 and September 2000 to determine mean line-of-sight (LOS) velocity in the Quito area (Champenois et al. (2013, 2015)). Quito and its surroundings include vegetated, cultivated and rapidly changing urban areas, involving a rapid loss of coherence of the radar phase with time. We therefore use the Persistent Scatterer technique (PS-InSAR) implemented in the Stanford Method for Persistent Scatterer version 4.0 (StaMPS) software package (Hooper (2008)). The StaMPS PS-InSAR approach identifies individual radar-bright and phase-stable points and allows to follow their change of phase over long periods without the assumption of linear displacement. The radar images are coregistered to the same master image, here May 06, 1998, selected in the middle of the observation period. As a result, the analysis provides 18 values of LOS change for every PS pixel during the 1993-2000 period. Interferograms are corrected for changes in atmospheric delay during the PS processing using space and time filters described in Hooper et al. (2007). The resulting mean LOS rate map is shown in Figure 3.3a. Aside the mean LOS rate, the StaMPS approach provides formal errors of the mean velocity and the LOS displacement time series at each acquisition date (Figure 3.3c). We carefully check the time series and find that for pixels located southwest of the Ilalo Volcano, LOS displacements during the 1995-1996 period exhibit significant departure from a constant velocity (Figures 3.3d-h). Additional information about this transient motion is provided in the discussion paragraph. In order to correct for this localized transient signal, we use the following approach: for every pixel, we extract the full time series and solve for a trend plus an offset at 1995.5 using weighted least-squares. If the estimated offset is larger than two times its formal uncertainty, the retained LOS velocity is the one obtained by simultane-

Table 3.1: GPS velocities with respect to our stable fault foot wall block reference frame (see section 3.2.1). Longitude, latitude in decimal degrees; Ve, Vn: east & north components of velocity in mm/yr; SVe, SVn: formal error (1-σ confidence level) of Ve, Vn.

Sites	**Long.**	**Lat.**	**Ve**	**Vn**	**SVe**	**SVn**
01AQ	-78.498	-0.147	3.49	1.16	0.35	0.43
ANTN	-78.162	-0.463	0.27	0.57	0.23	0.25
ANTS	-78.170	-0.497	-0.04	0.28	0.29	0.23
CASI	-78.480	-0.037	2.50	0.24	0.52	0.66
CATE	-78.428	0.000	1.72	-0.55	0.40	0.53
CORE	-78.524	-0.328	2.06	-0.63	0.34	0.44
CULA	-78.696	0.144	3.31	1.77	0.29	0.35
EPEC	-78.446	-0.315	1.12	-0.95	0.25	0.49
GGPA	-78.593	-0.180	4.74	0.38	0.32	0.19
HSPR	-78.850	-0.352	2.57	0.68	0.24	0.21
IGNA	-78.752	-0.451	2.60	-0.37	0.18	0.23
ILAL	-78.419	-0.263	1.60	0.18	0.13	0.16
JERU	-78.358	-0.006	0.70	0.56	0.24	0.31
LACH	-78.420	0.161	1.19	0.38	1.33	1.64
MIRA	-78.509	-0.270	3.24	-1.66	0.13	0.16
NAYO	-78.436	-0.157	2.02	-0.05	0.15	0.21
NONO	-78.599	-0.042	3.57	0.86	0.26	0.32
OYAM	-78.329	-0.203	0.38	0.07	0.28	0.34
PAM1	-78.209	-0.080	0.62	0.66	0.23	0.38
PAPA	-78.141	-0.381	0.03	0.78	0.10	0.52
PINT	-78.356	-0.420	0.69	-0.74	0.18	0.17
PLHA	-78.502	0.022	4.15	1.27	0.15	0.21
QUEM	-78.497	-0.237	4.27	-0.50	0.21	0.11
QUI1	-78.494	-0.215	3.30	0.15	0.09	0.49
UNGU	-78.557	-0.237	3.26	-1.24	0.18	0.23
LUMQ	-78.471	-0.216	1.95	-0.16	0.16	0.21
PAL0	-78.649	-0.219	3.33	-0.97	0.28	0.36
18AQ	-78.489	-0.185	4.22	0.91	0.23	0.41
SALF	-78.155	-0.233	1.13	-0.23	0.23	0.18

ously estimating a slope and an offset using least-squares. If the offset is less than twice its formal uncertainty, the retained LOS velocity is the one using all dates of the time series without an offset correction (Figure 3.3f). Finally, we keep only pixels with a formal error lower than 0.9 mm/yr for subsequent modelling. Such a value is found to ensure kilometers' scale consistency of LOS rates. Indeed, using a larger threshold value provides highly spatially scattered LOS rates, especially in the high relief of the western Cordillera (Figures 3.1c and 3.3b). With a total of more than 68,000 PS, the final LOS rate map is almost continuous over a length of 30 km along the Quito Fault system. Although the inconsistency of GPS vertical

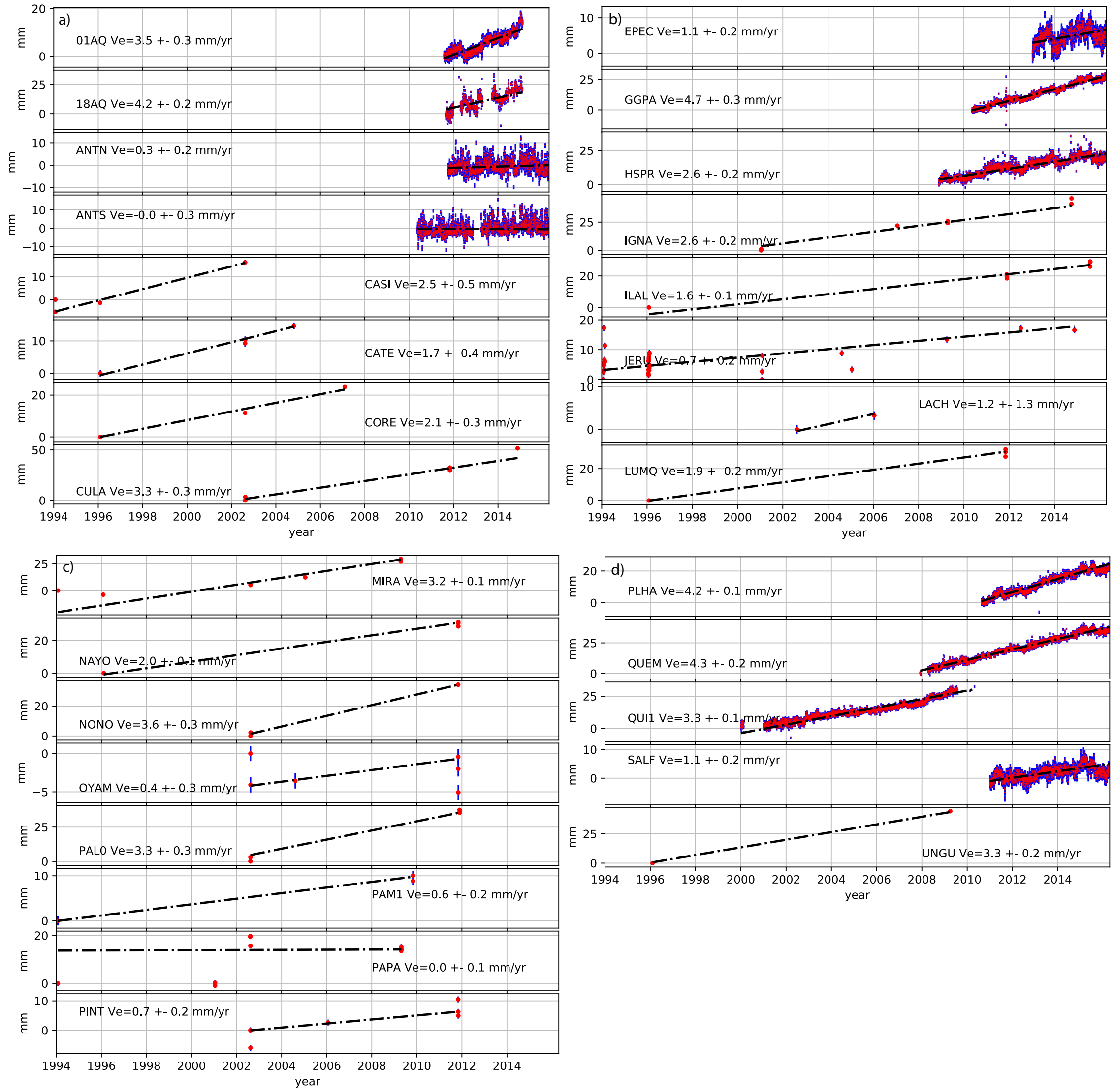

Figure 3.2: East component times series of GPS sites used in this study. The raw time series are expressed in the stable foot wall reference frame as described in section 3.4.2. The dotted line shows the estimated velocity.

rates prevents a full comparison of InSAR and GPS results to be made, we compare the relative 3D vector of GPS site QUEM with respect to EPEC projected along the LOS and PS-InSAR results. We find a differential GPS LOS rate of 1.63 mm/yr to be compared to 1.49 mm/yr for the PS-InSAR results, suggesting a good consistency between the GPS and PS-InSAR results.

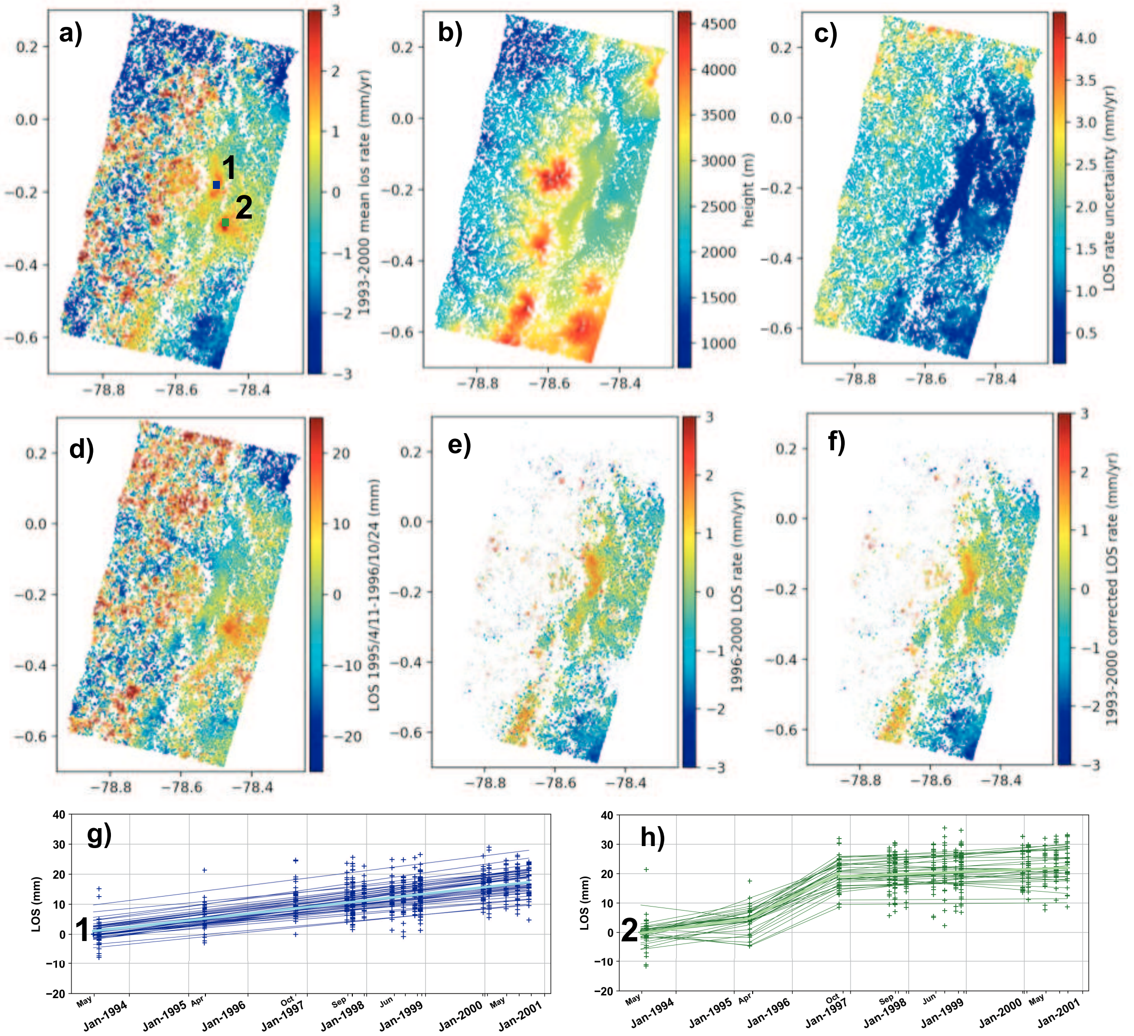

Figure 3.3: a) Mean LOS rate map from 19 ERS acquisitions collected in descending mode between 1993/05/23 and 2000/09/27. b) Topography elevation. c) LOS rate uncertainty map. d) LOS displacement map between 1995/04/11and 1996/10/23. e) LOS rate map between 1996/10/23 and 2000/09/27. f) LOS rate map from 1993/05/23 and 2000/09/27 with the 1995-1996 transient signal removed (see text) g-h) LOS time series for SAR pixels located at the areas 1 & 2 indicated in a). Dark (blue and green) lines are the slope estimated for the time series for every pixel and the thick light (blue and green) line indicates the median slope of all pixels' time series. For g) the thick light blue slope is estimated using all the data, while for h) the thick light green slope has been estimated for three different periods: 1993/05/23- 1995/04/11; 1995/04/11- 1996/10/23 and 1996/10/23- 2000/09/27.

3.2.3 Correction of the Elastic Contribution from the Subduction Interseismic Loading

Locking along the subduction interface induces shortening in the East-West direction, a signal that adds up to the signature of East-West shortening induced by the Quito fault. We use the interseismic model from Nocquet et al. (2016) to predict the contribution of elastic deformation induced by the subduction and remove it from our geodetic data in the Quito area. Expressed in an overriding plate reference frame (here, the North Andean Sliver), the elastic contribution due to locking along the megathrust is 2.5 mm/yr for the westernmost site of our networks and 1.3 mm/yr for the easternmost one, for the horizontal components. With respect to our stable hanging wall fault reference frame (see section 3.2.2), this translates into an almost linear East-West shortening rate of 0.013 mm/yr per km. Although small compared to the gradient observed across the Quito fault, applying this correction reduces by 0.8 mm/yr the relative horizontal shortening over our GPS network. For the vertical component, the maximum prediction reaches at most 0.2 mm/yr and is therefore negligible. Both the GPS horizontal velocity and the InSAR LOS rates were corrected prior modelling.

3.3 Results

The horizontal GPS velocity field shows a general pattern of 3 to 4.5 mm/yr of EW shortening between sites located west of the Quito fault system and sites located in the eastern part of the Inter-Andean valley (Figure 3.4). Unlike most across fault profiles which show a gentle monotonic decrease of velocity magnitude, here we notice that velocities on the hanging wall, in the Quito city area, show a velocity equal to or larger than the far-field velocity (QUEM 4.3 mm/yr and 18AQ 4.3 mm/yr compared to PAL0 and UNGU 3.5 mm/yr). Such a pattern is a potential indication of slip on the fault at shallow depth. Furthermore, the gradient across the Quito fault appears to be sharp: the velocity magnitude decreases by 50% over a distance of 2 km (e.g. QUI1-LUMQ) and becomes negligible 10 km away from the fault (OYAM 0.4 mm/yr, Figure 3.4). This pattern is an additional direct evidence of a very shallow locking depth.

PS-InSAR results also show a general LOS rate gradient of ∼2 mm/yr between the hanging wall and the footwall of the Quito fault. Maximum LOS rates are found in the central Quito area, with a sharp LOS rate decrease from 2 to 0 mm/yr over a distance of 2 km (Figure 3.4). Such a gradient indicates either a decrease of east velocity, a decreasing uplift rate, or a combination of both. The sharp LOS gradient spatially correlates with the high-shortening rate seen in the GPS (e.g. 01AQ/18AQ to NAYO and QUI1 to LUMQ, Figure 3.4) and therefore also constitutes an observation independently confirming the existence of shallow creep and an overall very shallow locking depth. In the central western part of the Quito Basin, close to the eastern flank of Guagua Pichincha volcano, the InSAR data show an opposite gradient with LOS rates decreasing westward. We further notice that the maximum LOS rate is offset by 3 km to the west of the fault trace, possibly indicating creep rates changing with depth.

As secondary features, GPS velocities show some changes of shortening direction, being N70° in the northern part of the fault, N90° in the central part and N110°

in its southern part. Roughly, this rotation of shortening direction corresponds to the average rotation of the fault strike, thus implying purely reverse motion across each individual segment. Both north and south of central Quito, the InSAR results show smoother gradient of LOS rates possibly reflecting along strike variations of the amount the shallow creep. Finally, we also notice that despite the removal of the transient deformation seen in the PS-InSAR analysis for the 1995-1996 period south west of the Ilalo Volcano, a small (1 mm/yr) signal persists in that area (location of point 2 in Figure 3.3a or Figure 3.14c)

3.4 Modelling approach

3.4.1 Potential Pichincha Volcano contribution to the deformation field

The change of shortening direction observed in the horizontal GPS velocity field raises the question of whether the velocity field or a fraction of it could be related to a volcanic deformation of the nearby Guagua Pichincha Volcano, located about 15 km west of the Quito fault. A magmatic eruption phase occurred between 1998 and 2001 overlapping the acquisition period for the SAR data used in our study. Garcia-Aristizabal et al. (2007) estimated a magma storage between 4 km and 11-12 km beneath the Guagua Pichincha caldera. Increase or decrease in pressure at such a depth would certainly not be able to explain the sharp gradient observed near the Quito Fault trace, but could impact our InSAR results with an additional gradient in the Quito area. We therefore carefully check any non-linear behaviour in the PS time series corresponding to the eruptive period and did not find any significant departure from a constant velocity aside the one already mentioned near the Ilalo Volcano (Figure 3.3). More recently, Morales Rivera et al. (2016) identified 6.5 cm of localized subsidence from mid-2007 to August 2009 from InSAR data. They modelled the InSAR signal by a single shallow (3 km) pressure source inducing negligible deformation a few kilometers away from the Guagua Pichincha caldera. The time series of CGPS QUEM starting in December 2007 do not show any departure from the average linear trend for this period (Figure 3.2d). Therefore, we believe that the Pichincha volcanic activity has a minor impact on our velocity field and certainly does not impact the main pattern of the velocity field such as the sharp gradient observed across the Quito fault.

3.4.2 Possible Anelastic Contribution to Surface Deformation

Physical models of thrust and fold evolution show that the long-term displacement at the surface results from the combination of slip along the fault at depth and of distributed folding above the fault tip (e.g. Johnson (2018)). However, the contribution of anelastic deformation over a few years during the interseismic

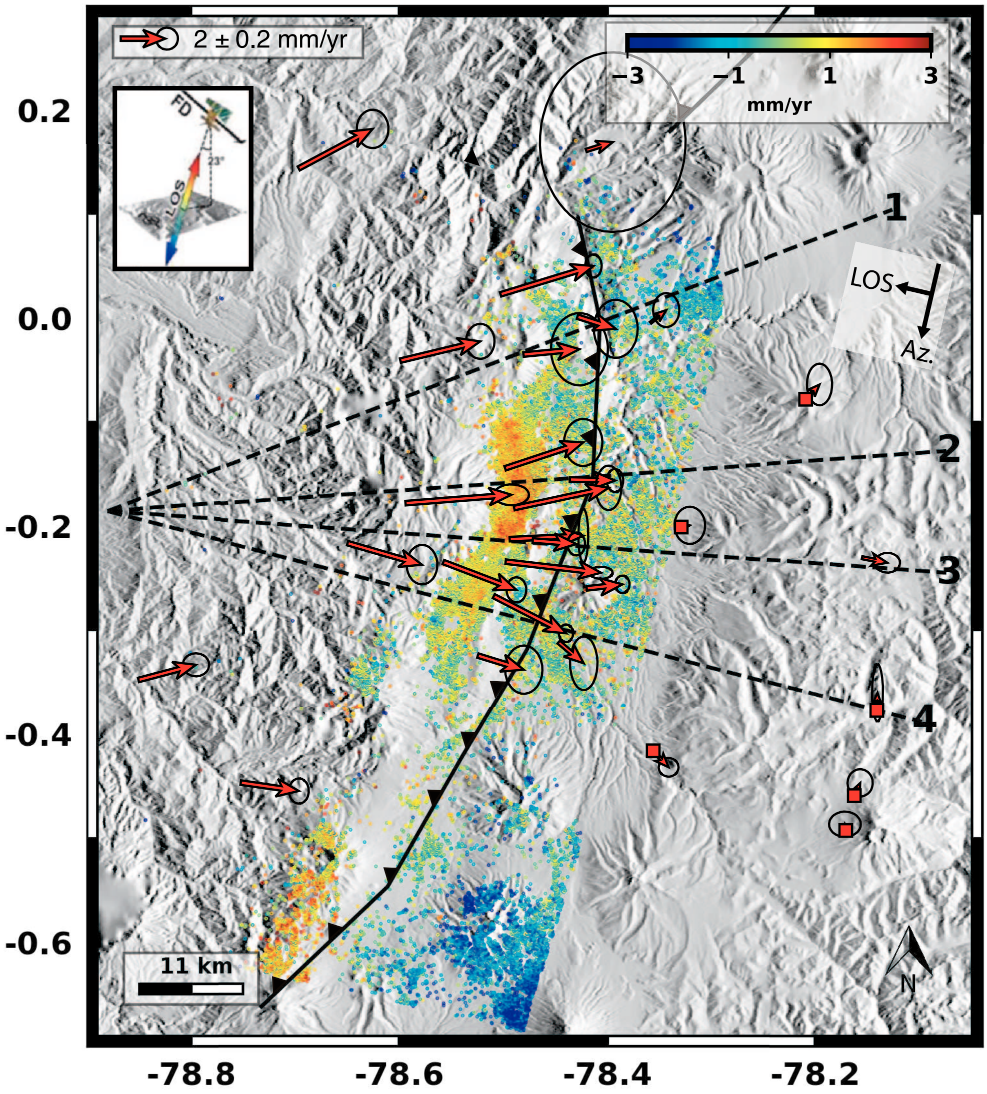

Figure 3.4: Horizontal GPS velocity field (1994-2016) and PS-InSAR LOS velocity map derived from 19 ERS acquisitions collected in descending mode between May 1993 and September 2000. Positive displacement corresponds to motion towards the satellite. The values are in mm/yr and color-coded according to the scale shown on the top right. Arrows are the GPS horizontal velocity field with respect to a reference frame defined by minimizing the velocities of GPS sites ANTN, ANTS, OYAM, PAM1, PAPA & PINT. Error ellipses are 95% confidence level. The barbed black line shows the simplified surface trace of the Quito thrust fault. Dashed lines indicate the location of the four profiles used for the two-dimensional modelling.

period is less clear. Although observed high strain near the fault trace has been proposed to include anelastic contribution for the Anza segment of the strike-slip San Jacinto Fault in Southern California (Lindsey et al. (2014)), we are not aware of similar conclusions for thrust faults. For instance, the narrow strip of high strain rate observed along the Longitudinal Valley Fault in Taiwan, a pattern very like our results for the Quito Fault, is successfully explained using elastic models (Thomas et al. (2014)). Nonetheless, in the Quito area, the upper stratigraphic layers (several hundreds of meters and even possibly more) are made of intercalated poorly consolidated volcanic ashes and lahar deposits, that certainly reduce the elastic strength and possibly undergo anelastic deformation. Furthermore, very steep slopes along the eastern flanks of the Quito basin (Figure 3.1b) are unstable and experience regular landslides, adding to the crustal motion in the PS-InSAR data (GPS sites were chosen away from unstable areas). In the subsequent modelling, we do not account for these processes, but acknowledge that they add some uncertainties, for instance on the amount and location of shallow creep estimates close to the surface.

3.4.3 Elastic Models

Despite the limitations described above, we attempt to quantify the rate of slip deficit accumulation along the Quito fault, assuming that the observed surface displacement can be explained by a set of dislocations at depth in a homogeneous elastic half-space. Although some studies have shown that viscoelastic relaxation plays a critical role for dip-slip faults when modelling the surface velocity during the earthquake cycle (e.g. Segall (2010)), purely elastic models are therefore correct to the first order when the observation is made at a date being several times the relaxation time since the last large earthquake, as it is the case for the Quito fault. For instance, Fukahata and Matsu'ura (2006) show that the elastic solution is equivalent to the fully relaxed deformation of a stratified viscoelastic models with a null rigidity of the underlying medium. Elastic models are further useful approximation to estimate the rate of slip deficit accumulation along faults.

Under the elastic assumption, different approaches can be used. A first type of model is to use a semi-infinite edge dislocation ending at a given depth from the surface. Above this depth, the fault is locked. A second approach is to consider the back-slip model (Savage (1983); McCaffrey (2005)), where the surface deformation is the sum of the long-term deformation modelled by rigid block motion and a virtual back-slip component aiming at reproducing the effect of a locked fault on the surface velocity field. The back-slip approach (hereafter noted BS) is strictly equivalent to the semi-infinite dislocation model, but offers the advantage of an easier modelling of far-field data by including block rotation for large areas (McCaffrey (2005); Meade (2005)). A third approach is to model the relative motion of tectonic blocks by a flat décollement (hereafter noted FD). Such a flat décollement predicts block-like motion in the far-field of the fault, a progressive decrease of the horizontal velocity spread over distance, centred at the tip of the décollement. In a fourth approach, the décollement merges a ramp slipping from the depth of the décollement to a given depth (hereafter referred as FDR) (e.g. Daout et al. (2016a,b); Thompson et al. (2015)). In some cases, the flat décollement and ramp corresponds to a real discontinuity imaged from geophysics as it is for the sub-andean domain, east of the Andean cordillera (e.g. Baby et al. (2013)). But, regardless its actual existence, the slip along a flat décollement offers a convenient way to mimic the block like behaviour in the far field of the fault and the elastic strain perturbation close to the fault. As Daout et al. (2016a) write, the FDR has to be considered as a conceptual model simultaneously describing “both elastic and permanent parts of the surface displacement field at the present time”.

For the BS models, under the assumption that the observed surface velocities do not reflect transient slip, the kinematic consistency and the assumption of constant horizontal slip vector require the long-term slip rate on the ramp to be equal to $V_h/cos(dip)$ where V_h is the horizontal shortening velocity between the two blocks separated by the fault. For the FDR model, one view is that the long-term slip rate on the ramp should also be equal to $V_h/cos(dip)$ to ensure that the fault accommodates all the far field shortening rate. The alternative view is that the slip rate along the flat décollement is transferred to the ramp. In that latter case, the long-term slip rate on the ramp is equal to the shortening rate V_h. In the supplementary material, we show that using one or the other assumption has a marginal impact on our results and all models presented hereafter are for a long-term slip rate equal to $V_h/cos(dip)$.

In the following we present a step-by-step modelling approach and progressively introduce more complexity as it is required by the data. We start with synthetic two-dimensional models for the BS, FD and FDR models to discuss the main patterns of the predicted surface velocity and the ability of each of these models to explain our GPS and PS-InSAR observations. Then, we perform a Bayesian exploration of the BS and FD model parameters using only the GPS observation. We discuss the resolution of the searched parameters and show that fitting PS-InSAR data requires introducing a ramp that connect to the flat décollement (FDR model). We then consider a two-dimensional FDR model including both GPS and PS-InSAR data, that indicates that variable slip along the ramp can simultaneously fit both GPS and PS-InSAR data. Building upon this result, we present a spatially variable slip three-dimensional interseismic model that allows us (1) to discuss the along strike and along dip variations of aseismic slip and (2) to quantify the rate of slip deficit accumulation along the whole fault system.

3.4.4 Two-dimensional synthetic elastic models

As a preliminary step before data inversion, we make simple forward models to assess the ability of the different approaches to explain the main patterns present in our GPS and InSAR observations. Figures 3.5a-d show the horizontal and vertical velocity prediction for the BS, FD two-dimensional models for a horizontal shortening rate of 4 mm/yr for a 30° and 60° dipping fault locked down to 10 km depth.

Figures 3.5e-h compare the prediction of the BS and FDR models for a fault locked to a depth of 5 km. Although both models predict a bell-like shape for the horizontal velocity profile close to the fault, the predicted magnitude for the maximum velocity is different and this difference is larger for steeper fault.

Finally, Figures 3.5i-l show the effect of adding a slipping patch at the otherwise locked fault. The slipping patch introduces a bell-like shape perturbation to the surface velocity profile, now shifted from the fault trace at the surface. The width of the velocity perturbation depends on the length and depth of the slipping patches. Narrow bell-like shapes found in our PS-InSAR observation are likely to be fitted by variable slip along the fault. We also see that allowing variable slip at the ramp will result in little sensitivity of surface displacement on the dip of the fault. Indeed, the same bell-like shape can be reproduced either by smaller or deeper slip on a steep fault or by larger and shallower slip on a shallow fault.

To conclude, Figure 3.5 shows that the BS approach is not suitable for modelling vertical rates away from the fault since it introduces a spurious step in the far-field (Segall (2010)). Therefore, this type of modelling is not suitable for modelling InSAR data, because the LOS might include a significant contribution from the vertical component. Figure 3.5 also shows that the predicted horizontal profile differs between the BS and FD models. This difference increases with steeper dip. Especially, the BS approach predicts that the surface displacement in the direction perpendicular to the fault trace close to the fault can exceed the far-field value, a pattern not predicted for the FD and FDR models.

3.4.5 Bayesian exploration of searched parameters

We use a Bayesian approach to rigorously evaluate the resolution of parameters and sample different models allowed by the data. Our observations of fault perpendicular velocities denoted d, are related to the vector of unknown m including slip and fault geometrical parameters through the functional g by $g(m) = d$. Because the vector m includes geometrical parameters, $g(m)$ is a nonlinear function. In Bayesian approaches, the a priori information about the searched parameters is combined with the observations to derive posterior probabilities of the searched parameters. The a posteriori probability density function (PDF) of the model m given the data d is $\rho(m|d) \propto \rho(d|m)\rho(m)$, where $\rho(m)$ is the a priori PDF on model parameters m and $\rho(d|m)$ the likelihood PDF of d given m given by $e^{-1/2(d-g(m))^T C_D^{-1}(d-g(m))}$ with C_D being the covariance matrix on the data d. Since the data covariance estimation was conservative (under-estimation), the confidence intervals of the model parameters are also under-estimated.

We use the PyMC library (Patil et al. (2010)) which implements a Metropolis algorithm to explore the posterior PDF. For all models, we used 500,000 initial samples, rejecting the first 100,000 samples to minimize the effect of the initial model, and decimate the resulting samples by a factor of 10.

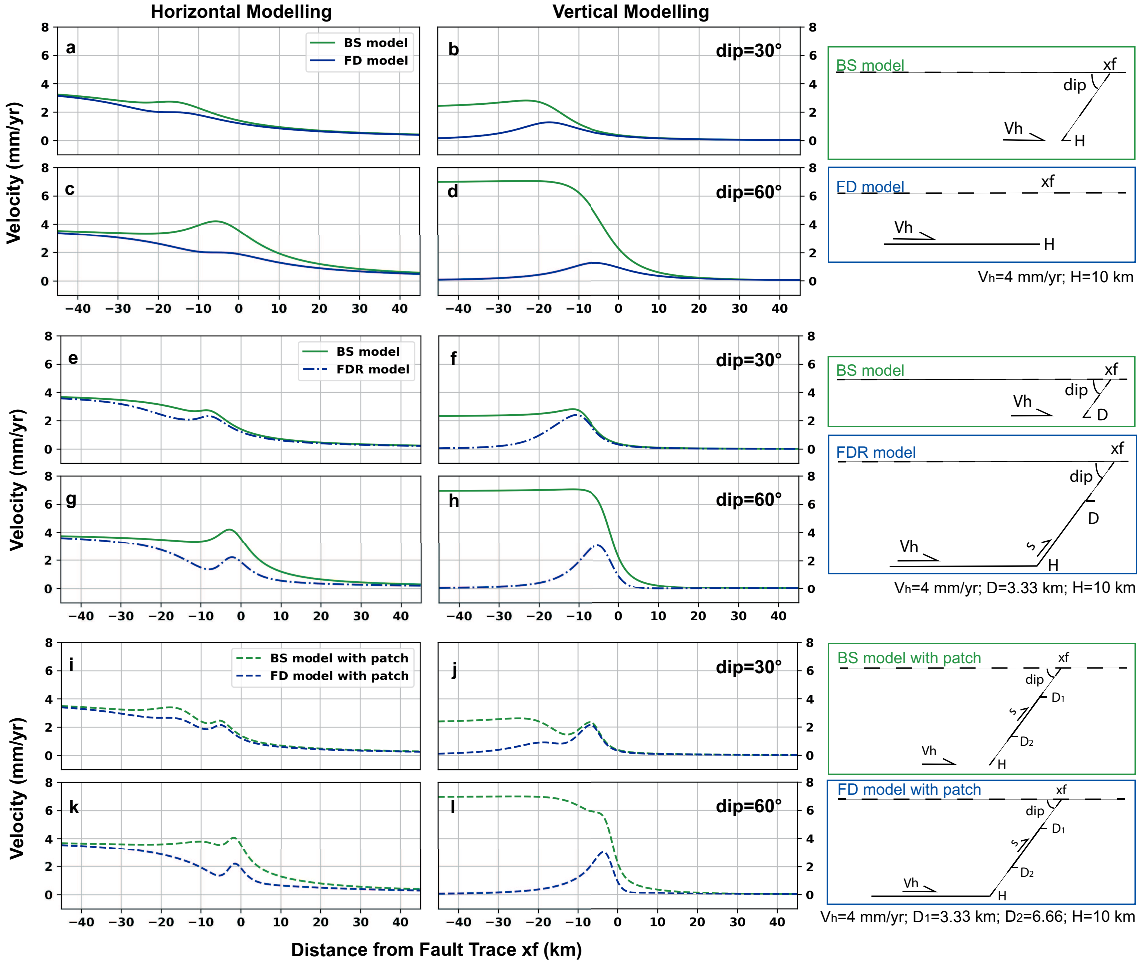

Figure 3.5: Comparison between horizontal and vertical velocity predictions for two-dimensional synthetic elastic models. All models are for a shortening rate of 4 mm/yr, and a locking depth down to 10 km depth. Velocity predictions are shown for a dip of 30° or 60° as indicated in the middle column subplots. The right column shows the model setting and parameters for the back-slip (BS), flat décollement (FD) and flat décollement-ramp (FDR) models. The fault is in solid line when slipping and dashed line when locked. xf corresponds to the location of the fault at the surface, or in the case of the FD model, the surface location of the decollement tip. xf=0 on the x-axis for model predictions.

3.4.6 Two-Dimensional Inversion from GPS Data

In a first approach, we test the BS and FD approaches using the GPS results only. The searched parameters for the BS models are the horizontal shortening rate V_h, the dip, the locking depth H and the location of the fault trace at the surface xf. The applied back-slip equals to $V_h/cos(dip)$ (Figure 3.6c). For the FD model, the searched parameters are V_h, the depth of the décollement H and the horizontal location of the décollement tip (Figure 3.7c). The input data are the horizontal velocities projected along 4 profiles perpendicular to the fault segment (Figure 3.4) where GPS data are dense enough. The fault strike is changing from north to south, hence we choose to angle the profiles to cut perpendicularly the fault and follow the

GPS pattern. For both BS and FD models, we use a uniform prior in the interval of 0-10 mm/yr for the shortening rate, and 0-15 km for the locking depth and ∼10 km of possible offset with respect to the fault trace. For the BS model, we use an interval of 5-85° for the dip. To increase the number of observations to resolve the searched parameters, profiles are inverted simultaneously sharing the same value of dip and shortening rate V_h. We assumed different values of locking depth or depth of the decollement H (H_1, H_2, H_3, H_4) for the four profiles as it is obvious that the velocity gradient across the fault is different among profiles. Similarly, the location of the fault is solved independently for each profile, by taking different values of xf (xf_1, xf_2, xf_3, xf_4) to reflect the variable location of the different segment with respect to our reference point.

We find that GPS site PLHA located on the Pululahua Volcano (Figure 3.1b) and used in the northernmost profile (profile 1) appears as being an outlier in many models. Therefore, PLHA has been removed from the inversions. Figures 3.6b and 3.7b show some of the components of the posterior PDF together with the fit achieved to the data for the mean model (Figures 3.6a and 3.7a). Both the BS and FD approaches provide good fit to the data (wrms = 0.51 and 0.44 mm/yr for the BS and FD model respectively, Figures 3.6a and 3.7a). The shortening rate V_h is consistently found to be in the range of 3.1 to 3.5 mm/yr at the 68% confidence level. We find that the locking depth is less than 1.3 km for profiles 2 and 3 in central Quito. Larger locking depths are found for the northern and southern segments (profiles 1 and 4). For the BS model, the preferred (Maximum A Posteriori, MAP) dip is very steep (∼65°) but both the mean and median models provide estimates around 45° with comparable misfit to the data.

Although both the BS and FD models could achieve a good fit of GPS observations and demonstrate a very small elastic strain accumulation at the Quito fault, we suspect that these results are not physically realistic and could bare to unrealistic slip deficit estimates. Indeed, for such models, the elastic strain would accumulate only within the very shallowest part of the fault (∼1 km), which is mostly made of unconsolidated material for which inelastic deformation is likely to occur.

3.4.7 Joint GPS-InSAR Based Models

In a second step, we include the InSAR data. One of the main patterns in the InSAR map is the 5 km narrow bell-like shape of LOS rate found for the central Quito basin along profile 2 and 3 (Figure 3.8a). None of the previous models explored can explain this pattern, but the synthetic tests described in paragraph 4.1 suggest that flat décollement-ramp models can reproduce this shape of signal. For the FDR model, two parameters are added with respect to the FD model: the dip of the ramp and top depth of the ramp. We find that if we leave all parameters free, that is having a uniform prior, the FDR model tends to choose values for the décollement depth (H) of the order of ∼2 km, providing similar results to the FD models.

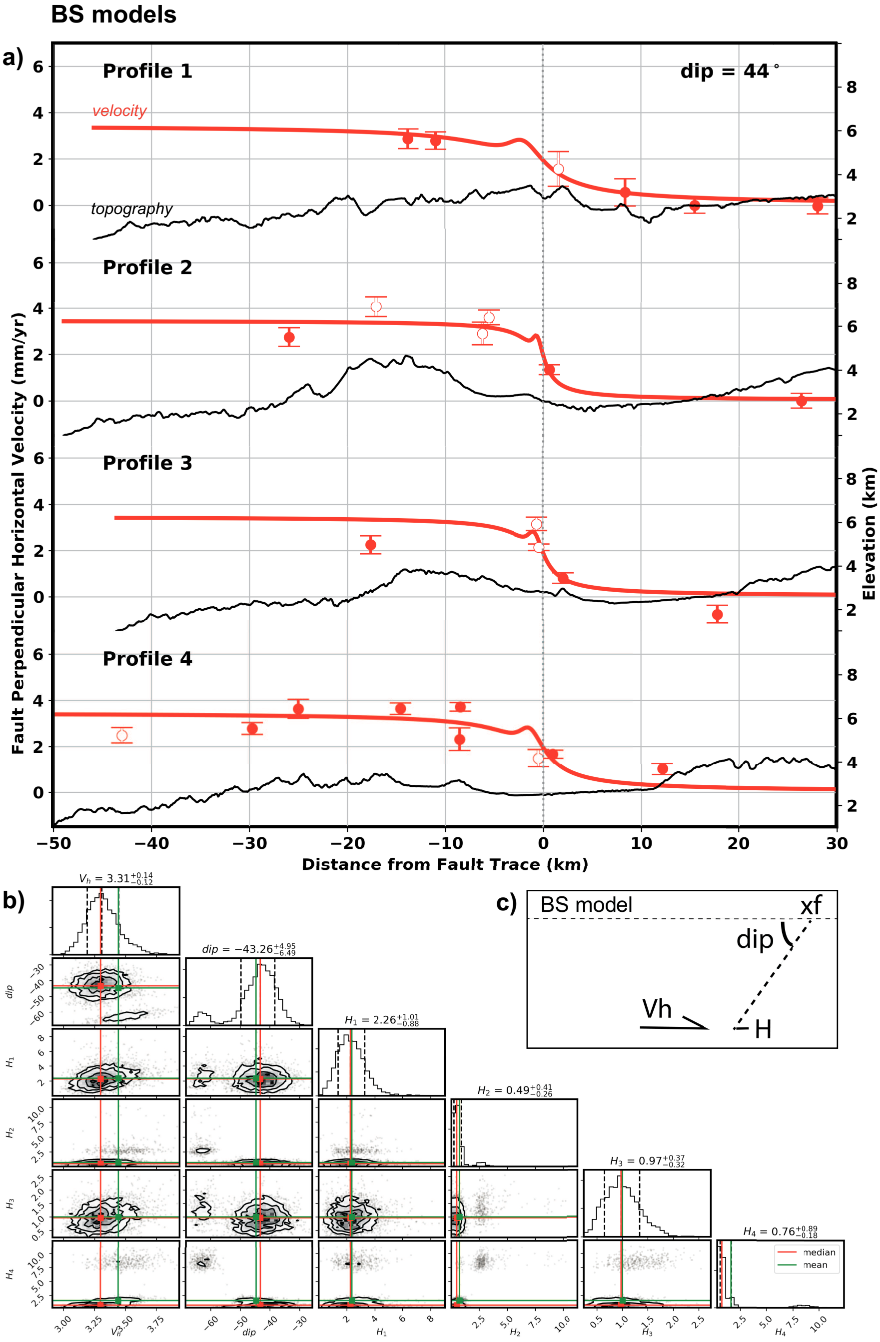

Figure 3.6: Results from the Bayesian inversion using GPS data only and the back-slip (BS) model along profiles crossing the Quito fault. Location of the profile are shown in Figure 3.4. a) Red curves are model prediction from the mean model for the along profile horizontal velocity. Circles filled in red are survey mode GPS whereas circles filled in white are continuous GPS. Black line shows the topography. b) One- and two-dimensional posterior PDF for the following parameters: the shortening rate (V_h), the dip and the four locking depths associated with each profile (H_1, H_2, H_3, H_4). c) Schematics Model of a BS with the parameters used for the inversion: dip; xf, location of the fault on the surface; V_h, shortening rate; H, locking depth.

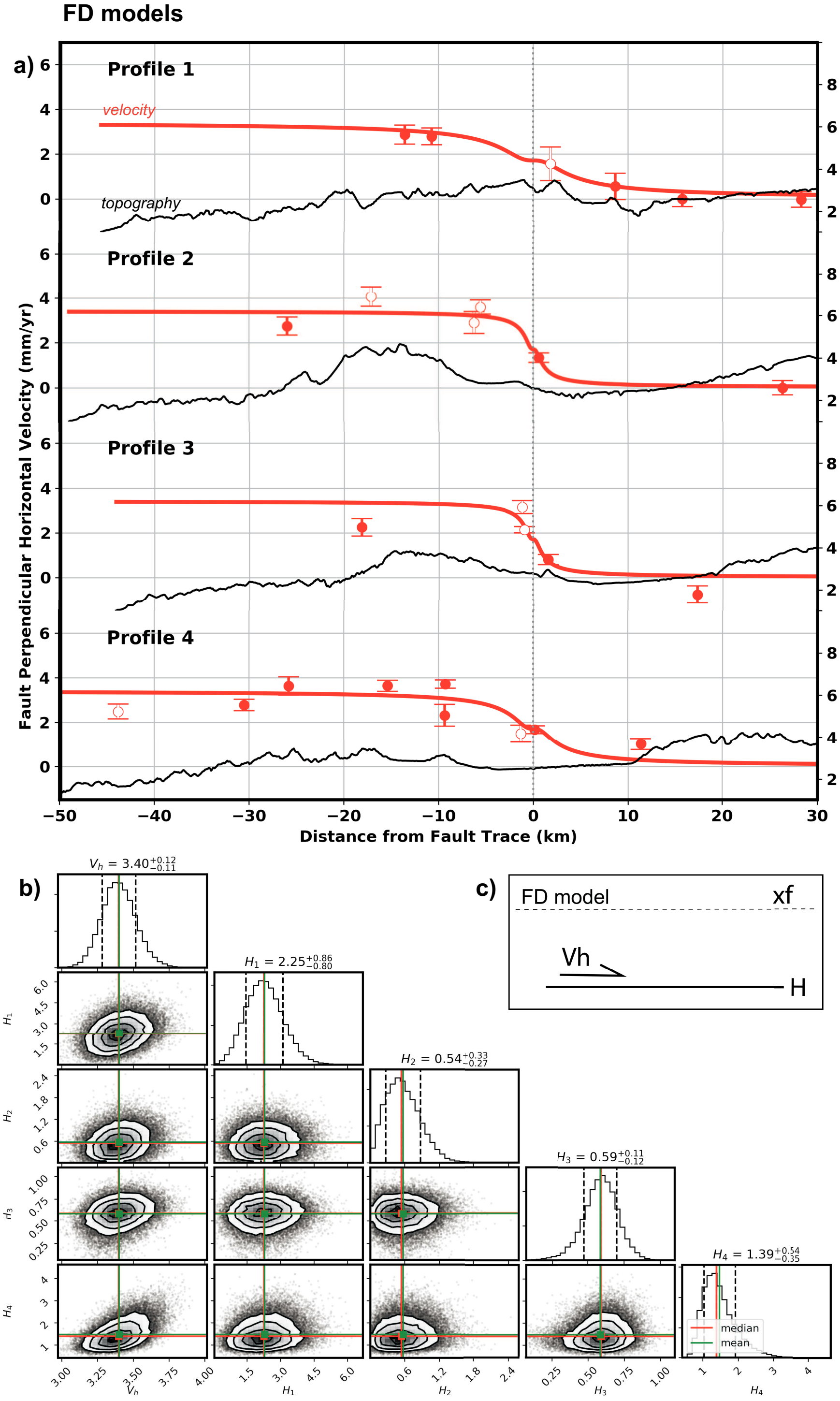

Figure 3.7: Same as Figure 3.6 but with a Flat Décollement (FD) model.

To force a more comprehensive exploration of the models allowed by the data, we run several inversions fixing the décollement depth at 3, 5, 7 and 10 km. For InSAR data, corrections for an offset and a tilt along the profile direction are estimated.

The InSAR profiles are decimated using a median filter. We exclude profile 4 from these inversions because the residual signal in the InSAR data southwest of the Ilalo Volcano cannot be fitted by a simple geometry with one single fault (see discussion).

For these models, we find that a décollement depth of 7 or 10 km with shallow (2-4 km) locking depth on the ramp can simultaneously fit the GPS and InSAR data. We find that there is little sensitivity to the dip because similar good fit is achieved for values of 10° to 50° (with slightly preferred values of 30°-35°) for profiles 1 and 3. For profile 3 in central Quito, the narrow bell-like LOS pattern is better fitted with a single slipping patch at 2-4 km depth on a ramp with a dip in the range of 20 to 35° (Figure 3.8). The FDR models reveal a wider range of horizontal shortening rate from 3 to 5 mm/yr allowed by the data.

In summary, the results from the two-dimensional tests show that (1) the horizontal shortening rate accommodated across the Quito fault is in the range of 3 to 5 mm/yr ; (2) fitting GPS data with a simple flat décollement or with back-slip models provides a very shallow locking depth but cannot explain the bell-like shape of InSAR LOS rate (Figs 4a and 4c) ; (3) simultaneously fitting the sharp gradient seen in both the GPS velocities and InSAR LOS rates requires shallow creep to occur along a ramp; (4) the amount of shallow creep along the ramp appears to be variable along strike with maximum aseismic slip occurring along the central Quito segment of the fault.

3.4.8 Three-dimensional spatial variable interseismic models

In the models of section 4.7, the shallow creep is modelled using a single creeping patch along the ramp, with the model build-in condition that the slip rate is constant along the patch. This is certainly a crude approximation since slip is likely to vary both along dip and along strike at the fault plane. To obtain a more realistic model of the shallow creep distribution, we design a three-dimensional inversion of spatially variable slip at depth. Our model follows the approach by Daout et al. (2016a). The block-like far-field velocity is modelled using a 110 x 110 km^2 horizontal dislocation at depth H slipping at velocity V_h. This length embeds the whole Quito fault system along strike (60 km) and also enables modelling of the PS-InSAR gradient seen north and south of the Quito fault. The width ensures a block-like behaviour for the far-field GPS data. The horizontal dislocation connects to a ramp reaching the surface along the fault trace in the central segment (Figures 3.9 and 3.10). We discretize the ramp into 2 x 2 km^2 subfaults. The surface fault trace is simplified by a single plane with a fixed strike of 200° that follows the foot of the main escarpment in the central part of the fault where more data are available to constrain the shallow behaviour of the fault.

Once V_h and the geometry are chosen, solving for spatially variable slip along the ramp is a linear inverse problem. We use the stochastic inversion approach described

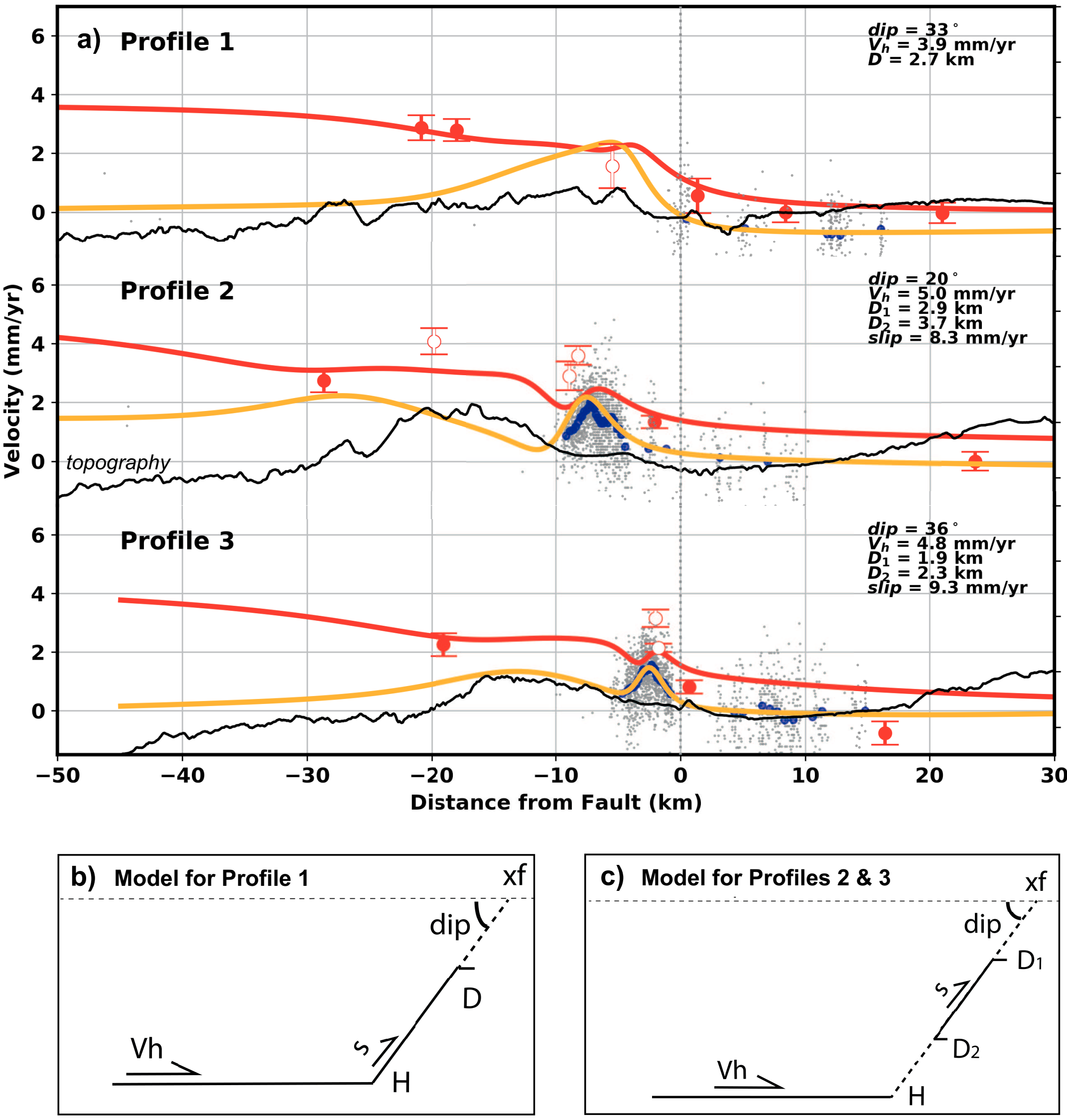

Figure 3.8: Results of the Bayesian inversion using GPS and InSAR data and the Flat Décollement Ramp (FDR) model with a décollement depth at 10 km. a) Red curves are along profile horizontal velocity model prediction from the mean model. Orange curves are model prediction from the mean model along the LOS. Light grey dots are LOS rates along a 400 m wide swath around the profile location. Blue circled are the selected points from the LOS velocity data used in the inversion a median filtered. Red filled circles indicate survey mode GPS whereas white filled circles are continuous GPS. Black line shows the topography. b) & c) Schematic models of a Flat Décollement Ramp (FDR) and a Flat Décollement (FD) with a slipping patch, with the parameters used for the inversion: dip; xf, location of the fault on the surface; V_h, shortening rate; D, locking depth (or D_1 to D_2: patch of the locking depth); H, décollement level; s, slip on the ramp.

in Nocquet (2018) to solve for slip at each individual subfault under the condition that the slip must be positive and lower or equal to $V_h/cos(dip)$ in the shortening direction. This condition implicitly enforces that the observed deformation is not transient since it does not exceed the slip imposed by the far-field horizontal shortening rate. We use a regularization condition in the form of a penalty function $(m - m_0)^T C_m^{-1}(m - m_0)$, where C_m is a covariance matrix of the form of $C_m = 2\sigma e^{-r_{ij}/rc}$ with σ being the constraint to the a priori model m_0, r_{ij} the distance between subfault i and j and rc a critical distance controlling the correlation between subfault slips. Because our simple geometry does not account for slight change in strike between different segments, we allow the rake to vary around 106° by setting a sigma value of 1 mm/yr on the conjugate component of slip at each subfault. Because InSAR data might be subject to systematic long wavelength errors, we also solve for an overall constant and a tilt of the LOS rates simultaneously to the two components of slip at each subfault.

We perform a grid search for V_h in [3.0, 4.5, 6.0, 8.0] mm/yr, dip in [20, 30, 40, 50] degrees, and depth in [7, 10, 13] km. For each V_h, dip and depth, we solve for both $m_0 = 0$ and $m_0 = V_h/cos(dip)$ with a constraint of 1 mm/yr and a critical distance rc of 4 km. Solving with a prior of $m_0 = 0$ provides a minimum slip rate solution, that leads to a maximum moment deficit rate model, while using $m_0 = V_h/cos(dip)$ provides a maximum slip rate solution, that is a minimum moment deficit rate model.

The 3D modelling confirms some of the results from the profile analysis. A horizontal shortening V_h=8 mm/yr overestimates the few far-field GPS data (Figure 3.10) while V_h=3 mm/yr underestimate them. The best agreement for far-field data is found for V_h=4.5 mm/yr but some models with V_h=6 mm/yr are also allowed by the data.

As for the two-dimensional models, our parameter exploration shows little sensitivity to the dip of the fault. For all models tested, a dip value of 50° provides underestimated magnitude for GPS velocities in the central Quito area. Otherwise, dip values from 20° to 40° are acceptable, with best fit achieved for dip values of 20° and 30°. Similarly, the three depths tested [7, 10, 13] km provide comparable fit to the data.

In terms of slip distribution, all models find shallow slip along the fault plane possibly reaching the surface in the central segment, decreasing north and south, as the gradient of the InSAR LOS rate and GPS, when available, become smoother (Figures 3.9 and 3.10). The length of the creeping segment is found to be ∼20 km. Its downdip extent is at least 5 km and some models find that the whole ramp is creeping along the central segment. Minimum slip models highlight two additional areas of slip at the southern and northern tip of the fault plane, but their extents are poorly constrained by spatially scarce data.

Overall, the size of the creeping areas, and notably their extension at depth, largely depends on the chosen a priori model. In some models, almost the whole fault is found to be creeping at a rate close to the one imposed by the far-field shortening.

The areas of our idealized fault that are not creeping correspond to areas where the fault trace is located a few kilometers west of the modelled fault trace (Figures 3.9 and 3.10). Therefore, those models indicate the possibility that the Quito fault might be almost entirely creeping. Alternatively, models with minimum slip prior show the possibility that shallow creep is restricted to the first shallowest kilometers of the fault and that significant coupling occurs north and south of the central segment.

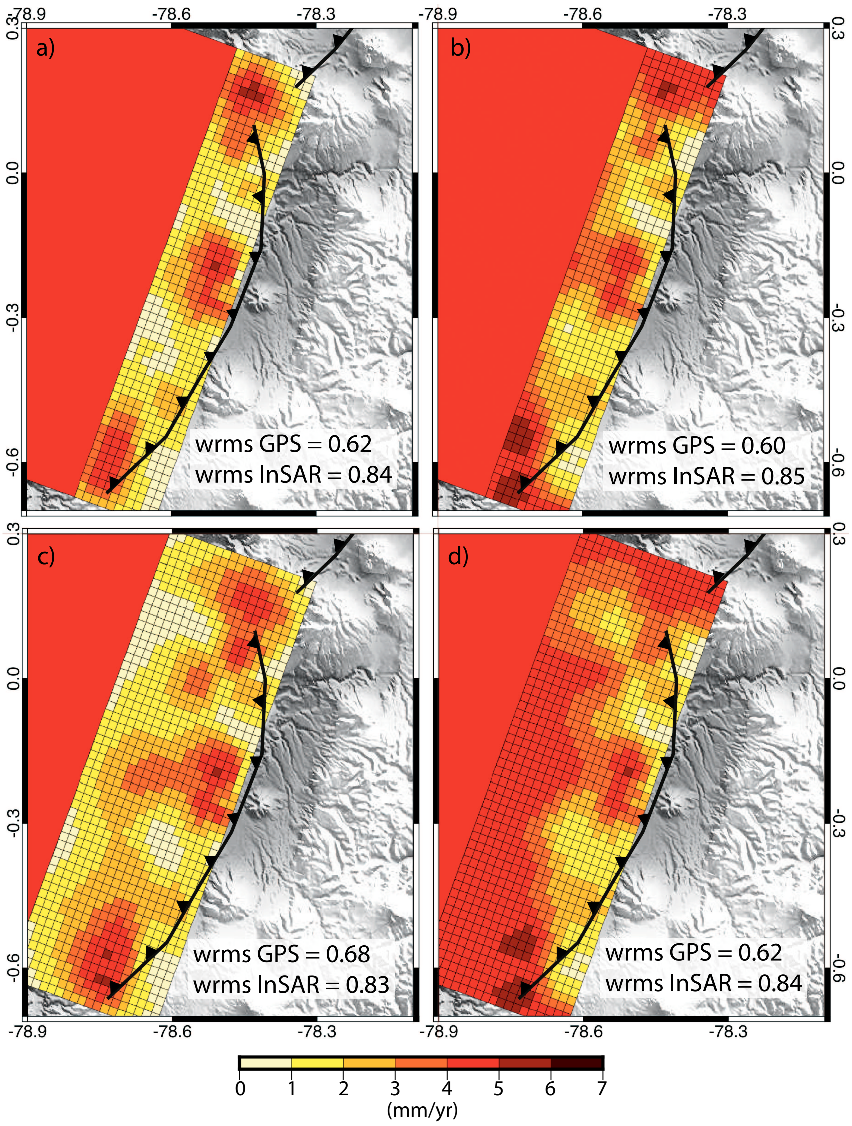

Figure 3.9: Selection of four different fault slip models along the Quito Fault System. Fault dipping at 20° with a shortening rate between 4.6 and 4.9 mm/yr and a flat décollement at either at 7 km depth (a and b) and 13 km depth (c and d). a) and c) have a prior $m_0 = 0$ (minimum slip rate solution). b) and d) have a prior $m_0 = V_h/cos(dip)$ (maximum slip rate solution). The values are in mm/yr and color-coded according to the scale shown at the bottom. The barbed black line shows the simplified surface trace of the fault. Fit to the data are shown in Figures 3.10 and 3.11.

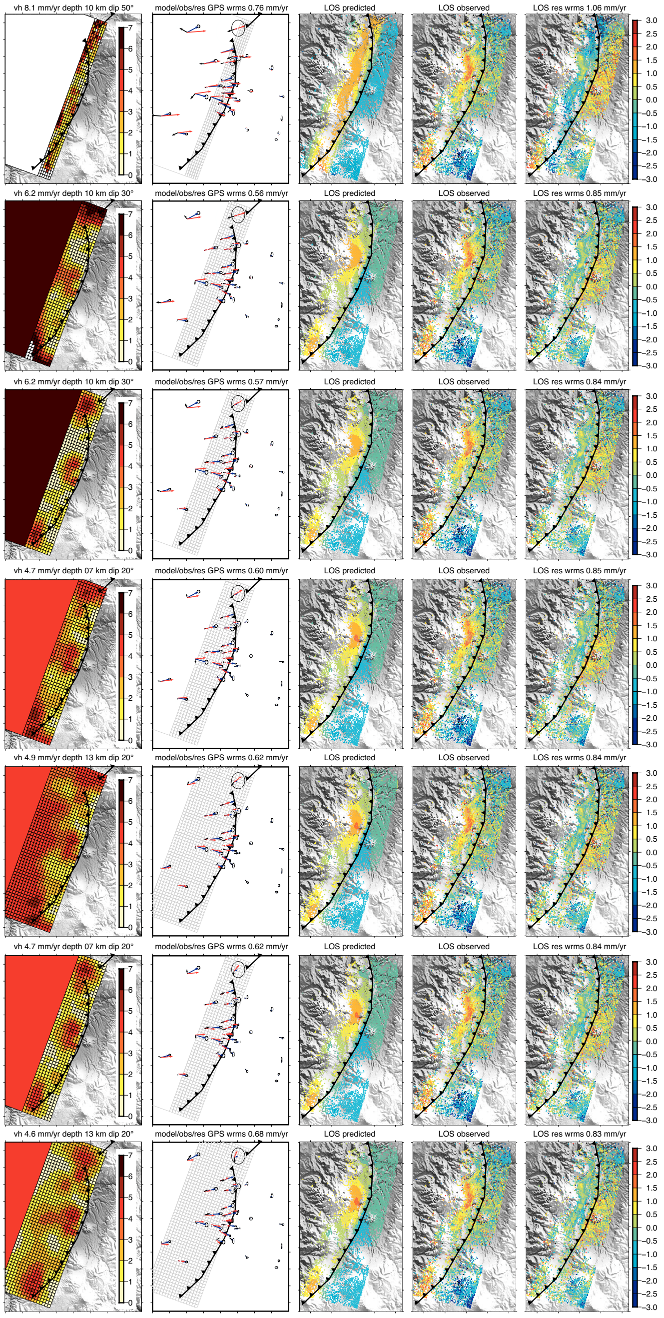

Figure 3.10: Results for a selection of models and fit to GPS and InSAR data. Column 1: Slip distribution. Slip values are indicated by the colour scale on the right side of the subplots on mm/yr. Horizontal shortening rate (mm/yr), depth (km) and dip (degrees) and indicated above each subplot. Column 2: Arrows indicate observations (blue), models (red) and residuals (black) respectively. The wrms of residuals is labelled on top of each subplot. Column 3: LOS rate model predictions (mm/yr). Column 4: LOS rate observations (mm/yr). Column 5: LOS rate residuals (mm/yr). All LOS rate maps use the same colour code indicated on the right of the figure. The selected best models from Figure 3.9 are the last four, with a fault dipping at 20° west and with a shortening rate between 4.6 and 4.9 mm/yr.

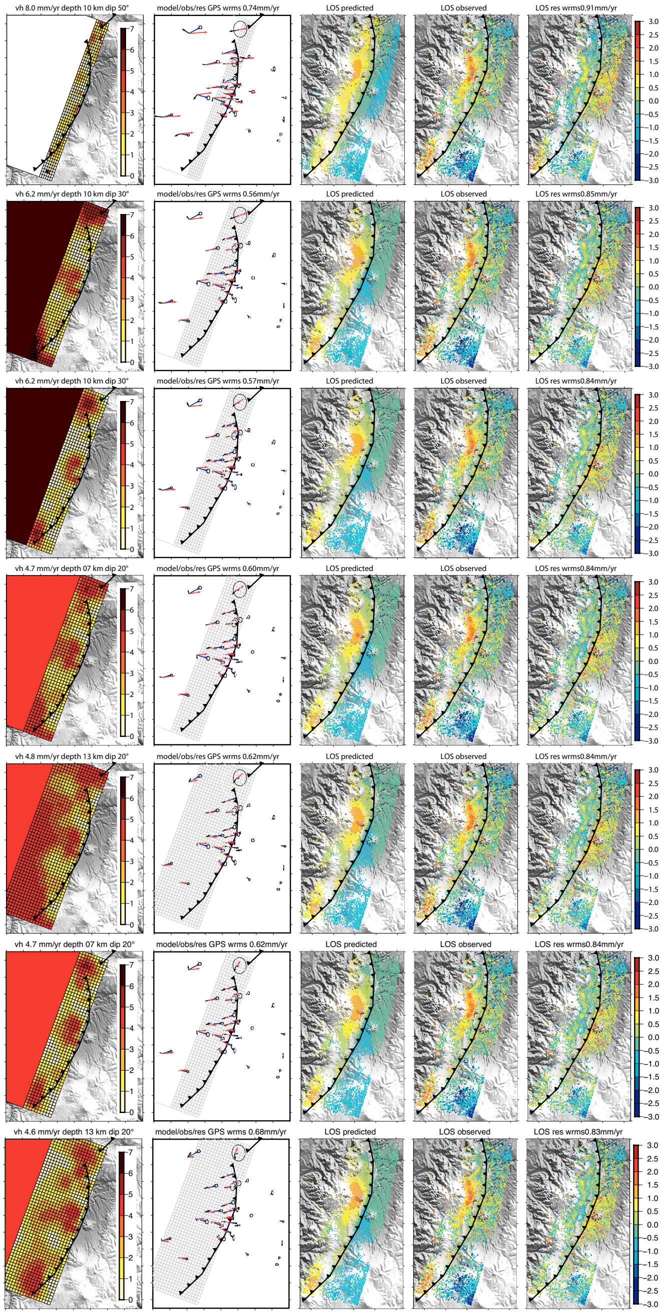

Figure 3.11: Same as Figure 3.10 with slip= V_h. The long-term slip rate on the ramp is equal to the shortening rate V_h.

3.5 Discussion

3.5.1 Comparison with the Seismicity Depth Distribution

Our preferred models include a flat décollement at a 10 km depth that connects to a ramp reaching the surface. Rather than a realistic description of the fault geometry at depth, such a model provides a first order approximation of the depth transition between ductile processes and elastic strain build-up. The depth of such a transition can independently be assessed by looking at the distribution of seismicity as a function of depth. Figure 3.12 shows the depth distribution of earthquakes in the Quito area, using the IG-EPN instrumental earthquake catalogue (https://www.igepn.edu.ec/red-nacional-de-sismografos). The IG-EPN earthquake catalogue covers the 2011-2018 period using the data from the national Ecuadorian permanent network (Alvarado et al. (2018)). When considering earthquakes with magnitude M_L above 2, the depth distribution is confined within the first 10 km (Figure 3.12). Although this distribution indicates that small earthquakes occur in a volume rather than being located on a single fault plane, the seismogenic depth derived from our inversion is consistent with the observed depth distribution of earthquakes.

3.5.2 Comparison with Fault Morphology

Morphology of fault related anticlines is also an indicator of the fault geometry at depth. Despite some variability among modelling approaches, models of fold evolution usually predict that the width of the fold roughly scales with the depth of the root of the underlying causative fault (e.g. Savage and Cooke (2003); Bernard et al. (2007); Johnson (2018)). If true, for the Quito fault, the characteristic width of the different segments is about 7 km, a value also consistent with our modelling results and the seismicity distribution with depth. Such a relatively thin seismogenic layer might be due to the thick (50-60 km, Reguzzoni et al. (2013), Araujo (2016)) crust documented beneath the Andes, therefore inducing a larger radiogenic thickness, relatively high heat flow and hence thin elastic thickness. The Inter-Andean valley in Ecuador is the locus of significant quaternary volcanic activity, and small volcanoes (Figure 3.1b) attest for magmatic intrusion reaching the surface. Therefore, the crust in the Quito area might be locally hot, therefore reducing the thickness of its elastic part.

3.5.3 Overall Slip Deficit Moment Rate and Implication for Seismic Hazard

The existence of an active fault poses a serious hazard to the growing city of Quito and its surroundings, especially considering that even moderate-size earthquakes have generated significant damages in the past. Within our present-day understanding of the earthquake cycle, significant creep reduces the accumulation

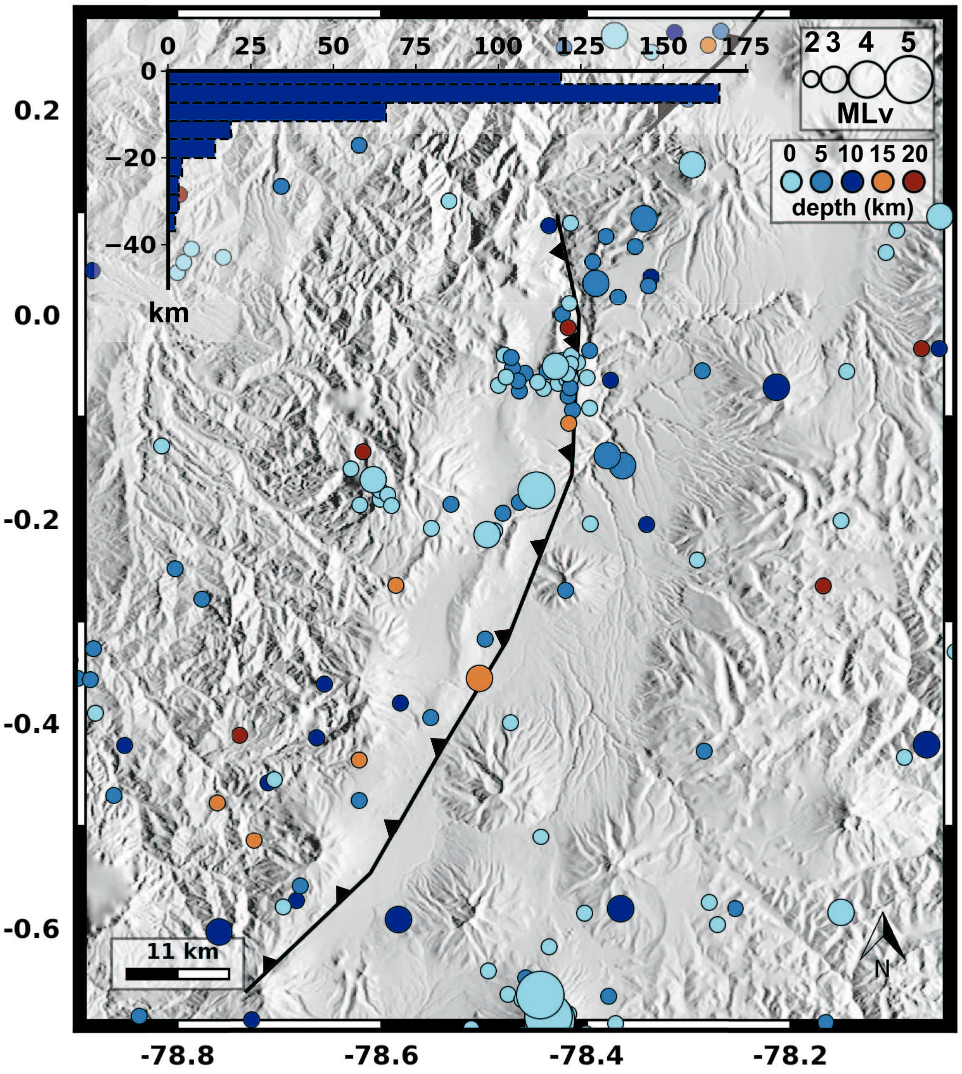

Figure 3.12: Distribution of the seismicity in the Quito area issued from the IG-EPN Catalogue (2011 to 2016). Earthquakes are selected starting from M_{Lv} 2+ and until 40 km deep, with an error in the depth location of less than 5 km. Top left is the histogram representing the number of earthquakes versus depth, with more than 80% of the seismicity located above 10 km depth.

of slip deficit at faults, then reducing the amount of elastic energy available for earthquakes. Although creeping faults recorded earthquakes up to magnitude 6.6 and possibly even larger events (Harris (2017)), earthquakes should, however, be less frequent at creeping segments than at their locked counterparts for the same slip rate and size. Under the assumption that the observed creep is steady through time and that the slip deficit is a first order indicator of the moment available for earthquakes, we can perform simple calculations. For all three-dimensional models explored, we can estimate the slip deficit at each sub-fault as the difference of the maximum slip rate provided by $Vh/cos(dip)$ and the inverted slip rate. We integrate it over the fault area and we calculate a rate of moment deficit accumulation over the whole fault. For this calculation, we remove sub-faults found with no slip that are located East of the known surface fault trace that would otherwise contribute to the slip deficit estimates. Such procedure roughly reduces by 30% the maximum moment rate deficit. Given the fact that we have inverted both for the maximum and minimum slips, the range of moment deficit rate is considered to reflect the amount of moment deficit accumulation rate allowed by the data. Taking the results from the most extreme models, our spatially variable slip inversions are equivalent to 20% to 80% of the average interseismic coupling along the fault. Under these assumptions, we find a moment deficit accumulation rate along the Quito fault to have a lower bound value of 0.3x10^{17} N.m.yr^{-1} and an upper bound value of 1.9x10^{17} N.m.yr^{-1}. These values are equivalent to a single M_W 6.7-7.3 earthquake every 500 years, a magnitude possible given the length of the fault (∼60 km).

In order to provide a more realistic description of earthquake recurrence, we use the geodetic moment accumulation rates to derive a cumulative exponential-truncated Gutenberg-Richter distribution (G-R, form 2 in Anderson and Luco (1983)). Both a b-value and an estimate of the maximum magnitude that the fault can generate must be assumed. Beauval et al. (2014) derived a magnitude-frequency distribution for the Quito fault system (Figure 3.13a), which is not well constrained due to the low number of events above M_W 4.5 in the area. Nonetheless, we compare our results to this catalog-based recurrence model. Applying Leonard (2010) scaling relationship for reverse events, a 90-100 km long and 20 km width fault corresponds to a magnitude of M_W 7.3. Assuming the same b-value and an M_{max} value of 7.3, we find that the geodetic-based G-R from the lower moment deficit accumulation requires an a-value lower than the one from seismicity rates, while the geodetic-based G-R from the larger moment deficit accumulation requires an a-value higher than observed from seismicity rates (Figure 3.13a). For earthquakes of magnitude larger or equal to 6.5, the geodetic-based models predict a mean interevent time between 200 and 1100 years, depending on the model chosen. We also determine the lowest maximum magnitude required so that the yearly seismic moment calculated from the integration of the G-R curve equates the yearly moment deficit accumulation. To make the lower geodesy-based and seismicity-based rates consistent, a smaller M_{max} of 6.8 is required (Figure 3.13b), predicting a mean interevent time between 150 and 900 years for an event $M_{max} \geq 6.5$.

Our results further highlight a segmentation of the slip deficit accumulation along the Quito fault, made of two segments accumulating strain separated by the 20 km long creeping segment in central Quito. While our model exploration shows that creep or locked behaviours are both possible at depth, our results highlight that the central segment is creeping along its shallow part, at least down to 5 km. An open question, as documented for subduction megathrusts, is to know whether this creeping segment could act as a barrier to the seismic rupture propagation. In this perspective, future earthquake scenarios for Quito could include the possibility of more frequent 30 km long ruptures occurring at the northern and southern segments than in the central part.

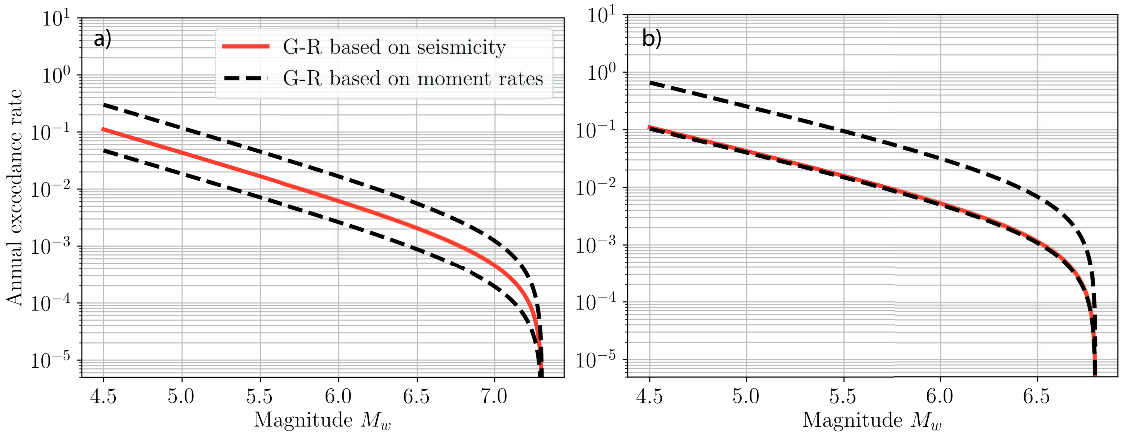

Figure 3.13: Quito Fault recurrence models based either on seismicity (red line) or on total geodetic moment rates (black dashed lines), with a b-value=0.81 (Beauval et al. (2014)). a) Maximum magnitude based on scaling laws (Leonard (2010)) with M_{max}=7.3; b) M_{max}=6.8 to obtain the same annual exceedance rate for the G-R based on the minimal moment rate (0.3x10^{17} N.m.yr^{-1}) and the G-R based on the seismicity.

3.5.4 The 1995-1996 Transient Motion – a Fold Growth Pulse?

Our PS-InSAR time series highlight a transient deformation, clearly seen for the interferograms spanning the April 11, 1995 - October 24, 1996, period (Figures 3.3d and 3.3h). It occurred southeast of the Ilalo Volcano, a few kilometers east of the main surface trace of the Quito fault in a semi-urban area. This transient signal has a LOS magnitude of ∼20 mm with a radial pattern over ∼4 km. The LOS rate map for the 1996-2000 period further shows a similar pattern at a smaller amplitude (1 mm/yr) and smaller length-scale (1 km, Figure 3.3f), indicating that deformation in this area persisted with a lower intensity during the 7 years of InSAR observation. The location of this signal correlates with a previously identified active Conocoto fold located east of the main Quito Escarpment at long. -78.47°, lat. -0.29° (Figure 3.14). The Conocoto fold is a 1.5 km long, 800 m wide and 100 m high structure. Its recent activity is attested by the deflection of the river course and it has been interpreted as a young growing fold induced by a secondary propagating west dipping thrust fault (Figure 3.14c and Alvarado et al. (2014)). Because of the observed radial pattern of deformation and the absence of negative LOS displacement, such a signal is unlikely to be modelled using reverse slip along an elastic dislocation. We speculate that this transient deformation signal arises from the ductile deformation of the top layers induced by local aseismic slip along the underlying fault. If we interpret the LOS displacement as being mainly vertical, this implies a steady uplift rate of ∼1 mm/yr calculated for the 1993-1995 and 1996-2000 periods. The LOS displacement is ∼20 mm during the 1.5 years separating the two SAR acquisitions (from 1995/4/11 to

1996/10/23), but we do not know when the uplift took place during this period. Nonetheless, the InSAR results indicate that the uplift rate accelerated by a factor of at least 20 with respect to the uplift rate before April 1995 and after October 1996. This fold growth pulse accounts for 70% of the finite displacement over the 1993 to 2000 period. Although longer measurements are required to know how frequent are these events, it suggests that fold growth pulses can contribute significantly to the building of fold topography.

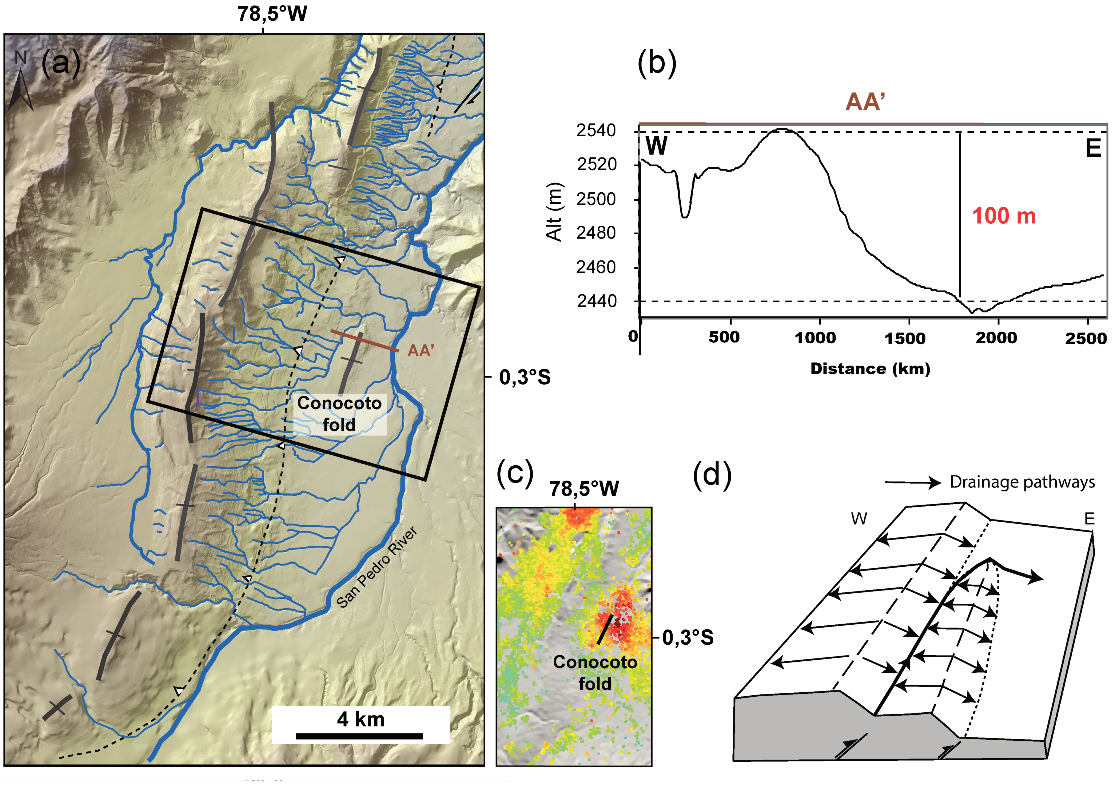

Figure 3.14: Drainage map on the Inter-Andean valley, east of the Quito Basin and neoctectonic interpretation (modified from Alvarado (2012)). a) Blue curves are rivers; thick black lines are the top fold locations and the dashed black line with white triangles is the surface location of the main thrust fault. Note the deflection of the drainage system to the north around the Conocoto fold. Black rectangle is the location of the inset b d. b) Topographic profile across the Conocoto fold. c) Same area as in a) with the LOS surface velocity from Figure 3.3a compared with the location of the Conocoto fold. d) Propagation model of thrust in New Zealand (modified from Jackson et al. (1996)).

3.6 Conclusions

We have derived a high spatial resolution interseismic surface velocity field from GPS data and PS-InSAR analysis around the Quito reverse fault system, directly threatening a highly-populated area of the northern Andes. We find that the Quito fault accommodates 3 to 5 mm/yr of horizontal shortening. As a whole, relatively sharp gradients across the Quito fault highlight a weak rate of elastic strain accumulation and a shallow ($<$3 km) locking depth. The central segment shows the sharpest velocity gradient, providing evidence of aseismic slip taking place at shallow depth along the fault plane and possibly reaching the surface, while segments north and south of it possibly hosts larger slip deficit accumulation rates. Aside these trends, the details of interseismic coupling distribution appear to be model dependent. In particular, some models including a flat décollement and a ramp allow for slip deficit to accumulate at depth. Overall, our results demonstrate that strain accumulation is spatially heterogeneous along the Quito fault. The observed shallow aseismic slip concurs to confirm that a significant percentage of crustal faults on Earth may be creeping at shallow depth (Harris (2017)). In terms of seismic hazards for the Quito area, our results help to refine previous estimates of earthquake time recurrence (Beauval et al. (2014, 2018)). Our estimates for the rate of moment deficit accumulation derived from a 3D spatially variable interseismic coupling translate into recurrence time for magnitude 6.5+ earthquake to be between 200 and 1100 years, a value consistent or slightly lower than proposed in previous studies (Beauval et al. (2014, 2018); Parra et al. (2016)).

Finally, we identify a transient deformation signal related to the development of a secondary fold, a few kilometers east of the main fault trace. This observation suggests that fold growth might result from pulses of accelerated deformation, possibly driven by slow slip events occurring along the fault plane underlying the soft top layers experiencing anelastic deformation. On the overall, our results emphasize a dominant contribution of aseismic processes for the Quito fault system.

3.7 Acknowledgments

We thank two anonymous reviewers for their thorough reading of the manuscript and comments that greatly helped us to improve the article. This research was supported by the French Agence National de la Recherche (ANR) through the project REMAKE (2016–2019, Grant Number ANR-15-CE04-004), and by the Institut de Recherche pour le Développement (IRD), the Geophysical Institute in Quito, part of the Escuela Politecnica Nacional, and ISTerre and Géoazur laboratories. InSAR data were processed thanks to an IRSN and CNES funding (2012-2014). We are grateful to R. Grandin for insightful discussions. This work has been carried out in the frame of the Joint International Laboratory “Seismes & Volcans dans les Andes du Nord” (LMI SVAN).

CHAPTER 4

Earthquake recurrence models combining seismic and geodetic data in the subduction zone of Ecuador, application for SHA

Contents

This chapter is the subject of an article produced in collaboration with Celine Beauval, Jean-Mathieu Nocquet, Mohamed Chlieh and Hugo Yepes and that is submitted to *Bulletin of the Seismological Society of America.* It focuses on the integration of the geodetic data into the recurrence models and the quantification of the associated uncertainties in order to better constrain seismic hazard assessment in the subduction zone of Ecuador.

Abstract

Probabilistic Seismic Hazard Assessment relies on long-term earthquake forecasts and ground-motion models. Our aim is to improve earthquake forecasts by including information derived from geodetic measurements, with an application to the Colombia-Ecuador megathrust. The annual rate of moment deficit accumulation at the interface is quantified from geodetically-based interseismic coupling models. We look for Gutenberg-Richter recurrence models that match both past seismicity rates and the geodetic moment deficit rate, by adjusting the maximum magnitude. We set up a logic tree for exploring the uncertainties on the seismic rates (a and b-values, form close to M_{max}) and on the geodetic moment deficit rate to be released in earthquakes. A distribution of maximum magnitudes M_{max} bounding a series of earthquake recurrence models is obtained for the Colombia-Ecuador megathrust. Models associated to M_{max} values compatible with the extension of the interface segment are selected. We show that the uncertainties influencing the most the moment-balanced recurrence model are the fraction of geodetic moment released through aseismic processes and the form of the Gutenberg-Richter model close to M_{max}. The distribution of moment-balanced recurrence models is combined with a ground-motion model to obtain a series of uniform hazard spectra representative of uncertainties at a site on the coast. Considering the recent availability of massive quantity of geodetic data, our approach could be used in other well-instrumented regions of the world.

4.1 Introduction

The Nazca/South American subduction zone is among the most seismically active convergent margins in the world. Between latitudes -3° to 2° (Figure 4.1), the oceanic Nazca plate subducts at a rate of ∼47 mm/yr below the North Andean Sliver, a continental domain moving independently from South America (Pennington (1981); Nocquet et al. (2014); Alvarado et al. (2016)). This subduction segment has experienced six large megathrust earthquakes since the beginning of the 20^{th} century: in 1906 (M_S ∼8.6, Ye et al. (2016)), 1942 ($M_{W(ISC-GEM)}$ 7.8), 1958 ($M_{W(ISC-GEM)}$ 7.6), 1979 ($M_{W(gCMT)}$ 8.1), 1998 ($M_{W(gCMT)}$ 7.1) and 2016 ($M_{W(gCMT)}$7.8) (Figure 4.1). In this area, the coast lies ∼15 to ∼40 km directly above the rupture area of megathrust earthquakes and is particularly exposed to strong shaking during large events. For instance, horizontal Peak Ground Accelerations (PGAs) recorded at stations above the Pedernales 2016 M_W 7.8 rupture plane exceeded 1.0 g (Beauval et al. (2017)), along with significant damages to buildings and more than 670 deaths (Secretaria de Gestion de Riesgos, Informe de Situacion N°65, 2016).

The present study aims at improving Probabilistic Seismic Hazard Assessment (PSHA) in Ecuador. It focuses on the hazard induced by earthquakes occurring at the subduction interface, considering the Esmeraldas segment as defined from the seismogenic source zonation proposed in Yepes et al. (2016) and updated in Beauval et al. (2018). The Esmeraldas segment is ∼600 km-long, it extends from north of the Grijalva rifted margin to southern Colombia (Figure 4.1), and encompasses all rupture areas of the 1906-2016 megathrust earthquake sequence (e.g. Chlieh et al. (2014)). GPS data indicate that this segment is presently highly coupled (Nocquet et al. (2014); Chlieh et al. (2014)). According to the recently published seismic hazard model for Ecuador (Beauval et al. (2018)), the highest hazard levels are found for sites located on the northern coast, with mean PGA values exceeding 0.6 g at 475 years return period for the sites closest to the subduction interface (generic rock site).

The earthquake recurrence model plays a key role in the determination of hazard levels, as it defines the magnitude range to expect for future earthquakes, with associated frequencies. Different models can be implemented to account for interface events. Gutenberg-Richter models can be derived from the available earthquake catalogs (e.g. Medina et al. (2017); Beauval et al. (2018); Petersen et al. (2018a)); characteristic models can also be developed with characteristic earthquake recurrence times inferred from the subduction slab convergence rates (e.g. Stirling et al. (2012); Pagani et al. (2020b)). In the seismic hazard model published by Beauval et al. (2018), the authors determined the Gutenberg-Richter recurrence parameters from the well-constrained observed seismic rates in the moderate magnitude range, and they extrapolated these rates up to maximum magnitudes. Unlike the crustal fault model, Beauval et al. (2018) did not use geodetic information to derive earthquake frequencies. The Esmeraldas segment is well instrumented with GPS stations at distances less than 100 km from the trench axis and high-resolution models of interseismic coupling are available (Nocquet et al. (2014); Chlieh et al. (2014); Gombert et al. (2018)). Our aim here is to combine both available seismic and geodetic data to constrain earthquake recurrence models for the ∼600 km-long subduction interface that extends from northern Ecuador to Central Colombia. As the quantification of uncertainties is a key aspect in PSHA studies, we identify uncertainties related to both the seismic and the geodetic data and propagate these uncertainties up to the hazard estimates.

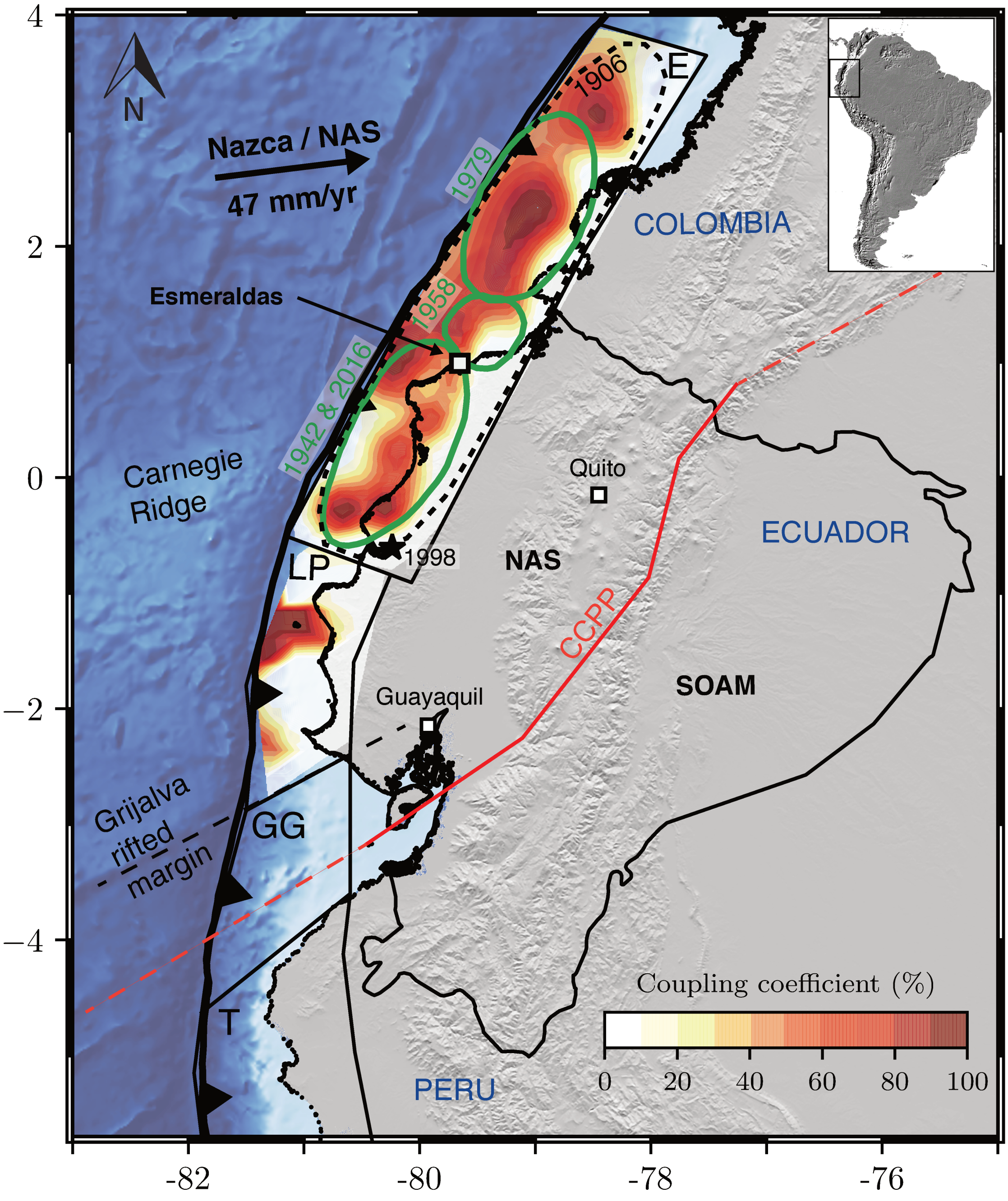

Figure 4.1: Geodynamic framework of Ecuador and surrounding areas. The North Andean Sliver (NAS) is bounded to the west by the Nazca subduction trench axis and to the east by the transpressive right-lateral CCPP fault system (Chingual-Cosanga-Pallatanga-Punà, Alvarado et al. (2016)). The CCPP is the main boundary between the NAS and the South America plate (SOAM). The relative convergence rate between the Nazca Plate and the NAS increases northward from 46 mm/yr in southern Ecuador to 50 mm/yr in central Colombia. The subduction interface fault segments defined by Yepes et al. (2016) and updated in Beauval et al. (2018) are reported, from north to south: Esmeraldas (E), La Plata (LP), Guayaquil Gulf (GG), Talara (T). The Interseismic coupling model from Nocquet et al. (2014) is displayed as well as the approximate rupture areas of the 1942 (M_W 7.8), 1958 (M_W 7.6), 1979 (M_W 8.1) and 2016 (M_W 7.8) megathrust events. The rupture area of the 1906 M_S ∼8.6 event corresponds approximately to the Esmeraldas segment (see Yepes et al. (2016)). The epicenter of the 1998 M_W 7.1 interface event is also displayed (ISC-GEM catalog, Di Giacomo et al. (2015)).

4.2 Modelling seismic and geodetic data

4.2.1 A seismic catalog extending over 117 years

In Ecuador, the earliest events reported in the historical intensity catalog date back to the middle of the 16^{th} century (Egred (2009)), a few years after the arrival of the Spaniards. Until the end of the 19^{th} century, the historical information mostly describes effects of earthquakes inland, in the Cordillera (see e.g. Beauval et al. (2013)). The first coastal earthquake for which several intensities are reported is the 1896 event. However the dataset is too sparse to infer a reliable location and magnitude for this event (Keller (2014)). Therefore, the earthquake catalog for the subduction interface extends at maximum over 117 years and includes early-instrumental and instrumental events. Nonetheless, marine paleoseismology studies are undergoing at the Ecuadorian margin (Migeon et al. (2017); Proust et al. (2016)). For now, they have identified turbidites dated approximately 600 years ago which could have been triggered by an event equivalent to the great 1906 subduction earthquake (Migeon et al. (2017)).

We build an earthquake catalog for the area, making use of global catalogs (Figure 4.2). We decide not to include local catalogs to ensure a certain level of homogeneity in moment magnitude. As a consequence, the minimum magnitude of completeness is quite high (M_W ~4.8 since 1964). Solutions in the ISC-GEM catalog (v. 7.0) are considered the most authoritative. All ISC-GEM hypocenter locations were computed with the same algorithm and velocity model (Storchak et al. (2015)); events are described by either a published moment magnitude, M_W from the global Centroid Moment Tensor catalog (gCMT, Ekström et al. (2012)), or a proxy M_W value inferred from an M_S or m_b magnitude (Di Giacomo et al. (2015)). For earthquakes which are not in the ISC-GEM catalog, we use solutions from the ISC event catalog (International Seismological Centre (2020), *On-line Bulletin*, https://doi.org/10.31905/D808B830, Storchak et al. (2017)) over its reviewed period. In this case, M_W is either retrieved from the gCMT catalog or obtained from ISC m_b and M_S magnitudes using the global conversion equations from Lolli et al. (2014) The exact selection scheme followed for building the catalog is detailed in the Appendix 4.9.1, *An earthquake catalog for seismic hazard assessment in Ecuador.*

Earthquakes that may be associated with the Esmeraldas interface segment are displayed in Figure 4.3. All events falling inside the segment with hypocentral depths between 0 and 50 km are considered (Yepes et al. (2016)). Since 1900, the area has been very active, experiencing 6 earthquakes with magnitudes M_W between 7.1 and ~8.6 and 38 events with magnitudes between 6.0 and 7.0. To estimate seismic rates representative of long-term seismicity, it is current practice in PSH studies to decluster the earthquake catalog (e.g. Teng and Baker (2019)). The strong aftershock sequences can bias the estimation of the rates and the b-value characterizing the exponential decrease of the number of events with respect to magnitude. We apply the Reasenberg (1985) declustering algorithm, with parameters indicated in Table 4.2 (Appendix 4.9.1, *An earthquake catalog for seismic hazard assessment in Ecuador*). In the Esmeraldas source zone, 52% of all events $M_W \geq 4.5$ are identified as clustered events (155 out of 297 events). Two-third of these clustered events belong to the aftershock sequences of the 1979 and 2016 megathrust earthquakes (Figure 4.3). However, in terms of seismic moment rate, these clustered events represent only 0.8% of the moment rate calculated over the whole catalog.

In the depth range considered, not all events are related to the interface, some might be related to crustal shallow faults. Given the large uncertainties on the depth solutions, discriminating between interface and crustal events based on the hypocentral locations is elusive. For most earthquakes with a magnitude $M_W \geq 5.0$-5.2 after 1979 the gCMT catalog provides a solution (Figure 4.2), including the focal mechanism. We apply some simple criteria, i.e. a rake within the range 30° to 150° and a dip lower than 45°, to select earthquakes which might correspond to reverse or reverse oblique faulting at the plate interface (see Fig. 4.18 in PEER Report 2020/0, *Data Resources for NGA-Subduction Project*, that displays the distribution of rake and dip angles for interface events in the Next Generation Attenuation Subduction (NGA-Sub) database). We find that within the Esmeraldas source zone limits, 88% of the earthquakes in the gCMT catalog fall in this category. Twelve percent of events might be related to crustal shallow faults. Observed seismic rates estimated from the newly built catalog will be corrected accordingly.

4.2.2 Modelling earthquake recurrence

The Weichert (1980) maximum likelihood method allows to determine the Gutenberg-Richter recurrence parameters from magnitude intervals with varying time-windows of completeness (productivity a and exponential coefficient b, Gutenberg and Richter (1944)). The catalog is considered to be complete for $M_W \geq 6.6$ in the early instrumental period from 1900 to 1920, for $M_W \geq 6.0$ in the period from 1920 to 1950, for $M_W \geq 5.7$ in the period from 1950 to 1964, and for $M_W \geq 4.8$ from 1964 on (Table 4.3, 0.3 magnitude bin width used). Applying the Weichert method over the magnitude range with populated bins, i.e. between M_W 4.5 and 7.2, we obtain from the declustered earthquake catalog a b-value of 0.62 ± 0.05 (with an a-value 3.06; Figure 4.4a). Seismic rates for larger magnitudes ($M_W > 7.2$) are not meaningful, as they are calculated from one or two occurrences. Although debated (Ye et al. (2016); Gombert et al. (2018)), the occurrence rate of large subduction earthquakes since 1906 has been proposed to be abnormally high and being part of an earthquake super-cycle (Nocquet et al. (2016)). In any case, the observation time window is too short to estimate the long-term average recurrence time of these large events. As there is no trace in the historical archives of a large megathrust earthquake that would have hit the coast during the 17^{th}, 18^{th} and 19^{th} century (Egred (2009); Beauval et al. (2013)), the rates of events $M_W > 7.2$ could also be calculated extending the time window to 400 years (resulting in the orange dots in Figure 4.4b).

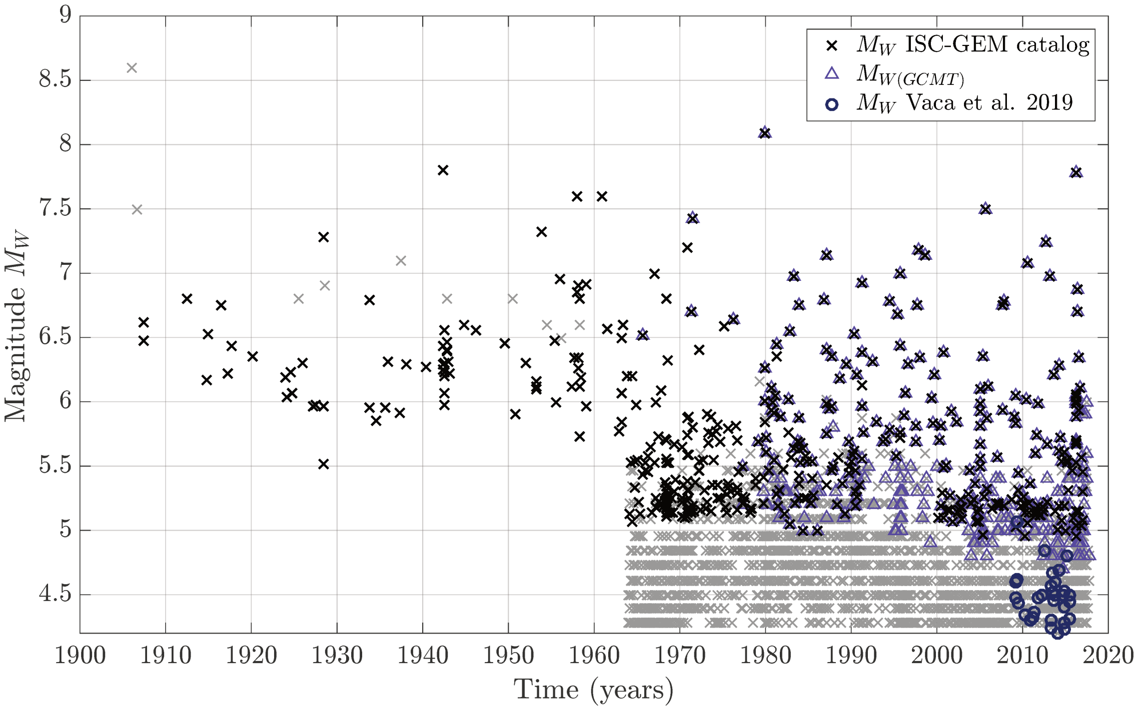

Figure 4.2: Earthquake catalog for Ecuador (longitudes -82° to -74° and latitudes -7° to 4°), built within this study, covering the time window 1906 to 2017. The ISC-GEM catalog provides the most authoritative solutions (black crosses); a large part of moment magnitudes in the ISC-GEM catalog are gCMT magnitudes (triangles). For events which are not in the ISC-GEM catalog, we use the solutions from the ISC event catalog (grey crosses); some of these events also have a gCMT moment magnitude (triangles), the other events are described by an m_b magnitude converted into M_W using the Lolli et al. (2014) equations. The moment magnitude earthquake catalog from Vaca et al. (2019) is included (circles). Details in the Appendix 4.9.1, *An earthquake catalog for seismic hazard assessment in Ecuador.*

Alternatively, we can obtain these rates by extrapolating the model established from the moderate magnitude range to the upper magnitude range, but again there is no unique way to proceed. Different forms have been proposed in the literature for modeling the rates close to the maximum magnitude. The selection of one model over the other remains arbitrary as the data in the upper magnitude range is always too sparse to discriminate between the different proposed forms (Zöller (2013)).

Here, we consider the three alternative Gutenberg-Richter recurrence models proposed by Anderson and Luco (1983)), which have been used in many subsequent studies. All models are truncated at the maximum magnitude M_{max}, but the three forms forecast different rates in the upper magnitude range ($M_W > 7.0$, Figure 4.4b). The total number of earthquakes above a given magnitude can be estimated as follows, depending on the form selected:

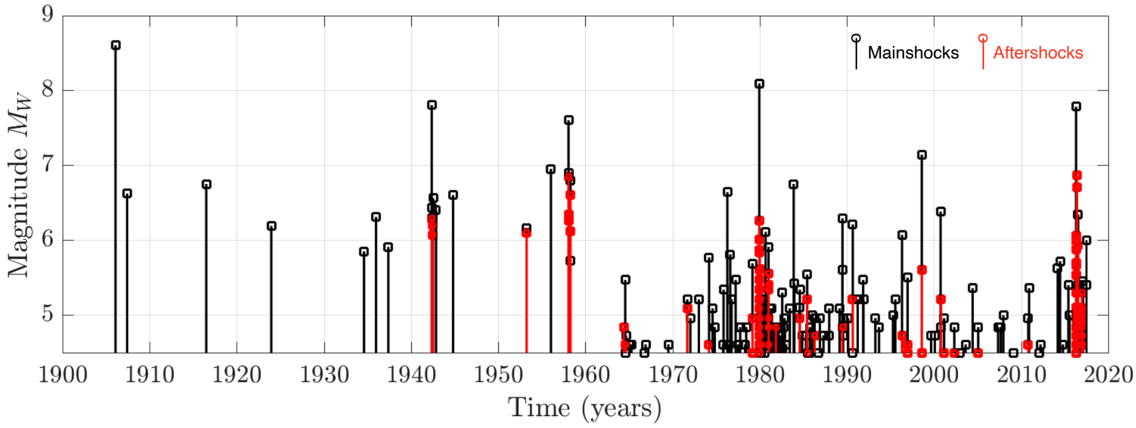

Figure 4.3: Magnitude versus time, catalog homogenized in M_W (this study, $M_W \geq 4.5$) in the Esmeraldas interface source zone (shown in Figure 4.1). Black: mainshocks; red: clustered events, as identified by the Reasenberg algorithm. Before 1964, the catalog only includes earthquakes with $M_W > 5.5$. The aftershock sequence following the 1979 $M_{W(gCMT)}$ 8.1 event and of the 2016 $M_{W(gCMT)}$ 7.8 represents respectively 38% and 31% of all clustered events in the zone.

$$N(m) = 10^{a-bm} \quad \text{for } m \leq M_{max} \tag{4.1}$$

$$N(m) = 10^{a-bm} - 10^{a-bM_{max}} \quad \text{for } m \leq M_{max} \tag{4.2}$$

$$N(m) = 10^{a-bm} - 10^{a-bM_{max}} - bln(10)(M_{max} - m)10^{a-bM_{max}} \quad \text{for } m \leq M_{max} \tag{4.3}$$

Equation (4.1) corresponds to the Form 1, equation (4.2) corresponds to the Form 2 and the equation (4.3) corresponds to the Form 3.

The corresponding discrete non-cumulative rates can be found in the Appendix 4.9.3, *Discrete non-cumulative rates for Gutenberg-Richter Forms 1, 2 and 3.* Form 1 has similarities with the Youngs and Coppersmith (1985) characteristic earthquake model, with rates for the last magnitude bin larger than predicted by the moderate-to-large magnitude range (Figure 4.17). Form 2 and Form 3 predict fewer large magnitude earthquakes than Form 1. Form 2 is the most prevalent in PSHA studies (e.g. Beauval et al. (2014); Mihaljević et al. (2017); Grünthal et al. (2018)). It is the form implemented in Openquake (Pagani et al. (2014), “Truncated Gutenberg-Richter MFD”). Form 1 has been less used in PSHA, but it is quite common in the literature comparing seismic moment accumulation from geodesy and moment released by earthquakes (e.g. D’Agostino (2014); Avouac (2015); Stevens and Avouac (2016, 2017)).

As in every seismic hazard study, the earthquake catalog and the seismic rates estimated bear significant uncertainties (see e.g. Beauval et al. (2013, 2018, 2020); Brax et al. (2019)). There are uncertainties on the selection of best magnitudes and locations from available solutions, on the choice of the magnitude conversion equations, on the determination of time windows of completeness, and on the cut-off magnitude used to model the recurrence. Here we consider the uncertainty related to the cut-off magnitude and use successively minimum magnitudes of 4.5, 4.8 and 5.1. Three alternative a and b pairs are derived (Figure 4.4c, b-values 0.62±0.05, 0.67±0.06 and 0.55±0.08). In the Weichert method, the magnitude bins which are the most populated control the parameter estimation. The model based on a magnitude cut-off 4.5 predicts fewer events with $M_W \geq 6.3$ than observed over the last 117 years; the model based on a magnitude cut-off 5.1 predicts approximately the rates observed up to magnitude 7.2 (Figure 4.4c). The b-values obtained are rather low, but they are within the range of b-values found in the literature for subduction interface segments. For instance, Medina et al. (2017) found b-values around ∼0.75 for the interface source zones in Chile. Marzocchi et al. (2016) analyzed the frequency-magnitude distribution of the interface earthquakes at different subduction zones worldwide; the b-values found vary between 0.62 and 2. In a study focused on the Nazca subduction zone, Pagani et al. (2020b) evaluated b-values between 0.64 and 1.11 depending on the interface segment of the South American subduction zone. They obtained a b-value of 0.64 for their ∼850 km segment extending from - 1.0° to 5.5° latitude, a segment that encompasses the Esmeraldas segment.

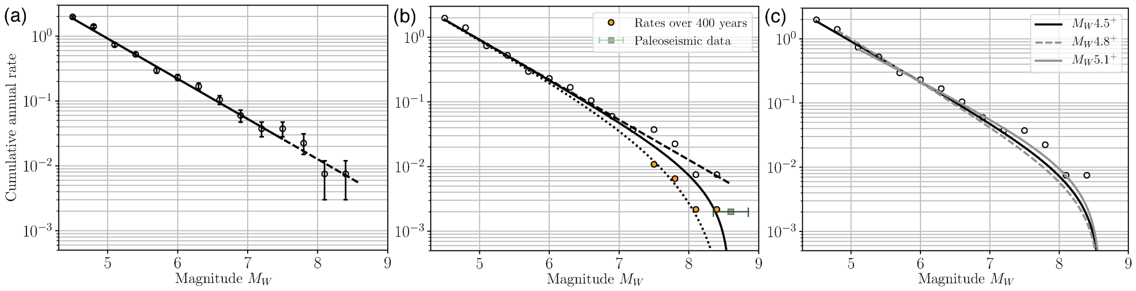

Figure 4.4: Magnitude-frequency distributions for Esmeraldas interface source zone (Figure 4.1); a and b recurrence parameters determined over the moment magnitude range M_W=4.5-7.2 (a=3.06, b=0.62). (a) The recurrence model (solid line) is superimposed to observed rates; error bars indicate the uncertainty on the rates assuming a Poisson model (percentiles 5^{th} and 95^{th}); model is extrapolated (dashed line) up to the maximum observed magnitude (M_S 8.6±0.25, Ye et al. (2016)). (b) Three different forms are used to extrapolate the model in the upper magnitude range (Anderson and Luco (1983)): Form 1 (dashed line), Form 2 (solid line), Form 3 (dotted line); orange dots: rates for $M_W \geq 7.5$ calculated over 400 years rather than 117 years; at least one earthquake equivalent to the 1906 event every 600 years according to Migeon et al. (2017) paleoseismic study (green square). (c) Uncertainty on the modeling of the recurrence from the earthquake catalog: three (a,b) pairs inferred from the magnitude intervals 4.5-7.2 (a=3.06, b=0.62±0.05, black), 4.8-7.2 (a=3.35, b=0.67±0.06, grey dashed line) and 5.1-7.2 (a=2.65, b=0.55±0.08, grey solid line). See the text.

4.2.3 The upper magnitude range controls the seismic moment budget

Using a Gutenberg-Richter model with parameters determined for the Esmeraldas zone, we now show how the seismic moment budget varies with the form selected and the magnitude range considered (Figure 4.5). An increase of 0.2 in magnitude degree corresponds to a two-fold increase in the corresponding seismic moment M_0 (Hanks and Kanamori (1979)):

$$M_0 = 10^{cM_W+d} \quad (N.m) \qquad \text{with c=1.5 and d=9.1} \tag{4.4}$$

Figure 4.5 displays Gutenberg-Richter models with increasing maximum magnitudes (Form 1 in Figure 4.5a, Form 2 in Figure 4.5c), together with the corresponding total seismic moment rate (obtained by integrating the model over the whole magnitude range). We calculate the contribution to the total seismic moment rate per magnitude bin, using a bin width of 0.25 (Figures 4.5b and 4.5d). We show that the exponential decrease of the seismic rates with increasing magnitude (Figures 4.5a and 4.5c) is counterbalanced by the exponential increase of the seismic moment. Considering Form 1 and a b-value of 0.67 (Figure 4.5b), the upper one-degree magnitude interval, i.e. [M_{max}-1 M_{max}], contributes to 93% of the total seismic moment rate. Considering Form 2 (Figures 4.5c and 4.5d), the upper one-degree magnitude interval contributes to 85% of the total seismic moment rate. With an M_{max} equal to 9.0, the contribution of events with magnitudes lower than 7 is around 2%.

The 117 year long earthquake catalog helps to constrain the moderate magnitude range but is useless to discriminate between forms close to M_{max}. Geodetic measurements provide an estimate of the rate of moment deficit accumulating on the subduction interface. Such information can be used to define the overall budget expected to be released in earthquakes. By combining this geodetic information with the information from the catalog in the moderate magnitude range, the rates in the upper magnitude range can be fully constrained.

4.2.4 Interseismic models available for the Ecuadorian subduction interface

Compared to other subduction segments, the Esmeraldas interface source zone benefits from relatively well-constrained interseismic coupling models. Indeed, a coastline-trench distance usually shorter than 80 km, with several peninsulas, combined with a shallow dipping interface, allows a precise determination of the coupling at depth greater than 10 km of the megathrust interface (Chlieh et al. (2014)). The GPS network has an average density of measurement sites every 70 km or less. Long time series dating back to the 1990's for campaign sites and 2008 for continuous GPS are available. Several interseismic coupling models have been proposed for Ecuador and the southern Colombia subduction zone (Nocquet et al. (2014); Chlieh et al. (2014); Gombert et al. (2018); Staller et al. (2018); Sagaiya and Mora-Paez (2020)). Here, we extend the existing coupling models from Nocquet et al. (2014) and Chlieh et al. (2014) up to latitude 4°N in Central Colombia (Figure 4.6). Both approaches use a back-slip approach (Savage (1983)) and invert the interseismic velocity field

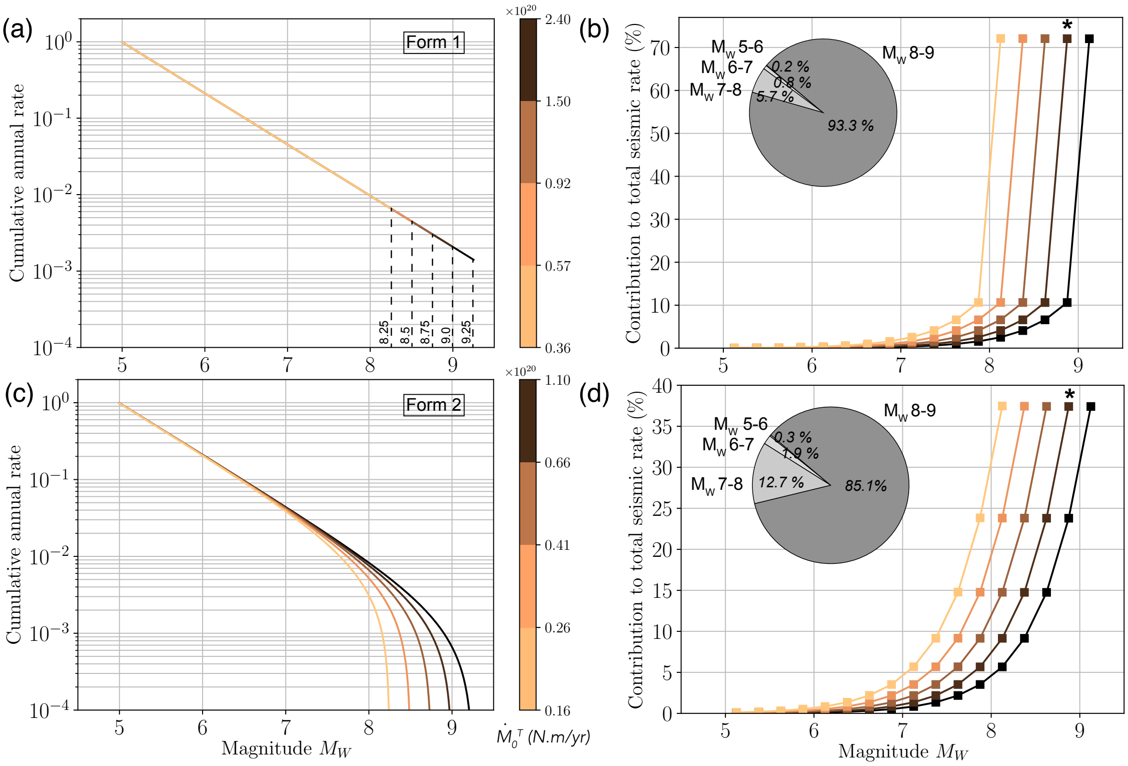

Figure 4.5: Implication of a Gutenberg-Richter earthquake recurrence model in terms of seismic moment rate, exercise with a model based on the a- and b-values calculated for the Esmeraldas source zone (a=3.35, b=0.67). a) and c) Impact of M_{max} on the total seismic moment rate (colorbar) with M_{max} arbitrarily varying from 8.25 to 9.25 with a 0.25 step. b) and d) Contribution of each magnitude bin to the total seismic moment rate, in percentage. The pie charts display the contribution per one-degree magnitude interval for the recurrence model with M_{max} 9.0 (indicated with a star). The total seismic moment rate is calculated with Form 1 according to: $\dot{M}_0^T = \frac{c}{c-b}10^{a+d+(c-b)M_{max}}$, and with Form 2 according to: $\dot{M}_0^T = \frac{b}{c-b}10^{a+d+(c-b)M_{max}}$. Contribution of each magnitude bin to the total seismic moment rate calculated according to: $\frac{1}{\dot{M}_0^T}\int_m^{m+0.25}\lambda(m)10^{cm+d}\mathrm{d}m$, with $\lambda(m)$ the annual seismic rate, c=1.5 and d=9.1 the coefficient to estimate seismic moment from the moment magnitude (cf. Appendix 4.9.2, *M_{max} ensuring a moment-balanced earthquake recurrence model*).

in a North Andean Sliver (NAS) reference frame. The uncertainties of their models are principally due to the limited spatial resolution of GPS data at less than 50 km of the trench axis (corresponding to the very 0 - 20 km shallowest portion of the megathrust interface).

Nocquet et al. (2014) discretized the subduction interface fault into 1,024 quasi-equilateral triangles each having an average edge length of 30 km, following the Slab 1.0 (Hayes et al. (2012)) geometry subduction interface. The inversion follows a linear Bayesian formulation (Tarantola (2005)) modified to account for Non-Negative constraints (Nocquet (2018)). This technique enables to explore the range of possible models, by varying the a priori model (from null to fully-coupled plate interface) as well as the damping and the smoothing parameters (through a model covariance matrix). From the range of acceptable interseismic models obtained (wrms $\leq$ 1.1 mm/yr), we select three models representatives of the uncertainties (Figures 4.6a-c): a minimum, best-estimate and maximum model.

Chlieh et al. (2014) applied a non-linear inversion of the GPS data based on a stochastic simulated annealing algorithm (Chlieh et al. (2011)). They divided the megathrust interface into 20 km diameter point source elements following the slab geometry. Local geologic and seismic data are used to establish the slab (Font et al. (2013); Gailler et al. (2007); Graindorge (2004); Hayes et al. (2012)). They used the local average slip vector direction from the gCMT catalog and the relative Nazca/NAS long-term plate rate to constrain the back-slip direction to ± 10° with respect to the Nazca/NAS predicted value. The acceptable range of models have a smoothing factor between 0.1 and 1.0 and a wrms $\leq$ 1.1 mm/yr. From these ranges of interseismic models, we select three models representatives of the uncertainties (Figures 4.6d-f): a minimum, best-estimate and maximum model.

The comparison of the models obtained by Nocquet et al. (2014) and Chlieh et al. (2014) indicates some differences in the spatial distribution of the highly-coupled areas over the megathrust interface but the range of moment deficit rate estimated is quite similar in both approaches. All models show that the coupling is principally restricted above the 40 km depth of the slab interface with a highly heterogeneous coupling distribution along the Esmeraldas segment, and a ~200 km long locked area at the center of the zone (at latitude of 2°N), connecting to smaller locked patches to the north and to the south. Three major asperities are distinguishable in rougher models. The rupture areas of the megathrust events, 1906 (M_S ~8.6, Ye et al. (2016)), 1942 ($M_{W(ISC-GEM)}$ 7.8), 1958 ($M_{W(ISC-GEM)}$ 7.6), 1979 ($M_{W(gCMT)}$ 8.1) and 2016 ($M_{W(gCMT)}$ 7.8), correlate well with regions of high interseismic coupling (Figure 4.1). The interseismic coupling for the whole Esmeraldas source zone is around 40-42%, if taken as an average from the trench down to 50 km depth. For the hazard study we keep three values to represent the uncertainty on the coupling: the minimum value of all models, the average of the best-estimate models, and the maximum value of all models. The rate of moment deficit derived from interseismic geodetic measurements and accumulating on the plate interface can be written as:

$$\dot{M}_{0G} = \int_{megathrust} \mu S \chi_i \mathrm{d}s \tag{4.5}$$

where μ is the shear modulus, S the long-term relative plate convergence rate and χ_i the interseismic coupling. The interseismic coupling χ_i is the ratio of the deficit of slip rate in the interseismic period to the long-term slip rate. It quantifies the degree of locking of the slab; $\chi_i = 1$ corresponds to a locked patch, $\chi_i = 0$ to a patch fully creeping at the plate convergence rate. The moment deficit rate obtained is in N.m/yr. The relative Nazca-North Andean Sliver convergent rate S along the

Esmeraldas subduction interface is around 47 mm.yr^{-1} (Nocquet et al. (2014).

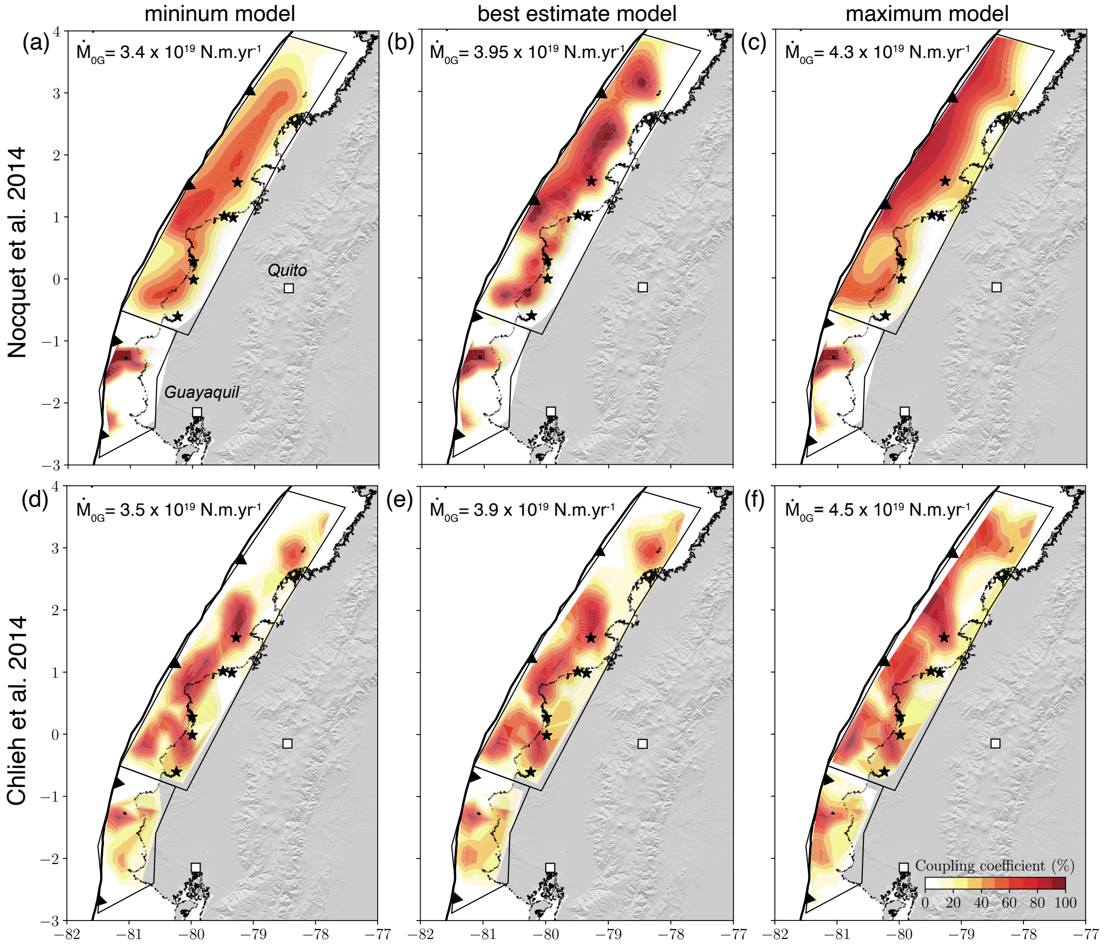

Figure 4.6: Interseismic coupling (ISC) maps. ISC quantifies the degree of locking of the subduction interface zone. (a) to (c) ISC models from Nocquet et al. (2014) (minimum, best-estimate and maximum ISC models), (d) to (f) ISC models from Chlieh et al. (2014) (minimum, best-estimate and maximum ISC models). A coupling coefficient (χ_i) equal to 100% corresponds to a fully locked fault patch, whereas a coupling coefficient equal to 0% corresponds to a patch creeping at the long-term slip rate. χ_i is defined as the ratio between the slip deficit and the long-term slip rate. Black stars: epicenters of megathrust events $M_W > 7.0$ in the ISC-GEM catalog (Di Giacomo et al. (2015)). The value of moment deficit rate (top left) is calculated over the Esmeraldas interface with μ= 30 GPa.

4.3 Combining seismic and geodetic information: moment-balanced earthquake recurrence models

4.3.1 Moment conservation principle

The general idea of moment conservation was introduced more than 40 years ago (Brune (1968); Anderson (1979); Molnar (1979)). Anderson (1979) suggested to use geological slip rates on faults to estimate seismic moment release and derive earthquake recurrence models. Anderson and Luco (1983) discussed how the slip rate constraints can be used either to estimate M_{max} from the occurrence rates of small magnitude earthquakes; or to estimate occurrence rates when M_{max} is already known e.g. from scaling relationships. In a paper focused on Southern California, Ward (1994) showed how seismological, geodetic and geological data can be combined to establish a recurrence model that forecasts earthquake frequencies for seismic hazard assessment. For the same region, Field et al. (1999) developed earthquake recurrence models matching the observed rates and consistent with the conservation of seismic moment rate. They demonstrated that some parameters such as the b-value, the choice of the magnitude-frequency distribution, or the exact moment-magnitude definition used, can have a non-negligible impact on the seismic rates and maximum magnitude. More recently, Kagan and Jackson (2013) and Rong et al. (2014)) applied the moment conservation principle in subduction zones to estimate maximum magnitudes, again by matching the geodetic deformation rate to that predicted by earthquakes with a magnitude-frequency distribution. Finally, in a review paper analyzing the partitioning between seismic and aseismic fault slip in areas where interseismic coupling maps are available, Avouac (2015) revisited this concept discussing the maximum magnitude earthquake required for the closure of the slip budget over the long-term.

In these publications, the Gutenberg-Richter model used varies, and usually only one model is employed. A large part of the literature uses Form 2 in Anderson and Luco (1983) (e.g. Ward (1994); Field et al. (1999); Hyndman et al. (2003); Mazzotti et al. (2011)). Some authors use Form 1 (e.g. Avouac (2015); Stevens et al. (2018); Michel et al. (2018)); while others (e.g. Kagan and Jackson (2013); Rong et al. (2014)) employ the "tapered Gutenberg-Richter distribution" introduced by Kagan (2002), a model that we do not consider here. We found only one study by Pancha (2006) that tested several forms for extrapolating the recurrence model up to M_{max}.

4.3.2 Determining M_{max} so that the recurrence model is moment-balanced

For subduction megathrust earthquakes in Ecuador and southern Colombia, we propose to derive recurrence models by anchoring the recurrence curve to the observed seismic rates in the moderate magnitude range (up to $M_W \sim 7.0$), then extrapolating this model to the upper magnitude range, and bounding the model with an M_{max} value ensuring that it is moment-balanced. Moment-balanced means that the rate of seismic moment accumulation estimated from e.g. geodesy is accommodated by the Gutenberg-Richter model (e.g. Petersen et al. (2008)). Our strategy is to obtain a distribution for potential M_{max} values, accounting for uncertainties on the observed seismic rates and on the form of the curve close to M_{max}, as well as on the estimation of the seismic moment budget. By anchoring the model to seismic rates estimated over the last 117 years, we assume that the Gutenberg-Richter model is stable in time, and that past seismicity is representative of future seismicity in this magnitude range.

From the moment deficit rate accumulating in the interseismic period, and assuming that a fraction of it is released through aseismic transient slip, the moment rate released in earthquakes can be estimated (Avouac (2015)). In this region, the interseismic strain models are inferred from GPS measurements mostly collected over the last 20 years. We need to assume that the loading rate estimated over that period is representative of the long-term interseismic rate.

In the long-term, the moment deficit rate $\dot{M}_{0G}$ (eq. (4.5)) is on average equal to the moment rate released by earthquakes and aseismic transients (i.e. afterslip following large earthquakes and episodic slow slip events). Following Avouac (2015), let α be the fraction of slip deficit that will be released in earthquakes. The earthquake recurrence model is moment-balanced if its corresponding cumulative annual seismic moment rate equals the fraction of moment deficit that is released seismically $\alpha\dot{M}_{0G}$. The equation to solve, in the case of Form 2 (eq. (4.2)) is:

$$\int_{-\infty}^{M_{max}} 10^{cm+d} \times bln(10) \times 10^{a-bm}\mathrm{d}m = \alpha\dot{M}_{0G} \tag{4.6}$$

with parameters c and d from the moment-magnitude definition (eq. (4.13) and Appendix 4.9.2, *M_{max} ensuring a moment-balanced earthquake recurrence model*), and Gutenberg-Richter a and b determined from observed rates on the moderate magnitude range (Section 4.2.2, *Modelling seismic and geodetic data*). Hence, the maximum magnitude bounding the recurrence model can be determined as follows (see Appendix 4.9.2, *M_{max} ensuring a moment-balanced earthquake recurrence model*):

$$M_{max} = \frac{1}{c-b}\left(\log_{10}(\alpha\dot{M}_{0G}) - \log_{10}\left(\frac{c}{c-b}\right) - a - d\right) \tag{4.7}$$

$$M_{max} = \frac{1}{c-b}\left(\log_{10}(\alpha\dot{M}_{0G}) - \log_{10}\left(\frac{b}{c-b}\right) - a - d\right) \tag{4.8}$$

$$M_{max} = \frac{1}{c-b}\left(\log_{10}(\alpha\dot{M}_{0G}) - \log_{10}\left(\frac{b^2}{c(c-b)}\right) - a - d\right) \tag{4.9}$$

Figure 4.7a displays different recurrence models having the same recurrence parameters a and b, and the same moment deficit rate $\dot{M}_{0G}$, considering Form 2. We show how varying the value of α impacts the maximum magnitude, meaning that the knowledge of aseismic slip is fundamental to assess seismic hazard. Considering that all the deformation measured is released in earthquakes (i.e. α=1) leads to a maximum magnitude of 8.7. Considering that only 50% of the deformation is released in earthquakes (i.e. α=0.5) leads to a model bounded at magnitude 8.4, a value lower than the great 1906 event, suggesting that $\alpha > 0.5$. The assumption on α impacts the recurrence model obtained. The uncertainty on the recurrence parameters a and b may also impact the recurrence model (Figure 4.4c). Keeping the moment deficit rate $\dot{M}_{0G}$ and α fixed, considering slightly lower a- and b-values, the M_{max} value decreases (Figure 4.7b); whereas slightly larger a- and b-values require a larger M_{max} value.

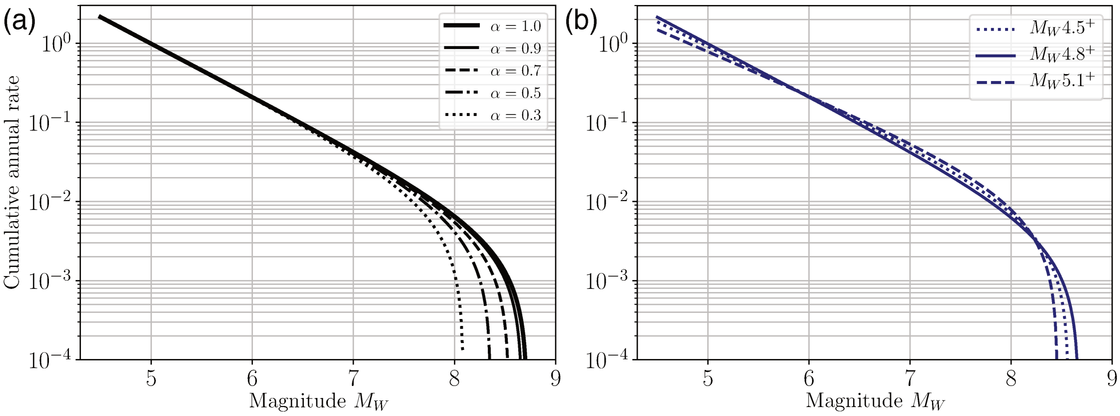

Figure 4.7: Moment-balanced earthquake recurrence models for Esmeraldas source zone, exercise to illustrate the influence of input parameters uncertainties. All models correspond to a constant moment deficit rate ($\dot{M}_{0G}$=3.92e+19 N.m/yr). (a) Recurrence parameters are fixed (a=3.35, b=0.67), the smaller the α value, the lower the resulting maximum magnitude M_{max}. (b) α is fixed to 0.9; three alternative a and b pairs are tested (see Figure 4.4c); the larger the a- and b-values, the larger the resulting maximum magnitude.

4.4 Moment-balanced recurrence models for Esmeraldas interface and associated hazard levels

4.4.1 A set of moment-balanced recurrence models accounting for uncertainties

We apply the methodology to the Esmeraldas interface source zone, modeled as a single plane dipping with 20° between the trench and 50 km depth. We use the same interface segmentation as in Beauval et al. (2018). The Esmeraldas segment corresponds approximately to the rupture area of the 1906 earthquake ($M_S \sim 8.6$, Ye et al. (2016)). The southern limit has been defined as the southern end of the 2016 M_W 7.8 rupture area and overlaps with the 1942 M_W 7.8 rupture limit (Ye et al. (2016)). The northern boundary was set at ~4°N at a kink in the Colombian trench azimuth, passing from a NW-SE trend to the south to ~N-S to the north; it also corresponds to a difference in sea floor ages. The reader is referred to Yepes et al. (2016) and Beauval et al. (2018) for detailed explanations on the segment limits.

The candidate recurrence models are anchored to the instrumental seismic rates, and their M_{max} values are calculated so that the models are moment-balanced with the moment deficit rate inferred from geodesy. We account for uncertainties on the observed seismic rates, on the moment deficit rates and on the fraction of slip deficit that is seismic. The logic tree (Figure 4.8) includes:

- three pairs of a and b recurrence parameters (Section 4.2.2, *Modelling earthquake recurrence*),
- three different forms to extrapolate the recurrence models up to M_{max} (Section 4.2.2, *Modelling earthquake recurrence*),
- three moment deficit rate estimates based on the interseismic coupling models available (Section 4.2.4, *Interseismic models available for the Ecuadorian subduction interface*), the best-estimate value is attributed a larger weight (50%) than the minimum and maximum values (25% each),
- three values for the average rigidity modulus used to determine the moment deficit rate: 30, 40 and 50 GPa (e.g. Bilek and Lay (1999); Scala et al. (2020)).
- For α, the fraction of the slip deficit that is released seismically, we include four alternative values (0.3, 0.5, 0.7 and 0.9). This large range of values reflect the important uncertainty on this parameter for the Esmeraldas zone, and is made to encompass different possible behaviors. Recurrent Slow Slip Events (SSE) have been commonly observed or inferred north of the 2016 Pedernales M_W 7.8 earthquake rupture area (Mothes et al. (2013); Vaca et al. (2018)). However, the lack of SSE moment estimates for events prior to 2013 prevents any moment budget to be determined. For the Pedernales area, Rolandone et al. (2018) show that early afterslip released as much as 30% of the co-seismic moment during one month following the earthquake, suggesting that α could be lower than 0.7.

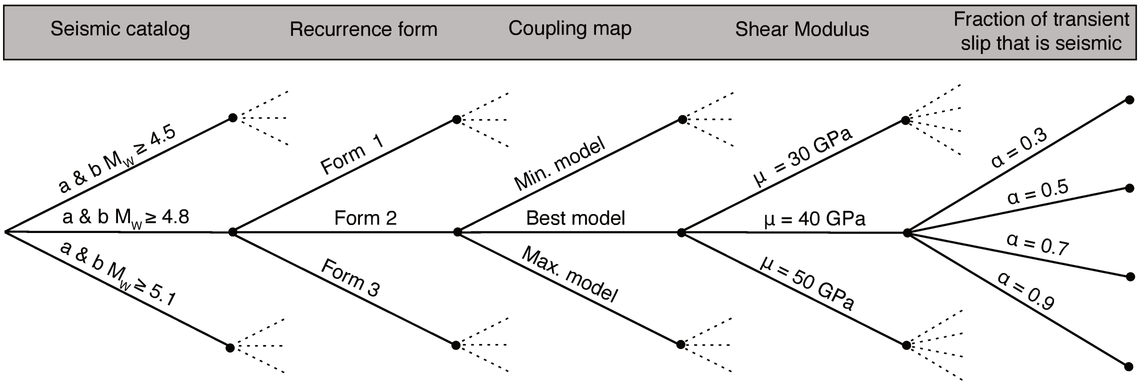

Figure 4.8: Logic tree explored to propagate uncertainties on the input parameters up to the final earthquake recurrence model for Esmeraldas interface source zone ($3 \times 3 \times 3 \times 3 \times 4 = 324$ combinations)). The alternative branches are equally weighted, except for the interseismic coupling (best model is weighted 50%, minimum and maximum models are weighted 25% each).

The exploration of the logic tree results in 324 different parameter combinations, that lead to 324 alternative maximum magnitudes. The distribution of maximum magnitudes obtained follow roughly a Gaussian distribution centered on $M_{max} \sim 8.4$ (Figure 4.9a). By sorting the M_{max} values according to the recurrence model form used, we show that the uncertainty on the choice of the form controls the overall uncertainty (Figure 4.9b). Form 1 leads to M_{max} values lower than Form 2, and Form 2 leads to M_{max} values lower than Form 3. This can be easily understood from Figure 4.10; for a fixed moment budget, Form 1 predicts larger rates for magnitudes $M_W >$ 7.5 than Form 2, and Form 2 larger rates than Form 3. Moreover, the distribution is also sorted successively according to the minimum magnitude used in the recurrence modeling (a and b pair), the interseismic coupling estimate, the rigidity modulus value, and the α value (Figure 4.11, following Beauval et al. (2020)). The parameters that influence the most the variability on M_{max} are the form of the recurrence model and α, the fraction of the slip deficit that is released seismically.

The limits of this interface source zone correspond approximately to the rupture area of the 1906 M_S 8.6 megathrust earthquake (Yepes et al. (2016)). Following the analysis of Ye et al. (2016), we adopted the Gutenberg and Richter (1954) M_S magnitude 8.6 for the 1906 earthquake and assumed $M_W = M_S$. The magnitude of this megathrust earthquake is a minimum bound for M_{max} in the source zone. All models with M_{max} values lower than 8.6 are not realistic and should be discarded. Form 1 is thus eliminated (Figures 4.9 and 4.11). Besides, to determine an upper bound for M_{max}, we apply the Strasser et al. (2010) scaling relationships adapted for interface earthquakes. The equations relying on the length (∼580 km), the width (∼130 km) and the area lead to magnitude values of respectively 9.0, 8.6 and 8.8, considering the mean plus one standard deviation. Therefore, we set the maximum value for an earthquake on the Esmeraldas interface to 9.0. Finally, 89 models out of the 324 obtained have a maximum magnitude within the range 8.6 to 9.0 (34

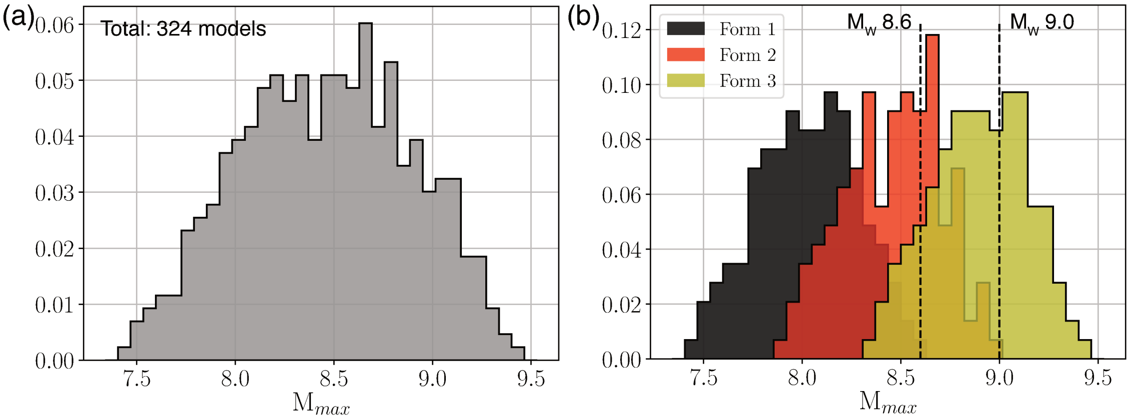

Figure 4.9: Distribution for the maximum magnitude M_{max} bounding the moment-balanced recurrence models for the Esmeraldas interface source zone. (a) Full distribution that accounts for the uncertainties considered in the logic tree (324 values, Figure 4.8). (b) The M_{max} values are sorted depending on the recurrence model form (Form 1 in black, Form 2 in red, Form 3 in yellow; 108 models per form). We consider that realistic M_{max} values are within the interval 8.6-9.0: the maximum magnitude earthquake must be larger or equal to the 1906 earthquake ($M_W \sim 8.6$) and lower or equal to 9.0, the maximum magnitude inferred from the scaling relationships Strasser et al. (2010). See the text.

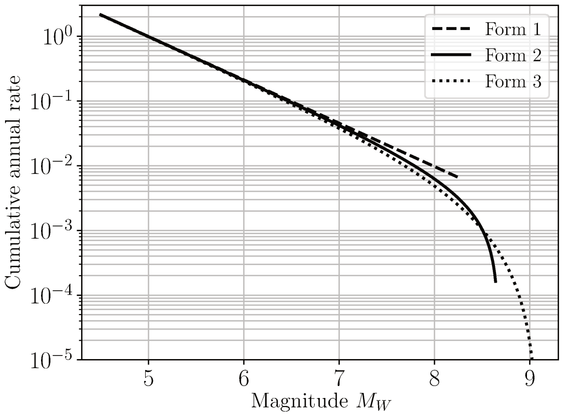

Figure 4.10: Moment-balanced earthquake recurrence models: strong impact on M_{max} of the form selected. The moment deficit rate is fixed ($\dot{M}_{0G}$=3.92e+19 N.m/yr) and α is assumed equal to 0.9. The a- and b-values are kept constant (a=3.35; b=0.67). The three alternative models correspond to the three alternative forms of Anderson and Luco (1983). Forms 1, 2 and 3 lead to respectively M_{max} values of 8.3, 8.7 and 9.1.

associated to Form 2, Figure 4.12a, and 55 to Form 3, Figure 4.12b). The α values associated to the selected models are also displayed (Figures 4.12c and 4.12d). As expected, because Form 2 predicts larger seismic rates in the upper magnitude range than Form 3, α values associated to Form 2 are larger than α values associated to Form 3. Considering Form 2, the α values required for the model to match past seismicity and to be consistent with the moment deficit rate are mostly in the range 0.7 to 0.9 (i.e. 70 to 90% of the interseismic deformation measured will be released

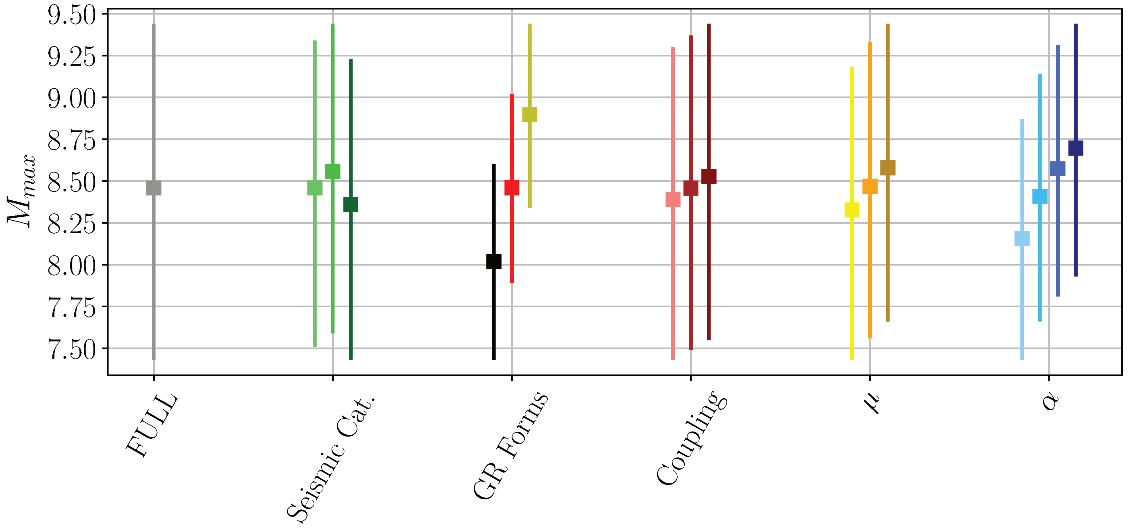

Figure 4.11: M_{max} values obtained for Esmeraldas interface, exploring the logic tree. Mean value (square), minimum and maximum values (vertical bar). 'FULL': full logic tree (324 branches). 'Seismic Cat.': choice of the minimum magnitude for modeling earthquake recurrence (from left to right): light green M_W 4.5+ (108 branches); green M_W 4.8+ (108 branches); dark green M_W 5.1+ (108 branches). 'GR Forms': choice of the form to extrapolate the Gutenberg-Richter model up to M_{max} (from left to right): Form 1 (black, 108 branches), Form 2 (red, 108 branches), Form 3 (yellow, 108 branches). 'Coupling': choice of the interseismic coupling estimates: minimum (108 branches), best model (108 branches), maximum (108 branches), from light pink to dark pink (from left to right). 'μ': choice of the shear modulus value (from left to right, 30 GPa in bright yellow, 40 GPa in orange, 50 GPa in brown, 108 branches each). 'α': choice of the α parameter (0.3, 0.5, 0.7, 0.9, from left to right, from light blue to dark blue, 81 branches each). We consider further that the magnitudes lower than 8.6 and larger than 9.0 are unrealistic.

in earthquakes); whereas considering Form 3, the barycenter of α values is around 0.5.

4.4.2 Seismic hazard assessment at Esmeraldas city

We estimate probabilistic seismic hazard at an example site, the Esmeraldas city, in northern Ecuador (latitude: 0.9869°N; longitude: -79.6513°W, Figure 4.1). The city hosts oil refineries important for the Ecuadorian economy. It is located at ∼24 km from the modeled interface (shortest distance between the city and the slab interface). For this site location on the coast, at 475 years return period, the seismic sources that control the hazard are subduction interface events (see Fig. 8 in Beauval et al. (2018)), therefore we do not include crustal or inslab sources. The set of moment-balanced magnitude-frequency distributions established for the Esmeraldas interface is combined with the Abrahamson et al. (2016)) ground-motion model to determine ground-motion exceedance rates. The Abrahamson et al. (2016) model has been developed from a global dataset that includes interface earthquakes with magnitudes 6.0 to 8.4 at distances up to 300 km. Hazard calculations are performed using a minimum magnitude M_W 4.5, a maximum source-site distance of 300 km,

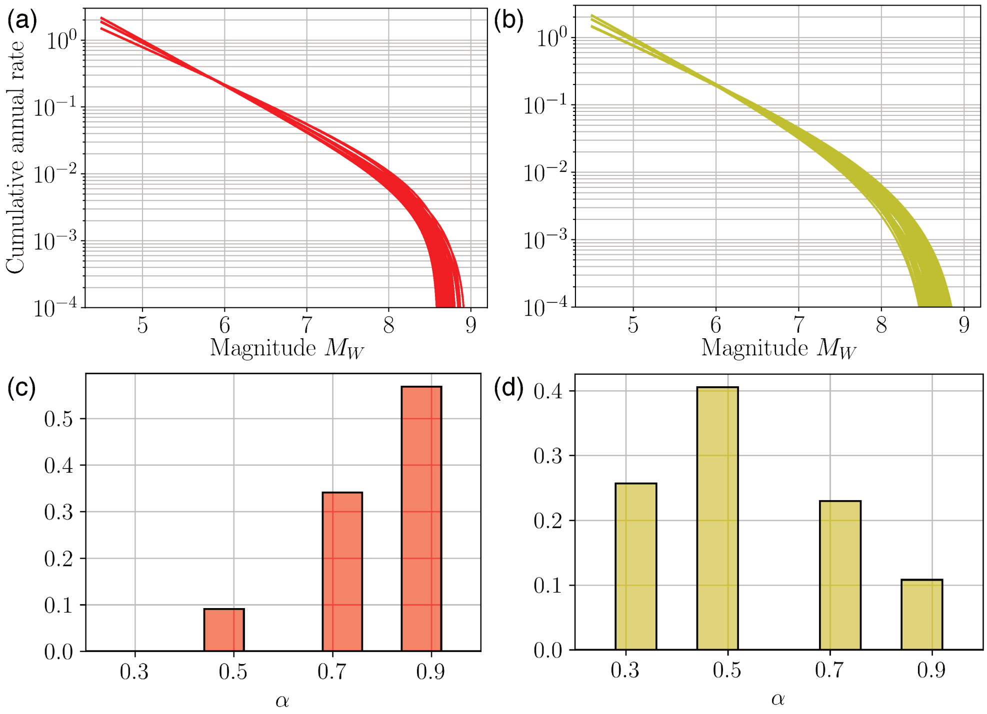

Figure 4.12: The set of moment-balanced earthquake recurrence models that passes the M_{max} criteria (i.e. with $8.6 \leq M_{max} \leq 9.0$) and associated α values. (a) 34 models Form 2 pass the M_{max} criteria; (b) 55 models Form 3 pass the M_{max} criteria; (c) distribution of α values associated with Form 2 models; (d) distribution of α values associated with Form 3 models.

and with the Gaussian distributions predicted by the ground-motion model truncated at $+4\sigma$.

The 89 magnitude-frequency distributions (Section 4.4.1, *A set of moment-balanced recurrence models accounting for uncertainties*) lead to 89 hazard curves for a given spectral period. Each hazard curve is interpolated to obtain the acceleration corresponding to an annual rate of 1/475. At last, a series of 89 Uniform Hazard Spectra (UHS) is obtained (Figure 4.13); each acceleration has a probability of 10% of being exceeded at least once in a 50 years' time window (equivalent to a mean return period of 475 years assuming Poisson occurrences). The hazard is calculated for a generic site on rock (V_{S30}=760 m/s) and a site on soil (V_{S30}=360 m/s) (Figure 4.13). On rock, mean values of 0.70 g and 1.54 g are obtained at the PGA and spectral period 0.2 s respectively. The variability of the hazard estimates, resulting from the exploration of uncertainties, is 0.60 - 0.82 g and 1.31 - 1.79 g at the PGA and 0.2 s respectively, considering the percentiles 16^{th} and 84^{th} percentiles (Figure 4.13). Abrahamson et al. (2016) model accounts for nonlinear site amplification; the accelerations obtained for a V_{S30}=360 m/s are lower than the accelerations on rock in the short period range, and larger in the intermediate and long period range. For comparison, the results obtained applying the Zhao (2006) ground-motion model, that does not account for non-linearity, are displayed in Figure 4.18).

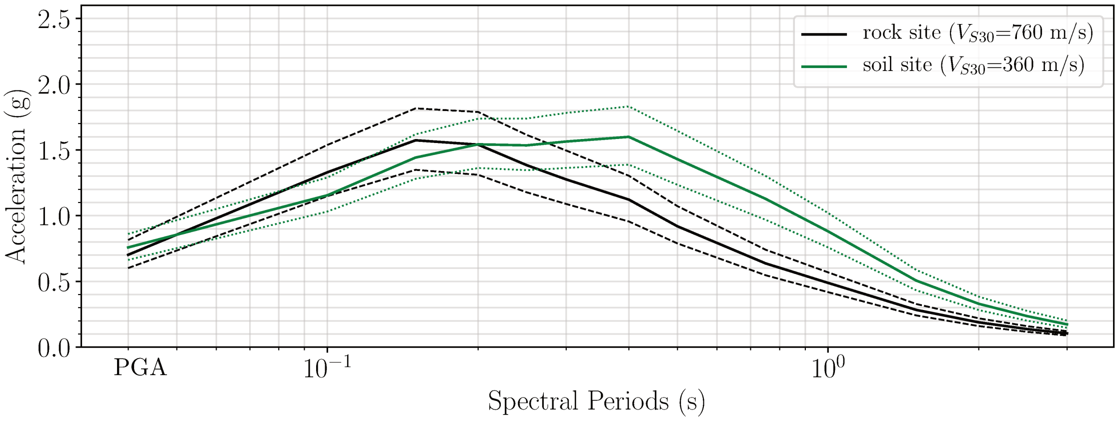

Figure 4.13: Distribution of Uniform Hazard Spectra at 475 years return period, for a site located in Esmeraldas city. Black: generic rock site (V_{S30}=760 m/s); green: soil site with V_{S30}=360 m/s. For each spectral period, the mean (solid line) and 16^{th} and 84^{th} percentiles (dashed lines) are estimated from 89 acceleration values, corresponding to the 89 alternative source models for the Esmeraldas interface fault plane. The ground-motion model used is Abrahamson et al. (2016).

To understand which magnitudes matter in terms of hazard for a site close to the interface (~24 km for Esmeraldas city), we perform a disaggregation in magnitude for the two alternative ground-motion models for the spectral period 0.2 s at 475 years return period (Figure 4.14). The results show that most contributions come from earthquakes with magnitudes larger than 7.0 - 7.5, i.e. the part of the recurrence model that bears the largest uncertainties.

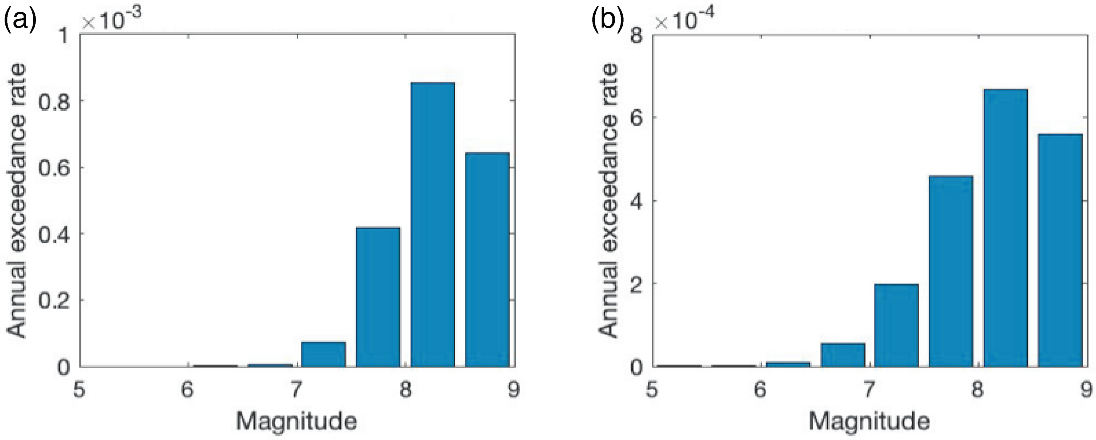

Figure 4.14: Disaggregation in magnitude, using either (a) the model Abrahamson et al. (2016) or (b) the model Zhao (2006) to predict the ground motions produced by earthquakes on the interface dipping segment. Earthquake frequencies are described by a Gutenberg-Richter model with parameters a=3.06, b=0.62 and M_{max}=9.0. The disaggregation is performed for a site in Esmeraldas city, considering the acceleration at 0.2 s spectral period with a return period of 475 years (1.88 g). This disaggregation results show that magnitudes lower than 7.0 have a negligible contribution to the hazard.

4.5 Comparisons with previous studies

4.5.1 Comparison with hazard estimates relying on catalog-based recurrence models

In the hazard model derived at the country scale published in Beauval et al. (2018), the recurrence models for the interface subduction sources relied only on earthquake catalogs. Gutenberg-Richter recurrence parameters were estimated from past seismicity over the moderate magnitude range, then extrapolated up to an M_{max} inferred from a scaling relationship applied to the maximum length of the segment, without additional constraints from geodesy. For Esmeraldas, a maximum magnitude of 8.8 was considered. In Figure 4.15, we superimpose the UHS distribution obtained within the present study to the UHS relying on the recurrence model assumed for Esmeraldas at that time (see Fig. 7b in Beauval et al. (2018), recurrence parameters from a global earthquake catalog, Form 2). The UHS based on the 2018 assumptions leads to hazard values that correspond to the 98^{th} percentile of the obtained distribution. Our search for recurrence models matching the seismic moment budget inferred from geodetic measurements leads to lower hazard values (0.6 - 0.8 g at the PGA, corresponding to the 16^{th} and 84^{th} percentiles, rather than 0.9 g).

To better understand these differences in hazard levels, we perform another calculation (Figure 4.15). A series of catalog-based recurrence models is generated, where the recurrence models are extrapolated to the maximum magnitude ignoring the constraints from geodesy. The models are obtained by exploring the uncertainty on the a- and b-values (3 couples, Figure 4.4c), on the Gutenberg-Richter forms (3 forms), and on the maximum magnitude (5 values, ranging from 8.6 to 9.0). These recurrence models are then combined with the Abrahamson et al. (2016) ground-motion model to evaluate uniform hazard spectra at 475 years return period. The amplitudes from these catalog-based recurrence models result much higher than the amplitudes relying on moment-balanced recurrence models (Figure 4.15, 1.0 g obtained for the percentile 84^{th}, rather than 0.8 g, at the PGA).

4.5.2 Comparison with hazard estimates from independent studies

To compare our results with independent studies, we looked for published PSHA studies delivering hazard estimates on the coast. Petersen et al. (2018a,b) evaluate seismic hazard at the scale of the South American continent. As the mean hazard maps presented are at a large scale, and values displayed in 0.2 g bin, we can only infer an approximate acceleration interval of 0.7 - 0.8 g for the PGA at 475 years for Esmeraldas city (V_{S30}=760 m/s). This interval falls within our estimation. The subduction interface is modeled as fault segments dipping with 45°; the segmentation considered is less detailed than in the present work. They use two alternative recurrence models for interface events with $M_W \geq 7.5$, a Gutenberg-Richter distri-

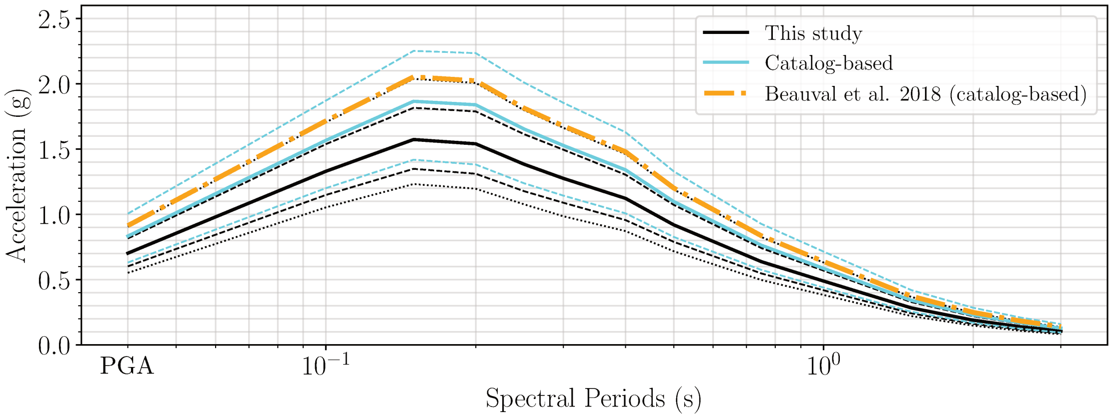

Figure 4.15: UHS at Esmeraldas city, at 475 years return period. Black: UHS distribution obtained from this study, solid line: mean values, dashed lines: 16^{th} and 84^{th} percentiles, dotted lines: 2^{nd} and 98^{th} percentiles. Orange curve: UHS based on the earthquake recurrence model from Beauval et al. (2018) (a=2.78, b=0.57, M_{max}=8.8; global catalog branch). Blue curves: UHS distribution based on catalog-based recurrence models, the recurrence models are extrapolated up to the maximum magnitude ignoring the constraints from geodesy; the logic tree includes the uncertainty on the a- and b-values (3 couples, Figure 4.4c), on the Gutenberg-Richter form (3 alternatives) and on the maximum magnitude (5 M_{max} values from 8.6 to 9.0), in total 45 end branches. The ground-motion model Abrahamson et al. (2016) is used in these calculations.

bution based on past seismicity with the maximum observed earthquake, and a simple characteristic model represented by one megathrust earthquake every 400 years (they consider this recurrence time as a first-order approximation for the convergence rate). Lower magnitude events are accounted for through a gridded-seismicity model. As we were interested in the exact hazard curves they obtain at Esmeraldas city, we retrieved all information available online that describes the source model (interface, inslab and crustal sources) and the ground-motion logic tree (Petersen et al. (2018b), Section 4.7, *Data and Resources*). We converted this information into OpenQuake format and run the hazard calculation. The results in Esmeraldas city resulted lower (0.5 g at the PGA) than what the map tells us. Unfortunately, we could not identify the reason. More work would be required to ensure that our translation into OpenQuake input files is in line with the Petersen et al. (2018b) model definition.

In another paper focused on subduction sources, Pagani et al. (2020b) propose a new shape for the magnitude-frequency distribution characterizing earthquake occurrences on interface segments. This distribution is comparable to the Youngs and Coppersmith (1985) characteristic model, with the rates in the upper magnitude range larger than predicted by the moderate magnitude range. The upper magnitude range has a characteristic behavior, the seismic rates being constrained by the convergence rate and the coupling of the interface. They apply this model to the South American subduction zone. However we cannot compare their seismic rates with our recurrence models, as they use longer interface segments. There are important differences with respect to the present work: 1) they consider the convergence rate of the Nazca plate with respect to South America (58 mm/yr), rather than the motion of the Nazca Plate with respect to the North Andean Sliver (47 mm/yr, Nocquet et al. (2016)); 2) they use an average interseismic coupling coefficient of 0.55 and a shear modulus of 32 GPa, taken from Scholz and Campos (2012); and 3) they do not account for transient aseismic deformation. This model has been implemented within the GEM Mosaic (Pagani et al. (2020a)). The uniform hazard spectrum obtained combining this source model with the Abrahamson et al. (2016) ground-motion model is superimposed to our estimations in Figure 4.16. The hazard levels obtained result comparable to our 2018 catalog-based estimate (global catalog branches, Beauval et al. (2018)).

The interface subduction model from Pagani et al. (2020b,a) is moment-balanced, but it ignores transient aseismic deformation. We perform a last calculation, applying the methodology developed in Section 4.4.1, *A set of moment-balanced recurrence models accounting for uncertainties*, exploring the logic tree detailed in Figure 4.8, but this time ignoring potential aseismic deformation and assuming $\alpha = 1$. A series of recurrence models is selected, under the condition that the maximum magnitude obtained is within the range 8.6-9.0. As expected, ignoring aseismic deformation leads to higher hazard levels (Figure 4.16).

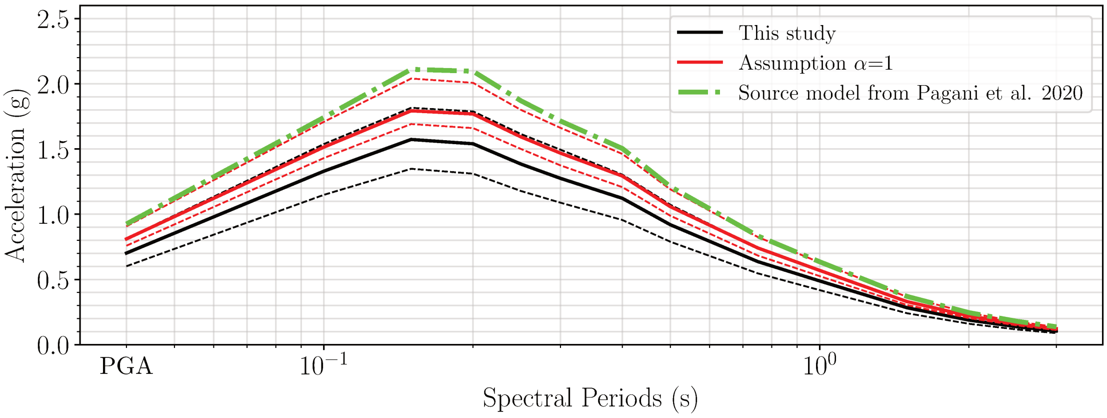

Figure 4.16: UHS at Esmeraldas city, at 475 years return period. Black: UHS distribution obtained from this study, solid line: mean values, dashed lines: 16^{th} and 84^{th} percentiles. Green curve: UHS based on the source model from Pagani et al. (2020a). Red curves: Comparison with the UHS distribution obtained applying the exact same methodology presented in this article (Section 4.4.1, *A set of moment-balanced recurrence models accounting for uncertainties* and the logic tree Figure 4.8), but considering $\alpha = 1.0$. Calculations performed with the ground-motion model Abrahamson et al. (2016).

4.6 Conclusions

We propose a method for combining seismic and geodetic data to constrain the recurrence models of earthquakes on the megathrust interface of Ecuador and Colombia. We focus on the Esmeraldas ~600 km-long segment, the approximate rupture segment of the 1906 M_W 8.6 earthquake. Available interseismic coupling models for Ecuador (Nocquet et al. (2014); Chlieh et al. (2014)) have been extended to Colombia up to latitude 4°N to determine the moment deficit rate that accumulates on the slab interface. We select the coastal city Esmeraldas, as an example site located above the dipping segment where probabilistic seismic hazard is estimated.

In the Esmeraldas source zone, the observed instrumental rates show an exponential decrease with increasing magnitude over the magnitude range 4.5-7. Our strategy relies on anchoring a Gutenberg-Richter model to these moderate magnitude rates and extrapolate the model up to the maximum magnitude. We look for moment-balanced recurrence models, i.e. models that fit the seismic moment estimated from geodesy, by adjusting the maximum magnitude bounding the Gutenberg-Richter model.

We set up a logic tree to account for the uncertainties characterizing the recurrence model (a- and b-values, extrapolation to M_{max}), as well as uncertainties underlying the estimation of the tectonic deformation to be released in earthquakes (coupling model; shear modulus, seismic versus aseismic slip). We show that the uncertainties influencing the most the recurrence model are:

- the fraction of the slip deficit that will be released in earthquakes (α value),
- the form of the Gutenberg-Richter model close to M_{max}.

We keep only the models associated with a realistic M_{max}, i.e. within the largest observed event in the zone and an upper bound inferred from a scaling law. Lastly, we obtain a distribution of uniform hazard spectra at Esmeraldas city by combining this subset of recurrence models with the Abrahamson et al. (2016) ground-motion model. We show that the moment-balanced models obtained lead on average to lower hazard values than the earthquake recurrence models relying only on seismicity data.

The use of geodetic data to constrain a long-term earthquake recurrence mode for PSHA implies strong assumptions, in particular that the deformation measured over a short time windows is steady and representative of long-term processes. However, given the uncertainty to forecast rates in the upper magnitude range ($M_W \geq 7.0$), the geodetic deformation measurements provide key constraints on this part of the recurrence model that controls the hazard at coastal sites.

Considering the recent availability of massive quantity of geodetic data, this new approach could be applied in other regions of the world to develop earthquake recurrence models consistent with geodetic measurements of tectonic deformation.

4.7 Data and Resources

The global Centroid Moment Tensor (gCMT) database was last accessed in April 10, 2020 at `https://www.ldeo.columbia.edu/~gcmt/projects/CMT/catalog/jan76_dec17.ndk`. The ISC-GEM Global Instrumental Earthquake Catalog (1904-2016) v.7.0 was last accessed in April 10, 2020 at http://www.isc.ac.uk/iscgem/download.php. The Bulletin of the International Seismological Centre was last accessed in April 10, 2020 at `http://www.isc.ac.uk/iscbulletin/search/bulletin/` (corresponding to a reviewed period until September 2017). The source model and the ground motion logic tree from Petersen et al. 2018b are accessible at `https://www.sciencebase.gov/catalog/item/58795a8ce4b04df303d97ed8`. The source model from Pagani et al. 2020b is accessible at `https://hazard.openquake.org/gem/`.

4.8 Acknowledgements

This research was supported by the French Agence Nationale de la Recherche (ANR) through the project REMAKE (2016–2019, Grant Number ANR-15-CE04-004), by the Institut de Recherche pour le Développement (IRD), the Geophysical Institute in Quito part of the Escuela Politecnica Nacional, as well as ISTerre and Géoazur laboratories. We thank the project SEMPLADES (Generación de capacidades para la difusión de alertas tempranas y para el desarrollo de instrumentos de decisión ante las amenazas sísmicas y volcánicas dirigidos al Sistema Nacional de Gestión de Riesgos). This work has been carried out in the frame of the Joint International Laboratory “Seismes & Volcans dans les Andes du Nord” (IRD LMI SVAN). The authors are grateful to the Global Earthquake Model Foundation and to the IT ISTerre team for constant support on the OpenQuake Engine software and server.

4.9 Appendices

4.9.1 An earthquake catalog for seismic hazard assessment in Ecuador

We develop an earthquake catalog for seismic hazard assessment in Ecuador, using global catalogs, following the approach described in Beauval et al. (2018). The spatial window extends from -82° to -74° in longitudes and from -7° to 4° in latitudes. The catalog extends from 1906 to September 2017.

We select solutions from several published catalogs: the ISC-GEM (1904-2016) v7.0, the global CMT catalog (1976-2017, Dziewonski et al. (1981); Ekström et al. (2012)) and the ISC event reviewed catalog (1906-2017, **?**Storchak et al. (2017)). Besides we have included the solutions from Vaca et al. (2019), moment magnitudes estimated for earthquakes between 2009 and 2015, in the spatial window from -6° to 2° in latitude and from -83° to -76° in longitude.

A "best" location and a "best" magnitude must be selected for each earthquake, among available solutions. The priority scheme is the following for selecting the magnitude: ISC-GEM $M_W >$ gCMT $M_W >$ Vaca et al. (2019) $M_W >$ ISC $m_b >$ NEIC m_b (or NEIS m_b, or USCGS m_b). Magnitudes ISC-GEM are always associated with the locations from the same catalog. Magnitudes from Vaca et al. (2019) are also associated with the locations from the same author. The ISC locations are used for the other events. In the early instrumental period (before 1964), there are nine events which appear in the ISC event catalog that are not included in the ISC-GEM. We keep them and make use of M_S newly determined by the ISC, as well as m_b magnitudes by ABE1 (Abe (1981)) and magnitudes estimated by Gutenberg and Richter (1954), 'PAS'.

We use the Lolli et al. (2014) global equation to convert m_b magnitudes into proxy M_W. Lolli et al. (2014) equation is preferred over the Di Giacomo et al. (2015) conversion equation (only valid for $M_W > 5.0$). The final catalog includes 3868 events above M_W 3.6 (Table 4.1). The bulk of the data is made of ISC m_b magnitudes (71%).

Lastly, we apply the Reasenberg (1985) algorithm to identify clustered events (foreshocks, aftershocks, swarms). Twenty-three percent of events are removed. The final declustered catalog includes 2978 earthquakes with $M_W \geq 3.6$.

Table 4.1: Content of the final earthquake catalog homogenized in moment magnitude. ISC-GEM, International Seismological Center - Global Earthquake Model; CMT, Centroid Moment Tensor; ISC-REV, the manually reviewed bulletin from the ISC; NEIC/NEIS, National Earthquake Information Center; USCGS, United States Coast and Geodetic Survey; ABE1,Abe (1981); PAS, Gutenberg and Richter (1954). Magnitude m_b converted in M_W applying $M_W = e^{0.741+0.210m_b} - 0.785$ (Lolli et al. (2014), global equation).

Catalog	**Author**	**Type Mag.**	**Min. Mag.**	**Max. Mag.**	**Min. Year**	**Max. Year**	**Total Events**
ISC-GEM	Various	M_W	5.1	8.75§	1906	2016	268
ISC-GEM	global CMT	M_W	5.0	8.1	1965	2016	191
ISC-GEM supp*	Various	M_W	5.6	6.5	1917	1966	5
global CMT	global CMT	M_W	4.8	6.0	1980	2017	100
ISC-REV	global CMT	M_W	4.7	5.6	1977	2017	62
ISC-REV	ISC	Proxy M_W from m_b	3.7	6.0	1964	2017	2757
ISC-REV	NEIC	Proxy M_W from m_b	3.7	5.6	1985	2017	217
ISC-REV	NEIS	Proxy M_W from m_b	3.8	6.2	1971	1984	153
ISC-REV	USCGS	Proxy M_W from m_b	3.8	4.8	1964	1970	32
ISC-REV	ABE1	m_b surrogate for M_W	6.9	7.5	1906	1937	3
ISC-REV	PAS	M_S surrogate for M_W	6.8	6.8	1925	1950	3
ISC-REV	PAS	M surrogate for M_W	6.5	6.6	1954	1958	3
Vaca et al. (2019) #	Vaca et al. (2019)	M_W	3.6	5.1	2009	2015	74

* ISC-GEM supplement: the supplementary catalog contains those earthquakes that are believed to be large enough yet either their location or magnitude or both are highly uncertain due to lack or contradiction in available arrival time or amplitude and period data (Di Giacomo et al. (2015)).
# Vaca et al. (2019) is the only regional catalog considered, earthquakes are located from -6° to 2° in latitude and from -83° to -76° in longitude.
§ 8.75 is the magnitude of the 1906/01/31 megathrust earthquake, we substitute this magnitude with 8.6 in our final catalog (M_S magnitude proxy for M_W, Gutenberg and Richter (1954), Ye et al. (2016)).

Table 4.2: Input parameters for the Reasenberg (1985) algorithm. τ_{min}/τ_{max}: look-ahead time window for building clusters. p_1: probability of detecting the next clustered event. x_k: coefficient for mainshock magnitude. x_{meff}: minimum magnitude cut-off for the catalog. r_{fact}: number of crack radii surrounding each earthquake within which to consider linking a new event into the cluster.

τ_{min} (in days)	10
τ_{max} (in days)	30
p_1	0.99
x_k	0.2
x_{meff}	4.5
r_{fact}	20
Uncertainty* – after 1970 - horizontal	5 km
Uncertainty* – after 1970 - vertical	10 km
Uncertainty* – before 1970 - horizontal	15 km
Uncertainty* – before 1970 - vertical	20 km

* on event location

Table 4.3: Time windows of completeness established for interface events in Ecuador, and number of events falling within the time windows of completeness for Esmeraldas source zone.

Magnitude Interval	**Time window of completeness**	**Number of events before declustering**	**Number of events after declustering**
[4.5-4.8[	1967-2017	89	33
[4.8-5.1[	1964-2017	90	41
[5.1-5.4[	1964-2017	30	13
[5.4-5.7[	1964-2017	24	14
[5.7-6.0[	1950-2017	11	5
[6.0-6.3[	1920-2017	18	7
[6.3-6.6[	1920-2017	8	7
[6.6-6.9[	1900-2017	10	6
[6.9-7.2[	1900-2017	3	3
[7.2-7.5[	1900-2017	0	0
[7.5-7.8[	1900-2017	2	2
[7.8-8.1[	1900-2017	2	2
[8.1-8.4[	1900-2017	0	0
[8.4-8.7[	1900-2017	1	1

4.9.2 M_{max} ensuring a moment-balanced earthquake recurrence model

We assume that the magnitude-frequency distribution follows the Anderson and Luco (1983) Form 2. N is the annual rate of events with magnitude larger or equal to m:

$$N(m) = 10^{a-bm} - 10^{a-bM_{max}} \quad \text{for } m \leq M_{max} \tag{4.10}$$

Its derivative provides the annual rate of events with magnitude equal to m:

$$n(m) = bln(10)10^{a-bm} \tag{4.11}$$

Hanks and Kanamori (1979) derived the relation:

$$\log_{10}(M_0) = 1.5M_W + 16.1 \quad \text{(dyn.cm)} \tag{4.12}$$

Equation (4.12) results in the following relation in N.m (1 dyn.cm = 10^{-7} N.m):

$$M_0(m) = 10^{cm+d} \tag{4.13}$$

where c=1.5 and d=9.1 for M_0 in units of N.m.

The total seismic moment rate corresponding to the magnitude-frequency distribution is:

$$\dot{M}_0^T(m) = \int_{-\infty}^{M_{max}} M_0(m)n(m)\mathrm{d}m \tag{4.14}$$

Integrating from $-\infty$ up to M_{max} or from M_W 4.5 up to M_{max} is equivalent, as the magnitudes lower than 4.5 have a negligible contribution to the total seismic moment rate (M_{max} ≥8.6).

$$\dot{M}_0^T(m) = 10^{a+d}bln(10)\int_{-\infty}^{M_{max}} 10^{(c-b)m}\mathrm{d}m \tag{4.15}$$

$$\dot{M}_0^T(m) = \frac{b}{c-b}10^{a+d+(c-b)M_{max}} \tag{4.16}$$

Therefore, if there is an independent estimate for the seismic moment rate, e.g. from geodesy, $\dot{M}_{0G}$, we can obtain the value of M_{max} from the recurrence parameters a, b and $\dot{M}_{0G}$:

$$M_{max} = \frac{1}{c-b}\left(\log_{10}(\dot{M}_{0G}) - \log_{10}\left(\frac{b}{c-b}\right) - a - d\right) \tag{4.17}$$

Note that some authors use d=9.0 or d=9.05, depending on how the coefficients are rounded in the equation relating moment and moment magnitude (see e.g. Pancha (2006)). Using d=9.0 rather than d=9.1 leads to a 20% decrease in the value of the moment rate, for a given magnitude.

4.9.3 Discrete non-cumulative rates for Gutenberg-Richter Forms 1, 2 and 3

The distributions of Figure 4.17 correspond to the discrete non-cumulative seismic rates of Forms 1, 2 and 3 in Anderson and Luco (1983). The recurrence parameters have been determined for the Esmeraldas source zone (a=3.35, b=0.67); an M_{max} of 8.6 is considered. These distributions are provided as input to the OpenQuake hazard Engine, to describe occurrence rates of earthquakes on the Esmeraldas dipping plane. The only difference between Form 1 and Form 2 lies in the last magnitude interval (see Fig. 1B and text page 474 in Anderson and Luco (1983)).

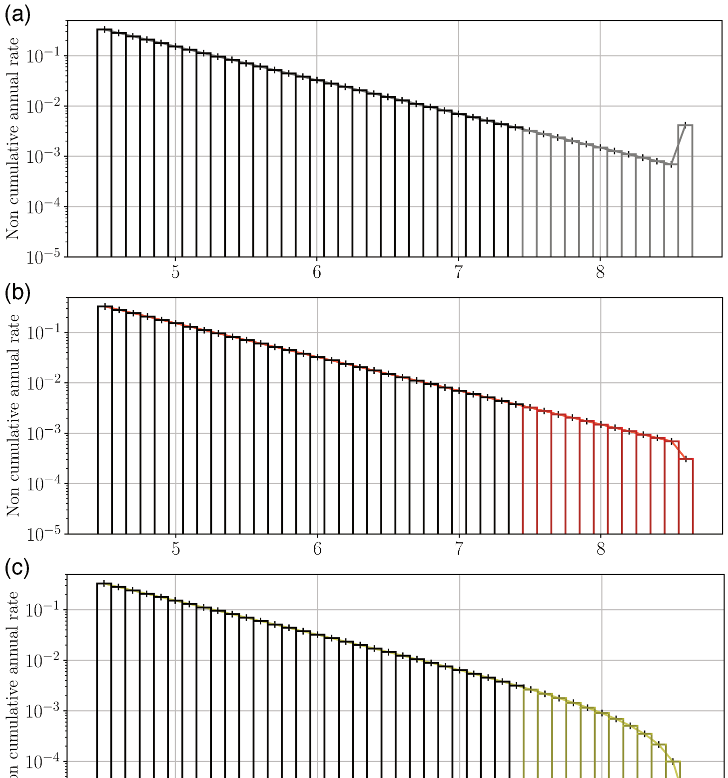

Figure 4.17: Discrete non-cumulative seismic rates considering Forms 1, 2 and 3 in Anderson and Luco (1983). The recurrence parameters correspond to the Esmeraldas source zone (a=3.35, b=0.67).

4.9.4 Distribution of the Uniform Hazard Spectra at 475 years return period, considering alternatively the Abrahamson et al. (2016) and Zhao (2006) models.

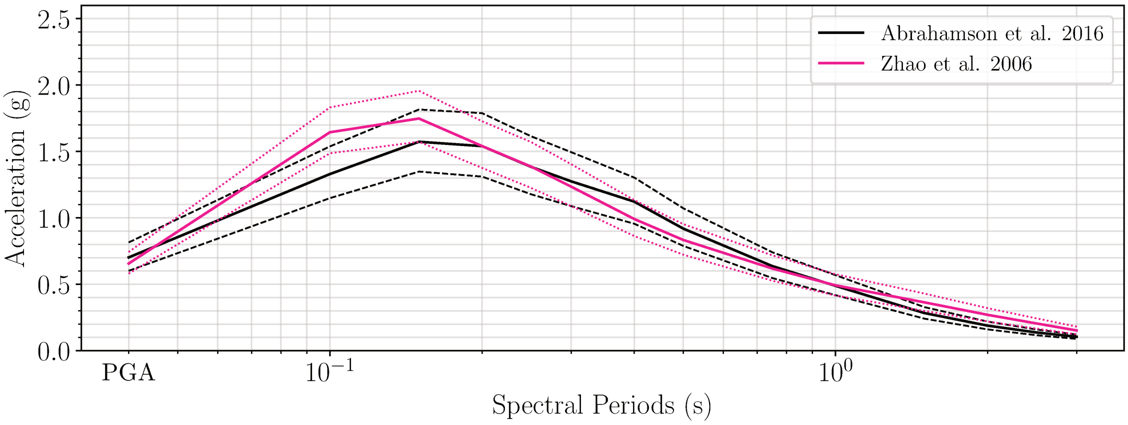

Figure 4.18: Distribution of Uniform Hazard Spectra at 475 years return period, for a generic site on rock (V_{S30}=760 m/s) located in Esmeraldas city. Black curves: calculation with Abrahamson et al. (2016) ground-motion model; magenta curves: with Zhao (2006) model. For each spectral period, the mean (solid line) and 16^{th} and 84^{th} percentiles (dashed lines) are estimated from 89 acceleration values, corresponding to the 89 alternative source models for the Esmeraldas interface fault plane.

General conclusions

The aim of this PhD thesis was to improve earthquake recurrence models by quantitatively including the information derived from geodetic measurements, with a special application to Ecuador. In this conclusion, I first summarize the main results obtained for every chapter. In a second step, I will discuss some of the issues raised by my studies and will propose some perspectives.

Conclusions on the work done

The second chapter presents a collaborative effort to produce probabilistic seismic hazard maps of Ecuador. The source model includes area source models, with magnitude-frequency distributions based on an earthquake catalog, and fault source with recurrence models based on geodetic and/or geologic slip rates. My main contribution to this work lies in 1) the development of the earthquake catalog, built from global datasets covering early instrumental and instrumental periods then homogenized in moment magnitude and declustered with the Reasenberg (1985) algorithm, in the 2) automatization of procedures for estimating earthquake recurrence parameters from the earthquake catalog for a set of source zones, and in 3) the building of the fault model through the derivation of slip rates estimates for a set of simplified faults using a GPS horizontal velocity field. These new hazard models show that Ecuador is characterized by a high hazard level, with PGA mean values at 475-years return period higher than 0.3 g almost everywhere except in some regions of the coastal plain and Amazonia, and reaching maximum values around 0.5 - 0.6 g on the coast and in the Cordillera. Our analysis shows that the uncertainty on the hazard estimate (percentiles 16^{th} and 84^{th}) varies largely along the northern coast and along some crustal faults in the Cordillera, including the Quito fault.

In the third chapter, we calculate the first interseismic coupling map of the Quito fault system using a combination of GPS data and PS-InSAR analysis. We show evidence for shallow aseismic slip on the central segment of the fault, with possibly larger slip deficit accumulation rate along the northern and southern sections. Additionally, we identify a transient deformation signal related to the development of a secondary fold, a few kilometers east of the main fault trace. Overall, our results demonstrate that strain accumulation is spatially heterogeneous and that aseismic processes dominate along the Quito fault system. In terms of seismic hazards for the Quito area, the interseismic coupling map translates into recurrence models that estimate a recurrence time between 200 and 1100 years for a magnitude M_W 6.5.

In the fourth chapter, we focus on the subduction zone in Ecuador to improve the earthquake recurrence models. We found that recurrence models matching both the past seismic rates and the seismic moment budget inferred from geodetic measurements leads to hazard values (0.6 - 0.8 g, PGA, 475-years return period) lower than hazard value obtained in Beauval et al. (2018) from a purely catalog-based recurrence model (0.9 g at the PGA, global catalog). Additionally, we show, using a disaggregation study that the magnitudes contributing the most in terms of hazards come from earthquakes with magnitudes larger than 7.0 - 7.5. Therefore, it is essential to consider the uncertainties related to the form of recurrence model close to the higher magnitudes. By considering geodetic moment conservation and having some knowledge on the possible range of M_{max}, we were able to identify the Forms 2 and 3 of the recurrence models (Anderson and Luco (1983)) as the most suitable for the Ecuadorian subduction zone, and to estimate a range for the aseismic component of deformation. The percentage of the deformation that will be released into earthquakes is on average 67%.

Perspectives

Overall the interseismic coupling models that we present on the Quito fault system would need to be improved on the northern and southern region of the fault where the inversion is not well-constrained due to a limited number of GPS stations and a poor InSAR coverage. As a consequence, the extension of the actual GPS network to the north and to the south would be one of the next steps to improve the model; as well as modeling the fault with a non-rectilinear geometry to reduce the poor constraints on the northern and southern edges of the fault. Additionally, the new era of satellite mission with highly frequent repeat cycle such as Sentinel-1, would be key in refining the spatial and temporal coverage of the InSAR time series. Similar studies have used those data to calculate interseismic coupling models in other regions of the world (Lasserre et al. (2019); Ji et al. (2020)). European initiatives have already started to evolve in this direction, proposing operational services that produce continuous ground deformations using these new sensors (Doin et al. (2011); Kalia et al. (2017); Raspini et al. (2018)). The use of similar methods applied to other regions in the world, along with their analysis and inversion, would be one of the first steps to extend the approach proposed in this study, to the rest of Ecuador. While our purely elastic model assumption is correct considering the elapsed time since the last larger earthquake, some studies have shown that viscoelastic relaxation plays a critical role for dip-slip faults (Segall (2010)). Hence, the implementation of such model could be important to refine our understanding of the 3-D fault slip rate deficit. Finally, the methodology develops in this chapter should be extended to other active crustal faults region in Ecuador, such as the strike-slip Chingual-Cosanga-Pallatanga-Puna Fault System (CCPP), where no interseismic coupling map has been produced yet.

Our new method that uses geodetic data helps to better constrain the seismic hazard assessment, but several points could be further developed in the future. We identify two sources of uncertainties that have a large impact on recurrence models and hazard levels: (1) the form of the recurrence models close to M_{max}, (2) the part of the deformation that is aseismic. Recurrence models in this study are limited to three forms. The implementation of a larger range of recurrence models such as a characteristic model (Schwartz and Coppersmith (1984)) or the tapered Gutenberg-Richter (Kagan (2002)), would enlarge the range of candidate models depending on the study region. A better estimation of earthquake recurrence times in the upper magnitude range would also help considerably in constraining the recurrence model close to M_{max}, hence future paleoseismic studies are essential to extend our knowledge on the earthquake potential of subduction interface zones. Second, the quantification of an accurate moment budget related to aseismic processes such as slow slip events and afterslip (Rolandone et al. (2018)), would be the key to better quantify the aseismic deformation (α parameter). Finally, we have shown how interseismic coupling map can help constrain earthquake recurrence models to be used in seismic hazard assessment. The availability of such maps depends on the instrumentation of the other active faults in the Ecuadorian Cordillera, as well as the use of the new era of satellite SAR data. The method developed in this thesis can be applied to the entire South American subduction zone, provided that detailed interseismic coupling maps are produced (e.g. Villegas-Lanza et al. (2016) in southern Ecuador and northern Peru).

Appendix

In this appendix, I attached the article I contributed as a second author, when I was an engineer at ISTerre for 8 months, before starting my thesis. This article focuses on ground motion models. We compare the observed ground-motion recordings of the megathrust earthquake of M_W 7.8 that occurred on April 16^{th} 2016 with preexisting four ground-motion prediction equations (GMPEs) developed for interface earthquakes, the global Abrahamson et al. (2016) model, the Japanese equations by Zhao (2006) and Ghofrani and Atkinson (2014), and one Chilean equation (Montalva et al. (2017)). We also compare the two largest aftershocks that occurred one month later, on May 18^{th}, of magnitude M_W 6.7 and M_W 6.9.

SRL Early Edition

Ⓔ

Comparison of Observed Ground-Motion Attenuation for the 16 April 2016 M_w 7.8 Ecuador Megathrust Earthquake and Its Two Largest Aftershocks with Existing Ground-Motion Prediction Equations

by Céline Beauval, J. Marinière, A. Laurendeau, J.-C. Singaucho, C. Viracucha, M. Vallée, E. Maufroy, D. Mercerat, H. Yepes, M. Ruiz, and A. Alvarado

ABSTRACT

A megathrust subduction earthquake (M_w 7.8) struck the coast of Ecuador on 16 April 2016 at 23:58 UTC. This earthquake is one of the best-recorded megathrust events to date. Besides the mainshock, two large aftershocks have been recorded on 18 May 2016 at 7:57 (M_w 6.7) and 16:46 (M_w 6.9). These data make a significant contribution for understanding the attenuation of ground motions in Ecuador. Peak ground accelerations and spectral accelerations are compared with four ground-motion prediction equations (GMPEs) developed for interface earthquakes, the global Abrahamson *et al.* (2016) model, the Japanese equations by Zhao, Zhang, *et al.* (2006) and Ghofrani and Atkinson (2014), and one Chilean equation (Montalva *et al.*, 2017). The four tested GMPEs are providing rather close predictions for the mainshock at distances up to 200 km. However, our results show that high-frequency attenuation is greater for back-arc sites, thus Zhao, Zhang, *et al.* (2006) and Montalva *et al.* (2017), who are not taking into account this difference, are not considered further. Residual analyses show that Ghofrani and Atkinson (2014) and Abrahamson *et al.* (2016) are well predicting the attenuation of ground motions for the mainshock. Comparisons of aftershock observations with the predictions from Abrahamson *et al.* (2016) indicate that the GMPE provide reasonable fit to the attenuation rates observed. The event terms of the M_w 6.7 and 6.9 events are positive but within the expected scatter from worldwide similar earthquakes. The intraevent standard deviations are higher than the intraevent variability of the model, which is partly related to the poorly constrained V_{S30} proxies. The Pedernales earthquake produced a large sequence of aftershocks, with at least nine events with magnitude higher or equal to 6.0. Important cities are located at short distances (20–30 km), and magnitudes down to 6.0 must be included in seismic-hazard studies. The next step will be to constitute a strong-motion interface database and test the GMPEs with more quantitative methods.

Electronic Supplement: Figures of V_{S30} values based on topography versus rupture distance and difference between reference V_{S30} and V_{S30} based on topography versus distance, residuals, event terms, and intraevent standard deviations.

INTRODUCTION

The megathrust Pedernales earthquake (M_w 7.8) struck the coast of Ecuador on 16 April 2016 at 23:58 UTC. Sixty-nine accelerometric stations recorded the earthquake at fault distances ranging from 26 to 427 km (Fig. 1). One month after the mainshock, two large aftershocks have been recorded on 18 May 2016 at 7:57 and 16:46 (Table 1; M_w 6.7 and 6.9, respectively). The accelerometric network in Ecuador started in 2009 with nine stations installed in the framework of the French–Ecuadorian research project Andes du Nord (ADN). In 2010, the Ecuadorian research agency Secretaría Nacional de Educación Superior, Ciencia y Tecnología (SENESCYT) granted the Geophysical Institute in Quito with an ambitious project for instrumenting the whole country with high-level instruments, accelerometric, broadband, and Global Positioning System (GPS) stations. The accelerometric network, now called Red Nacional de Acelerógrafos (National Accelerometric Network, RENAC), is

doi: 10.1785/0220160150

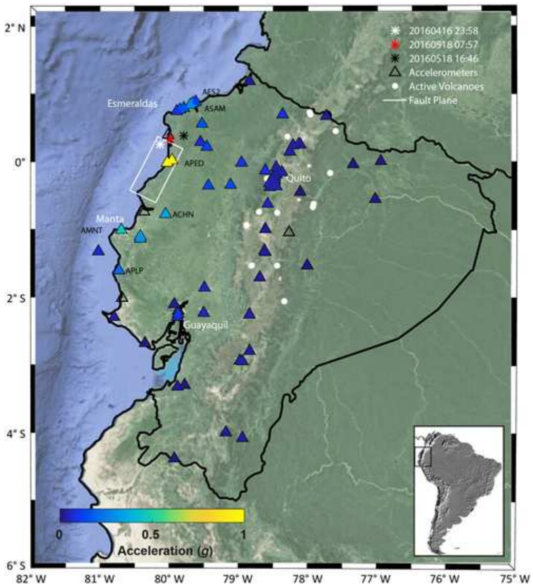

▲ **Figure 1.** Location map with fault rupture and stations. The white rectangle shows the surface projection of the Pedernales mainshock M_w 7.8 (inferred from Nocquet *et al.*, 2016). Epicenters of the mainshock and its two largest aftershocks are indicated (stars). Triangles show locations of strong-motion stations, which recorded the mainshock and/or the aftershocks. Stations with acceleration indicated (scale bar) recorded the mainshock. Background map produced with Google Maps. The color version of this figure is available only in the electronic edition.

still in a developing phase, with ∼30% of the stations telemetered and the characterization of the sites undergoing.

Ecuador is exposed to a high seismic risk, both from earthquakes on the subduction interface, such as the 2016 event, and from earthquakes on shallow crustal faults in the Andean Cordillera. Since 2007, a French–Ecuadorian cooperation aims at leading research on all aspects related to probabilistic seismic-hazard assessment (PSHA) to improve PSHA in Ecuador (e.g., Beauval *et al.*, 2010, 2013, 2014; Alvarado *et al.*, 2014; Yepes *et al.*, 2016). PSHA aims at providing ground motions with probabilities of being exceeded in future time windows. The results can be used to establish seismic zoning for national building codes. Because the strong-motion database was still in its development phase, no study has been published yet on the testing of ground-motion prediction equations (GMPEs) against accelerometric data. In the PSHA calculations, GMPEs have been selected based on tectonic similarities criteria (e.g., Beauval *et al.*, 2014). The M_w 7.8 earthquake and its largest aftershocks produced a unique dataset. These data make a significant contribution for understanding the attenuation of ground motions in Ecuador. In the present study, peak ground accelerations (PGAs) and spectral accelerations are compared with four GMPEs developed for interface earthquakes: the recent global Abrahamson *et al.* (2016) model as well as two Japanese equations, Zhao, Zhang, *et al.* (2006) and Ghofrani and Atkinson (2014), and a new Chilean model (Montalva *et al.*, 2017).

STRONG-MOTION DATA

Strong-motion data are obtained from the RENAC, which includes seven accelerometers from the Oleoducto de Crudos Pesados network as well as nine ADN accelerometers. Figure 1 shows the distribution of the 69 stations triggered by the Pedernales event relative to the earthquake fault-plane surface projection. There are 16 stations at rupture distances ranging from 26 to 100 km, distributed in the coastal plain. Thirty-three stations are located in the north–south Andean Cordillera hosting many volcanoes, and 14 stations are installed in the Quito basin (Laurendeau *et al.*, 2017). Approximately half of the stations are located in the fore-arc region, west of the volcanic front, and the other half lie in the back-arc region. The records at six example stations are displayed in Figure 2. The M_w 6.9 and 6.7 aftershocks were recorded, respectively, by 61 and 64 stations; 5 of these stations did not record the mainshock (Fig. 1).

Table 1
Finite-Fault Parameters Used in the Present Study for the 2016 M_w 7.8 Pedernales Earthquake and Its Two Largest Aftershocks, M_w 6.9 and 6.7

Date (yyyy/mm/dd)	Time (UTC) (hh:mm)	Hypocenter Latitude (°)	Hypocenter Longitude (°)	Hypocenter Depth (km)	Fault Strike (°)	Dip Angle (°)	Fault Length (km)	Fault Width (km)	M_w Global CMT*
2016/04/16	23:58	0.35†	80.17†	17†	26.5†	23†	110†	60†	7.8
2016/05/18	07:57	0.43387‡	−80.00961‡	17‡	29‡	26‡	28§	30§	6.7
2016/05/18	16:46	0.47301‡	−79.81545‡	21‡	47‡	25‡	36§	34§	6.9

*Obtained from the Global Centroid Moment Tensor Project (Global CMT; see Data and Resources).
†Deduced from Nocquet *et al.* (2016).
‡Determined by Geophysical Institute in Quito (dip and strike obtained with Nakano *et al.*, 2008 method).
§Determined with the scaling law for interface events in Strasser *et al.* (2010).

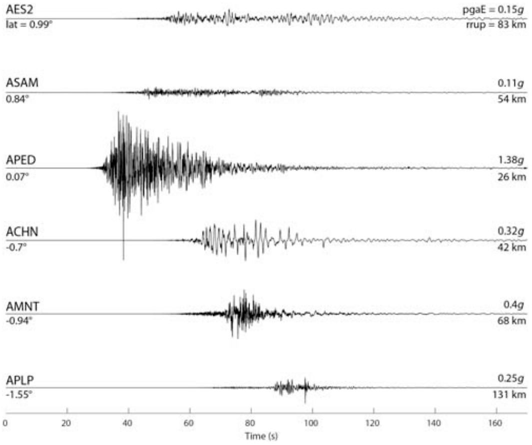

▲ **Figure 2.** Pedernales earthquake on 16 April 2016 M_{w} 7.8. Accelerograms recorded at six stations around the fault plane (see Fig. 1, east component). Latitudes of stations, maximum amplitude, and rupture distance to the fault plane are indicated.

All stations are installed on the ground surface and record continuously. Different digital accelerometer devices are used (Güralp, RefTek, and Kinemetrics; see Table 2). For this study, a simple processing was applied. Acceleration time histories were visually inspected and windows extracted. A first-order baseline operator and a simple baseline correction are applied on each window for each component. Signal-to-noise Fourier spectral ratios have been carefully calculated with the signal processing tools of Perron *et al.* (2016). Given the magnitude of the three events, these ratios are, in most cases, high for the frequencies of interest (PGA and 0.5–5 Hz). At the stations located at distances between 300 and 500 km, the signal-to-noise ratios are still higher or equal to 3 in this frequency range. Response spectra were then calculated with critical damping at 5%. For each record, the geometric-mean horizontal component is calculated for PGA and spectral periods up to 3 s.

The site conditions at a recording station have a strong influence on ground motions. The most common proxy for the simplified classification of a site in terms of its seismic response is V_{S30}, the time-average shear-wave velocity in the upper 30 m. In Ecuador, few RENAC stations have been characterized with geophysical methods, and significant efforts still need to be made to evaluate the geotechnical information of the sites. In Quito (14 sites), V_{S30} are inferred from geophysical investigations of the subway project (TRX Consulting C.A., 2011a, b) and from a microzoning study (Evaluacion de Riesgos Naturales [ERN], 2012). For each station, V_{S30} is inferred from the shear-wave velocity profile closest to the site. In Guayaquil (three sites), V_{S30} values come from the work of Vera-Grunauer (2014). A new project was started after the mainshock by the Geophysical Institute to investigate the site effects in the coastal cities, which to this date yields V_{S30} values for three sites based on multichannel analysis of surface waves techniques.

For the other sites, following Zhao, Irikura, *et al.* (2006), horizontal-to-vertical (H/V) response spectral ratios are computed to determine the natural period of the site (Tg) and to classify the sites into four broad site classes (SC I, II, III, IV, from rock to soft soil). The number of recordings available at each station varies from 3 to 203 (15 on average, see Laurendeau *et al.*, 2016). The entire signal windows are used. At 33 sites, the natural period can be estimated, and V_{S30} is deduced as $V_{S30} = 4H/Tg$, with $H = 30$ m. At 16 sites with a natural period estimated higher or equal to 0.6 s (soft soil, SC IV, Zhao, Zhang, *et al.*, 2006), V_{S30} is fixed to 200 m/s. At six sites showing a flat H/V ratio with amplitudes lower than 2, the site is classified in the rock and stiff soil class with a V_{S30} of 800 m/s. There are 14 sites for which there was no clear peak but broadband frequency amplification. The method cannot be applied, and an average V_{S30} of 400 m/s is arbitrarily attributed. More work is required to understand the limits of the method and how to adapt it to sites in Ecuador. This set of estimated V_{S30} is considered as the reference V_{S30} set (Fig. 3).

To take into account the huge uncertainty on the V_{S30} values, a second set of V_{S30} is used. It is based on the weighting of the four closest points given in the database on the Global U.S. Geological Survey V_{S30} Slope Topography website (see Data and Resources). These V_{S30} are based on a relationship between the topographic slope and V_{S30} (Wald and Allen, 2007). The V_{S30} values based on topography are compared with the reference V_{S30} values in Ⓔ Figure S1 (available in the electronic supplement to this article). At

Table 2
Description of Red Nacional de Acelerógrafos (National Accelerometric Network, RENAC) Accelerometer Devices

	Sensor	Digitizer	Full-Scale Range (g)	Dynamic Range	Frequency Response (Hz)	Sample Frequency (Hz)
1	Güralp CMG-5TD		±4	127 dB at 3–30 Hz	DC–100	100
2	RefTek 130-SMA		±4	112 dB at 1 Hz	DC–500	100
3	Kinemetrics EpiSensor FBA ES-T	Kephren	±2	155 dB	DC–200	125 or 250

DC, direct current.

distances shorter than 100 km, in the fore-arc region, the difference does not exceed 200 m/s. At larger distances, up to 600 m/s, difference can be observed for stations in the Cordillera. In the present work, the comparisons between observations and predictions are systematically led for both V_{S30} sets, showing that this uncertainty does not impact the results. All results displayed in the article rely on the reference V_{S30} set, whereas results based on the alternative V_{S30} set based on topography are in the Ⓔ electronic supplement.

GMPES SELECTED

GMPEs describe the median and the variability of ground-motion amplitudes, depending on magnitude, site-source distance, site conditions, and other parameters. Four equations are considered here, two Japanese models, one Chilean, and one global model: Zhao, Zhang, *et al.* (2006), Ghofrani and Atkinson (2014), Montalva *et al.* (2017), and Abrahamson *et al.* (2016). The Zhao, Zhang, *et al.* (2006) model does not include the recent interface events but proved to be quite stable and to fit reasonably the data available in South America (e.g., Arango *et al.*, 2012; Beauval, Cotton, *et al.*, 2012). The Abrahamson *et al.* (2016) model is our favorite candidate for PSHA applications, because it includes the largest amount of global data, and an earlier version of the model proved to be stable and to fit well datasets from various subduction environments (Beauval, Cotton, *et al.*, 2012). All four models use the geometric mean of the two horizontal components, moment magnitude, and rupture distance (closest distance to the fault plane). All are providing the total sigma, as well as the intraevent (variability from the median-predicted value for a particular recording station in a given earthquake) and interevent variabilities (variability between earthquakes of the same magnitude).

The Abrahamson *et al.* (2016) model is based on the combined datasets used in several of the past subduction GMPEs (e.g., Youngs *et al.*, 1997; Atkinson and Boore, 2003), as well as additional ground-motion data obtained in Japan, Taiwan, south and central America, and Mexico. This new global GMPE is intended to replace the older global GMPEs. The metadata were carefully checked and improved, and recent events around the world were included. The final dataset includes 43 interface earthquakes ($6.0 \le M_w \le 8.4$) at distances up to 300 km. About 57% interface records are from Japan and 29% from Taiwan. The model is predicting a stronger attenuation for sites located in the back-arc region with respect to sites located in the fore-arc region. The model is including site nonlinearity.

Ghofrani and Atkinson (2014) developed a GMPE for interface earthquakes of M_w 7.0–9.0, based on data from Japan. The >600 strong ground motion records from the 2011 M_w 9.0 Tohoku earthquake are used to derive an event-specific GMPE, which is then extended to represent the shaking from four other $M_w > 7.0$ interface events in Japan, which occurred in 2003, 2004, and 2005. Three GMPEs are finally available to represent the epistemic uncertainty, an upper and lower model, as well as a median model. The median central model is used here. The equation accounts for the difference in the attenuation between fore-arc and back-arc region using separate anelastic attenuation factors. The soil response is treated as linear. Ghofrani and Atkinson (2014), like Abrahamson *et al.* (2016), explicitly use V_{S30}.

Zhao, Zhang, *et al.* (2006) developed an attenuation model for Japan based on events with M_w 5.0–8.3, at distances up to 300 km. Four site classes are used in the present study, SC I, II, III and IV, approximately corresponding to the four classes, rock, hard soil, medium soil, and soft soil (site classification scheme used in Japanese engineering design; Zhao, Zhang, *et al.*, 2006). The authors associated with these site classes approximate National Earthquake Hazards Reduction Program (NEHRP) site classes and V_{S30} intervals (table 2 in Zhao, Zhang, *et al.*, 2006). The near-source data (<30 km) are mostly constrained by the records from crustal events; however, this should not affect the predictions for subduction events for distances >30 km.

Montalva *et al.* (2017) developed a GMPE relying on Chilean subduction earthquakes that occurred between 1985 and 2015, including the three recent megathrust earthquakes (2010 M_w 8.8 Maule, 2014 M_w 8.1 Iquique, and 2015 M_w 8.3 Illapel). The median model is based on the same functional form as the Abrahamson *et al.* (2016) model. The attenuation is predicted only for fore-arc sites, because all recording stations are located in the fore-arc region. Montalva *et al.* (2017) indicate that the number of strong-motion stations with measured V_{S30} is limited and that V_{S30} proxies have been inferred both from the topographic slope (Wald and Allen, 2007) and the site's predominant period (Zhao, Irikura, *et al.*, 2006). Montalva *et al.* (2017), like Abrahamson *et al.* (2016) and Zhao, Zhang, *et al.* (2006), do not include data beyond 300 km.

Abrahamson *et al.* (2016) and Ghofrani and Atkinson (2014) predict different attenuation depending on the location of the station with respect to the volcanic front. The fore-arc region is between the subduction trench axis and the axis of volcanic front. The back-arc region is behind the volcanic front. The high-attenuation low-velocity region in the crust and upper mantle related to the volcanic activity filters the high-frequency content of ground motion, as shown by Ghofrani and Atkinson (2011) on in-slab events and by Ghofrani and Atkinson (2014) on interface events.

Most of the interface models published up to now have been coded in the strong-motion toolkit used here for predicting accelerations (Weatherill, 2014). This toolkit relies on the GMPE libraries of the OpenQuake PSHA software (Pagani *et al.*, 2014). The Lin and Lee (2008) GMPE established on Taiwanese data was not selected because the equation is using the hypocentral distance, and given the short distances involved in Ecuador this might not be adequate. The Kanno *et al.* (2006) GMPE is not included because it would be a third Japanese model, and it uses an unconventional definition for the horizontal component of motion. The Mexican equation by Arroyo *et al.* (2010) is not considered either because it predicts ground motions at rock sites only (NEHRP B class).

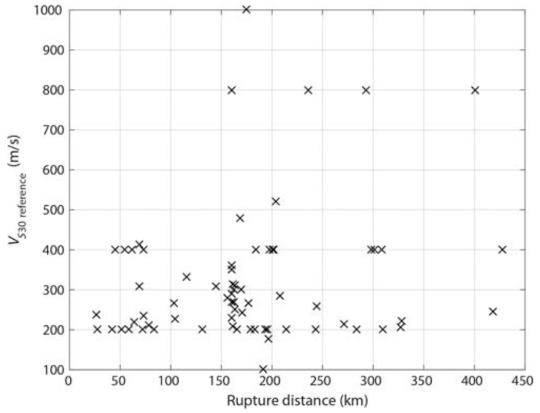

▲ **Figure 3.** V_{S30} reference set versus rupture distance (see the Strong-Motion Data section). Alternative V_{S30} values based on topography are in Ⓔ Figure S1, available in the electronic supplement to this article.

FAULT-PLANE SOLUTION AND DISTANCE CALCULATION

The site-source distances are calculated using the closest distance to the fault rupture plane (rupture distance). The fault must be approximated by a rectangular plane. There is no unique solution for the finite-fault plane (e.g., Goda and Atkinson, 2014). Different fault models can be derived using various datasets and methods in source inversion analysis. The inversion might include GPS data, Interferometric Synthetic Aperture Radar, teleseismic body wave, surface-wave data, and near-source strong-motion data. Goda and Atkinson (2014) explored the uncertainty related to the choice of the rupture plane for three Japanese megathrust earthquakes and showed that the impact on the comparison between observations and models can be significant. For now, for the 2016 Pedernales event, we are aware of only one elaborated model by Nocquet *et al.* (2016). The maximum slip is about 6.2 m. From this slip model, we extracted the fault plane, which includes approximately the 100-cm slip contour. The resulting plane is a rectangular of 100 km in length and 50 km in width, dipping to the east with a strike of 26.50° and a dip of 23°, extending from 13 to 33 km (Table 1; Fig. 1). The hypocenter solution is up-dip on the northern border of the fault plane.

The Pedernales earthquake is one of the best-recorded megathrust events to date, in terms of distribution of stations around the fault plane and number of recording stations. Records are available above the fault plane (two stations, Fig. 1), at short distances from the fault plane to the north and northeast (10 stations between 45 and 100 km), east (2 stations at 73 and 103 km), and south and southeast (4 stations between 40 and 75 km).

The rupture distance measure, taking into account the extension of the fault plane, only captures macroscopic features of the source. The more detailed components of recorded strong motions in the near-source region are not taken into account (e.g., short periods affected by local asperities). Besides, the 2016 Pedernales event is presenting evidences of directivity effects, with higher ground motions in the direction of the slip, south of the rupture plane, than in the north. These observations cannot be modeled by current published interface GMPEs.

Because no fault-plane solution has been inverted yet for the aftershocks, the length and width of the faults are based on a Strasser *et al.* (2010) relations (Table 1). The fault plane is arbitrarily centered on the hypocenter.

COMPARING OBSERVATIONS AND PREDICTIONS

Mainshock M_w 7.8

At first, predictions and observations are compared based on simple attenuation plots. As a second step, residual analyses are performed in which the predictions include the V_{S30} for each site.

Predictions from Abrahamson *et al.* (2016) are superimposed onto the observations, for the PGA (Fig. 4a). To begin with, predictions are provided with the fore-arc/unknown option (Abrahamson *et al.*, 2016). Three V_{S30} are considered (200, 400, and 760 m/s), producing slightly different amplitudes. The attenuation rate predicted is consistent with the observations for distances lower or equal to 130 km. For distances between 130 and 400 km, the observed attenuation rate appears steeper than predicted. Stations within 130 km from the rupture plane are all in the fore-arc region. At distances larger than 130 km, half of the stations are within or behind the volcanic arc (Fig. 1). Taking into account the back-arc option in the equation yields a steeper attenuation with distance, in accordance with the observations at back-arc stations (Fig. 4c). In Quito, located at around 150 km from the earthquake in the Cordillera (Fig. 1), recorded PGA varies between $0.017g$ and $0.081g$.

The rupture propagated to the south, producing directivity effects on ground motions. At rupture distances 40–80 km, stations located to the south of the rupture experienced larger amplitudes than stations located to the north or to the east (Figs. 1 and 5). A specific study will need to be performed to investigate the source contribution on the Pedernales ground motions. The recorded data might need to be corrected for path and site effects to explain the difference of amplitudes in terms of source directivity (see, e.g., Cultrera *et al.*, 2008).

As expected, long-period ground motions decay less rapidly with distance than do short-period motions. Figure 4b displays predictions superimposed on observations at $T = 1.0$ s. Amplitudes predicted are more V_{S30} dependent than for short periods. Overall, the attenuation rate predicted is consistent with observations. Considering predictions for V_{S30} from 200 to 760 m/s and considering the predicted variability (total sigma), most of the observations are within the predicted range.

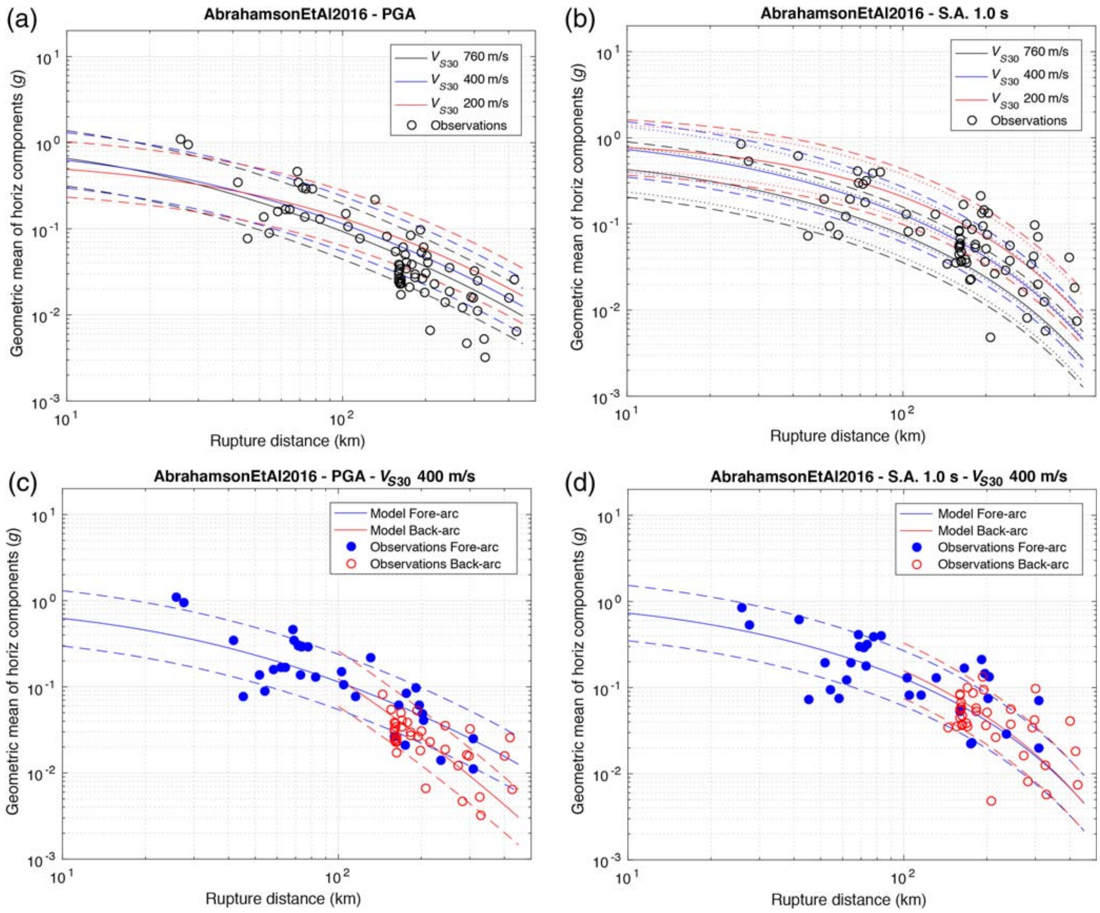

▲ **Figure 4.** Observed spectral amplitudes of the mainshock M_w 7.8, overlaid by the Abrahamson *et al.* (2016) predicted amplitudes (median $\pm\sigma$). Total sigma is indicated with dashed lines. (a) Peak ground acceleration (PGA) for three different V_{S30} values, fore-arc/unknown coefficients used for all stations; (b) spectral acceleration $T = 1.0$ s for three different V_{S30} values, fore-arc/unknown coefficients used for all stations; (c) PGA predictions for fore-arc sites and for back-arc sites for a V_{S30} of 400 m/s; (d) spectral acceleration $T = 1.0$ s predictions for fore-arc sites and for back-arc sites for a V_{S30} of 400 m/s. The color version of this figure is available only in the electronic edition.

The model predicts similar decay with distance for fore-arc and back-arc regions, and the observations indeed do not present significant differences (Fig. 4d).

Predictions by Zhao, Zhang, *et al.* (2006), Ghofrani and Atkinson (2014), and Montalva *et al.* (2017) are now superimposed onto the observed data, considering an average V_{S30} value (400 m/s, Fig. 6). For distances in the 30–150 km range, PGA median predictions from the four GMPEs are quite similar and consistent with the observed attenuation rate, with around $0.3g$ predicted at 40 km and $0.1g$–$0.11g$ at 100 km. The total sigma predicted are also close. For distances larger than 150 km, the two Japanese models predict stronger distance decay. The Zhao, Zhang, *et al.* (2006) model does not differentiate attenuation between fore-arc and back-arc stations, but its generating dataset includes many Japanese back-arc stations. Applying the fore-arc/back-arc station classification, the Ghofrani and Atkinson (2014) model predicts a stronger attenuation for back-arc stations at distances larger than 100 km, with predictions very close to the Abrahamson *et al.* (2016) model (Fig. 7a, PGA). At $T = 1.0$ s, the Abrahamson *et al.* (2016) model predicts larger accelerations at distances <200 km than the Japanese and Chilean models (Fig. 6b). The generating datasets of Abrahamson *et al.* (2016), Zhao, Zhang, *et al.* (2006), and Montalva *et al.* (2017) do not include records beyond 300 km, and the models are therefore extrapolated at these distances.

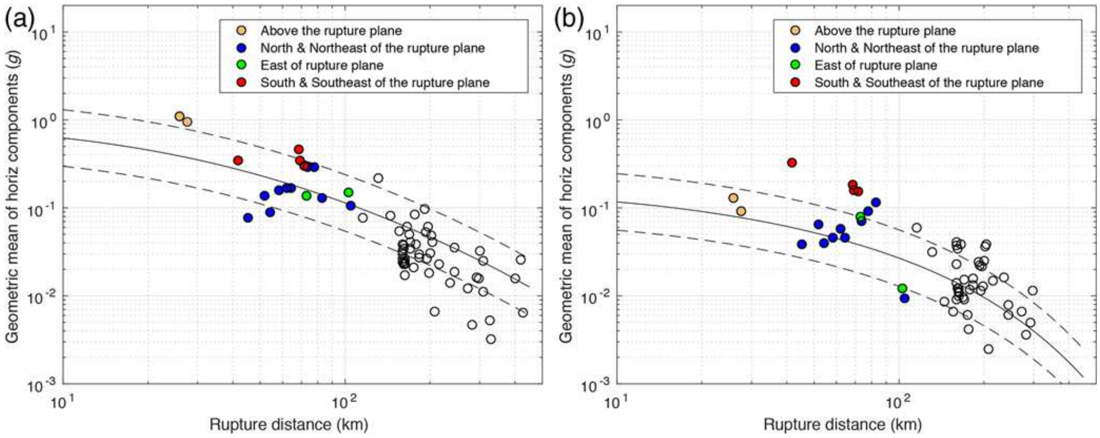

▲ **Figure 5.** Evidence of directivity effects at (a) PGA and (b) 3 s. The stations located at rupture distances lower or equal to 100 km are highlighted, and their location with respect to the fault plane is indicated. Abrahamson *et al.* (2016) predicted amplitudes with $V_{S30} = 400$ m/s (see legend of Fig. 4a). The color version of this figure is available only in the electronic edition.

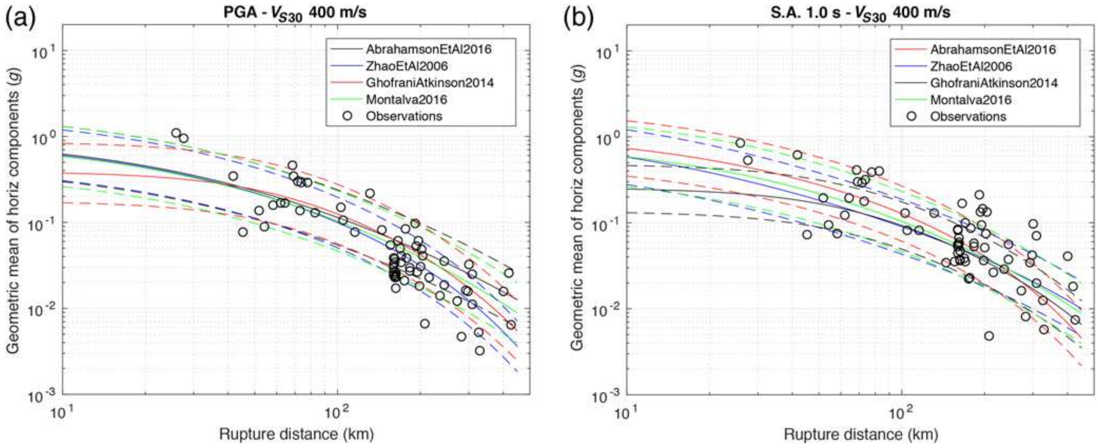

▲ **Figure 6.** Observed spectral amplitudes of the mainshock M_w 7.8 at (a) PGA and (b) spectral acceleration $T = 1.0$ s, overlaid by four ground-motion prediction equation (GMPE) curves: Abrahamson *et al.* (2016), Ghofrani and Atkinson (2014), Zhao, Zhang, *et al.* (2006), and Montalva *et al.* (2017). Total sigma is indicated with dashed lines. Predictions for an average V_{S30} of 400 m/s. The color version of this figure is available only in the electronic edition.

To more accurately evaluate the performance of the GMPEs relative to the data, total residuals are calculated considering V_{S30} for each station (V_{S30} reference set, see the Strong-Motion Data section). Residuals are calculated first ignoring the fore-arc/back-arc distinction, and then including this attenuation difference. At the PGA, a trend in the distance dependence of residuals is observed with back-arc sites showing a negative slope (Fig. 8a). Applying back-arc coefficient to the sites in the back-arc region, the slope becomes flatter, with mean residuals closer to zero (Fig. 8b). The same observation can be made for the residuals relative to the equation of Ghofrani and Atkinson (2014) (Ⓔ Fig. S2). At 1 s, as expected, no difference can be seen in the distance-decay rates for the fore-arc and the back-arc stations (Fig. 8c,d). The Ghofrani and Atkinson (2014) model is slightly underestimating the observations, as shown by the mean residuals higher or equal to zero.

At present, the uncertainty on V_{S30} estimate is huge for the RENAC stations (see the Strong-Motion Data section). The second set of V_{S30} values based on topographic slope is considered as an attempt to evaluate the impact of V_{S30} uncertainty on the results. The residuals obtained with the Abrahamson *et al.*

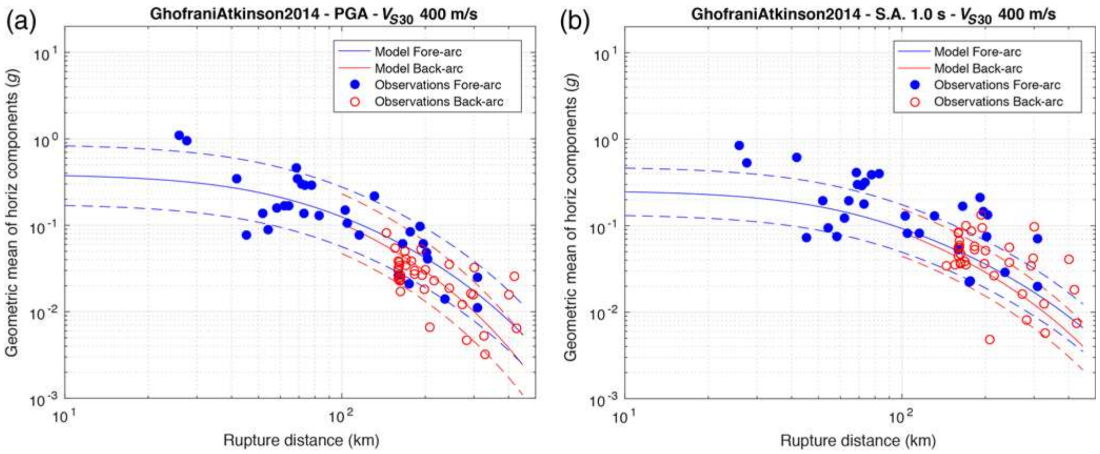

▲ **Figure 7.** Observed spectral amplitudes of the mainshock M_w 7.8 overlaid by the Ghofrani and Atkinson (2014) predicted amplitudes (median $\pm\sigma$), for (a) PGA and (b) spectral acceleration $T = 1.0$ s, for an average V_{S30} of 400 m/s. The color version of this figure is available only in the electronic edition.

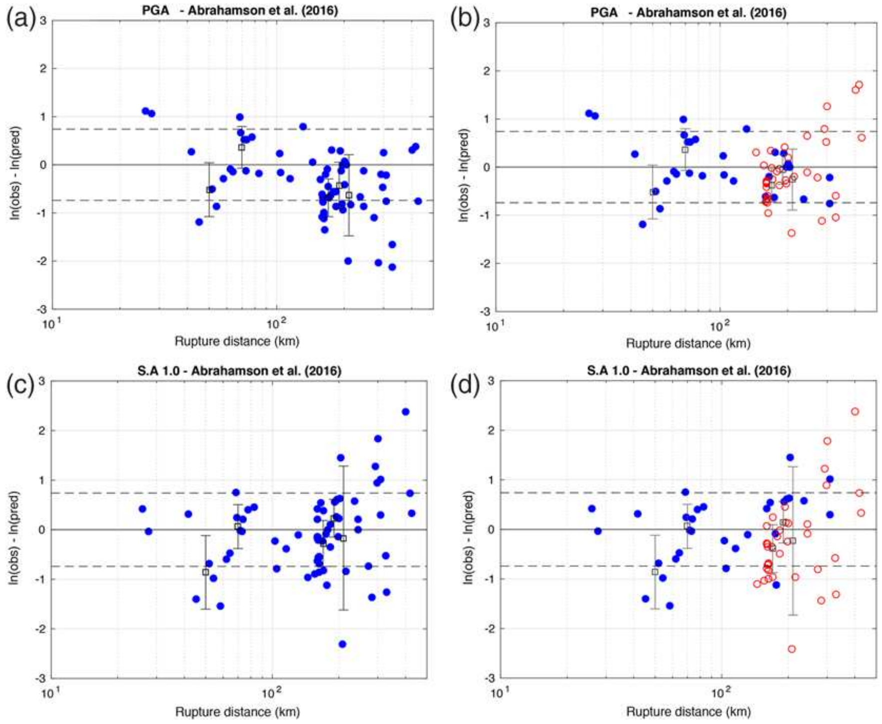

▲ **Figure 8.** Total residuals, mainshock, the Abrahamson *et al.* (2016) model. The residuals are binned into intervals of 20 km width, and the corresponding means (squares) and standard deviations (bars) are displayed when calculated on at least four values. Dashed lines indicate ±total sigma (0.74). Event term is the mean of the residuals. V_{S30} reference set considered (see the Strong-Motion Data section). Abrahamson *et al.* (2016) generating dataset does not include records beyond 300 km, and the model is therefore extrapolated at these distances. The color version of this figure is available only in the electronic edition.

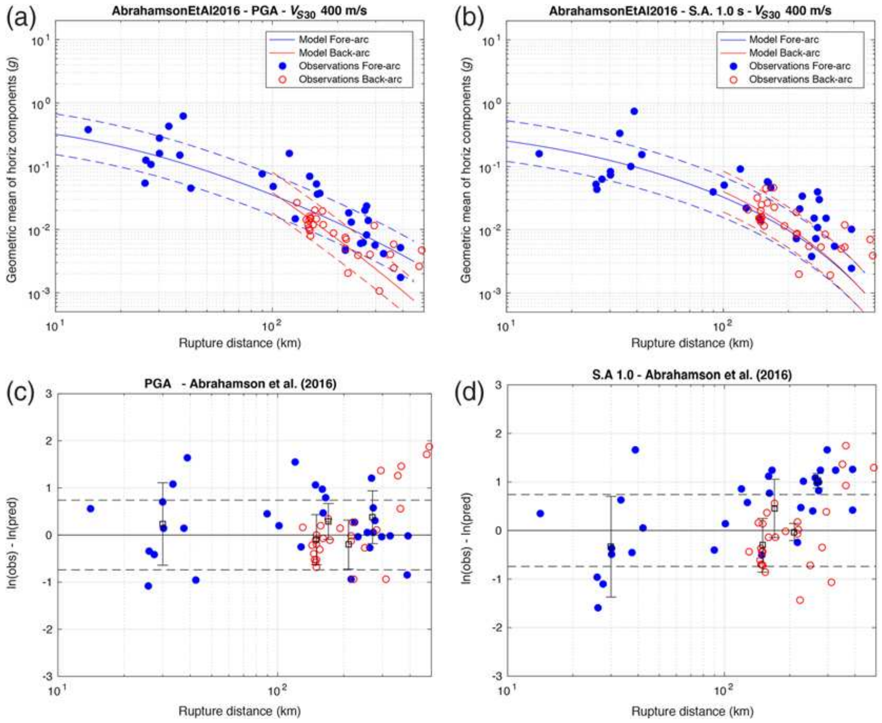

▲ **Figure 9.** Aftershock on 16 May 2016 M_w 6.9 at 16:46. (a) and (b) Attenuation of PGA and spectral accelerations at $T = 1.0$ s with distance and comparison to Abrahamson *et al.* (2016) GMPE for an average V_{S30} of 400 m/s. (c) and (d) Total residuals of data relative to Abrahamson *et al.* (2016) model; residuals binned in 20-km-width intervals and displayed if calculated over more than four observations; dashed lines indicates ±total sigma. Abrahamson *et al.* (2016) generating dataset does not include records beyond 300 km, and the model is therefore extrapolated at these distances. The color version of this figure is available only in the electronic edition.

(2016) model are presented in Ⓔ Figure S3. Residuals are quite stable with respect to the previous ones. At the PGA, for distances lower than 100 km, residuals are identical to the ones calculated with the reference V_{S30} set. This is expected; at these distances the difference in the V_{S30} values is not exceeding 200 m/s (Ⓔ Fig. S1). At larger distances, only slight difference in the mean residuals can be noticed. At spectral period $T = 1.0$ s, the mean of residuals is slightly shifted to positive values with respect to Figure 8, but still no major change is observed. Throughout the study, all residuals have been derived on both sets of V_{S30} values, showing that the results are stable.

Aftershocks M_w 6.9 and 6.7

Because the mainshock data show clearly an attenuation effect due to wave passage through the volcanic front, the models applied in Ecuador should take this difference into account. The equation of Ghofrani and Atkinson (2014) is made for events with magnitude higher than 7.0. Thus, only the Abrahamson *et al.* (2016) model is considered further for the aftershocks.

Figure 9 shows geometric mean PGA and $T = 1.0$ s spectral acceleration as a function of rupture distance for the M_w 6.9 event. The median and sigma predicted by the Abrahamson *et al.* (2016) model are superimposed onto the data, for an average V_{S30} value of 400 m/s. The residuals are also calculated. Observations are more scattered than for the mainshock; however, comparable observations can be made. The attenuation rate predicted is roughly consistent with the observations, with a stronger attenuation at back-arc sites for PGA. Mean of residuals are in general within one standard deviation. At $T = 1.0$ s, mean residuals at distances larger than 150 km are larger or equal to sigma, indicating that the model is predicting a stronger attenuation than observed.

Results for the M_w 6.7 aftershocks are displayed in Figure 10. At short period (PGA), the difference in attenuation between fore-arc and back-arc stations is less clear (Fig. 10a). The attenuation rate for back-arc sites appears to better fit the observations for distances larger than 100 km for all stations (fore-arc and back-arc). Residuals indeed show a negative slope (Fig. 10c). The residuals at $T = 1.0$ s show a flatter slope, with

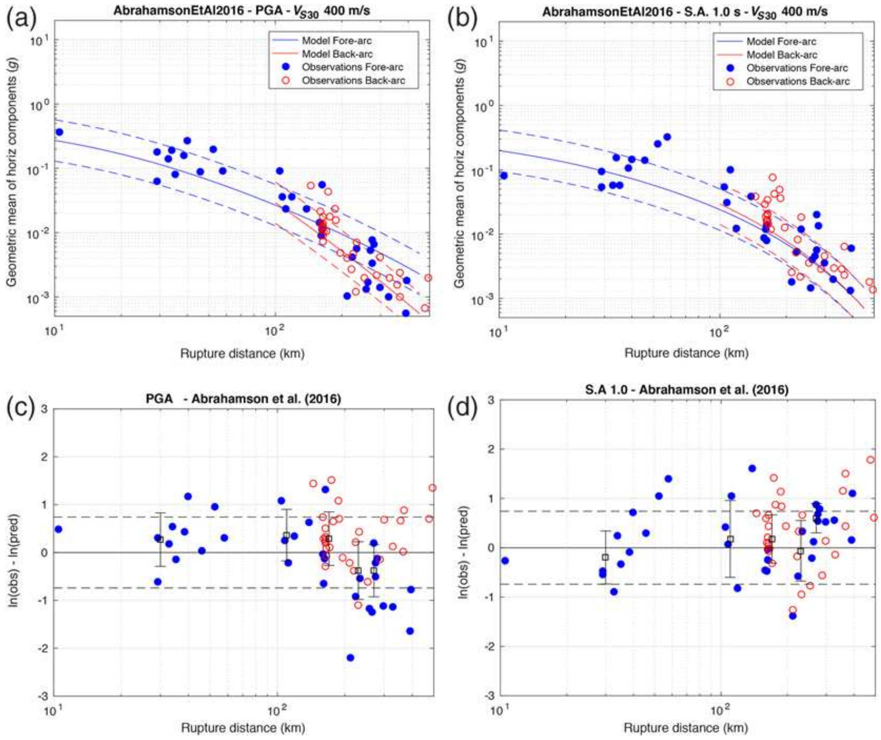

▲ **Figure 10.** Aftershock on 18 May 2016 M_w 6.7 at 7:57. (a) and (b) Attenuation of PGA and spectral accelerations at $T = 1.0$ s with distance and comparison to Abrahamson *et al.* (2016) GMPE for an average V_{S30} of 400 m/s. (c) and (d) Total residuals of data relative to Abrahamson *et al.* (2016) model; residuals binned in 20-km-width intervals and displayed if calculated over more than four observations; dashed lines indicates ±total sigma. Abrahamson *et al.* (2016) generating dataset does not include records beyond 300 km, and the model is therefore extrapolated at these distances. The color version of this figure is available only in the electronic edition.

positive mean residuals at distances larger than 100 km, indicating that the model is predicting, on average, lower ground motions than observed (Fig. 10d). Part of the data is indeed above the predictions (Fig. 10b).

Event Terms and Intraevent Standard Deviations

For the three events, the event term and intraevent standard deviations are calculated for a suite of six periods between PGA and 2 s (Fig. 11). Residuals at distances larger than 300 km, the validity limit of the Abrahamson *et al.* (2016) model, are not included. The event term is the mean of the residuals in a single event over all stations. The intraevent residual is the misfit between an individual observation at a station from the earthquake-specific median prediction, which is defined as the median prediction of the model plus the event term for the earthquake (Al Atik *et al.*, 2010). The general trend of the event terms with spectral period is consistent for the three earthquakes (Fig. 11a). Event terms are mostly within the expected scatter for interface subduction earthquakes worldwide ($\tau = 0.43$). Event terms are both negative and positive for the mainshock but always positive for the aftershocks (larger than expected ground motions). Intraevent standard deviations for the mainshock are close to the expected scatter ($\phi = 0.6$) for spectral periods lower than 1 s (Fig. 11b). At 1 and 2 s, the intraevent variability is higher than expected. This might be partly due to the poorly constrained V_{S30} parameter and to the directivity effects on the ground motions.

Residuals, event terms, and intraevent standard deviations based on the second set of V_{S30} values, relying on topography, are displayed in Ⓔ Figures S4 and S5. Results are quite stable with respect to the calculations based on the reference V_{S30}. Intraevent standard deviations are again higher or equal to the intraevent variability predicted by the model.

CONCLUSIONS

The Pedernales interface earthquake of 16 April 2016 produced a unique dataset which enables us to analyze the attenuation of ground motion with distance in Ecuador and to evaluate the per-

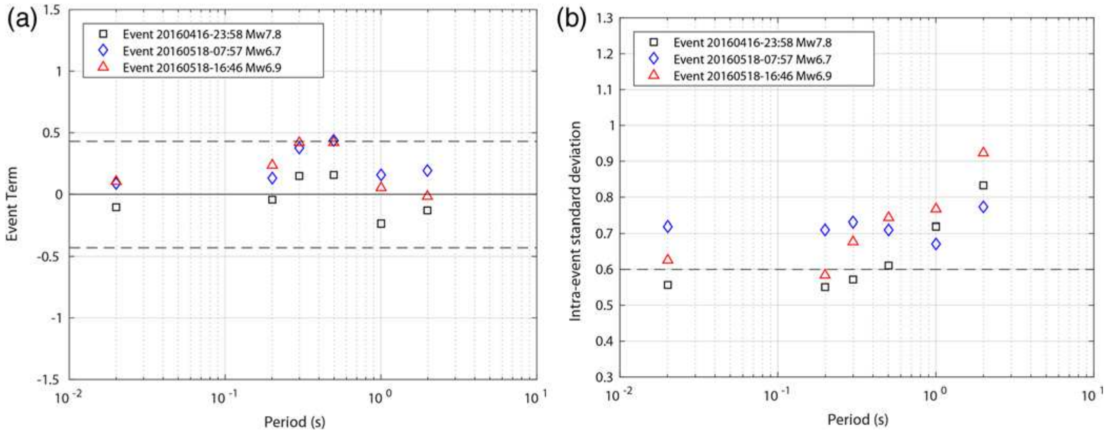

▲ **Figure 11.** (a) Event terms of the Pedernales mainshock and its two largest aftershocks, compared to the Abrahamson *et al.* (2016) interevent standard deviation τ (0.43); (b) intraevent standard deviation for Pedernales mainshock and its two largest aftershocks compared to the Abrahamson *et al.* (2016) intraevent standard deviation ϕ (0.6). Recordings at distances larger than 300 km are not included. Results for PGA are indicated at the frequency 50 Hz. The color version of this figure is available only in the electronic edition.

formance of interface models currently in use to predict strong ground motions in seismic-hazard studies. The national accelerometric network RENAC is young, and most stations still require site characterization, limiting the precision in the comparison of observations with existing ground-motion models.

The four considered GMPEs, Zhao, Zhang, *et al.* (2006), Ghofrani and Atkinson (2014), Montalva *et al.* (2017), and Abrahamson *et al.* (2016), are providing rather close predictions for an M_w 7.8 earthquake at distances up to 200 km. However, our results show that high-frequency attenuation is greater in the back-arc region, thus Zhao, Zhang, *et al.* (2006) and Montalva *et al.* (2017), which are not taking into account this difference, are not considered further. Overall, residual analyses show that the Ghofrani and Atkinson (2014) and Abrahamson *et al.* (2016) models are rather well predicting the attenuation of ground motions for the mainshock, both for short and long periods. A specific study investigating the signature of directivity effects in the recorded ground motions remains to be done.

Comparisons of aftershock observations with the Abrahamson *et al.* (2016) predictions indicate that the GMPE provides a reasonable fit to the attenuation rates observed. The event terms of the M_w 6.7 and 6.9 events are positive but within the expected scatter from worldwide similar earthquakes. The intraevent standard deviations are higher than the intraevent variability of the model, which is partly related to the poorly constrained V_{S30} proxies.

The Pedernales earthquake produced a large sequence of aftershocks, with at least nine events with magnitude equal to or higher than 6.0 recorded to date. Because the coast is close to the trench and the slab dip is shallow, important cities are located at short distances (20–30 km), and magnitudes down to 6.0 must be included in seismic-hazard studies. The next step will be to constitute a strong-motion interface database and test the GMPEs with more quantitative methods (e.g., Scherbaum *et al.*, 2009; Beauval, Tasan, *et al.*, 2012). Onsite measurements of velocity using geophysical techniques have begun and are planned for all RENAC sites. In a year or two, hopefully, the site conditions of the stations will be much better known.

DATA AND RESOURCES

The accelerometric dataset was recorded by the National Accelerometric Network of Ecuador (RENAC) maintained by the Geophysical Institute, Escuela Politécnica Nacional, Quito, and by the Oleoducto de Crudos Pesados (OCP) network. The Global Centroid Moment Tensor Project database was searched using www.globalcmt.org/CMTsearch.html (last accessed August 2016). The OpenQuake Ground Motion Toolkit is available online at https://github.com/GEMScienceTools/gmpe-smtk (last accessed August 2016). The programs developed by D. Boore to calculate fault-to-station distances are available online at http://www.daveboore.com/software_online.html (last accessed August 2016). The global V_{S30} Map Server was searched using http://earthquake.usgs.gov/hazards/apps/vs30/ (last accessed August 2016). ◼

ACKNOWLEDGMENTS

This work was supported by the Instituto Geofísico, Escuela Politécnica Nacional, Quito, by the Institut de Recherche pour le Développement (IRD), Centre national de la recherche scientifique–Institut national des sciences de l'Univers (CNRS-INSU), and by the Agence Nationale de la Recherche through the project REMAKE (Grant Number ANR-15-CE04-004). On the Ecuadorian side, additional support was available from the Secretaría Nacional de Educación Superior, Ciencia y Tecnología (SENESCYT; LAE-5 y Proyecto PIN_08-EPNGEO-00001). This work has been carried out in the frame of the Joint International Laboratory "Seismes & Volcans dans les Andes du Nord" (IRD LMI SVAN). Previous funding from the Agence Nationale de la Recherche of France is acknowledged (Grant Number ANR-07-BLAN-0143-01). We also acknowledge the Oleoducto de Crudos Pesados (OCP) for the use of their accelerometric data. We thank Dave Boore for sharing his programs to calculate fault-to-station distances and Gonzalo Montava for sharing his MATLAB script to predict ground motions with the new Chilean ground-motion prediction equation (GMPE). We are also grateful to Graeme Weatherhill and the Global Earthquake Model Modeling Facility for constant support on OpenQuake. At last, we would like to acknowledge Pierre-Yves Bard for fruitful interactions and discussions, as well as two anonymous reviewers for their constructive comments.

REFERENCES

Abrahamson, N., N. Gregor, and K. Addo (2016). BC hydro ground motion prediction equations for subduction earthquakes, *Earthq. Spectra* **32,** no. 1, 23–44.

Al Atik, L., N. Abrahamson, J. J. Bommer, F. Scherbaum, F. Cotton, and N. Kuehn (2010). The variability of ground-motion prediction models and its components, *Seismol. Res. Lett.* **81,** no. 5, 794–801, doi: 10.1785/gssrl.81.5.794.

Alvarado, A., L. Audin, J. M. Nocquet, S. Lagreulet, M. Segovia, Y. Font, G. Lamarque, H. Yepes, P. Mothes, F. Rolandone, *et al.* (2014). Active tectonics in Quito, Ecuador, assessed by geomorphological studies, GPS data, and crustal seismicity, *Tectonics* **33,** no. 2, 67–83, doi: 10.1002/2012TC003224.

Arango, M., F. Strasser, J. Bommer, J. Cepeda, R. Boroschek, D. Hernandez, and H. Tavera (2012). An evaluation of the applicability of current ground-motion models to the south and central American subduction zones, *Bull. Seismol. Soc. Am.* **102,** 143–168.

Arroyo, D., D. Garcia, M. Ordaz, M. A. Mora, and S. K. Singh (2010). Strong ground-motion relations for Mexican interplate earthquakes, *J. Seismol.* **14,** 769–785.

Atkinson, G. M., and D. M. Boore (2003). Empirical ground-motion relations for subduction-zone earthquakes and their application to Cascadia and other regions, *Bull. Seismol. Soc. Am.* **93,** no. 4, 1703–1729.

Beauval, C., F. Cotton, N. Abrahamson, N. Theodulidis, E. Delavaud, L. Rodriguez, F. Scherbaum, and A. Haendel (2012). Regional differences in subduction ground motions, *World Conf. on Earthquake Engineering*, Lisbon, Portugal, 24–28 September, 10 pp.

Beauval, C., H. Tasan, A. Laurendeau, E. Delavaud, F. Cotton, P. Guéguen, and N. Kuehn (2012). On the testing of ground-motion prediction equations against small magnitude data, *Bull. Seismol. Soc. Am.* **102,** no. 5, 1994–2007.

Beauval, C., H. Yepes, L. Audin, A. Alvarado, J.-M. Nocquet, D. Monelli, and L. Danciu (2014). Probabilistic seismic hazard assessment in Quito, estimates and uncertainties, *Seismol. Res. Lett.* **85,** no. 6, doi: 10.1785/0220140036.

Beauval, C., H. Yepes, W. Bakun, J. Egred, A. Alvarado, and J.-C. Singaucho (2010). Locations and magnitudes of historical earthquakes in the Sierra of Ecuador (1587–1996), *Geophys. J. Int.* **181,** no. 3, 1613–1633, doi: 10.1111/j.1365-246X.2010.04569.x.

Beauval, C., H. Yepes, P. Palacios, M. Segovia, A. Alvarado, Y. Font, J. Aguilar, L. Troncoso, and S. Vaca (2013). An earthquake catalog for seismic hazard assessment in Ecuador, *Bull. Seismol. Soc. Am.* **103,** 773–786, doi: 10.1785/0120120270.

Cultrera, G., F. Pacor, G. Franceschina, A. Emolo, and M. Cocco (2008). Directivity effects for moderate-magnitude earthquakes (M_w 5.6–6.0) during the 1997 Umbria–Marche sequence, central Italy, *Tectonophysics* **476,** nos. 1/2, doi: 10.1016/j.tecto.2008.09.022.

Evaluacion de Riesgos Naturales (ERN) (2012). Microzonificacion sismica del distrito metropolitan de Quito: studio de la amenaza sismica a nivel local, *Informe Final*, 198 pp. (in Spanish).

Goda, K., and G. Atkinson (2014). Variation of source-to-site distance for megathrust subduction earthquakes: Effects on ground motion prediction equations, *Earthq. Spectra* **30,** no. 2, 845–866.

Ghofrani, H., and G. Atkinson (2011). Forearc versus backarc attenuation of earthquake ground motion, *Bull. Seismol. Soc. Am.* **101,** 3032–3045.

Ghofrani, H., and G. Atkinson (2014). Ground-motion prediction equations for interface earthquakes of M 7 to M 9 based on empirical data from Japan, *Bull. Earthq. Eng.* **12,** 549–571.

Kanno, T., A. Narita, N. Morikawa, H. Fujiwara, and Y. Fukushima (2006). A new attenuation relation for strong ground motion in Japan based on recorded data, *Bull. Seismol. Soc. Am*, **96,** no. 3, 879–897.

Laurendeau, A., L. F. Bonilla, D. Mercerat, F. Courboulex, A. Alvarado, J. C. Singaucho, P. Guéguen, and E. Bertrand (2017). Seismic response of the basin of Quito from continuous accelerometric records of RENAC-Quito, *16th World Conf. on Earthquake Engineering*, Santiago, Chile, January 2017, 11 pp., Extended Abstract.

Laurendeau, A., M. Perrault, D. Mercerat, L.-F. Bonilla, F. Courboulex, C. Beauval, J.-G. Barros, F. Vasconez, J. Marinière, J.-C. Singaucho, *et al.* (2016). Preliminary observations of site effects during the M_w 7.8 Pedernales (Ecuador) earthquake on April 16th 2016, *5th IASPEI/IAEE International Symposium: Effects of Surface Geology on Seismic Motion*, Taipei, Taiwan, 15–17 August, 12 pp.

Lin, P.-S., and C.-T. Lee (2008). Ground-motion attenuation relationships for subduction-zone earthquakes in northeastern Taiwan, *Bull. Seismol. Soc. Am.* **98,** no. 1, 220–240.

Montalva, G., N. Bastias, and A. Rodriguez-Marek (2017). Ground motion prediction equation for the Chilean subduction zone, *Bull. Seismol. Soc. Am.* **107,** no. 2, doi: 10.1785/0120160221.

Nakano, M., H. Kumagai, and H. Inoue (2008). Waveform inversion in the frequency domain for the simultaneous determination of earthquake source mechanism and moment function, *Geophys. J. Int.* **173,** 1000–1011, doi: 10.1111/j.1365-246X.2008.03783.x.

Nocquet, J.-M., P. Jarrin, M. Vallée, P. A. Mothes, R. Grandin, F. Rolandone, B. Delouis, H. Yepes, Y. Font, D. Fuentes, *et al.* (2016). Supercycle at the Ecuadorian subduction zone revealed after the 2016 Pedernales earthquake, *Nature Geosci.* doi: 10.1038/ngeo2864.

Pagani, M., D. Monelli, G. Weatherill, L. Danciu, H. Crowley, V. Silva, P. Henshaw, L. Butler, M. Nastasi, L. Panzeri, *et al.* (2014). OpenQuake-engine: An open hazard (and risk) software for the global earthquake model, *Seismol. Res. Lett.* **85,** 692–702.

Perron, V., C. Gélis, F. Hollender, P.-Y. Bard, B. Froment, E. M. Cushing, and G. Cultrera (2016). Broadband site effect assessment: comparison between approaches based on earthquakes and microtremors on two sites, *5th IASPEI/IAEE International Symposium:*

Effects of Surface Geology on Seismic Motion, Taipei, Taiwan, 15–17 August.

Scherbaum, F., E. Delavaud, and C. Riggelsen (2009). Model selection in seismic hazard analysis: An information-theoretic perspective, *Bull. Seismol. Soc. Am.* **99,** no. 6, 3234–3247.

Strasser, F. O., M. C. Arango, and J. J. Bommer (2010). Scaling of the source dimensions of interface and intraslab subduction-zone earthquakes with moment magnitude, *Seismol. Res. Lett.* **81,** 941–950.

TRX Consulting C.A. (2011a). *Estudio de Caracterización de Ruta con Métodos Geofísicos no Invasivos*, TRX Consulting C.A. (in Spanish).

TRX Consulting C.A. (2011b). *Aplicación Métodos Geofísicos en Caracterización de Sitio*, TRX Consulting C.A. (in Spanish).

Vera-Grunauer, X. (2014). Seismic response of a soft, high plasticity, diatomaceous naturally cemented clay deposit, Ph.D. dissertation, University of California, Berkeley, 909 pp.

Wald, D. J., and T. I. Allen (2007). Topographic slope as a proxy for seismic site conditions and amplification, *Bull. Seismol. Soc. Am.* **97,** no. 5, 1379–1395.

Weatherill, G. A. (2014). OpenQuake ground motion toolkit—User guide, *Global Earthquake Model (GEM). Technical Report*, 88 pp.

Yepes, H., L. Audin, A. Alvarado, C. Beauval, J. Aguilar, Y. Font, and F. Cotton (2016). A new view of Ecuador's geodynamic context and its implications for seismogenic sources definition and seismic hazard assessment, *Tectonics* **35,** doi: 10.1002/2015TC003941.

Youngs, R. R., S. J. Chiou, W. J. Silva, and J. R. Humphrey (1997). Strong ground motion attenuation relationships for subduction zone earthquakes, *Seismol. Res. Lett.* **68,** no. 1, 58–73.

Zhao, J. X., K. Irikura, J. Zhang, Y. Fukushima, P. G. Somerville, A. Asano, Y. Ohno, T. Oouchi, T. Takahashi, and H. Ogawa (2006). An empirical site-classification method for strong-motion stations in Japan using H/V response spectral ratios, *Bull. Seismol. Soc. Am.* **96,** no. 3, 914–925.

Zhao, J. X., J. Zhang, A. Asano, Y. Ohno, T. Oouchi, T. Takahashi, H. Ogawa, K. Irikura, H. K. Thio, P. G. Somerville, *et al.* (2006). Attenuation relations of strong ground motion in Japan using site classification based on predominant period, *Bull. Seismol. Soc. Am.* **96,** no. 3, 898–913.

Céline Beauval
J. Marinière
E. Maufroy
ISTerre, Université Grenoble Alpes, IRD, CNRS, OSUG
CS 40700
38058 Grenoble, CEDEX 9
France
celine.beauval@univ-grenoble-alpes.fr

A. Laurendeau
J.-C. Singaucho
C. Viracucha
H. Yepes
M. Ruiz
A. Alvarado
Escuela Politecnica Nacional
Instituto Geofísico
Ladrón de Guevara E11-253, Apartado 2759
Quito 170143, Ecuador

M. Vallée
Institut de Physique du Globe de Paris
1 Rue Jussieu, 75005 Paris
France

D. Mercerat
CEREMA
56, Boulevard Stalingrad
06359 Nice, CEDEX 4
France

Published Online 15 February 2017

Bibliography

Abe, K. (1981). Magnitudes of large shallow earthquakes from 1904 to 1980. *Physics of the Earth and Planetary Interiors*, 27(1):72–92.

Abrahamson, N., Gregor, N., and Addo, K. (2016). BC Hydro Ground Motion Prediction Equations for Subduction Earthquakes. *Earthquake Spectra*, 32(1):23–44. Publisher: SAGE Publications Ltd STM.

Akkar, S. and Bommer, J. J. (2010). Empirical Equations for the Prediction of PGA, PGV, and Spectral Accelerations in Europe, the Mediterranean Region, and the Middle East. *Seismological Research Letters*, 81(2):195–206.

Altamimi, Z., Rebischung, P., Metivier, L., and Collilieux, X. (2016). ITRF2014: A new release of the International Terrestrial Reference Frame modeling nonlinear station motions: ITRF2014. *Journal of Geophysical Research: Solid Earth*, 121(8):6109–6131.

Alvarado, A. (2012). *Neotectonique et cinematique de la deformation continentale en Equateur*. PhD thesis, Universite Grenoble Alpes.

Alvarado, A., Audin, L., Nocquet, J. M., Jaillard, E., Mothes, P., Jarrin, P., Segovia, M., Rolandone, F., and Cisneros, D. (2016). Partitioning of oblique convergence in the Northern Andes subduction zone: Migration history and the present-day boundary of the North Andean Sliver in Ecuador: Eastern limit of the north andean sliver. *Tectonics*, 35(5):1048–1065.

Alvarado, A., Audin, L., Nocquet, J. M., Lagreulet, S., Segovia, M., Font, Y., Lamarque, G., Yepes, H., Mothes, P., Rolandone, F., Jarrin, P., and Quidelleur, X. (2014). Active tectonics in Quito, Ecuador, assessed by geomorphological studies, GPS data, and crustal seismicity. *Tectonics*, 33(2):67–83.

Alvarado, A., Ruiz, M., Mothes, P., Yepes, H., Segovia, M., Vaca, M., Ramos, C., Enriquez, W., Ponce, G., Jarrin, P., Aguilar, J., Acero, W., Vaca, S., Singaucho,

J. C., Pacheco, D., and Córdova, A. (2018). Seismic, Volcanic, and Geodetic Networks in Ecuador: Building Capacity for Monitoring and Research. *Seismological Research Letters*, 89(2A):432–439.

Anderson, J. G. (1979). Estimating the seismicity from geological structure for seismic-risk studies. *Bulletin of the Seismological Society of America*, 69(1):135–158.

Anderson, J. G. and Luco, J. E. (1983). Consequences of slip rate constraints on earthquake occurrence relations. *Bulletin of the Seismological Society of America*, 73(2):471–496.

Ang, A. H.-S. and Tang, W. H. (1975). *Probability concepts in engineering planning and design Vol. 1, Vol. 1,*. Wiley, New York; London.

Araujo, S. (2016). *Travel time tomography of the crust and the mantle beneath Ecuador from data of the national seismic network*. PhD thesis, Universite Grenoble Alpes, Institut des Sciences de la Terre.

Atkinson, G. and Boore, D. (2006). Earthquake ground-motion prediction equations for eastern North America. *Bulletin of the Seismological Society of America*, 96(6):2181–2205.

Avouac, J.-P. (2015). From Geodetic Imaging of Seismic and Aseismic Fault Slip to Dynamic Modeling of the Seismic Cycle. *Annual Review of Earth and Planetary Sciences*, 43(1):233–271.

Baby, P., Rivadeneira, M., Barragan, R., and Christophoul, F. (2013). Thick-skinned tectonics in the Oriente foreland basin of Ecuador. *Geological Society, London, Special Publications*, 377(1):59.

Baize, S., Audin, L., Winter, T., Alvarado, A., Pilatasig Moreno, L., Taipe, M., Reyes, P., Kauffmann, P., and Yepes, H. (2015). Paleoseismology and tectonic geomorphology of the Pallatanga fault (Central Ecuador), a major structure of the South-American crust. *Geomorphology*, 237:14–28.

Baize, S., Cushing, E. M., Lemeille, F., and Jomard, H. (2013). Updated seismotectonic zoning scheme of Metropolitan France, with reference to geologic and seismotectonic data. *Bulletin de la Societe Geologique de France*, 184(3):225–259.

Beauval, C., Bard, P.-Y., and Danciu, L. (2020). The influence of source- and ground-motion model choices on probabilistic seismic hazard levels at 6 sites in France. *Bulletin of Earthquake Engineering*, 18(10):4551–4580.

Beauval, C., Mariniere, J., Laurendeau, A., Singaucho, J.-C., Viracucha, C., Vallee, M., Maufroy, E., Mercerat, D., Yepes, H., Ruiz, M., and Alvarado, A. (2017). Comparison of Observed Ground-Motion Attenuation for the 16 April 2016 M_{w} 7.8 Ecuador Megathrust Earthquake and Its Two Largest Aftershocks with

Existing Ground-Motion Prediction Equations. *Seismological Research Letters*, 88(2A):287–299.

Beauval, C., Mariniere, J., Yepes, H., Audin, L., Nocquet, J.-M., Alvarado, A., Baize, S., Aguilar, J., Singaucho, J.-C., and Jomard, H. (2018). A New Seismic Hazard Model for Ecuador. *Bulletin of the Seismological Society of America*, 108(3A):1443–1464.

Beauval, C., Yepes, H., Audin, L., Alvarado, A., Nocquet, J.-M., Monelli, D., and Danciu, L. (2014). Probabilistic Seismic-Hazard Assessment in Quito, Estimates and Uncertainties. *Seismological Research Letters*, 85(6):1316–1327.

Beauval, C., Yepes, H., Bakun, W. H., Egred, J., Alvarado, A., and Singaucho, J.-C. (2010). Locations and magnitudes of historical earthquakes in the Sierra of Ecuador (1587-1996). *Geophysical Journal International*.

Beauval, C., Yepes, H., Palacios, P., Segovia, M., Alvarado, A., Font, Y., Aguilar, J., Troncoso, L., and Vaca, S. (2013). An Earthquake Catalog for Seismic Hazard Assessment in Ecuador. *Bulletin of the Seismological Society of America*, 103(2A):773–786.

Bernard, S., Avouac, J.-P., Dominguez, S., and Simoes, M. (2007). Kinematics of fault-related folding derived from a sandbox experiment. *Journal of Geophysical Research*, 112(B3):B03S12.

Bilek, S. L. and Lay, T. (1999). Rigidity variations with depth along interplate megathrust faults in subduction zones. *Nature*, 400(6743):443–446.

Brax, M., Albini, P., Beauval, C., Jomaa, R., and Sursock, A. (2019). An Earthquake Catalog for the Lebanese Region. *Seismological Research Letters*, 90(6):2236–2249.

Brune, J. N. (1968). Seismic moment, seismicity, and rate of slip along major fault zones. *Journal of Geophysical Research*, 73(2):777–784.

Champenois, J., Audin, L., Baize, S., Jomard, H., Nocquet, J.-M., and Alvarado, A. (2013). Interseismic deformations along Ecuador active fault systems: Contribution of space-borne SAR Interferometry.

Champenois, J., Baize, S., and Jomard, H. (2015). Apport des methodes d'imagerie radar satellitaire pour l'etude des deformations de surface. PRP-DGE/SCAN/BERSSIN.

Chlieh, M., Mothes, P., Nocquet, J.-M., Jarrin, P., Charvis, P., Cisneros, D., Font, Y., Collot, J.-Y., Villegas-Lanza, J.-C., Rolandone, F., Vallee, M., Regnier, M., Segovia, M., Martin, X., and Yepes, H. (2014). Distribution of discrete seismic asperities and aseismic slip along the Ecuadorian megathrust. *Earth and Planetary Science Letters*, 400:292–301.

Chlieh, M., Perfettini, H., Tavera, H., Avouac, J.-P., Remy, D., Nocquet, J.-M., Rolandone, F., Bondoux, F., Gabalda, G., and Bonvalot, S. (2011). Interseismic coupling and seismic potential along the Central Andes subduction zone. *Journal of Geophysical Research*, 116(B12).

Collot, J.-Y., Michaud, F., Alvarado, A., Marcaillou, B., Sosson, M., Ratzov, G., Migeon, S., Calahorrano, A., and Pazmino, A. (2009). Vision general de la morfologia submarina del margen convergente de Ecuador-Sur de Colombia : implicaciones sobre la transferencia de masa y la edad de la subduccion de la Cordillera de Carnegie. In *Geologia y geofisica marina y terrestre del Ecuador : desde la costa continental hasta las Islas Galapagos*, pages 47–74. CNDM ; IRD ; INOCAR.

Cornell, C. A. (1968). Engineering seismic risk analysis. *Bulletin of the Seismological Society of America*, 58(5):1583–1606.

D'Agostino, N. (2014). Complete seismic release of tectonic strain and earthquake recurrence in the Apennines (Italy). *Geophysical Research Letters*, 41(4):1155–1162.

Daout, S., Barbot, S., Peltzer, G., Doin, M.-P., Liu, Z., and Jolivet, R. (2016a). Constraining the kinematics of metropolitan Los Angeles faults with a slip-partitioning model: Slip partitioning in southern california. *Geophysical Research Letters*, 43(21):11,192–11,201.

Daout, S., Jolivet, R., Lasserre, C., Doin, M.-P., Barbot, S., Tapponnier, P., Peltzer, G., Socquet, A., and Sun, J. (2016b). Along-strike variations of the partitioning of convergence across the Haiyuan fault system detected by InSAR. *Geophysical Journal International*, 205(1):536–547.

Di Giacomo, D., Bondar, I., Storchak, D. A., Engdahl, E. R., Bormann, P., and Harris, J. (2015). ISC-GEM: Global Instrumental Earthquake Catalogue (1900–2009), III. Re-computed MS and mb, proxy MW, final magnitude composition and completeness assessment. *Physics of the Earth and Planetary Interiors*, 239:33–47.

Doin, M.-P., Lodge, F., Guillaso, S., Jolivet, R., Lasserre, C., Ducret, G., Grandin, R., Pathier, E., and Pinel, V. (2011). Presentation of the small baseline nsbas processing chain on a case example: The etna deformation monitoring from 2003 to 2010 using envisat data. *Proc. 'Fringe 2011 Workshop', Frascati, Italy.*

Dumont, J., Santana, E., Valdez, F., Tihay, J., Usselmann, P., Iturralde, D., and Navarette, E. (2006). Fan beheading and drainage diversion as evidence of a 3200-2800 BP earthquake event in the Esmeraldas-Tumaco seismic zone: A case study for the effects of great subduction earthquakes. *Geomorphology*, 74(1-4):100–123.

Dziewonski, A. M., Chou, T.-A., and Woodhouse, J. H. (1981). Determination of earthquake source parameters from waveform data for studies of global and regional seismicity. *Journal of Geophysical Research: Solid Earth*, 86(B4):2825–2852.

Egred, J. (2009). Catalogo de terremotos del Ecuador 1541–2009,.

Ekström, G., Nettles, M., and Dziewoński, A. (2012). The global CMT project 2004–2010: Centroid-moment tensors for 13,017 earthquakes. *Physics of the Earth and Planetary Interiors*, 200-201:1–9.

Field, E. H., Arrowsmith, R. J., Biasi, G. P., Bird, P., Dawson, T. E., Felzer, K. R., Jackson, D. D., Johnson, K. M., Jordan, T. H., Madden, C., Michael, A. J., Milner, K. R., Page, M. T., Parsons, T., Powers, P. M., Shaw, B. E., Thatcher, W. R., Weldon, II, R. J., and Zeng, Y. (2014). Uniform California Earthquake Rupture Forecast, Version 3 (UCERF3)—The Time-Independent Model. *Bulletin of the Seismological Society of America*, 104(3):1122–1180.

Field, E. H., Jackson, D. D., and Dolan, J. F. (1999). A mutually consistent seismic-hazard source model for southern California. *Bulletin of the Seismological Society of America*, 89(3):559–578.

Floyd, M. A., Billiris, H., Paradissis, D., Veis, G., Avallone, A., Briole, P., McClusky, S., Nocquet, J.-M., Palamartchouk, K., Parsons, B., and England, P. C. (2010). A new velocity field for Greece: Implications for the kinematics and dynamics of the Aegean. *Journal of Geophysical Research: Solid Earth*, 115(B10).

Font, Y., Segovia, M., Vaca, S., and Theunissen, T. (2013). Seismicity patterns along the Ecuadorian subduction zone: new constraints from earthquake location in a 3-D a priori velocity model. *Geophysical Journal International*, 193(1):263–286.

Fukahata, Y. and Matsu'ura, M. (2006). Quasi-static internal deformation due to a dislocation source in a multilayered elastic/viscoelastic half-space and an equivalence theorem. *Geophysical Journal International*, 166(1):418–434.

Gailler, A., Charvis, P., and Flueh, E. R. (2007). Segmentation of the Nazca and South American plates along the Ecuador subduction zone from wide angle seismic profiles. *Earth and Planetary Science Letters*, 260(3-4):444–464.

Garcia-Aristizabal, A., Kumagai, H., Samaniego, P., Mothes, P., Yepes, H., and Monzier, M. (2007). Seismic, petrologic, and geodetic analyses of the 1999 dome-forming eruption of Guagua Pichincha volcano, Ecuador. *Journal of Volcanology and Geothermal Research*, 161(4):333–351.

Gardner, J. K. and Knopoff, L. (1974). Is the sequence of earthquakes in Southern California, with aftershocks removed, Poissonian? *Bulletin of the Seismological Society of America*, 64(5):1363–1367.

Ghofrani, H. and Atkinson, G. M. (2014). Ground-motion prediction equations for interface earthquakes of M7 to M9 based on empirical data from Japan. *Bulletin of Earthquake Engineering*, 12(2):549–571.

Gombert, B., Duputel, Z., Jolivet, R., Simons, M., Jiang, J., Liang, C., Fielding, E., and Rivera, L. (2018). Strain budget of the Ecuador–Colombia subduction zone: A stochastic view. *Earth and Planetary Science Letters*, 498:288–299.

Graindorge, D. (2004). Deep structures of the Ecuador convergent margin and the Carnegie Ridge, possible consequence on great earthquakes recurrence interval. *Geophysical Research Letters*, 31(4).

Grünthal, G., Stromeyer, D., Bosse, C., Cotton, F., and Bindi, D. (2018). The probabilistic seismic hazard assessment of Germany—version 2016, considering the range of epistemic uncertainties and aleatory variability. *Bulletin of Earthquake Engineering*, 16(10):4339–4395.

Guillier, B., Chatelain, J.-L., Jaillard, E., Yepes, H., Poupinet, G., and Fels, J.-F. (2001). Seismological evidence on the geometry of the Orogenic System in central-northern Ecuador (South America). *Geophysical Research Letters*, 28(19):3749–3752.

Gutenberg, B. and Richter, C. F. (1944). Frequency of earthquakes in California*. *Bulletin of the Seismological Society of America*, 34(4):185–188.

Gutenberg, B. and Richter, C. F. (1954). *Seismicity of the Earth*. Princeton press edition.

Gutscher, M.-A., Malavieille, J., Lallemand, S., and Collot, J.-Y. (1999). Tectonic segmentation of the North Andean margin: impact of the Carnegie Ridge collision. *Earth and Planetary Science Letters*, 168(3):255–270.

Hanks, T. C. and Kanamori, H. (1979). A moment magnitude scale. *Journal of Geophysical Research*, 84(B5):2348.

Harris, R. A. (2017). Large earthquakes and creeping faults: Large Earthquakes and Creeping Faults. *Reviews of Geophysics*, 55(1):169–198.

Hayes, G. P., Wald, D. J., and Johnson, R. L. (2012). Slab1.0: A three-dimensional model of global subduction zone geometries. *Journal of Geophysical Research: Solid Earth*, 117(B1):n/a–n/a.

Herring, T., King, R., Floyd, M. A., and McClusky, S. C. (2018). *GAMIT reference manual, GPS Analysis at MIT, Release 10.70*. Cambridge, mass. inst. of technol. edition.

Hey, R. (1977). Tectonic evolution of the Cocos-Nazca spreading center. *GSA Bulletin*, 88(10):1404–1420.

Hooper, A. (2008). A multi-temporal InSAR method incorporating both persistent scatterer and small baseline approaches. *Geophysical Research Letters*, 35(16).

Hooper, A., Segall, P., and Zebker, H. (2007). Persistent scatterer interferometric synthetic aperture radar for crustal deformation analysis, with application to Volcan Alcedo, Galapagos. *Journal of Geophysical Research*, 112(B7).

Hyndman, R. D., Mazzotti, S., Weichert, D., and Rogers, G. C. (2003). Frequency of large crustal earthquakes in Puget Sound-Southern Georgia Strait predicted from geodetic and geological deformation rates: GPS and Earthquakes in the Pacific Northwest. *Journal of Geophysical Research: Solid Earth*, 108(B1).

Jackson, J., Norris, R., and Youngson, J. (1996). The structural evolution of active fault and fold systems in central Otago, New Zealand: evidence revealed by drainage patterns. *Journal of Structural Geology*, 18(2-3):217–234.

Ji, L., Zhang, W., Liu, C., Zhu, L., Xu, J., and Xu, X. (2020). Characterizing interseismic deformation of the xianshuihe fault, eastern tibetan plateau, using sentinel-1 sar images. *Advances in Space Research*, 66(2):378 – 394.

Johnson, K. M. (2018). Growth of Fault-Cored Anticlines by Flexural Slip Folding: Analysis by Boundary Element Modeling. *Journal of Geophysical Research: Solid Earth*, 123(3):2426–2447.

Kagan, Y. Y. (2002). Seismic moment distribution revisited: I. Statistical results: Seismic moment distribution: I. *Geophysical Journal International*, 148(3):520–541.

Kagan, Y. Y. and Jackson, D. D. (2013). Tohoku Earthquake: A Surprise? *Bulletin of the Seismological Society of America*, 103(2B):1181–1194.

Kalia, A., Frei, M., and Lege, T. (2017). A copernicus downstream-service for the nationwide monitoring of surface displacements in germany. *Remote Sensing of Environment*, 202:234 – 249. Big Remotely Sensed Data: tools, applications and experiences.

Kanamori, H. and Anderson, D. L. (1975). Theoretical basis of some empirical relations in seismology. *Bulletin of the Seismological Society of America*, 65(5):1073–1095.

Keller, E. (2014). Caracterisation de Seismes Historiques. Application sur les Grands Seismes de Subduction en Equateur. Memoire de stage de Master 2, Master SML, UBO.

Kendrick, E., Bevis, M., Smalley, R., Brooks, B., Vargas, R. B., Lauria, E., and Fortes, L. P. S. (2003). The Nazca–South America Euler vector and its rate of change. *Journal of South American Earth Sciences*, 16(2):125–131.

Knopoff, L. and Gardner, J. K. (1972). Higher Seismic Activity During Local Night on the Raw Worldwide Earthquake Catalogue. *Geophysical Journal International*, 28(3):311–313.

Kramer, S. L. (1996). *Geotechnical Earthquake Engineering.* Prentice Hall, Upper Saddle River, New Jersey, USA.

Lasserre, C., Marconato, L., Sassolas-Serrayet, T., Zan, F. D., Ansari, H., Doin, M. P., Mazzotti, S., Cattin, R., and Ferry, M. A. (2019). Lateral variations of interseismic coupling along the himalayan arc in bhutan : Clues from time series analysis of sentinel-1 insar data ? *American Geophysical Union, Fall Meeting 2019.*

Leonard, M. (2010). Earthquake Fault Scaling: Self-Consistent Relating of Rupture Length, Width, Average Displacement, and Moment Release. *Bulletin of the Seismological Society of America*, 100(5A):1971–1988.

Lindsey, E. O., Sahakian, V. J., Fialko, Y., Bock, Y., Barbot, S., and Rockwell, T. K. (2014). Interseismic Strain Localization in the San Jacinto Fault Zone. *Pure and Applied Geophysics*, 171(11):2937–2954.

Lolli, B., Gasperini, P., and Vannucci, G. (2014). Empirical conversion between teleseismic magnitudes (mb and Ms) and moment magnitude (Mw) at the Global, Euro-Mediterranean and Italian scale. *Geophysical Journal International*, 199(2):805–828.

Marzocchi, W., Sandri, L., Heuret, A., and Funiciello, F. (2016). Where giant earthquakes may come. *Journal of Geophysical Research: Solid Earth*, 121(10):7322–7336.

Mazzotti, S., Leonard, L. J., Cassidy, J. F., Rogers, G. C., and Halchuk, S. (2011). Seismic hazard in western Canada from GPS strain rates versus earthquake catalog. *Journal of Geophysical Research*, 116(B12).

McCaffrey, R. (2005). Block kinematics of the Pacific–North America plate boundary in the southwestern United States from inversion of GPS, seismological, and geologic data. *Journal of Geophysical Research: Solid Earth*, 110(B7). Publisher: John Wiley & Sons, Ltd.

McCalpin, J. (2009). *Paleoseismology.*

Meade, B. J. (2005). Block models of crustal motion in southern California constrained by GPS measurements. *Journal of Geophysical Research*, 110(B3):B03403.

Medina, F., Harmsen, S. C., and Barrientos, S. E. (2017). Probabilitic Seismic Hazard Analysis for Chile. page 16.

Michel, S., Avouac, J.-P., Jolivet, R., and Wang, L. (2018). Seismic and Aseismic Moment Budget and Implication for the Seismic Potential of the Parkfield Segment of the San Andreas Fault. *Bulletin of the Seismological Society of America*, 108(1):19–38.

Migeon, S., Garibaldi, C., Ratzov, G., Schmidt, S., Collot, J.-Y., Zaragosi, S., and Texier, L. (2017). Earthquake-triggered deposits in the subduction trench of the north Ecuador/south Colombia margin and their implication for paleoseismology. *Marine Geology*, 384:47–62.

Mihaljević, J., Zupančič, P., Kuka, N., Kaluđerović, N., Koçi, R., Markušić, S., Šalić, R., Dushi, E., Begu, E., Duni, L., Živčić, M., Kovačević, S., Ivančić, I., Kovačević, V., Milutinović, Z., Vakilinezhad, M., Fiket, T., and Gülerce, Z. (2017). BSHAP seismic source characterization models for the Western Balkan region. *Bulletin of Earthquake Engineering*, 15(10):3963–3985.

Mogi, K. (1962). Magnitude-Frequency Relationship for Elastic Shocks Accompanying Fractures of Various Materials and Some Related Problems in Earthquakes. *Bulletin of the Earthquake Research Institute, , University of Tokyo*, 40:831–853.

Molnar, P. (1979). Earthquake recurrence intervals and plate tectonics. *Bulletin of the Seismological Society of America*, 69(1):115–133.

Montalva, G. A., Bastias, N., and Rodriguez-Marek, A. (2017). Ground-Motion Prediction Equation for the Chilean Subduction Zone. *Bulletin of the Seismological Society of America*, 107(2):901–911.

Mora-Paez, H., Kellogg, J. N., Freymueller, J. T., Mencin, D., Fernandes, R. M., Diederix, H., LaFemina, P., Cardona-Piedrahita, L., Lizarazo, S., Pelaez-Gaviria, J.-R., Diaz-Mila, F., Bohórquez-Orozco, O., Giraldo-Londoño, L., and Corchuelo-Cuervo, Y. (2019). Crustal deformation in the northern Andes – A new GPS velocity field. *Journal of South American Earth Sciences*, 89:76–91.

Morales Rivera, A. M., Amelung, F., and Mothes, P. (2016). Volcano deformation survey over the Northern and Central Andes with ALOS InSAR time series: Deformation survey over the andes. *Geochemistry, Geophysics, Geosystems*, 17(7):2869–2883.

Mothes, P. A., Nocquet, J.-M., and Jarrin, P. (2013). Continuous GPS Network Operating Throughout Ecuador. *Eos, Transactions American Geophysical Union*, 94(26):229–231. Publisher: John Wiley & Sons, Ltd.

Mothes, P. A., Rolandone, F., Nocquet, J.-M., Jarrin, P. A., Alvarado, A. P., Ruiz, M. C., Cisneros, D., Paez, H. M., and Segovia, M. (2018). Monitoring the Earthquake Cycle in the Northern Andes from the Ecuadorian cGPS Network. *Seismological Research Letters*, 89(2A):534–541.

Nocquet, J.-M. (2018). Stochastic static fault slip inversion from geodetic data with non-negativity and bounds constraints. *Geophysical Journal International*, 214(1):366–385.

Nocquet, J.-M., Jarrin, P., Vallee, M., Mothes, P. A., Grandin, R., Rolandone, F., Delouis, B., Yepes, H., Font, Y., Fuentes, D., Regnier, M., Laurendeau, A., Cisneros, D., Hernandez, S., Sladen, A., Singaucho, J.-C., Mora, H., Gomez, J., Montes, L., and Charvis, P. (2016). Supercycle at the Ecuadorian subduction zone revealed after the 2016 Pedernales earthquake. *Nature Geoscience*, 10(2):145–149.

Nocquet, J.-M., Villegas-Lanza, J. C., Chlieh, M., Mothes, P. A., Rolandone, F., Jarrin, P., Cisneros, D., Alvarado, A., Audin, L., Bondoux, F., Martin, X., Font, Y., Regnier, M., Vallee, M., Tran, T., Beauval, C., Maguiña Mendoza, J. M., Martinez, W., Tavera, H., and Yepes, H. (2014). Motion of continental slivers and creeping subduction in the northern Andes. *Nature Geoscience*, 7(4):287–291.

Pagani, M., Garcia-Pelaez, J., Gee, R., Johnson, K., Poggi, V., Silva, V., Simionato, M., Styron, R., Viganò, D., Danciu, L., Monelli, D., and Weatherill, G. (2020a). The 2018 version of the Global Earthquake Model: Hazard component. *Earthquake Spectra*, page 8755293020931866. Publisher: SAGE Publications Ltd STM.

Pagani, M., Johnson, K., and Garcia Pelaez, J. (2020b). Modelling subduction sources for probabilistic seismic hazard analysis. *Geological Society, London, Special Publications*, pages SP501–2019–120.

Pagani, M., Monelli, D., Weatherill, G., Danciu, L., Crowley, H., Silva, V., Henshaw, P., Butler, L., Nastasi, M., Panzeri, L., Simionato, M., and Vigano, D. (2014). OpenQuake Engine: An Open Hazard (and Risk) Software for the Global Earthquake Model. *Seismological Research Letters*, 85(3):692–702.

Pancha, A. (2006). Comparison of Seismic and Geodetic Scalar Moment Rates across the Basin and Range Province. *Bulletin of the Seismological Society of America*, 96(1):11–32.

Parra, H., Benito, M. B., and Gaspar-Escribano, J. M. (2016). Seismic hazard assessment in continental Ecuador. *Bulletin of Earthquake Engineering*, 14(8):2129–2159.

Patil, A., Huard, D., and Fonnesbeck, C. (2010). **PyMC** : Bayesian Stochastic Modelling in *Python*. *Journal of Statistical Software*, 35(4).

Pennington, W. D. (1981). Subduction of the Eastern Panama Basin and seismotectonics of northwestern South America. *Journal of Geophysical Research: Solid Earth*, 86(B11):10753–10770.

Petersen, M. D., Frankel, A. D., Harmsen, S. C., Mueller, C. S., Haller, K. M., Wheeler, R. L., Wesson, R. L., Zeng, Y., Boyd, O. S., Perkins, D. M., Luco, N., Field, E. H., Wills, C. J., and Rukstales, K. S. (2008). Documentation for the 2008 update of the United States National Seismic Hazard Maps. Report 2008-1128, Reston, VA. Edition: Version 1.0: April 2008; Version 1.1: May 2008.

Petersen, M. D., Harmsen, S. C., Jaiswal, K. S., Rukstales, K. S., Luco, N., Haller, K. M., Mueller, C. S., and Shumway, A. M. (2018a). Seismic Hazard, Risk, and Design for South America. *Bulletin of the Seismological Society of America*.

Petersen, M. D., Harmsen, S. C., Jaiswal, K. S., Rukstales, K. S., Luco, N., Haller, K. M., Mueller, C. S., and Shumway, A. M. (2018b). Seismic Hazard, Risk, and Design for South America: U.S. Geological Survey data release.

Pino, D. and Yepes, H. (1990). Apuntes para una historia sismica de Quito. Centro Historico de Quito. Problematica y perspectivas.

Proust, J. N., Martillo, C., Michaud, F., Collot, J. Y., and Dauteuil, O. (2016). Subduction of seafloor asperities revealed by a detailed stratigraphic analysis of the active margin shelf sediments of Central Ecuador. *Marine Geology*, 380:345–362.

Raspini, F., Bianchini, S., Ciampalini, A., Del Soldato, M., Solari, L., Novali, F., Del Conte, S., Rucci, A., Ferretti, A., and Casagli, N. (2018). Continuous, semi-automatic monitoring of ground deformation using Sentinel-1 satellites. *Scientific reports*, 8(1):7253–7253. Publisher: Nature Publishing Group UK.

Reasenberg, P. (1985). Second-order moment of central California seismicity, 1969-1982. *Journal of Geophysical Research: Solid Earth*, 90(B7):5479–5495.

Reguzzoni, M., Sampietro, D., and Sansò, F. (2013). Global Moho from the combination of the CRUST2.0 model and GOCE data. *Geophysical Journal International*, 195(1):222–237.

Reiter, L. L. (1990). *Earthquake hazard analysis : issues and insights / Leon Reiter*. Number Accessed from https://nla.gov.au/nla.cat-vn1099068. Columbia University Press, New York.

Rolandone, F., Nocquet, J.-M., Mothes, P. A., Jarrin, P., Vallee, M., Cubas, N., Hernandez, S., Plain, M., Vaca, S., and Font, Y. (2018). Areas prone to slow slip events impede earthquake rupture propagation and promote afterslip. *Science Advances*, 4(1):eaao6596.

Rong, Y., Jackson, D. D., Magistrale, H., and Goldfinger, C. (2014). Magnitude Limits of Subduction Zone Earthquakes. *Bulletin of the Seismological Society of America*, 104(5):2359–2377.

Sagaiya, T. and Mora-Paez, H. (2020). Interplate coupling along the Nazca subduction zone on the Pacific coast of Colombia deduced from GeoRED GPS observation data. In *The Geology of Colombia, Volume 4 Quaternary.*, Servicio Geológico Colombiano, Publicaciones Geológicas Especiales 38, page 15. Bogota, gómez, j. & pinilla–pachon, a.o. edition.

Sallares, V. and Charvis, P. (2003). Crustal thickness constraints on the geodynamic evolution of the Galapagos Volcanic Province. *Earth and Planetary Science Letters*, 214(3):545–559.

Savage, H. M. and Cooke, M. L. (2003). Can flat-ramp-flat fault geometry be inferred from fold shape?: A comparison of kinematic and mechanical folds. *Journal of Structural Geology*, 25(12):2023–2034.

Savage, J. C. (1983). A dislocation model of strain accumulation and release at a subduction zone. *Journal of Geophysical Research: Solid Earth*, 88(B6):4984–4996.

Scala, A., Lorito, S., Romano, F., Murphy, S., Selva, J., Basili, R., Babeyko, A., Herrero, A., Hoechner, A., Løvholt, F., Maesano, F. E., Perfetti, P., Tiberti, M. M., Tonini, R., Volpe, M., Davies, G., Festa, G., Power, W., Piatanesi, A., and Cirella, A. (2020). Effect of Shallow Slip Amplification Uncertainty on Probabilistic Tsunami Hazard Analysis in Subduction Zones: Use of Long-Term Balanced Stochastic Slip Models. *Pure and Applied Geophysics*, 177(3):1497–1520.

Scholz, C. H. and Campos, J. (2012). The seismic coupling of subduction zones revisited. *Journal of Geophysical Research: Solid Earth*, 117(B5). Publisher: John Wiley & Sons, Ltd.

Schorlemmer, D. and Gerstenberger, M. C. (2007). RELM Testing Center. *Seismological Research Letters*, 78(1):30–36.

Schwartz, D. P. and Coppersmith, K. J. (1984). Fault behavior and characteristic earthquakes: Examples from the Wasatch and San Andreas Fault Zones. *Journal of Geophysical Research: Solid Earth*, 89(B7):5681–5698. Publisher: John Wiley & Sons, Ltd.

Scotti, O., Clement, C., and Baumont, D. (2014). Seismic hazard for design and verification of nuclear installations in france: regulatory context, debated issues and ongoing developments. *Bollettino Di Geofisica Teorica Ed Applicata*, 55(1):135–148.

Segall, P. (2010). *Earthquake and volcano deformation*. Princeton University Press, Princeton, N.J. OCLC: ocn318057871.

Staller, A., Álvarez Gómez, J., Luna, M., Bejar, M., Gaspar-Escribano, J., and Martinez-Cuevas, S. (2018). Crustal motion and deformation in Ecuador from cGNSS time series. *Journal of South American Earth Sciences*, 86:94–109.

Stauder, W. (1975). Subduction of the Nazca Plate under Peru as evidenced by focal mechanisms and by seismicity. *Journal of Geophysical Research (1896-1977)*, 80(8):1053–1064. Publisher: John Wiley & Sons, Ltd.

Stevens, V. L. and Avouac, J.-P. (2016). Millenary Mw>9.0 earthquakes required by geodetic strain in the Himalaya. *Geophysical Research Letters*, 43(3):1118–1123.

Stevens, V. L. and Avouac, J.-P. (2017). Determination of Mmax from Background Seismicity and Moment Conservation. *Bulletin of the Seismological Society of America*, 107(6):2578–2596.

Stevens, V. L., Shrestha, S. N., and Maharjan, D. K. (2018). Probabilistic Seismic Hazard Assessment of Nepal. *Bulletin of the Seismological Society of America*, 108(6):3488–3510.

Stirling, M., McVerry, G., Gerstenberger, M., Litchfield, N., Van Dissen, R., Berryman, K., Barnes, P., Wallace, L., Villamor, P., Langridge, R., Lamarche, G., Nodder, S., Reyners, M., Bradley, B., Rhoades, D., Smith, W., Nicol, A., Pettinga, J., Clark, K., and Jacobs, K. (2012). National Seismic Hazard Model for New Zealand: 2010 Update. *Bulletin of the Seismological Society of America*, 102(4):1514–1542.

Storchak, D., Di Giacomo, D., Engdahl, E., Harris, J., Bondar, I., Lee, W., Bormann, P., and Villaseñor, A. (2015). The ISC-GEM Global Instrumental Earthquake Catalogue (1900–2009): Introduction. *Physics of the Earth and Planetary Interiors*, 239:48–63.

Storchak, D. A., Harris, J., Brown, L., Lieser, K., Shumba, B., Verney, R., Di Giacomo, D., and Korger, E. I. M. (2017). Rebuild of the Bulletin of the International Seismological Centre (ISC), part 1: 1964–1979. *Geoscience Letters*, 4(1):32.

Strasser, F. O., Arango, M. C., and Bommer, J. J. (2010). Scaling of the Source Dimensions of Interface and Intraslab Subduction-zone Earthquakes with Moment Magnitude. *Seismological Research Letters*, 81(6):941–950.

Tarantola, A. (2005). *Inverse Problem Theory and Methods for Model Parameter Estimation.* Other Titles in Applied Mathematics. Society for Industrial and Applied Mathematics.

Teng, G. and Baker, J. W. (2019). Seismicity Declustering and Hazard Analysis of the Oklahoma–Kansas Region. *Bulletin of the Seismological Society of America*, 109(6):2356–2366.

Thomas, M. Y., Avouac, J.-P., Champenois, J., Lee, J.-C., and Kuo, L.-C. (2014). Spatiotemporal evolution of seismic and aseismic slip on the Longitudinal Valley Fault, Taiwan. *Journal of Geophysical Research: Solid Earth*, 119(6):5114–5139.

Thompson, T. B., Plesch, A., Shaw, J. H., and Meade, B. J. (2015). Rapid slip-deficit rates at the eastern margin of the Tibetan Plateau prior to the 2008 mw 7.9 Wenchuan earthquake. *Geophysical Research Letters*, 42(6):1677–1684.

Tibaldi, A., Rovida, A., and Corazzato, C. (2007). Late Quaternary kinematics, slip-rate and segmentation of a major Cordillera-parallel transcurrent fault: The Cayambe-Afiladores-Sibundoy system, NW South America. *Journal of Structural Geology*, 29(4):664–680.

Trenkamp, R., Kellogg, J. N., Freymueller, J. T., and Mora, H. P. (2002). Wide plate margin deformation, southern Central America and northwestern South America, CASA GPS observations. *Journal of South American Earth Sciences*, 15(2):157–171.

Vaca, S., Vallee, M., Nocquet, J.-M., and Alvarado, A. (2019). Active deformation in Ecuador enlightened by a new waveform-based catalog of earthquake focal mechanisms. *Journal of South American Earth Sciences*, 93:449–461.

Vaca, S., Vallee, M., Nocquet, J.-M., Battaglia, J., and Regnier, M. (2018). Recurrent slow slip events as a barrier to the northward rupture propagation of the 2016 Pedernales earthquake (Central Ecuador). *Tectonophysics*, 724-725:80–92.

Van Stiphout, T., Zhuang, J., and Marsan, D. (2012). Seismicity declustering, Community Online Resource for Statistical Seismicity Analysis. page 25.

Vergne, J., Cattin, R., and Avouac, J. P. (2001). On the use of dislocations to model interseismic strain and stress build-up at intracontinental thrust faults. *Geophysical Journal International*, 147(1):155–162.

Villegas-Lanza, J. C., Chlieh, M., Cavalie, O., Tavera, H., Baby, P., Chire-Chira, J., and Nocquet, J.-M. (2016). Active tectonics of Peru: Heterogeneous interseismic coupling along the Nazca megathrust, rigid motion of the Peruvian Sliver, and Subandean shortening accommodation. *Journal of Geophysical Research: Solid Earth*, 121(10):7371–7394. Publisher: John Wiley & Sons, Ltd.

Ward, S. N. (1994). A multidisciplinary approach to seismic hazard in southern California. *Bulletin of the Seismological Society of America*, 84(5):1293–1309.

Weichert, D. H. (1980). Estimation of the earthquake recurrence parameters for unequal observation periods for different magnitudes. *Bulletin of the Seismological Society of America*, 70(4):1337–1346.

White, S. M., Trenkamp, R., and Kellogg, J. N. (2003). Recent crustal deformation and the earthquake cycle along the Ecuador–Colombia subduction zone. *Earth and Planetary Science Letters*, 216(3):231–242.

Wiemer, S. (2001). A Software Package to Analyze Seismicity: ZMAP. *Seismological Research Letters*, 72(3):373–382.

Williams, S. (2005). Create and Analyse Time Series : CATS software V3.1. pages 1–13.

Ye, L., Kanamori, H., Avouac, J.-P., Li, L., Cheung, K. F., and Lay, T. (2016). The 16 April 2016, M7.8 (M7.5) Ecuador earthquake: A quasi-repeat of the 1942 M7.5 earthquake and partial re-rupture of the 1906 M8.6 Colombia–Ecuador earthquake. *Earth and Planetary Science Letters*, 454:248–258.

Yepes, H., Audin, L., Alvarado, A., Beauval, C., Aguilar, J., Font, Y., and Cotton, F. (2016). A new view for the geodynamics of Ecuador: Implication in seismogenic source definition and seismic hazard assessment: Ecuador Geodynamics and PSHA. *Tectonics*, 35(5):1249–1279.

Youngs, R. and Coppersmith, K. (1985). Implications of fault slip rates and earthquake recurrence models to probabilistic seismic hazard estimates. *International Journal of Rock Mechanics and Mining Sciences & Geomechanics Abstracts*, 23(4):125.

Zhao, J. X. (2006). Attenuation Relations of Strong Ground Motion in Japan Using Site Classification Based on Predominant Period. *Bulletin of the Seismological Society of America*, 96(3):898–913.

Zöller, G. (2013). Convergence of the frequency-magnitude distribution of global earthquakes: Maybe in 200 years: frequency-magnitude distribution. *Geophysical Research Letters*, 40(15):3873–3877.